



Durham E-Theses

Photophysical Investigations of Triplet Harvesting Mechanisms in Metal-Free Organic Emitters

HUANG, RONGJUAN

How to cite:

HUANG, RONGJUAN (2019) *Photophysical Investigations of Triplet Harvesting Mechanisms in Metal-Free Organic Emitters*, Durham theses, Durham University. Available at Durham E-Theses Online: <http://etheses.dur.ac.uk/13250/>

Use policy

The full-text may be used and/or reproduced, and given to third parties in any format or medium, without prior permission or charge, for personal research or study, educational, or not-for-profit purposes provided that:

- a full bibliographic reference is made to the original source
- a [link](#) is made to the metadata record in Durham E-Theses
- the full-text is not changed in any way

The full-text must not be sold in any format or medium without the formal permission of the copyright holders.

Please consult the [full Durham E-Theses policy](#) for further details.

Photophysical Investigations of Triplet Harvesting Mechanisms in Metal-Free Organic Emitters

Rongjuan Huang

A Thesis presented for the degree of
Doctor of Philosophy



Organic Electroactive Materials Research Group
Department of Physics
University of Durham
England

May 2019

Dedicated to

My parents,
For giving me my life,
endless love and support throughout my life.

My sister and brother,
For always standing by me,
giving continuous care and encouragement.

Photophysical Investigations of Triplet Harvesting Mechanisms in Metal-Free Organic Emitters

Rongjuan Huang

Submitted for the degree of Doctor of Philosophy

May 2019

Abstract

Metal-free organic molecules exhibiting thermally activated delayed fluorescence (TADF) and/or room temperature phosphorescence (RTP) have attracted great attention due to their promising potential for applications in emerging optoelectronic technologies, including sensors, imaging, anti-counterfeiting and organic light-emitting diodes (OLEDs). TADF is a mechanism that can upconvert dark triplet states to emissive singlet excited states *via* reverse intersystem crossing (RISC). RTP emitters instead show a substantial high triplet formation yield along with a relatively fast triplet radiative decay rate and suppressed non-radiative deactivation pathways. Both TADF and RTP are promising and efficient approaches to harvesting the non-emissive triplet states, which can overcome the limitation of 25% internal quantum efficiency imposed by spin-statistics in OLEDs.

Although the development of metal-free organic TADF and RTP emitters has greatly progressed in recent years, various challenges still exist concerning the full understanding of the mechanisms. The photophysical properties of metal-free organic donor-acceptor-donor (D-A-D or D-A) molecules were investigated in this thesis. The aim is to investigate the roles of isomerization and molecular conformation, and the effects of energy alignment of relevant electronic excited states on the TADF and RTP mechanisms.

The work starts with the study of a series of D-A-D molecules and their structural isomers. Dual emission with contributions from both TADF and RTP is observed in some of these isomers, while others are purely fluorescent. This work

highlights the similarity of these two mechanisms and the influence of D–A linkage on the intersystem crossing rates. This is followed by an investigation of the influence of molecular conformation on the TADF and RTP mechanisms, using the steric effect induced by the presence of alkyl substituents to manipulate the conformation of D–A–D emitters. The exciting topic of conformational control of RTP and TADF mechanisms in molecular crystals is then explored. Subsequent chapters address the effects of the substituents with different electron-donating, and electron-withdrawing strength on TADF emitters as a facile way to tune the electronic interactions and the energy of TADF luminescence. A clear understanding of how these effects influence the mechanisms will give clear guidelines for the design of novel and more efficient TADF and RTP emitters.

Declaration

The work in this thesis is based on research carried out at the Organic Electroactive Materials Group, the Department of Physics, England. No part of this thesis has been submitted elsewhere for any other degree or qualification and it is all my own work unless referenced to the contrary in the text.

Copyright © 2019 by Rongjuan Huang.

“The copyright of this thesis rests with the author. No quotations from it should be published without the author’s prior written consent and information derived from it should be acknowledged”.

Acknowledgements

Upon the completion of my thesis, a great many people deserve my gratitude for their enthusiastic help throughout all my PhD studies.

To my supervisor, thank you Dr. Fernando Dias for patient guidance, encouragement and advice during my study. Since this field was brand new for me in the beginning, it would be very difficult to progress without your continuous support. To my co-supervisor, thanks Prof. Andrew Monkman for confident and enthusiastic attitude on research giving me great motivation.

To all the members in OEM group, thanks for creating an enjoyable working environment. Great thanks to Roberto, Paloma and Daniel, who gave me unwavering friendship both in personal and academic support. Many thanks to Drs. Andrew Danos, Chris Manolaou, Marc Etherington and Nadya Kukhta, for donating time and never tiring of revising my thesis. Thanks also to Heather, Przemysław, Peter, Chunyong and Patricja for helpful suggestions regarding daily research. To all my collaborators, thanks for enriching my study, especially to Prof. Martin Bryce's research group.

To all my lovely friends, thanks for never leaving me alone. Particularly to Huizhe, Xiangwen and Ningning, thanks for mutual encouragement and day-to-day shenanigans making my PhD life so enjoyable. Thank you Helen, for giving me great suggestions during writing. Thank you Jin, Fei, Peng and your families, Zhengkun, Jipeng, Zhao, Guangfu, Xialei, Wei, Xuwen and other friends for organizing various activities and enriching my spare time life. I wish you all the best in the future.

To my dearest family, thanks for all the understanding and support behind me.

Finally to Durham University, thanks for the financial support of Durham Doctoral Scholarship (DDS) during my PhD study.

Abbreviations

CBP	4,4'-Bis(carbazol-9-yl)biphenyl
CT	Charge transfer
CV	Cyclic voltammetry
DCM	Dichloromethane
DF	Delayed fluorescence
DPEPO	Bis[2-(diphenylphosphino)phenyl]ether oxide
EA	Electron affinity
EBL	Electron blocking layer
EIL	Electron injection layer
EL	Electroluminescence
EML	Light-emitting layer
EQE	External quantum efficiency
ΔE_{ST}	Singlet-triplet energy splitting
ETL	Electron transport layer
HBL	Hole blocking layer
HFC	Hyperfine coupling
HIL	Hole injection layer
HOMO	Highest occupied molecular orbital
HTL	Hole transport layer
IC	Internal conversion
iCCD	Intensified charge-coupled device
IP	Ionization potential
IQE	Internal quantum efficiency
IRF	Instrument response function

ISC	Intersystem crossing
ITO	Indium tin oxide
LE	Local excited state
LUMO	Lowest unoccupied molecular orbital
MCH	Methylcyclohexane
mCP	1,3-Bis(carbazol-9-yl)benzene
NPB	<i>N,N'</i> -Di(1-naphthyl)- <i>N,N'</i> -diphenyl-(1,1'-biphenyl)-4,4'-diamine
OLED	Organic light-emitting diode
PBrS	Poly(4-bromostyrene)
PF	Prompt fluorescence
PL	Photoluminescence
PLQY	Photoluminescence quantum yield
RISC	Reverse intersystem crossing
RTP	Room temperature phosphorescence
SOC	Spin-orbit coupling
TADF	Thermally activated delayed fluorescence
TCSPC	Time correlated single photon counting
TCTA	Tris(4-carbazoyl-9-ylphenyl)amine
THF	Tetrahydrofuran
TPBi	2,2',2''-(1,3,5-Benzenetriyl)-tris(1-phenyl-1- <i>H</i> -benzimidazole)
TSBPA	4,4'-(Diphenylsilanediyl)bis(<i>N,N</i> -diphenylaniline)
TSPO1	Diphenylphosphine oxide-4-(triphenyl silyl)phenyl
TTA	Triplet-triplet annihilation

Contents

Abstract	iii
Declaration	v
Acknowledgements	vi
Abbreviations	vii
List of Figures	xiii
List of Tables	xxiii
1 Background	1
1.1 Motivation	1
1.2 Thesis outline	3
2 Introduction	6
2.1 Fundamental Concepts	7
2.1.1 Molecular Orbitals	7
2.1.2 Singlet and Triplet States	8
2.1.3 Singlet-Triplet Energy Splitting	10
2.2 Electronic Transitions in Organic Molecules	11
2.2.1 Franck-Condon Principle	11
2.2.2 Jablonski Diagram	13
2.2.3 Lifetimes and Quantum Yields	20
2.2.4 Charge-Transfer and Solvatochromism	21
2.3 Triplet Harvesting Mechanisms	24

2.3.1	Thermally Activated Delayed Fluorescence	24
2.3.2	Room Temperature Phosphorescence	31
2.4	Organic Light-Emitting Diodes	33
2.4.1	Evolution of Organic Light-Emitting Diodes	33
2.4.2	Working Principle of Organic Light-Emitting Diodes	34
3	Materials and Experimental Methods	38
3.1	Organic Materials Studied	39
3.2	Sample Preparation	39
3.2.1	Solution	39
3.2.2	Solid-State Film	39
3.3	Steady-State Measurements	40
3.3.1	Optical Absorption	40
3.3.2	Steady-State Photoluminescence	41
3.3.3	Oxygen-Degassing	42
3.3.4	Photoluminescence Quantum Yield	43
3.4	Time-Resolved Spectroscopy	46
3.4.1	Time-Correlated Single-Photon Counting	46
3.4.2	Time Gated Acquisition - iCCD	48
3.5	Cyclic Voltammetry	50
3.6	Organic Light-Emitting Diodes	52
3.6.1	Fabrication of Organic Light-Emitting Diodes	52
3.6.2	Device Characterization	54
4	The Contributions of Molecular Vibrations and Higher Triplet Levels to the Intersystem Crossing Mechanism in Metal-Free Organic Emitters	58
4.1	Introduction	60
4.2	Results and Discussion	61
4.2.1	Chemical Characterization	61
4.2.2	Photophysical Properties in Solution	63
4.2.3	Photophysical Properties in zeonex Films	68

4.2.4	Photophysical Properties in Polar Hosts	71
4.2.5	Theoretical Calculations	76
4.3	Conclusions	79
5	The Influence of Molecular Conformation on the Photophysics of Organic Room Temperature Phosphorescent Luminophores	80
5.1	Introduction	82
5.2	Results and Discussion	83
5.2.1	Chemical Characterization	83
5.2.2	Theoretical Calculations	86
5.2.3	Photophysical Properties	88
5.2.4	Rates and Luminescence Yields	98
5.3	Conclusions	101
6	Intramolecular Charge Transfer Controls Switching Between Room Temperature Phosphorescence and Thermally Activated Delayed Fluorescence	103
6.1	Introduction	105
6.2	Results and Discussion	106
6.2.1	Chemical Characterization	106
6.2.2	Theoretical Calculations	109
6.2.3	Photophysical Properties	111
6.2.4	Device Performance	120
6.3	Conclusions	122
7	Achieving Highly Efficient Deep-Blue TADF Emitters by Subtly Tuning Donor Strength with Unconventional Electron-Rich Acceptor	123
7.1	Introduction	125
7.2	Results and Discussion	126
7.2.1	Chemical Characterization	126
7.2.2	Theoretical Calculations	128

7.2.3	Steady-State Properties	130
7.2.4	Time-Resolved Spectroscopy	134
7.3	Conclusions	139
8	The Effect of Substitution Patterns on Tuning Emission and Luminescence Efficiency in TADF Emitters	141
8.1	Introduction	142
8.2	Results and Discussion	143
8.2.1	Fundamental Photophysical Characterization	143
8.2.2	Photophysical Properties in DPEPO	149
8.2.3	Device Performance	151
8.3	Conclusions	154
9	Concluding Remarks	155
9.1	General Conclusion	156
9.2	Future Work	157
	Bibliography	159
	Appendix	180
A		180
A.1	Chemical Structures	180
A.2	Publications	187

List of Figures

2.1	a) A schematic of the hydrogen molecular orbital. b) Energy levels of molecular orbitals in formaldehyde and all possible electronic transitions. [1]	7
2.2	a) A schematic showing the ground and excited states in relevant molecular orbital configurations, arrows here indicate the direction of electron spins. b) The vector diagram illustrating the relative orientations of two electron spins for singlet and triplet states.	9
2.3	The Franck-Condon principle energy diagram with vertical transitions.	13
2.4	Jablonski diagram illustrating key optical and electronic processes in organic emitters: nonradiative decays–vibrational relaxation (VR), internal conversion (IC), intersystem crossing (ISC) and reverse ISC (RISC); radiative decays–fluorescence and phosphorescence. The spin configurations of all the states are also shown in the orbital occupancy diagrams to the side of each electronic state.	14
2.5	A schematic showing the derivation of Beer-Lambert law.	15
2.6	An example of a D–A molecule.	22
2.7	A schematic of the proposed origin of the solvatochromism. The dipole moments of the solvent molecules (blue) are randomly distributed when the solute molecule (grey) is in its ground state, then reorientate to align (parallel or antiparallel) to the dipole moment of the excited state of the solute molecule when the molecule is excited. [2]	23

2.8	a) A schematic showing the TADF mechanism in organic molecules. b) Four proposed models for the RISC mechanisms between singlet and triplet excited states.	26
2.9	A simplified schematic of RTP mechanism.	31
2.10	Evolution of OLED architectures: a) single-layer OLED, b) two-layer OLED, c) three-layer OLED, d) multi-layer OLED.	34
2.11	A schematic energy level diagram of a multi-layer OLED device.	35
3.1	A diagram showing the setup of a double-beam UV–3600 spectrophotometer.	41
3.2	Linear plots of integrated fluorescence intensity <i>vs.</i> absorbance of reference and sample solutions used to determine relative PLQYs.	44
3.3	An example of the absolute PLQY measurement using integrating sphere.	45
3.4	A diagram illustrating the setup of the TCSPC system.	47
3.5	A schematic diagram of time-gated iCCD system.	48
3.6	a) A schematic diagram of cyclic voltammetry apparatus and b) cyclic voltammogram of a studied molecule as an example.	51
3.7	a) A simplified diagram of Kurt-Lesker Spectros II deposition system used for OLEDs production. b) A schematic illustration of top view of device fabrication.	53
3.8	CIE 1931 (x, y)	56
4.1	a) Energy level diagram describing the photophysical mechanisms that give rise to RTP and TADF emissions. b) Molecular structures of studied compounds in this chapter and the numbering code for molecular isomers. Molecular structures of hosts c) poly(4-bromostyrene) (PBrS) and d) diphenylphosphine oxide-4-(triphenylsilyl)phenyl (TSPO1).	62
4.2	Absorption spectra of a) 1 and 2, b) 3 and 4, c) 5 and 6, and d) 7, 8, 9 and 10. Emission spectra of compounds e) 1–6 and f) 7–10. All spectra were collected in dilute hexane solution at room temperature.	64

- 4.3 Dependence of the IC rate on the ISC rate in compounds 2, 7, 8 and 9, all with the same donor (carbazole) but different acceptors. The size of the dot represents the strength of CT character of the singlet state as evaluated by solvatochromism in the fluorescence spectra. . . . 67
- 4.4 Steady-state emission in zeonex films at room temperature in vacuum and in the presence of oxygen of compounds 1 to 9. 68
- 4.5 Fluorescence decays of compounds 1–4 in zeonex solid films at room temperature, collected at the fluorescence band. 69
- 4.6 Temperature dependence of steady-state emission spectra of compound 2 in zeonex film. 70
- 4.7 Steady-state emission spectra of compounds 1–4 dispersed in PBrS, in vacuum (red) and in air (black) equilibrated conditions at room temperature. 72
- 4.8 Steady-state emission spectra of compound 4 dispersed in different hosts a) 7, b) 9 and c) TSPO1, in vacuum (red) and under air (black) equilibrated conditions at room temperature. 73
- 4.9 a) Time-resolved luminescence decays of compound 4 in TSPO1, in vacuum (red) and in the presence of oxygen (black). b) Time-resolved spectra of 4 in TSPO1, showing the spectra of the prompt fluorescence (black) and long-lived TADF and RTP (red). Both spectra are compared with the steady-state emission of 4 in zeonex (blue). c) Steady-state emission spectra of 4 in TSPO1 and d) 4 in PBrS as a function of temperature. 74
- 4.10 Time-resolved luminescence decay of compound 4 in hosts a) 7 and b) 9, in vacuum (red) and in the presence of oxygen (black). c) 7 and d) 9 showing the spectra of the prompt fluorescence (black), and long-lived TADF and RTP (red). Both spectra are compared with the steady-state emission of 4 in zeonex (blue). 75
- 4.11 HOMO and LUMO frontier molecular orbitals of compounds 1 to 4, optimized using (U)DFT(PBE0) and a 6-31G* basis set as implemented within the Gaussian09 quantum chemistry package. 76

4.12	Energy level diagram of the singlet and triplet states in compounds 1 to 4, obtained from calculations.	77
5.1	Molecular structures of the four compounds studied in this chapter. .	83
5.2	X-ray molecular structures of a) DPTZ–DBT·CDCl ₃ and b) DPTZ– ^{<i>i</i>} Pr–DBT showing equatorial and axial PTZ groups, respectively. Thermal ellipsoids are drawn at the 50% probability level, H atoms are omitted for clarity, and primed atoms are generated by the twofold axis. c) DPTZ–Me–DBT molecule in the crystal of its CHCl ₃ solvate. Thermal ellipsoids are drawn at the 30% probability level. Occupancies of the disordered groups/atoms are cited.	85
5.3	Molecular orbitals, HOMO and LUMO distributions of DPTZ–DBT (equatorial), DPTZ–Me–DBT (axial), DPTZ– ^{<i>i</i>} Pr–DBT (axial) and DPTZ– ^{<i>t</i>} Bu–DBT (axial) forms at DFT (M062X)/Def2SVP level of theory.	86
5.4	The UV–Vis absorption (toluene) and fluorescence (zeonex) spectra of a) DPTZ–DBT, and three substituted derivatives b) DPTZ–Me–DBT, c) DPTZ– ^{<i>i</i>} Pr–DBT and d) DPTZ– ^{<i>t</i>} Bu–DBT, in comparison to the spectra of their individual units at room temperature.	88
5.5	Absorption and emission spectra of a) DPTZ–DBT, b) DPTZ–Me–DBT, c) DPTZ– ^{<i>i</i>} Pr–DBT and d) DPTZ– ^{<i>t</i>} Bu–DBT in solvents of different polarity at room temperature.	90
5.6	Steady-state emission spectra (zeonex at RT, in air and under vacuum) of a) DPTZ–DBT, b) DPTZ– ^{<i>i</i>} Pr–DBT and c) DPTZ– ^{<i>t</i>} Bu–DBT, in comparison to the phosphorescence of PTZ and DBT units. Time-resolved prompt fluorescence and phosphorescence spectra of d) DPTZ–DBT, e) DPTZ– ^{<i>i</i>} Pr–DBT and f) DPTZ– ^{<i>t</i>} Bu–DBT, PF and phosphorescence were collected at 80 K with delay times of 1.1 ns and 50 ms, respectively.	91

5.7	a) Comparison of the absorption (dot lines) and emission (full lines) spectra of PTZ and substituted PTZ units, PTZ–Me, PTZ– ⁱ Pr and PTZ– ^t Bu. Absorption were measured in toluene and fluorescence in zeonex at room temperature. b) Phosphorescence of PTZ derivatives in zeonex film collected at 80 K. Excitation at 355 nm.	92
5.8	DPTZ–Me–DBT emission spectra in zeonex film: a) Steady-state emission spectra in air and in vacuum at RT. The phosphorescence of the DBT and the PTZ units are also shown, matching the two phosphorescence bands in DPTZ–Me–DBT. b) Time-resolved PF and phosphorescence spectra at RT, collected at delay time of 1.1 ns and 50 ms, respectively. c) Phosphorescence spectra at RT and 80 K, compared with the phosphorescence of DBT and PTZ–Me fragments. d) Phosphorescence as a function of temperature collected at delay times of 50 ms.	93
5.9	Temperature dependence of steady-state emission spectra in zeonex of a) DPTZ–DBT, b) DPTZ–Me–DBT, c) DPTZ– ⁱ Pr–DBT and d) DPTZ– ^t Bu–DBT.	94
5.10	Emission decays of DPTZ–DBT, DPTZ–Me–DBT, DPTZ– ⁱ Pr–DBT and DPTZ– ^t Bu–DBT collected at the fluorescence bands in air at RT in a) toluene solution and b) zeonex film.	94
5.11	Schematic representation of the excited state relaxation in the studied molecules.	95
5.12	Time-resolved phosphorescence decays in zeonex obtained as a function of temperature of a) DPTZ–DBT, b) DPTZ–Me–DBT, c) DPTZ– ⁱ Pr–DBT and d) DPTZ– ^t Bu–DBT.	97
6.1	Molecular structures of a) studied molecules OP, OMP, OPM and OP2M. b) Images of α –OP, β –OP, OPM, α –OMP, β –OMP and γ –OMP crystals irradiated at 365 nm.	106

6.2	Single crystal X-ray molecular structures of α -OP, OPM and OP2M with axial conformers, and b) β -OP, α -OMP, β -OMP and γ -OMP with equatorial conformers. Thermal ellipsoids are drawn at the 50% probability level.	108
6.3	Cyclic voltammetry analysis by the estimation of the electron affinity and the ionization potentials for OMP (red) and OPM (blue) at room temperature.	109
6.4	Frontier molecular orbitals of α -OP and OPM, and electronic transitions at B3LYP/6-31G* (H = HOMO; L = LUMO). The same components of S_1 are in red text.	110
6.5	Plots of visualized orbitals based on the single crystal geometry of β -OP, α -OMP and β -OMP and γ -OMP; positive electron density in grey and negative in blue (B3LYP/6-31G*).	111
6.6	UV-Vis absorption spectra of a) OP, b) OPM, c) OP2M and d) OMP in diluted toluene solutions (1.0×10^{-5} M) at room temperature. The spectra of their individual units are shown for comparison.	112
6.7	Photoluminescence spectra of a) the individual units: BP, BPM, PTZ, PTZ-Me and PTZ-2Me and b) OP, OPM, OP2M and OMP in diluted toluene (1.0×10^{-5} M) at room temperature. The second-harmonic peak at <i>ca.</i> 660 nm from the excitation beam has been removed in Figure b.	113
6.8	Steady-state emission in vacuum and air of a) OP, b) OPM, c) OP2M and d) OMP in zeonex films at room temperature. The % figures are the decrease in emission intensity in air.	114
6.9	Time-resolved area normalized spectra of α -OP crystals at a) 80 K, b) 290 K; and of OPM crystals at c) 80 K, d) 290 K. Excitation wavelength at 355 nm.	115
6.10	Time-resolved area normalized spectra of β -OP crystals at a) 80 K, b) 290 K; and of OMP (α -OMP) crystals at c) 80 K, d) 290 K at room temperature. Excitation wavelength at 355 nm.	116

6.11	Time-resolved temperature dependent decays of a) α -OP, b) β -OP, c) OPM and d) OMP (α -OMP) crystals from 290 K to 80 K. Excitation at 355 nm.	117
6.12	The DF intensity dependence on laser power of a) β -OP with delay and integration times of 200 ns and 200 μ s, respectively; b) OMP with delay and integration times of 200 ns and 800 μ s, respectively. Excited at 337 nm at room temperature.	118
6.13	Time-resolved area normalized emission spectra of crystals: β -OMP a) at 80 K, b) 290 K and c) temperature dependence of emission decay over a temperature range from 290 K to 80 K; γ -OMP d) at 80 K, e) at 290 K and f) temperature dependence of emission decay over a temperature range from 290 K to 80 K.	119
6.14	Energy level diagrams showing the HOMO/LUMO levels and structures of a) Device 1 based on OMP as an emitter and b) Device 2 based on OPM. c) Molecular structures of materials used in OLEDs. d) EL spectra of devices operating at 8 V. e) Current density-voltage-luminance characteristics. f) EQE <i>vs.</i> luminance characteristics. . . .	120
7.1	Molecular structures of the studied compounds.	126
7.2	Cyclic voltammograms of a) DAc-DBT, b) DtBuAc-DBT and DOMEAc-DBT at concentrations of 1 mM.	127
7.3	Optimized molecular geometries with HOMO (red) and LUMO (black) levels and energies of DAc-DBT, DtBuAc-DBT and DOMEAc-DBT (rBMK/6-31G(d) level of theory).	128
7.4	a) Natural transition orbitals (NTO) corresponding to the first triplet transitions. b) Singlet and triplet energy diagram of DAc-DBT, DtBuAc-DBT and DOMEAc-DBT along with the energy levels of the individual units (TD-DFT rBMK/6-31G(d)). [3] Hole refers to the Highest Occupied Natural Transition Orbital (HONTO), while particle refers to Lowest Unoccupied Natural Transition Orbital (LUNTO).	129

- 7.5 a) UV-Vis absorption and fluorescence spectra of DAc-DBT, DtBuAc-DBT and DOMEAc-DBT in toluene solutions (1.0×10^{-5} M) measured at room temperature. b) Steady-state fluorescence collected at room temperature and time-resolved phosphorescence spectra collected with delay time of 56 ms at 80 K in zeonex films (1 wt%). . . . 130
- 7.6 The normalized absorption and photoluminescence in various solvents of a) DAc-DBT, b) DtBuAc-DBT and c) DOMEAc-DBT. 131
- 7.7 Phosphorescence spectra of a) DAc-DBT and b) DtBuAc-DBT collected at 80 K, c) DOMEAc-DBT measured at room temperature (dark green line) and 80 K (black line). All in zeonex films in comparison to their individual D and A units. 132
- 7.8 A schematic energy diagram of DAc-DBT, DtBuAc-DBT and DOMEAc-DBT. All energies are given in eV and were calculated from the onsets of the corresponding spectra in zeonex films, compared with their individual D and A moieties. 133
- 7.9 The steady-state emission spectra of DAc-DBT, DtBuAc-DBT and DOMEAc-DBT in a) diluted toluene solution (1×10^{-5} M) and b) zeonex films (1 wt%) in the absence (red) and presence (black) of oxygen at room temperature. 133
- 7.10 a) Time-resolved area normalized emission of DAc-DBT zeonex film at 320 K. Steady-state emission before and after laser radiation of b) DAc-DBT, c) DtBuAc-DBT and d) DOMEAc-DBT in zeonex films collected at room temperature. 135
- 7.11 Temperature dependent time-resolved decays of a) DtBuAc-DBT and b) DOMEAc-DBT in zeonex films (1 wt%) collected at various temperatures. Power dependent measurements with delay/integration times of $1 \mu\text{s}/1 \text{ ms}$, $1 \mu\text{s}/200 \mu\text{s}$ for c) DtBuAc-DBT and) DOMEAc-DBT films, respectively, excitation at 337 nm at room temperature. . 136
- 7.12 Time-resolved area normalized emission spectra of DtBuAc-DBT in zeonex matrix at a) 290 K and b) 80 K. 137

7.13	DOMeAc–DBT in zeonex film: time-resolved area normalized emission spectra at a) 290 K and b) 80 K. c) Phosphorescence spectra recorded at delay times of 5 ms and 500 ms, compared with that of the donor OMe–Ac unit measured at 80 K.	138
8.1	Molecular structures of the reported and studied compounds.	143
8.2	a) UV–Vis absorption and b) emission spectra of the studied D–A–D molecules in dilute toluene solutions (1.0×10^{-5} M) at room temperature.	144
8.3	Comparison of the absorption and emission spectra of a) DBTO2–DAc, b) MeODBTO2–DAc, c) MeSDBTO2–DAc, d) FDBTO2–DAc and e) CNDBTO2–DAc in solvents of different polarities at room temperature.	144
8.4	a) Fluorescence (dotted line) and phosphorescence (solid line) spectra of DBTO2–DAc, MeODBTO2–DAc, MeSDBTO2–DAc, FDBTO2–DAc and CNDBTO2–DAc in zeonex solid films, collected at room temperature and 80 K, respectively. b) Steady-state emission spectra of all five molecules in zeonex matrix in the presence (black) and absence (red) of oxygen at room temperature.	146
8.5	CNDBTO2–DAc zeonex film: a) Temperature dependent time-resolved decays. b) The dependence of DF intensity on laser power with delay and integration times of 1 μ s and 1 ms, respectively. Excitation at 337 nm at room temperature. Time-resolved area normalized spectra c) at room temperature and d) 80 K.	147
8.6	Time-resolved decays of DBTO2–DAc, MeODBTO2–DAc, MeSDBTO2–DAc and FDBTO2–DAc films at room temperature, excitation at 355 nm. b) Power dependence of DF with excitation dose. Excitation at 337 nm at room temperature.	149

- 8.7 a) Comparison of fluorescence (dotted line) and phosphorescence (solid line) spectra of the doped DPEPO films, collected at room temperature and 80 K (delay time of 56.2 ms), respectively. b) Steady-state emission of CNDBTO2–DAc in DPEPO (10% w/w) in the presence and absence of oxygen at room temperature. c) Temperature dependent time-resolved decays of CNDBTO2–DAc doped DPEPO film. Excitation at 355 nm. 150
- 8.8 a) Steady-state emission of DBTO2–DAc, MeODBTO2–DAc, MeSDBTO2–DAc and FDBTO2–DAc doped DPEPO films in aerated and vacuum conditions at room temperature. b) Time-resolved decays at room temperature. Excitation at 355 nm. 152
- 8.9 a) Architecture and energy levels of OLED devices. b) EL spectra collected at 9 V. c) Current density-voltage-luminance characteristics. d) EQE *vs.* luminance characteristics. 153

List of Tables

4.1	Singlet and triplet energies (S_1 and T_1), fluorescence quantum yields (Φ_f), fluorescence lifetime (τ_f) and triplet yields (Φ_T). All determined in hexane at room temperature, with exception of T_1 energies, which were determined at 80 K in ethanol solution.	65
4.2	Quantum yields of fluorescence (Φ_f) and phosphorescence (Φ_{ph}); fluorescence (τ_f) and phosphorescence lifetimes (τ_{ph}); radiative decay rates of the S_1 (k_f) and T_1 states (k_{ph}); internal conversion rate (k_{IC}), intersystem crossing rate from S_1 (k_{ISC}) and intersystem crossing rate from T_1 to S_0 ($k_{ISC}^{T_1}$) for studied compounds. All determined in zeonex films at room temperature.	71
5.1	Calculated energies of studied molecules in different conformations. S_0^{abs} is the energy (eV) of the ground state calculated relative to the lower energy. The energy (eV) of the S_1 state at the Franck-Condon (Absorption, S_1^{abs}) and excited state optimised (Emission, S_1^{em}) geometries are also reported. The oscillator strengths are in brackets. Each structure was optimized in the absence of a solvent model to aid convergence. The final excited state emission energies were calculated using a SS-PCM approach using the solvent parameters of toluene.	87
5.2	Photophysical parameters of DPTZ-DBT, DPTZ-Me-DBT, DPTZ- <i>i</i> Pr-DBT and DPTZ- <i>t</i> Bu-DBT in zeonex at RT.	98
5.3	Photophysical parameters of DPTZ-DBT, DPTZ-Me-DBT, DPTZ- <i>i</i> Pr-DBT and DPTZ- <i>t</i> Bu-DBT in toluene at RT.	99

5.4	The calculated variables required for equation 5.1 and the corresponding k_{ISC} . Due to energy considerations k_{ISC} for DPTZ–DBT was calculated in the equatorial and axial forms, while the remaining substituted compounds were calculated in their axial form.	100
6.1	Summary of OLED device characteristics.	121
7.1	Photophysical parameters of DAc–DBT, DtBuAc–DBT and DOMEAc–DBT in zeonex films.	137
8.1	Photophysical, electrochemical parameters of the investigated molecules in solution and zeonex films.	145
8.2	Photophysical parameters of the investigated molecules in DPEPO films.	151
8.3	Summary of OLED device characteristics.	152

Chapter 1

Background

1.1 Motivation

Light is the primary way by which we observe our environment, for example sunlight in daytime and artificial lighting at night time (originally fire). Incandescent and gas-discharge lamps were the most advanced lighting sources a century ago. However, incandescent lamps are energy inefficient, and over 90% of the consumed power is converted to heat. [4] Gas-discharge lamps have higher efficiency (still used for road lights today), but poor colour quality and the requirement of high voltage and toxic mercury for white emission limit their wide applications. Solid-state lighting instead exhibits great potential to be the light source of the future. In contrast to gas-discharge lamps, in solid-state devices charge carriers are injected into semiconductor materials at low voltages, and radiative recombination of the injected carriers generates light. Currently, light-emitting diodes (LED) show remarkable efficiencies and long lifetimes, and are the dominant type of solid-state devices used in lighting applications. However, the performance of these light sources is still below the ever-growing requirements of industrial and household consumers.

In parallel to the inorganic materials used in conventional LEDs, organic LEDs (OLEDs) based on eco-friendly organic materials have opened an entire new field of research, since Tang *et al.* reported the first organic electroluminescent device in 1987. [5] OLEDs exhibit enormous potential for commercial applications in solid-state lighting, flat panel display and wearable optoelectronic devices. Desirable

qualities include low mass, large viewing angle, high contrast, fast response time, and high efficiency. Moreover, OLEDs can be fabricated on flexible substrates, which open completely new applications for flexible and transparent devices. Nowadays, OLEDs have attracted great interest and deep investment from many companies, such as BOE, Samsung, LG, Cynora, Merck and Novaled. After a decade of investigation, the technology of OLEDs is gradually taking over the current LED market.

Despite the enormous progress made in recent years, there is still significant work to be done in terms of increasing the efficiency and operational lifetime of OLEDs. A primary limitation of OLEDs is that charge recombination gives rise to more localized excitons that are affected by significant exchange interactions. As a consequence, two different types of excitons are created depending on the arrangement of their electron and hole spins: singlet excitons that have total spin of zero and decay radiatively in a few nanoseconds, and triplet excitons with total spin of one that mostly decay through non-radiative pathways and thus do not participate in light generation. [6] Unfortunately, upon electrical excitation of an OLED the fraction of singlet excitons generated is only 25%, and the remaining 75% are triplet excitons. Therefore, this leads to a major loss mechanism for the efficiency of OLEDs in conventional fluorescent materials.

Phosphorescent materials containing heavy-metals such as Ir(III) and Pt(II) were later introduced to improve the efficiency of OLEDs as a second generation of emitters. In these materials, the presence of heavy atoms introduces some singlet character in the triplet state and opens radiative pathways through phosphorescence. Up to 100% internal efficiency is thus attainable as both singlet and triplet excitons participate in the light generation process. [7,8] Despite this improvement, the heavy-metals commonly used in phosphorescent materials are scarce and expensive. Degradation issues especially for emitters in the blue region [9,10] and the potential environmental problems that arise from heavy-metal processing following product disposal make them undesirable final candidates for mass-production of technologically mature phosphorescent OLEDs. [11] Instead, finding ways to preserve triplet harvesting while avoiding noble metal-containing phosphorescent materials is a high priority.

Recently, metal-free molecules designed to have small energy gaps between the singlet and triplet states were proposed by Adachi *et al.* as an alternative method to harvest triplet states in OLEDs and increase device efficiency. [12] These molecules are commonly identified as thermally activated delayed fluorescent (TADF) materials, and form the third generation of OLEDs. Unlike conventional fluorescent and phosphorescent emitters, TADF compounds can utilize up to 100% of excitons *via* a thermally activated reverse intersystem crossing (RISC) process, which converts the excitons in the triplet state to the nearly isoenergetic emissive singlet states. The TADF mechanism is therefore strongly dependent on the energy difference between the singlet and triplet states. [13–15]

Complementary to TADF, room temperature phosphorescence (RTP) is also an efficient mechanism for triplet harvesting and creates new opportunities in optoelectronic and photonic applications. [16, 17] To achieve efficient RTP, the intersystem crossing (ISC) rate from the lowest excited singlet to the triplet state needs to be enhanced and the nonradiative relaxation from triplet to the ground state needs to be suppressed.

Although great progress has been achieved in TADF and RTP emitters, many issues still remain to meet the demanding requirements of commercial applications. Current examples of blue TADF emitters in particular lag far behind phosphorescent and inorganic blue LEDs in many critical aspects: the triplet harvesting efficiencies of TADF and RTP emitters need to be effectively 100% for any commercial system, and the efficiency roll-off of OLEDs needs to be addressed urgently for efficient operation at high brightnesses. Therefore, detailed investigations of molecular structure-property relationships are needed to achieve a better understanding of the triplet state dynamics to allow future design improvements to current TADF and RTP structured motifs in a rational manner.

1.2 Thesis outline

This thesis presents a series of investigations on the triplet harvesting mechanisms in metal-free organic molecules, mostly focusing on TADF and RTP properties in

solutions, films and crystals.

Chapter 2 presents the relevant background theory supporting the experimental studies. This includes a description of the electronic energy states in organic molecules and a qualitative interpretation of the most common photophysical transitions, followed by a discussion of relevant triplet harvesting mechanisms. This chapter closes by discussing the working principles and current challenges in OLEDs.

Chapter 3 provides background information regarding experimental procedures, data collection and processing used in this thesis, including sample preparation, optical and electrochemical measurements, and device fabrication and characterization methods.

Chapter 4 presents an investigation of a series of donor-acceptor-donor (D–A–D) molecules with the D units linked in different substituting positions of the acceptor. The aim is to probe the effect of regio-isomerization on the triplet harvesting mechanisms supporting TADF and RTP. A profound influence on the activity of dual luminescence (simultaneous TADF and RTP) can be observed by simple manipulations of the way D and A units are linked. This illustrates the similarity of the two mechanisms and commonalities amongst the properties required to facilitate both high ISC and RISC rates in organic molecules.

Chapter 5 gives a detailed investigation on the influence of molecular conformation on RTP emitters. Changes of the molecular conformation are induced by the steric effects of the methyl, *iso*-propyl and *tert*-butyl substituents. Strong RTP green emission with a high phosphorescence quantum yield is observed in the parent molecule. In contrast, the alkyl substituted derivatives change their molecular conformations due to the influence of the bulky substituents, and instead exhibit blueshifted phosphorescence occurring from a higher triplet state. Interestingly, dual RTP is observed in the less bulky substituted molecule.

Chapter 6 explores a fundamental approach to tune the emission behaviours in molecular crystals of two TADF/RTP emitters. The geometry of the intramolecular charge transfer (CT) state is modified by a simple chemical modification in two D-A molecules. Planar and twisted geometries are obtained in different crystal forms and exhibit different triplet harvesting mechanisms (TADF or RTP).

Chapter 7 investigates the influence of different energy alignments among locally excited and CT states on the RISC mechanism of a series of D–A–D molecules, which are induced by fine-tuning the donor strength. A desirable deep-blue TADF emitter with aligned singlet and triplet states is obtained in this fashion.

Chapter 8 discusses the effects of different acceptor substitution patterns on the photophysical properties of a series of TADF molecules. The changes of electron-withdrawing strength imposed by the substituents (methoxy, methylthio, fluorine and cyano) result in a colour-tuning effect towards the red region. Molecules with small energy gaps while retaining quite high photoluminescence quantum yields are obtained.

Finally, Chapter 9 summarizes all the work done in this thesis and highlights the insights that can be drawn from all chapters synergistically and simultaneously.

Chapter 2

Introduction

Fundamental photophysical and photochemical concepts and principles central to the investigations carried out in following chapters are present in this chapter. A description of the electronic energy states in organic molecules and a qualitative interpretation of the common photophysical transitions are presented, followed by a discussion of the triplet harvesting mechanisms and the applications in OLEDs.

2.1 Fundamental Concepts

2.1.1 Molecular Orbitals

Organic materials are the central focus of this thesis, and are mainly based on carbon and hydrogen along with other atoms such as sulphur, nitrogen and oxygen. In an atom consisting of electrons and nucleus, the electron has a set of well-defined allowed energies and spatial distributions around the nucleus, which are called orbitals. In molecules, a linear combination of atomic orbitals can be used to generate molecular orbitals, which similarly describe the energies and distribution of electrons shared between two or more atoms.

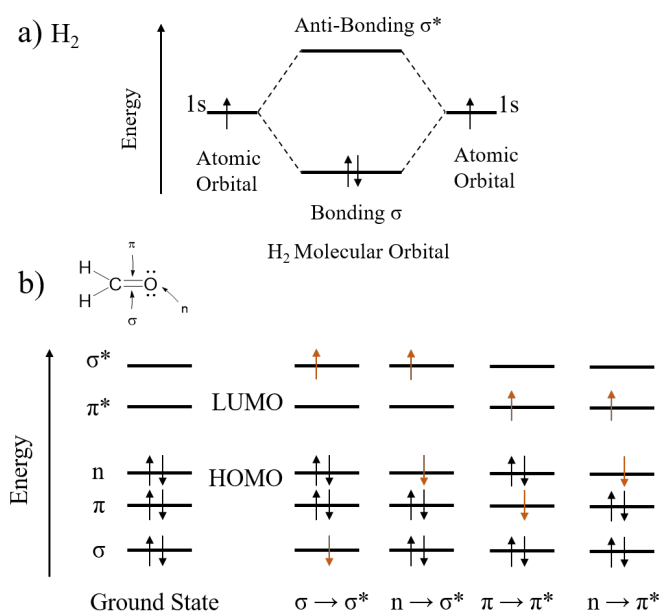


Figure 2.1: a) A schematic of the hydrogen molecular orbital. b) Energy levels of molecular orbitals in formaldehyde and all possible electronic transitions. [1]

Figure 2.1a shows the molecular orbitals in the diatomic hydrogen: the lower energy bonding molecular orbital (σ) has a high occupancy and is lower than the two 1s atomic orbitals of hydrogen atoms, and the upper energy antibonding orbital (σ^*) has a low occupancy and a central node in the electronic wavefunction. The two hydrogen atoms are kept in close proximity due to the overall lowering of the electronic energy in the σ orbital ($E(\sigma(\uparrow\downarrow)) < 2E(1s^1)$), which is the mechanism by which the atoms become “bonded”. In molecular systems with more electrons,

covalent bonding occurring between one s and one p atomic orbital or between two parallel head-to-head p orbitals can also form σ bonds. For two aligned p atomic orbitals overlapping laterally, π and π^* orbitals are formed and the resulting bond is called a π bond. By absorbing a photon with appropriate energy, an electron can be promoted from a bonding orbital (σ or π) to its corresponding antibonding orbital (σ^* or π^*), with the transition labelled $\sigma \rightarrow \sigma^*$ or $\pi \rightarrow \pi^*$. Some carbon based molecules also possess non-bonding electrons located on heteroatoms such as nitrogen or oxygen. The unaligned p orbitals in these electrons form non-bonding orbitals (n), which can be excited giving origin to an $n \rightarrow \pi^*$ transition by promoting a non-bonding electron to an antibonding π^* orbital.

In the ground state of the molecule, the molecular orbitals are filled by the available electrons. The filled orbital highest in energy is called the highest occupied molecular orbital (HOMO) and the lowest empty orbital just above it is the lowest unoccupied molecular orbital (LUMO). The energy levels of molecular orbitals in formaldehyde are shown in Figure 2.1b with all possible molecular orbital transitions. [1]

2.1.2 Singlet and Triplet States

Electrons show both wavelike and particle-like behaviours. [18] The electronic wavefunction $\Psi(x, y, z)$ describes the spatial distribution of an electron. The probability of finding an electron at a particular point is described by the product of Ψ and its complex conjugate Ψ^* , $\langle \Psi^* | \Psi \rangle$, at that point. In the quantum mechanical model of a one electron hydrogen system, the principle (n), angular (l) and magnetic (m) quantum numbers are used to describe the function $\Psi_{nlm}(x, y, z)$ that satisfies the Schrödinger equation for that system:

$$\left[\frac{\hat{p}^2}{2m} + V(x, y, z) \right] \Psi = \hat{E} \Psi, \quad (2.1)$$

where \hat{p} is the momentum operator, m is the electron mass, $V(x, y, z)$ is the potential and \hat{E} is the energy operator. In multi-electron systems, a fourth quantum number is required to distinguish electrons that occupy the same orbital, which is called the spin quantum number (s). This represents an intrinsic and quantized amount

of electron angular momentum completely independent from the motion required to possess classical angular momentum. The electron's spin can be either spin up ($m_s = +\frac{1}{2}$) or spin down ($m_s = -\frac{1}{2}$) in an external magnetic field. [19,20] According to the Pauli exclusion principle, no more than two electrons in an atom can occupy a given quantized orbital, as this would otherwise give them identical quantum numbers n , l , m and s . Therefore if an orbital contains two electrons, they must possess opposite spin states. [21]

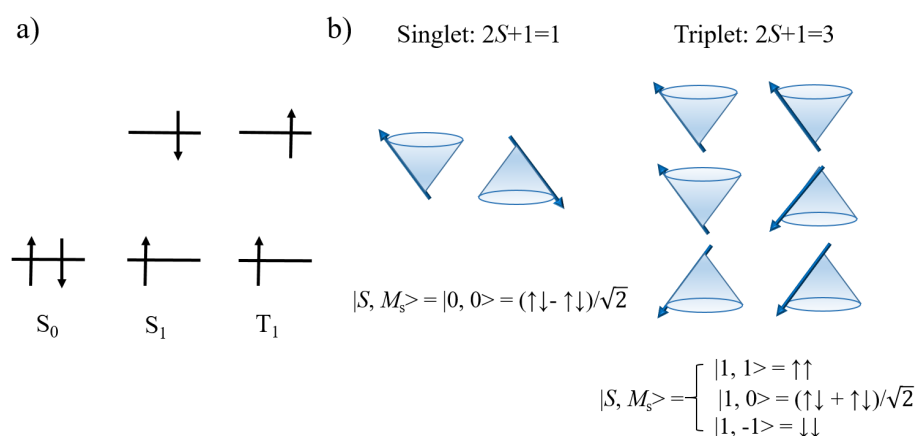


Figure 2.2: a) A schematic showing the ground and excited states in relevant molecular orbital configurations, arrows here indicate the direction of electron spins. b) The vector diagram illustrating the relative orientations of two electron spins for singlet and triplet states.

Figure 2.2a shows a schematic of the electronic states in three important molecular orbital configurations. Two electrons with antiparallel spins occupy the lowest energy orbital resulting in a total spin of zero, and this configuration is also most commonly the lowest energy state or “ground” state (S_0). The electrons in the ground state configuration both occupy the HOMO. Upon excitation, a singlet or triplet excited state is formed when one electron is promoted from HOMO to LUMO. The excited electron can have either the same or opposite spin orientation as the one in the ground state, giving origin to the singlet (S_1 , antiparallel spins) or triplet (T_1 , parallel spins) excited states. [22]

The relative orientations of the two electron spins in the singlet and triplet excited states are illustrated in Figure 2.2b. The total wavefunction of an electron is given by the product of the spatial and spin wavefunctions. Taking only the spin angular momentum into consideration, the two electron system can be diagonalized to give eigenstates of \hat{S}^2 and S_z . The corresponding eigenvalues are the total spin (S) and its z -component (M_s) for the spin wavefunctions. In the singlet state ($S = 0$), the total spin is cancelled due to the antiparallel spins of the two electrons, which has only one single possible value of z -component $M_s=0$. In the triplet state, $S = 1$ gives three possible M_s values (-1, 0 and 1) showing antisymmetric spatial and symmetric spin wavefunctions. [20]

The first and second excited singlet states located energetically above the ground state S_0 are labelled as S_1 and S_2 , respectively. Similar notation is used to label higher excited triplet states (T_n).

Molecular Oxygen Molecular oxygen is a special case where the HOMO of the oxygen molecule has an electron configuration of two antibonding π^* orbitals of the same energy. Therefore, the electronic ground state formed is a triplet state (T_0), which makes molecular oxygen an efficient triplet quencher. In the presence of oxygen, when a molecule (*i.e.* a chromophore) is in an excited triplet state (T_1), energy transfer from T_1 of the chromophore to the T_0 of oxygen will occur. This promotes oxygen molecule to an excited singlet state which has a low energy of *ca.* 1 eV, while the triplet state of the chromophore molecule is quenched and returns to the ground state. [23] For this reason, materials that emit by a triplet harvesting mechanism must be studied in the absence of oxygen.

2.1.3 Singlet-Triplet Energy Splitting

The energies of the lowest singlet (S_1) and triplet (T_1) excited states are mainly determined by three factors and defined by

$$E_{S_1} = E_0 + K + J, \quad (2.2)$$

$$E_{T_1} = E_0 + K - J, \quad (2.3)$$

where E_0 represents the one-electron orbital energy of the excited state in a fixed nuclear framework. K is the classical coulombic electron-electron repulsion energy. J is the electron exchange energy and is derived from the first-order quantum mechanical correction of the electron-electron repulsion energy due to the Pauli exclusion principle. In the classical model, E_0 and K contribute equally in both singlet and triplet excited states with the same electronic configuration. However, if the electron exchange term is taken into account, singlet and triplet state energies will differ. The exchange energy term reduces the total energy of the triplet state while increasing the energy of the singlet state. [24]

The energy difference between S_1 and T_1 (ΔE_{ST}) of the same electronic configuration is defined as

$$\Delta E_{ST} = E_S - E_T = 2J, \quad (2.4)$$

with

$$J = \iint \phi(r_1)\psi(r_2) \left(\frac{e^2}{r_1 - r_2} \right) \phi(r_2)\psi(r_1) dr_1 dr_2, \quad (2.5)$$

where J is proportional to the wavefunction overlap of the ground and excited states, *i.e.* the overlap between HOMO and LUMO frontier orbitals (equation 2.5). Here ϕ and ψ represent the HOMO and LUMO wavefunctions, respectively, and e is the electron charge. [25]

2.2 Electronic Transitions in Organic Molecules

2.2.1 Franck-Condon Principle

The rates of transitions between two vibronic (electronic and vibrational) states are related to the similarity of both the electron and the nuclear wavefunctions in the initial and final states. In an atom, electrons can move much faster (10^{-16} – 10^{-15} s) than the nuclei (10^{-14} – 10^{-13} s) due to their large difference in mass. Thus, the timescales of electron and nuclear motion can be separated, which is the essence of the Born-Oppenheimer (BO) approximation. [26] Electrons redistribute quickly according to the electronic wavefunction of the final state while the nuclei are essentially stationary during an electronic transition. [1] Following the fast electronic

redistribution, the nucleus starts to move under the unchanged electric fields of the new state. The adjustment of the nuclear configurations follows until it reaches equilibrium with the new electronic state.

The Franck-Condon (FC) principle states that transitions with larger orbital overlaps are faster, and relies on the BO approximation. According to Fermi's golden rule [27], which describes the transition rate from one energy to , the transition probability magnitude (P) between an initial state defined by Ψ_1 and a final state defined by Ψ_2 is given by

$$\begin{aligned} P &= \langle \Psi_1 | \mu | \Psi_2 \rangle = \langle \phi_1 \psi_1 | \mu | \phi_2 \psi_2 \rangle \\ &= \langle \psi_1 | \mu | \psi_2 \rangle \langle \phi_1 | \phi_2 \rangle, \end{aligned} \quad (2.6)$$

where ψ and ϕ represent the electronic and vibrational wavefunctions, respectively, μ is the molecular transition dipole operator and depends on the electron coordinates.

The oscillator strength (f), which is proportional to the square of μ , is used to quantify the intensity or probability of an electronic transition induced by the interaction of electrons with the electromagnetic field of a light wave, [28, 29]

$$f \propto \mu^2. \quad (2.7)$$

Corresponding to a single excited oscillating electron (oscillating dipole), f is related qualitatively to the experimental extinction coefficient (ε) given by

$$f \propto \int \varepsilon d\bar{\nu}. \quad (2.8)$$

Experimentally, the integral corresponds to the value of the area under a curve of the absorption spectrum plotted by the extinction coefficient against wavenumber $\bar{\nu}$. The oscillator strength of 1 corresponds to a strong electronic transition that is fully allowed, and 0 is of a forbidden transition.

In equation (2.6), the square of the vibrational overlap integral $\langle \phi_1 | \phi_2 \rangle$ is called the Franck-Condon factor, which is proportional to the probability of the transition. Qualitatively, larger vibrational overlap gives higher vibronic transition probability.

A schematic of the Franck-Condon principle is depicted in Figure 2.3, showing both the electronic levels and vibrational sublevels. In Figure 2.3a, the final nuclear geometry in the excited state shows essentially an identical shape as the nuclear

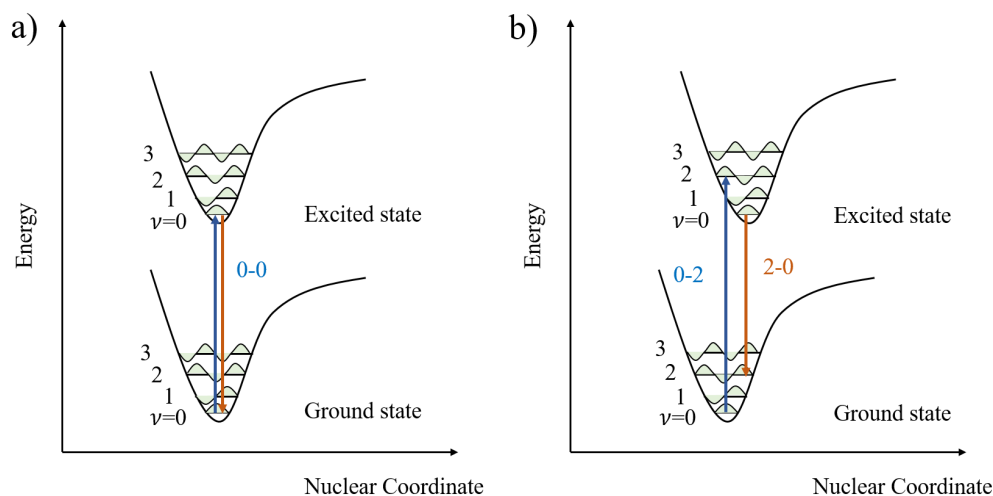


Figure 2.3: The Franck-Condon principle energy diagram with vertical transitions.

geometry in the ground state (initial state), resulting in a large orbital overlap. For such an arrangement of levels, it is likely that a transition of 0 - 0 will be observed unless forbidden by symmetry. However, a more realistic situation is depicted in Figure 2.3b. In this case, the nuclear separation is considerably longer as the excitation of an electron to an antibonding orbital gives a weaker bond. The potential wells are shown favouring transitions between $\nu = 0$ and $\nu = 2$, a transition is more likely to occur if the two vibrational wavefunctions show a large overlap, giving different values (FC factors) for different transitions. In contrast, the 0 - 0 transition in Figure 2.3b will have almost zero overlap and is unlikely to be absorbed.

2.2.2 Jablonski Diagram

Common transitions occurring between electronic states are summarized in the Jablonski diagram in Figure 2.4, arranged with energy ascending on the vertical axis. Horizontal lines represent the electronic states of a molecule, with thinner lines and blue shading representing vibrational excited sublevels of each electronic state. The lowest lines labelled as S_0 represent the ground state, which for most organic molecules is a singlet state. The upper lines represent the excited electronic states: S_1 and T_1 , the lowest singlet and triplet excited states, respectively. S_n represents a higher singlet state and T_n is similarly a higher triplet state. The bold

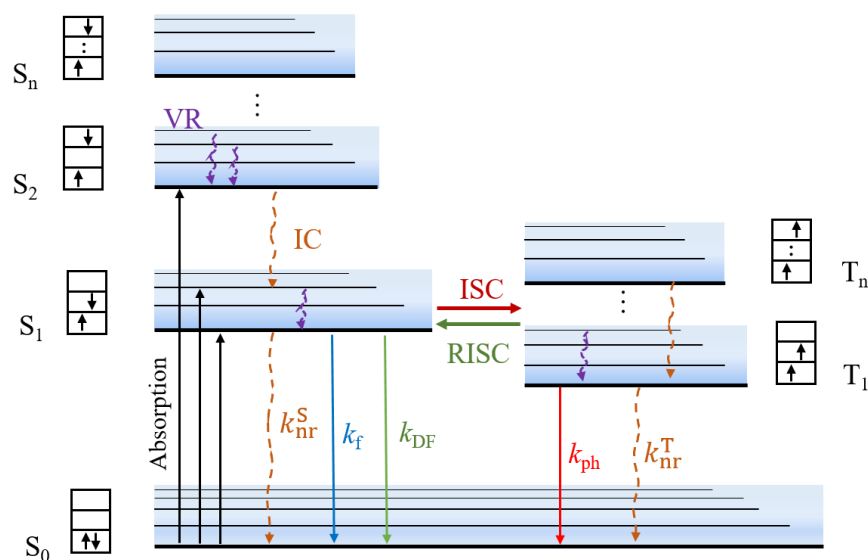


Figure 2.4: Jablonski diagram illustrating key optical and electronic processes in organic emitters: nonradiative decays—vibrational relaxation (VR), internal conversion (IC), intersystem crossing (ISC) and reverse ISC (RISC); radiative decays—fluorescence and phosphorescence. The spin configurations of all the states are also shown in the orbital occupancy diagrams to the side of each electronic state.

horizontal line represents the vibrational base of the electronic state.

i) Absorption

Light absorption by molecular systems results from the promotion of an electron from the ground state to one of the various vibrational levels in the excited state. It is represented by vertical arrows, and occurs on a much faster timescale than nuclear motion (10^{-15} to 10^{-14} s). Therefore, it can be considered to occur in a fixed nuclear framework.

Absorption must conserve the total angular momentum. Thus, a transition between S_0 and S_1 (which both have total spin of 0, while photons have $S=1$) has to involve a change in the orbital angular momentum to account for the “lost” spin as the photon disappears. For example, upon absorption of a photon the angular momentum of the wavefunction can change from $l=0$ to $l=1$, but cannot remain at

its initial value. Electronic transitions between S_0 and T_1 can conserve total angular momentum but are spin forbidden according to the spin selection rule and have a very small probability of occurrence as a result of direct light absorption unless there is significant spin coupling to allow intermixing of spin and orbital angular momenta.

Beer-Lambert Law Experimentally, absorbance is described quantitatively by the Beer-Lambert law, which is a linear relationship between the absorbance and concentration of the sample [1] and defined as

$$A(\lambda) = \log \frac{I_0}{I} = \varepsilon(\lambda)lc, \quad (2.9)$$

where $\varepsilon(\lambda)$ is the wavelength-dependent molar absorptivity coefficient ($\text{L}\cdot\text{mol}^{-1}\cdot\text{cm}^{-1}$), l is the absorption path length (cm) and c is the concentration of the absorbing species ($\text{mol}\cdot\text{L}^{-1}$).

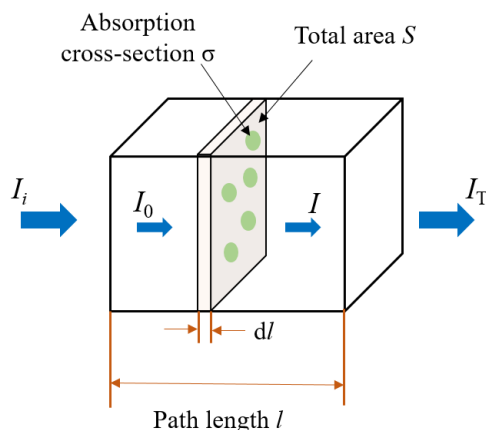


Figure 2.5: A schematic showing the derivation of Beer-Lambert law.

The derivation of the Beer-Lambert law relates the absorbance of a sample to both the concentration and the path length. Considering an incident beam with intensity I_0 hitting a sample and passing through it, the intensity of the light reduces to I (Figure 2.5). Then the fraction of light that is absorbed is given by $-dI/I$. In a thin layer with thickness of dl , the number of molecules dN is given by $c(Sdl)N_a$. Here S represents the cross-section of the incident beam and N_a is the Avogadro's number.

If each molecule has an absorption cross-section area σ associated with the photons absorbed area, which depends on the wavelength, then the total absorption cross-section area is the sum of all molecular cross-sections σdN . Therefore, the probability of photons absorbed (ratio of total cross-section to actual area, $\sigma dN/S$) is equal to the fraction of light ($-dI/I$) that is absorbed by the sample:

$$-\frac{dI}{I} = \frac{\sigma dN}{S} = N_a \sigma c dl. \quad (2.10)$$

If we integrate from 0 to l , where l is the whole absorption path length, the following equation is obtained

$$\log \frac{I_0}{I} = \frac{1}{2.303} N_a \sigma c l = \varepsilon c l. \quad (2.11)$$

In the most common form, the Beer-Lambert law is given as equation (2.9), which is in terms of the molecular extinction coefficient (ε) with $\varepsilon = N_a \sigma / 2.303$ and can be experimentally determined from absorbance spectra of solutions with known concentrations.

ii) Vibrational Relaxation

Following excitation, a molecule can dissipate part or all of its excess energy by relaxing to one of the several vibrational levels at a lower energy in the same excited state, with transition probabilities determined by the Franck-Condon principle (section 2.2.1). Vibrational relaxation (VR) is usually significantly faster (10^{-14} to 10^{-11} s) than electronic transitions occurring between different electronic excited states, such as internal conversion (10^{-13} to 10^{-10} s) or fluorescence (10^{-12} to 10^{-6} s). This difference in timescale is because the properties of electrons are virtually unchanged during the VR process, requiring only slight nuclear motion (*i.e.* vibration) with correspondingly large FC factors.

iii) Internal Conversion

As a decreased energy difference between different states usually increases the wavefunction overlap between those states, the probability of a transition from a higher electronic state to an isoenergetic vibrational level of a lower electronic state with the same multiplicity is usually large. This process is called internal conversion (IC),

and similar to VR which relies on nuclear motion, it is also a very fast non-radiative transition with a timescale of 10^{-13} to 10^{-10} s. Therefore, the electrons in an upper excited state often decay rapidly to the vibrational levels of the lowest excited state (*i.e.* S_1) through multiple VR and IC steps after photon absorption. However, owing to the generally larger energy gap between S_1 and S_0 , the IC between these two states is much slower with a timescale of 10^{-9} to 10^{-7} s. Slower IC allows the radiative decay processes (*i.e.* fluorescence) to effectively compete. This is the reason why fluorescence is mostly independent on the excitation wavelength. This general feature of the emission is stated as Kasha's rule: photons tend to emit from the lowest vibrational level of the lowest energy excited state, regardless of how high it is originally promoted by absorption. [19, 30]

iv) Fluorescence

Fluorescence involves a rapid radiative transition from S_1 to S_0 , which is a spontaneous and spin-allowed process between states of the same multiplicity. Owing to the energy dissipation from vibrational relaxation following excitation, the maximum energy fluorescence photons are generally observed at a lower energy than the lowest energy absorbed photons. In most molecules, fluorescence involves transitions of π - π^* or n - π^* orbitals, as similarly to absorption a change in angular momentum is required to conserve spin, compensating for the generated $S=1$ photon. The timescale for fluorescence emission is between 10^{-12} to 10^{-6} s.

v) Intersystem Crossing

Intersystem crossing (ISC) is a nonradiative adiabatic transition between two isoenergetic vibronic states with different multiplicity. For example, a singlet excited state can transfer energy to an isoenergetic vibrational level on the triplet manifold (T_n) or *vice versa*. ISC is in principle a spin-forbidden transition as the spin selection rule ($\Delta S = 0$) specifies that there should be no change in the total spin during an electronic transition. However, spin-orbit interactions (SOC) that promote the coupling between the spin magnetic moment (μ_S) and the orbital magnetic moment (μ_L) allow this transition to occur, as only the total angular momentum needs to be

strictly conserved during transitions. The Hamiltonian spin-orbit operator (\hat{H}_{SO}) determines the strength of SOC between the spin and orbital magnetic moments. The magnitude of SOC is given by [24]

$$E_{\text{SO}} = \langle \psi_1 | \hat{H}_{\text{SO}} | \psi_2 \rangle \sim \langle \psi_1 | \zeta_{\text{SO}} \mu_S \mu_L | \psi_2 \rangle, \quad (2.12)$$

where ψ_1 and ψ_2 represent the wavefunctions of the initial and final states. ζ_{SO} represents the SOC magnitude constant, which is related to the nuclear charge in the vicinity of the involved electrons. In organic molecules, the ζ_{SO} of lighter atoms is much smaller than the vibrational energies, resulting in weak SOC and thus slower ISC transition. One way to enhance the probability of ISC is to increase the overlap of the singlet and triplet vibrational levels, *i.e.* maximize $\langle \psi_1 | \psi_2 \rangle$. In addition, ISC can also be enhanced by the introduction of heavy atoms (*i.e.* Ir and Pt), which have larger \hat{H}_{SO} and can accelerate the ISC process.

Conservation of angular momentum requires that ISC preserves the total angular momentum of the system. Therefore, an electron spin-flip (from singlet to triplet state) has to be compensated for by a simultaneous transition from a p orbital of an orbital momentum of 1 to a p orbital of an orbital momentum of 0, *i.e.* $p_x \rightarrow p_y$. This concept is known as El-Sayed's rule, which states that the ISC rate is relatively large if the non-radiative transition involves a change in the orbital type. [31] In organic systems, conjugation is achieved through mixing of multiple aligned p orbitals on different atoms to form π bonding molecular orbitals. In contrast, unaligned p orbitals break this conjugation and form non-bonding molecular orbitals (n), while filling aligned p orbitals with opposite orientations gives antibonding π^* orbitals. ISC transitions such as $^1(\pi, \pi^*) \rightarrow ^3(\text{n}, \pi^*)$ is therefore more favourable than $^1(\pi, \pi^*) \rightarrow ^3(\pi, \pi^*)$, and $^1(\text{n}, \pi^*) \rightarrow ^3(\pi, \pi^*)$ is more favourable than $^1(\text{n}, \pi^*) \rightarrow ^3(\text{n}, \pi^*)$. The timescale of ISC is at the order of 10^{-11} to 10^{-6} s.

In addition to SOC, hyperfine coupling (HFC) can also promote ISC from singlet to triplet states. HFC arises from the spin-spin interactions between the electron's spin and the nuclear spin of individual nuclei. [32, 33] However, HFC is a short-range interaction (0.2 cm^{-1}) because nuclei are very small, making it a much weaker contributor in comparison to SOC in most cases. [34]

ISC is usually understood to progress from singlet to triplet states, although it

can also occur in a reverse direction, *i.e.* reverse intersystem crossing (RISC). As the triplet state is at a lower energy than the singlet state ($E_T < E_S$), RISC is usually an endothermic process, *i.e.* a kind of thermally activated upconversion. It can be an efficient transition to harvest triplet states and gives rise to unimolecular delayed fluorescence (DF). When the energy difference between the singlet and triplet states is small, efficient upconversion of a triplet state to an isoenergetic vibronic singlet state can occur *via* thermal activation at rates up to 10^7 s^{-1} .

vi) Phosphorescence

Phosphorescence is a radiative deactivation process occurring between states of different multiplicity ($T_1 \rightarrow S_0$). The phosphorescence spectrum is generally shifted to a longer wavelength relative to the fluorescence due to the lower energy of the triplet state. As the electronic ground state of molecular oxygen is a triplet state (T_0), the triplet excited states in organic molecules can be easily quenched by collisions with oxygen molecules, where energy is transferred to oxygen and excited singlet oxygen is created. Therefore, the observation of phosphorescence often requires oxygen-free conditions. [17,23]

Moreover, owing to the forbidden nature of the transition from T_1 to S_0 , a slower emission rate is associated with phosphorescence, on a timescale of 10^{-3} to 10^2 s. During such a slow process, faster nonradiative transitions associated with molecular vibrations (such as IC and ISC) and collisions can easily intervene and deactivate the excited triplet firstly, which makes the observation of phosphorescence very difficult at room temperature. In order to favour the radiative transitions, the nonradiative transitions need to be suppressed, often by restricting vibrations at low temperatures or dispersing materials in rigid matrices. Another effective method is to employ heavy atoms (Pt, Ir) in molecules, which can facilitate the ISC process through strong SOC and thus enhance the phosphorescence rate.

As phosphorescence lifetimes are typically in milliseconds up to seconds, phosphorescent materials are attractive to many applications involving counterfeit labels, signal and sensing due to their “glow-in-the-dark” luminescence properties.

2.2.3 Lifetimes and Quantum Yields

The transition rate constants (k) describe the probability of a transition per unit time between states, as sketched in Figure 2.4. They are also involved in expression for the lifetime ($\tau = 1/k$) of an excited state and the quantum yields ($\Phi = k/\sum k$) of transitions between states. Therefore, rate constants of relevant processes can be used to characterize and evaluate the potential of new organic materials for applications. To distinguish rates associated with different processes subscripts are used: k_{nr} denotes the rate constant of a non-radiative process, while k_{ISC} and k_{RISC} are for the ISC and RISC processes. For radiative decays, the rate constants of the fluorescence and phosphorescence processes are represented by k_{f} and k_{ph} , respectively.

The lifetime of an excited state is approximately the average time that a chromophore spends in the excited state before decaying to the ground state by emitting a photon. [35] In organic molecules, direct radiative decay from the singlet excited state occurs on a timescale from tens of picoseconds to hundreds of nanoseconds, while the lifetime of triplet state ranges from microseconds to milliseconds. The lifetimes of fluorescence (τ_{f}) and phosphorescence (τ_{ph}) are given by [19]

$$\tau_{\text{f}} = \frac{1}{k_{\text{f}} + k_{\text{nr}}^{\text{S}} + k_{\text{ISC}}}, \quad (2.13)$$

$$\tau_{\text{ph}} = \frac{1}{k_{\text{ph}} + k_{\text{nr}}^{\text{T}}}. \quad (2.14)$$

The photoluminescence quantum yield (PLQY, Φ) measures the efficiency of the radiative decay in organic molecules and is defined as the ratio of the number of photons emitted to the number of photons that are absorbed to generate the emission. Fluorescence quantum yield (Φ_{F}) reflects the fraction of excited molecules that decays to the ground state by emitting fluorescence and is given by [1]

$$\Phi_{\text{F}} = \frac{k_{\text{f}}}{k_{\text{f}} + k_{\text{nr}}^{\text{S}} + k_{\text{ISC}}} = k_{\text{f}}\tau_{\text{f}}. \quad (2.15)$$

The quantum yield of intersystem crossing (Φ_{ISC}), which is also referred as the triplet yield (Φ_{T}), representing the efficiency of the triplet formation and denoted as

$$\Phi_{\text{ISC}} = \frac{k_{\text{ISC}}}{k_{\text{f}} + k_{\text{nr}}^{\text{S}} + k_{\text{ISC}}} = k_{\text{ISC}}\tau_{\text{f}}. \quad (2.16)$$

While the reverse intersystem crossing quantum yield (Φ_{RISC}), *i.e.* singlet yield (Φ_{S}) representing the yield of triplets that are upconverted to the singlet state, is written as

$$\Phi_{\text{RISC}} = \frac{k_{\text{RISC}}}{k_{\text{RISC}} + k_{\text{nr}}^{\text{T}} + k_{\text{ph}}}. \quad (2.17)$$

The quantum yield of phosphorescence (Φ_{ph}) is given by

$$\Phi_{\text{ph}} = \frac{k_{\text{ph}}}{k_{\text{ph}} + k_{\text{nr}}^{\text{T}}} \Phi_{\text{ISC}} = \Phi_{\text{ISC}} k_{\text{ph}} \tau_{\text{ph}}. \quad (2.18)$$

Based on the determination of the quantum yields and lifetimes, rate constants can be calculated according to the following equations [25]

$$k_{\text{f}} = \frac{\Phi_{\text{F}}}{\tau_{\text{f}}}, \quad (2.19)$$

$$k_{\text{ISC}} = \frac{\Phi_{\text{ISC}}}{\tau_{\text{f}}}, \quad (2.20)$$

$$k_{\text{nr}}^{\text{S}} = \frac{1}{\tau_{\text{f}}} - k_{\text{f}} - k_{\text{ISC}}, \quad (2.21)$$

where Φ and τ can be determined experimentally, allowing various rate constants to be calculated.

2.2.4 Charge-Transfer and Solvatochromism

Charge-Transfer

Charge-transfer (CT) plays an important role in both fundamental and applied physical chemistry and is exploited in many types of molecules such as photocatalytic systems, proteins, ferromagnetic complexes and conjugated materials. In terms of luminescent applications, vast numbers of molecular complexes exhibiting CT character have been explored and have shown promising potential to achieve high performance OLEDs.

CT is a process in which a fraction of the electronic charge in the electron-donor (D) species is transferred to the electron-acceptor (A), with electrons occupying one fragment while holes are located at the adjacent fragment, and the electron-hole separated state of the molecule is its lowest-energy configuration. This can occur in systems with two or more different molecules, [36] or within individual molecules constituting both D and A fragments. Figure 2.6 depicts an example of a D–A

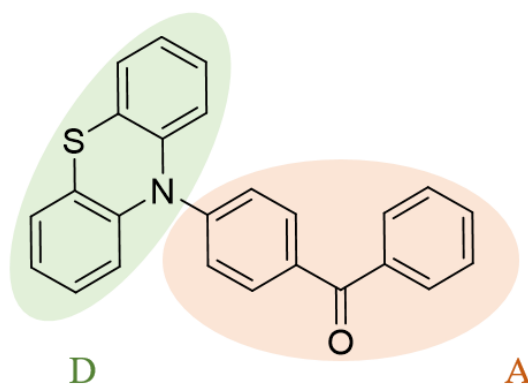


Figure 2.6: An example of a D–A molecule.

molecular structure with phenothiazine acting as the D and benzophenone as the A unit. These can easily undergo an electronic transition to the excited CT state, and have a high sensitivity to surrounding environmental factors such as temperature, concentration and solvent polarity. CT states are usually identified by their broad Gaussian-type luminescence, a result of numerous unresolved vibronic states densely packed within the bond. In a D–A type molecule, the individual D or A unit also has its own localized excite states (LE), which have negligible wavefunction overlap with adjacent quantum states and are usually not affected by changes of the environment. [37] Therefore, LE states can be identified by their structured luminescence and lack of response to a change on the surrounding polarity.

In order to enhance the ISC (RISC) process and utilize triplet excitons, a small energy gap between the singlet and triplet states (ΔE_{ST}) is needed, which is determined by their exchange energy ($\Delta E_{ST} = 2J$). [38] Owing to the small wavefunction overlap, intramolecular and intermolecular CT states always have small ΔE_{ST} . Therefore, D–A type molecules with CT character are currently considered as the most promising design strategy for organic TADF molecules. [39–41]

Solvatochromism

Solvatochromism is the phenomenon whereby the spectrum of a molecule varies in different solvents. This observed spectral shift is called solvatochromic shift, which

is an experimental evidence of changes in the solvation energy. [1,42] As the various solvents have different impacts on the electronic ground state and excited state of the solute, the energy gap between them changes accordingly. As a result, the absorption and emission spectra can change their position, intensity and shape. The extent of the change depends on the action of intermolecular forces between the solvent and solute.

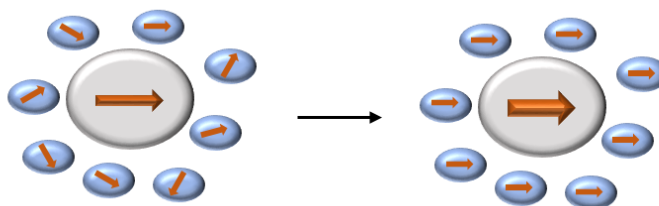


Figure 2.7: A schematic of the proposed origin of the solvatochromism. The dipole moments of the solvent molecules (blue) are randomly distributed when the solute molecule (grey) is in its ground state, then reorientate to align (parallel or antiparallel) to the dipole moment of the excited state of the solute molecule when the molecule is excited. [2]

For the absorption process, the effect mainly reflects the influence of the solvent on the ground state giving a slight change on the spectrum. However, much more significant changes are observed in the emission. A schematic of the solvatochromism is shown in Figure 2.7. During an electronic transition, the dipole moment of the excited state molecule interacts to a varying degree with the dipole moment of the surrounding solvent molecules before relaxing to the ground state. As the timescale of the fluorescence is much longer than that of the absorption, the solvent molecules have time to reorganize to stabilize the excited state dipole moment of the new system *via* relaxation over this period of time. The emission spectrum in this situation loses the vibrational structure and appears as a Gaussian shape. [43, 44] Redshift in more polar solvents is because solvent molecules can reorient to a greater extent. It happens in solid hosts as well but to a lesser degree as reorientation motion is not as easy as the solvent. In contrast, the LE state is of localized character and independent of the polarity of the environment as it has a negligible dipole moment.

2.3 Triplet Harvesting Mechanisms

The weak emissive properties of the triplet state make the utilization of triplet states in luminescence applications almost impossible at room temperature. A well-known case is the limitation on the efficiency of organic light-emitting diodes (OLEDs) imposed by spin statistics. In OLEDs, only 25% of excitons are formed as singlet states from random charge recombination of evenly distributed spins. These can be utilized to generate luminescence under electrical excitation. However, the remaining 75% excitons are of triplet character that are unable to participate in the electroluminescence process in normal conditions. The internal quantum efficiency (IQE) of an OLED is thus limited to 25%, which is unacceptably low for most applications. [45]

To increase the exciton utilization, phosphorescent emitters with heavy atoms are employed. Both singlet and triplet states are harnessed in phosphorescent OLEDs, and theoretically 100% IQE can be achieved. [7] However, the heavy metals commonly used in the emissive organic molecules, such as Pt(II) and Ir(III), are expensive and prone to photolytic and electrolytic cleavage which leads to less stable compounds. [46]

Therefore, developing strategies to accelerate triplet harvesting in metal-free organic molecules is a major goal of modern OLED research and requires detailed understanding of ISC/RISC. In particular, diverse mechanisms have been proposed to promote full utilization of singlet and triplet excitons in the luminescent processes of organic molecules. These are reviewed in the following subsections:

2.3.1 Thermally Activated Delayed Fluorescence

Delayed fluorescence has been observed as a result of thermally activated delayed fluorescence (TADF). This promising and efficient approach to harvesting triplets in organic molecules is an intramolecular mechanism, and was first observed in eosin by Parker and Hatchard in 1961 who identified it as an *E*-type DF. [47] TADF is analogous to a *P*-type triplet-triplet annihilation (TTA), which was firstly observed in pyrene [48] and is a bimolecular process controlled by diffusion that involves the interaction between pairs of excited triplet states. [49–51] Following the work done

by Adachi *et al.* in 2012, [52] TADF has emerged as one of the most promising mechanisms to promote triplet harvesting and achieve high efficiency in OLEDs.

In TADF emitters, following light absorption and ISC processes a population of triplet states is created. TADF molecules are specifically designed to have a small energy difference between the singlet and triplet states (ΔE_{ST}). Therefore, thermal energy can be used to upconvert the non-emissive triplet states directly into luminescent singlet states *via* a thermally activated reverse intersystem crossing (RISC) mechanism. [12] RISC is a temperature dependent process and can be expressed by a Boltzmann distribution

$$k_{\text{RISC}} = A \exp\left(-\frac{\Delta E_{ST}}{k_B T}\right), \quad (2.22)$$

where A is a pre-exponential factor, k_B is the Boltzmann constant and T is the temperature. High temperatures therefore accelerate the RISC process.

As discussed in section 2.1.3, the energy gap ΔE_{ST} is equal to twice the exchange integral ($2J$) between the spatial wavefunction overlap of the ground and excited states. [25] Therefore, a small ΔE_{ST} can be achieved by minimizing the frontier orbital overlap between HOMO and LUMO. This in turn can be achieved by designing molecules where electron donor (D) and electron acceptor (A) units are covalently linked in D–A–D or D–A type structures, which leads to the formation of intramolecular charge transfer (CT) states. This general strategy provides great tactical flexibility for designing and modifying molecular structures and fine-tuning the emission wavelength over the whole visible spectrum. As such, TADF materials provide a promising pathway for high efficiency display and lighting applications.

While empirical molecular design strategies for TADF emitters are already well established, the TADF mechanism itself is still unclear in some aspects. Figure 2.8a gives a schematic representation of the TADF mechanism, showing the relevant energy levels and rate constants. In many cases, molecules can be excited to the locally excited singlet state (^1LE) of the D or A unit through a π - π^* transition. Excitons in the higher ^1LE state may decay to either the ^1CT or ^3CT state through electron transfer, or radiatively decay to the ground state in picoseconds or nanoseconds depending on the relative rate constants. The ^1LE state may also undergo the ISC

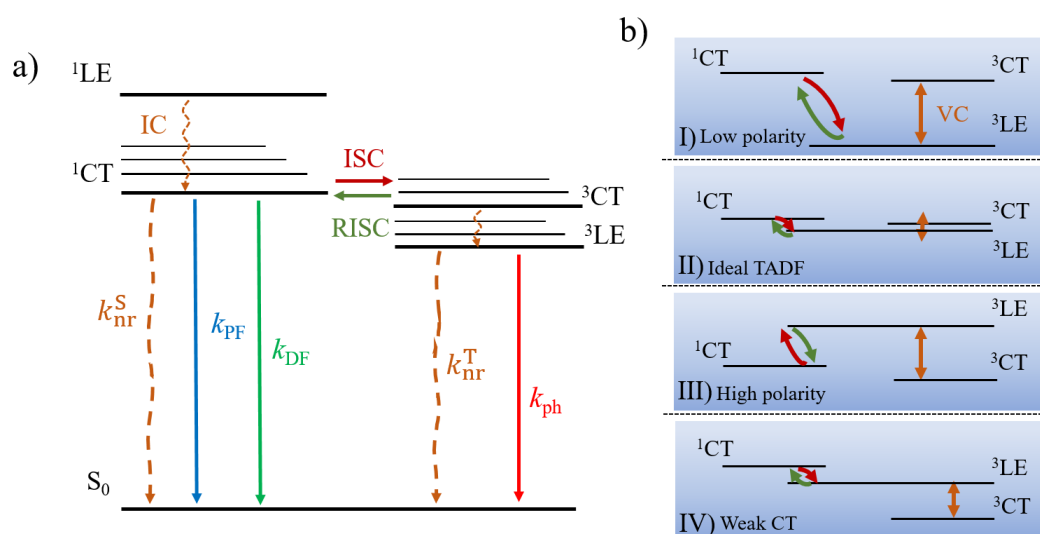


Figure 2.8: a) A schematic showing the TADF mechanism in organic molecules. b) Four proposed models for the RISC mechanisms between singlet and triplet excited states.

process to the locally excited triple state (${}^3\text{LE}$). Alternatively, excitation directly to the ${}^1\text{CT}$ is also sometimes possible through relatively weak $n-\pi^*$ or a mixed $\pi-\pi^*/n-\pi^*$ transition. [41]

After accumulation of a population of excitons in ${}^1\text{CT}$, three main pathways compete. Direct radiative decay (k_f) to the ground state gives prompt fluorescence (PF) on a timescale of nanoseconds, and is accompanied by non-radiative processes to S_0 (k_{nr}^S), or to the triplet states by ISC (k_{ISC}). The triplet states themselves will then decay to the ground state *via* a radiative process yielding phosphorescence (k_{ph}), or through a nonradiative decay (k_{nr}^T). In addition, the thermally activated RISC process (k_{RISC}) can also occur from the triplet states in TADF molecules if the energy gap ΔE_{ST} is small enough (generally less than a few hundred meV, but ideally around tens of meV for efficient RISC). When the RISC process is enhanced, ISC is in turn also very rapid as these processes are conjugate of each other. The excitons that return to the singlet state (from the upconverted triplet states) emit as delayed fluorescence (DF), or can undergo additional cycles of ISC/RISC decaying normally at any stage. The luminescent process is “delayed” by the additional processes before fluorescence, which leads to a longer DF lifetime in the range of microseconds to milliseconds. The origin of TADF emission from the long-lived

triplet states makes it a sensitive process to temperature (controlling k_{RISC}) and oxygen (contributing to k_{nr}^{T}).

TADF Excited-State Dynamics

The energy alignment between singlet and triplet excited states has critical control over the efficiency of RISC mechanism, with different possible scenarios depicted in Figure 2.8b. As there is no change in the spatial orbital configuration (which is required to compensate for an electronic spin-flip by changing orbital angular momentum), the interconversion between ^1CT and ^3CT states is a strictly forbidden SOC process, *i.e.* $\langle ^1\text{CT} | \hat{H}_{\text{SO}} | ^3\text{CT} \rangle = 0$. [53, 54] Therefore, it is also forbidden to harvest the ^3CT population into the ^1CT state directly by RISC. [14, 41] Hyperfine coupling (HFC) allows angular momentum exchange between the spins of the electrons and the nuclei in the same molecule, and is a local mechanism between ^1CT and ^3CT states. However, it is unlikely to contribute, as it shows a very weak oscillator strength (f) and only contributes in a short range (0.2 cm^{-1}), due to the very small orbital overlap between electrons and protons/neutrons confined to the nucleus. [33, 55]

Instead, nonadiabatic coupling between the two relevant low-lying triplet excited states (^3CT or ^3LE) is now understood to play an important role in the TADF mechanism. [56, 57] Therefore, along with the initial and final states an additional intermediate (near isoenergetic) state is required to explain the high efficiency of RISC in the absence of strong HFC or SOC. Recently, Gibson *et al.* developed this second-order perturbation theory based on a D–A molecule composed of phenothiazine (PTZ) donor and a dibenzothiophene-*S,S'*-dioxide (DBTO2) acceptor. They demonstrated that both ^3CT and ^3LE energies are crucial to the RISC process. [53] Therefore, at least two energy gaps ($\Delta E_{^1\text{CT}-^3\text{LE}}$ and $\Delta E_{^3\text{LE}-^3\text{CT}}$) need to be taken into consideration when optimizing TADF efficiency. A key insight from this work is the population transfer between ^3CT and ^3LE states *via* vibronic coupling (a specific form of IC), which is mediated by rocking of the D–A bond dihedral angle. Then adiabatic SOC can occur between the ^3LE and ^1CT states, as with different orbitals $\langle ^3\text{LE} | \hat{H}_{\text{SO}} | ^1\text{CT} \rangle \neq 0$. The critical role of the vibronic coupling between the

two triplet states is evidenced by comparison of the simulated population kinetics of PTZ-DBTO2 with and without the nonadiabatic coupling calculated by Penfold *et al.* using quantum dynamics. [58, 59] The mixing of the triplet states can also reduce the activation energy for RISC by forming an equilibrium between these two triplet states, even without thermal activation.

Figure 2.8b illustrates four distinct energy level alignments possible for TADF molecules. In the first case (type I), both CT states have higher energy levels than that of the ^3LE state. State mixing between ^3CT and ^3LE is followed by a direct RISC process to ^1CT to give TADF in this scenario. Type II represents the most ideal case with a negligible energy gap. The three states (^1CT , ^3CT and ^3LE) are in resonance, giving a highly efficient TADF mechanism. In case III, both CT states are below ^3LE , which can occur in a high polarity environment which lowers the CT states but not the ^3LE . Type IV represents an intermediate ^3LE state between the higher ^1CT and lower ^3CT states, which normally occurs in molecules with weaker CT character. In this case, although the ΔE_{ST} between CT states increases, the isoenergetic ^1CT and ^3LE states and vibronic coupling between the two triplet states can still facilitate RISC. [59, 60]

Photophysical Parameters

The photoluminescence quantum yield (PLQY, Φ) represents the ratio of number of photons emitted to photons absorbed upon optical excitation, with components arising from PF and DF (Φ_{PF} and Φ_{DF}) that can be determined from aerated (assumed PF only) and degassed (PF+DF) measurements. The interconversion between singlet and triplet excited states can occur many times before achieving an equilibrium condition. This equilibrium between singlet and triplet excited states is a crucial feature of TADF, which depends on the ISC quantum yield (Φ_{ISC} , *i.e.* triplet yield Φ_{T}) and RISC quantum yield (Φ_{RISC} , *i.e.* singlet yield Φ_{S}). According to equation (2.17), high Φ_{RISC} can be achieved on the condition that the energy gap of the system is small and nonradiative processes are suppressed, *i.e.* $k_{\text{RISC}} \gg k_{\text{ph}} + k_{\text{nr}}^{\text{T}}$. The rate constant of RISC (k_{RISC}) is a key parameter to quantitatively evaluate the TADF efficiency. All of these important parameters can be accessed through

steady-state and time-resolved measurements.

Based on the multiple cycles of ISC and RISC between singlet and triplet states, the total fluorescence quantum yield (Φ_F) of TADF molecules can be described by

$$\begin{aligned}\Phi_F &= \Phi_{PF} + \Phi_{DF} = \sum_{i=0}^{\infty} \Phi_{PF} (\Phi_T \Phi_S)^i \\ &= \Phi_{PF} \frac{1}{1 - \Phi_T \Phi_S},\end{aligned}\quad (2.23)$$

with

$$\Phi_{DF} = \Phi_T \Phi_S \Phi_{PF} + (\Phi_T \Phi_S)^2 \Phi_{PF} + \dots + (\Phi_T \Phi_S)^n \Phi_{PF} + \dots \quad (2.24)$$

As the ISC efficiency is limited by the fluorescence yield, the maximum value of Φ_T can only be up to $1 - \Phi_{PF}$. When the ratio between DF and PF is around or above four ($\Phi_{DF}/\Phi_{PF} \geq 4$), the product of singlet and triplet yields ($\Phi_T \Phi_S$) is very high (around 80%). [25] In this case, the DF contribution is huge on account of the efficient RISC process, and a Φ_S (Φ_{RISC}) close to unity is readily achieved. [41, 61] Derived from equation (2.23), the triplet yield is therefore given by

$$\Phi_T(\Phi_{ISC}) = \frac{\Phi_{DF}/\Phi_{PF}}{1 + \Phi_{DF}/\Phi_{PF}} = \frac{\Phi_{DF}}{\Phi_{PF} + \Phi_{DF}}. \quad (2.25)$$

In many materials with small DF/PF ratios (low TADF efficiencies), equation (2.25) is not valid though (when $\Phi_{DF}/\Phi_{PF} < 4$). In these cases the triplet yield needs to be experimentally determined using ultrafast spectroscopy or otherwise.

The important rate constant of RISC (k_{RISC}) can then be estimated from the quantum yields and the DF lifetime, which is given by

$$k_{RISC} = \frac{1}{\tau_{DF}} \frac{\Phi_{RISC}}{1 - \Phi_{ISC} \Phi_{RISC}} = \frac{\Phi_{RISC}}{\tau_{DF}} \left(\frac{\Phi_{PF} + \Phi_{DF}}{\Phi_{PF}} \right). \quad (2.26)$$

As mentioned, Φ_{RISC} can be taken as 1 in efficient TADF systems, where nonradiative processes from triplet state must be greatly suppressed as deduced by the high TADF efficiency.

Challenges

Although the potential of metal-free organic TADF molecules has already been greatly developed, many challenges still exist on the path to commercialization. As

discussed above, a small ΔE_{ST} is one of the key parameters to achieve efficient RISC. It can be minimized by decreasing the excited state interactions and spatial overlap of electrons between the D and A units in TADF molecules with near orthogonal conformation. The distribution of HOMO and LUMO is then localized on the D and A units, respectively. However, this small orbital overlap also diminishes the fluorescence rate (k_f). [62]. A high k_f is necessary to utilize the harvested triplets in singlet excited states before they cycle back to the triplet state, possibly then decaying *via* nonradiative pathways. This requires a strong coupling between ^1CT and S_0 , which is mutually exclusive with a small HOMO and LUMO overlap. Therefore, it is necessary to design molecules with well-balanced ΔE_{ST} and k_f . Nonetheless, several investigations have reported efficient TADF molecules with small gaps ΔE_{ST} and high Φ_f (large k_f) at the same time, for example by using a combination of weak D and stronger A units [63–66] or molecular structures with multiple D/A units [12, 67]. Therefore, there is certainly scope for innovative design strategies to overcome previously assumed limitations or trade-offs for TADF emitters.

For OLEDs, molecular design for the preparation of red, green and even sky-blue TADF emitters has already worked remarkably well, [68–71] whereas effective matching of D and A units for deep-blue or pure-blue TADF emitters remains challenging. [72–76] A balance between the weak CT character of the excited states and the minimized energy gap ΔE_{ST} needs to be considered. [77] Accordingly, compounds with short conjugation length of the constituting moieties are preferred to obtain high-lying triplet excited states, which have the potential to be in resonance with the high energy singlet states for blue emission. [77, 78] The substituents and substituting positions must be carefully selected for D and A units to ensure the molecules emit in the blue region. [79] Efficiency roll-off at a practical brightness is another unresolved issue for commercial applications. As triplet states have relatively long lifetimes, the excitons are easily quenched *via* singlet-triplet annihilation or TTA before upconverting to singlet states and by charge interactions in devices. [14, 80–83] Thus, both small ΔE_{ST} and short τ_{DF} are crucial to improve the roll-off and operational stability of devices.

2.3.2 Room Temperature Phosphorescence

Room temperature phosphorescence (RTP) is another effective mechanism to harvest triplet states in metal-free organic molecules. The discovery of organic RTP emitters has attracted great attention due to their potential for optoelectronic and photonic applications, such as OLEDs [84–86], luminescence labels [87], imaging [88, 89], sensing [90, 91], optical thermometry [92] and anti-counterfeiting [93]. Like TADF materials, the potential advantages of RTP emitters (including low-cost, various molecular design and good processability) remain challenging to fully control and exploit.

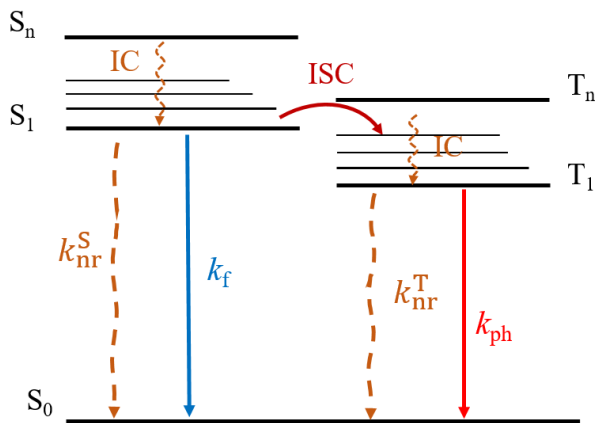


Figure 2.9: A simplified schematic of RTP mechanism.

Figure 2.9 depicts a simplified schematic of the RTP mechanism. Upon excitation, excitons accumulate in the excited triplet manifolds *via* a spin-flipping ISC process from S_1 , followed by a radiative decay emitting phosphorescence from T_1 to S_0 . The nonradiative relaxations *via* thermal and collisional processes are concurrently competitive to phosphorescence emission, which is why phosphorescence is normally only observed at low temperatures. [94, 95] Thus, efficient RTP is only possible when the ISC is enhanced and the nonradiative relaxation from T_1 to S_0 due to molecular vibrations is suppressed.

According to the first-order perturbation theory and Marcus semiclassical approach, the rate constant of ISC (k_{ISC}) at room temperature is expressed as [96]

$$k_{\text{ISC}} \propto \frac{\langle {}^1\Psi | \hat{H}_{\text{SO}} | {}^3\Psi \rangle^2}{\exp(\Delta E_{\text{ST}}^2)}, \quad (2.27)$$

where ${}^1\Psi$ and ${}^3\Psi$ represent the total electronic wavefunctions of singlet and triplet excited states, respectively. This shows that k_{ISC} is proportional to the electron's spin and orbital interactions (\hat{H}_{SO}) and singlet-triplet energy gap (ΔE_{ST}).

As described in section 2.2.2, SOC can also be enhanced by the heavy-atom effect. To promote SOC and thus increase k_{ISC} , an effective approach is to mix the molecular orbital configurations of singlet and triplet states *via* the introduction of heavy atoms (*e.g.* Br and I). For example, Bolton *et al.* reported a series of new organic RTP emitters with efficient ISC by incorporating halogen bonding into their crystals. [97] By substituting iodine atoms in crystals, Xiao *et al.* similarly achieved highly efficient organic RTP. [93] Recently, Wang *et al.* proposed a facile method of heavy-atom-participated anion- π^+ interaction to construct RTP-active organic salts and achieved single-molecule white light emission. [98] However, halogen-carbon bonds are weak and prone to photolytic cleavage, which make such emitters unstable. According to El-Sayed's rule, efficient SOC occurs when the transition between the two excited states involves a change in the orbital type. [31] Therefore, the existence of n orbitals can enhance SOC, provided by the incorporation of carbonyl group or heteroatoms (*e.g.* N, O, S and P). [99–101] For example, Yang *et al.* reported an efficient RTP with coupled intermolecular n and π units in organic crystals. [87]

Another efficient way to accelerate ISC is to decrease the singlet-triplet energy gap ΔE_{ST} , which is also a promising way to design TADF molecules as discussed in section 2.3.1. ΔE_{ST} can be minimized by the introduction of CT state containing moieties in aromatic molecules. [101–103] An H-aggregated system with a small ΔE_{ST} was reported *via* aggregation induced ISC by Yang *et al.* [104] Recently, Xiong *et al.* proposed a design method of structural isomerism and achieved efficient and ultralong RTP emitters with small ΔE_{ST} and pure ${}^3\pi\pi^*$ configurations. [105]

Looking back at Figure 2.9, the vibrational quenching of the triplet population must be suppressed by rigidification of molecular conformations and isolation from oxygen. RTP is therefore typically achieved by doping the emitter in rigid hosts. [16, 106] For example, a simple RTP emitter with a D–A–D structure was reported, showing a high phosphorescence quantum yield of 60% when doped into a polymer matrix. [100] In addition, both crystallization [97, 101, 107] and molecu-

lar aggregation [108, 109] are popular strategies to achieve efficient RTP, which can effectively restrict the nonradiative decays by forming a rigid environment for RTP molecules.

Other strategies have also been employed to obtain efficient organic RTP. Recently, Sun *et al.* designed a molecule with a twisted crystal structure showing a lifetime of 402 ms under ambient conditions, which is based on a common phosphor with two methylene groups to break molecular conjugation. [110] The influence of molecular packing with strong $\pi - \pi$ interactions in the solid state was reported by Yang *et al.*, showing great potential in live imaging of mice. [111]

As RTP with a long lifetime (τ_{ph} , in hundreds of milliseconds or even second range) is desirable for some applications such as emergency lighting, traffic signs and anti-counterfeiting, [89, 112] a slow decay process of the triplet state is sometimes sought after. However, only a few reported examples exist in organic RTP with both high efficiency and a long lifetime. [87, 113, 114] This puts at odds the conflicting desires of high ISC quantum yield (large ISC of $S_1 \rightarrow T_1$) and long phosphorescence lifetime (low comply of $T_1 \rightarrow S_0$), since the rate constants of nonradiative ISC from T_1 to S_0 and from S_1 to T_n increase simultaneously. [95, 114] Therefore, further investigations to fully understand the RTP mechanism are of great importance to guide the synthetic design strategies and improve RTP performance for this range of novel applications.

2.4 Organic Light-Emitting Diodes

2.4.1 Evolution of Organic Light-Emitting Diodes

With extensive research efforts following the discovery of efficient electroluminescence in organic materials, organic light-emitting diodes (OLEDs) have attracted great interest and have already been widely applied in flat panel displays. OLEDs exhibit excellent advantages compared to inorganic OLEDs and fluorescent tubes, including lightweight, large viewing angle, fast response time, high efficiency and potential flexibility. Following initial optical characterization of organic molecules showing promising properties, OLEDs are fabricated for electrical investigations to

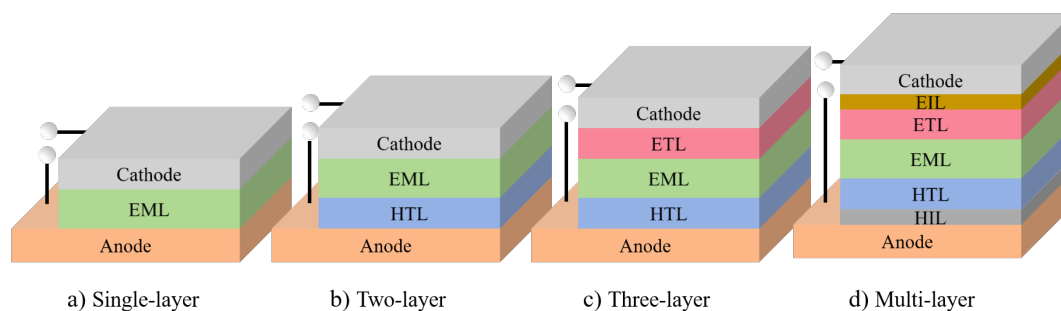


Figure 2.10: Evolution of OLED architectures: a) single-layer OLED, b) two-layer OLED, c) three-layer OLED, d) multi-layer OLED.

evaluate their performance in real applications.

The basic operating principle of an OLED is that they generate light as holes and electrons are injected into the light-emitting layer (EML). The first practical OLED was built by C. W. Tang *et al.* in 1987, which was made of a single organic layer sandwiched between a transparent anode and a metallic cathode as shown in Figure 2.10a. [5] To achieve a high efficiency, the single layer should ideally have a high luminescence yield and good hole/electron transporting properties. However, it is exclusively rare to find a single molecule possessing all these properties. Therefore, two or more layers are introduced to share the required functions for efficient OLEDs.

In a two-layer OLED (Figure 2.10b), a hole or electron transport layer (HTL or ETL) is added. However, the small recombination zone (which is mainly in the interface between the layers) restricts the luminescent efficiency. An additional layer can then be used between the two charge transport layers in a three-layer OLED to achieve the charge balance for the hole-electron recombination (Figure 2.10c). To further improve OLED performance, hole/electron injection layers (HIL/EIL) are included in a multi-layer structure, which can effectively eliminate the charge carrier leakage, exciton quenching and improve the charge balance (Figure 2.10d). [115,116]

2.4.2 Working Principle of Organic Light-Emitting Diodes

In OLEDs, electrons are injected from the cathode into the LUMO level of the adjacent organic layer, while holes are injected from the anode into the HOMO level of the adjacent layer. The charges hop through any intermediate functional

organic layers (such as hole blocking or electron blocking layer to prevent short circuit current) and recombine in the emissive layer to produce photons. The general architecture of a modern OLED is shown in Figure 2.11. Materials with appropriate HOMO and LUMO levels should be carefully chosen to align HOMO/LUMO and minimize losses at the interfaces between layers. [117] In addition, a well-balanced charge injection and recombination system is also required. Therefore, careful design strategies are needed in terms of materials and structures for OLEDs. Some of the commonly used materials for research OLEDs and their functions are described below.

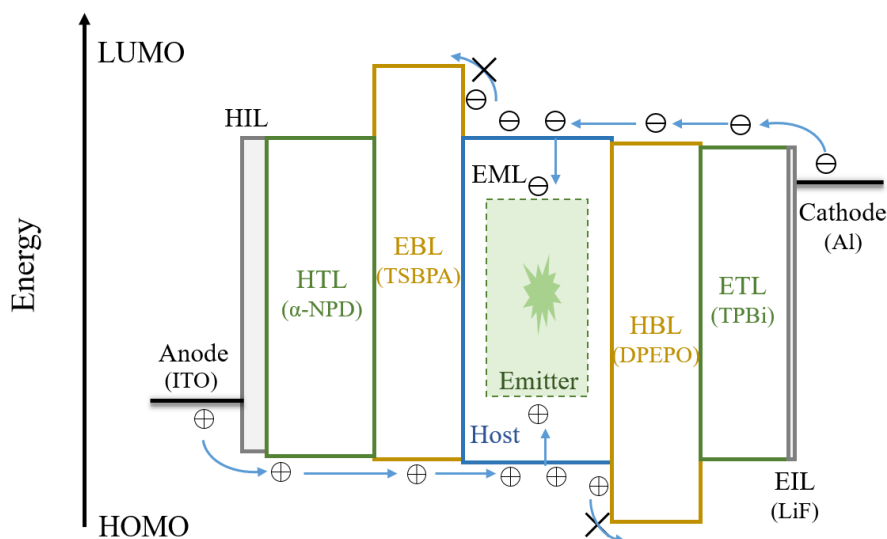


Figure 2.11: A schematic energy level diagram of a multi-layer OLED device.

Indium tin oxide (ITO) is a widely used transparent conducting anode in OLEDs, situated on top of a substrate (*e.g.* plastic, glass) due to its good electrical conductivity and optical transparency with a high work function. It is through this transparent anode that photons generated in the emissive layer can emerge. Metals with low work functions are typically employed as the cathode materials, such as Al, Ag and Au [45, 118] Among these, Al is the most commonly used material since it is more stable in ambient conditions and much cheaper than Ag or Au. To improve the electron injection efficiency, lithium fluoride (LiF) with a thickness of less than 1 nm is deposited as a buffer layer between Al and organic layers to lower the injection

barrier. [119]

In device design, the selection of appropriate compounds for the secondary transporting layers and the recombination layer is of great importance. Hole transport layers (HTL) with high hole mobility are introduced to facilitate the migrations of holes into the EML. For example, α -NPD (*N,N'*-di(1-naphthyl)-*N,N'*-diphenyl-(1,1'-biphenyl)-4,4'-diamine) and TCTA (tris(4-carbazoyl-9-ylphenyl)amine) are used as HTL in this thesis. Ideally, the HOMO of the HTL should lie close to the work function of the anode and the EML for easier hole injection. On the other hand, a HTL with a high-lying LUMO level is important to prevent electrons from reaching the anode. Generally, an electron blocking layer (EBL), *e.g.* TSBPA (4,4'-(diphenylsilanediy)bis(*N,N*-diphenylaniline)), with a high LUMO and high triplet state can also be used between the HTL and EML, which can largely prevent the leakage of electrons and confine the charge carriers in the EML. [4] In addition, the hole injection layer (HIL) such as MoO₃ (molybdenum trioxide) is commonly evaporated as an injection buffer layer between the anode and HTL to lower the injection barrier.

Similarly, the injection and transport of electrons from the cathode to the EML follows the same principle. The electron transport layer (ETL) is introduced to facilitate the migrations of electrons from the cathode into the EML, which should possess a good electron mobility. For example, TPBi (2,2',2''-(1,3,5-benzenetriyl)-tris(1-phenyl-1-*H*-benzimidazole) is commonly used as an ETL. The LUMO level of this layer should lie close to the cathode work function and the EML for easier electron injection, while its low-lying HOMO can prevent escaped holes from reaching the cathode. A hole blocking layer (HBL) can also be used when required, such as DPEPO (bis[2-(diphenylphosphino)phenyl]ether oxide) which has a deep HOMO and high triplet energy.

The EML is located in the centre of the device, where charges recombine and form excitons. A non-doped single material EML is desirable to simplify the device structure, but this approach presents many challenges. Instead, appropriate host matrices are commonly used in EML to improve the recombination efficiency. The host often possesses much better transport properties than the emitter alone,

and its presence increases the charge balance and prevents concentration quenching of emitter excitons. Polarity of the host also tunes the ΔE_{ST} and triplet harvesting of the emitter. [120, 121] However, it must have a higher triplet than the emitting materials otherwise it will quench any higher triplets. This high triplet requirement is a big challenge for blue OLEDs where triplet energies are around 3 eV. Luckily, most of the materials in this thesis are not blue, so more common lower triplet energy hosts (mCP (1,3-bis(carbazol-9-yl)benzene) and CBP (4,4'-bis(carbazol-9-yl)biphenyl)) can be used without concern for host quenching.

Significant progress has been achieved in the development of OLEDs, which can be fabricated by two common methods – vacuum thermal evaporation and solution process. Vacuum thermal evaporation involves the evaporation of materials after heating and the deposition in the cold substrates to form thin films. It is a widely used method for the deposition of small molecules and allows for the fabrication of complicated multilayer OLED structures. Despite high device performance obtained using this method, it needs a high vacuum condition and wastes materials during evaporation. Solution process instead provides a low-cost approach to fabricating OLEDs in large area. However, the fabrication of multilayer devices by solution process is still a great challenge. First of all, small molecules are hard to form homogeneous thin films as there is no chain entanglement between them. More importantly, the intermixing of layers in devices is another constraint due to the dissolution problem between layers, that is, the solvent used in the later layer may dissolve or intermix with the former layer. One way to solve this problem is to use orthogonal solvents, where materials have different solubility avoiding the dissolution of the adjacent layers. An alternative way is to use photo or thermal cross-linkable organic functional materials as the cross-linked layer is not soluble in solvents avoiding the interfering with the former layer. In this thesis, vacuum thermal evaporation is employed to fabricate OLEDs with multilayer structures for high efficiency.

Chapter 3

Materials and Experimental Methods

The success of photoluminescence and electroluminescence experiments requires a clear understanding of the equipment used for measurements. In this thesis, two types of samples are mainly investigated for optical studies: solutions and solid-state films. Solution studies are important to collect information about the “individual” molecular properties, as they can be performed at low concentrations where intermolecular interactions are less likely to occur. Studies in solid films mimic conditions found in devices, where the emitter is dispersed in a host with nuclear motions restricted and host-guest intermolecular interactions come into play.

Steady-state and time-resolved optical spectroscopy measurements provide deep understanding of molecular properties and photophysical mechanisms that are relevant to the application of organic emitters in devices. Additionally, electrochemistry studies give extremely valuable information about the redox potentials and the HOMO and LUMO energy levels for device fabrication. While the fabrication and characterization of devices give unambiguous information about the performance of new materials in electroluminescence applications.

3.1 Organic Materials Studied

The molecules investigated in this thesis are all based on electron donor and electron acceptor units covalently linked in donor-acceptor (D–A) or donor-acceptor-donor (D–A–D) architectures. All chemical structures, names and the corresponding chapters are summarized in Appendix A. The investigated compounds were synthesized by our collaborators from Prof. Martin Bryce’s group in the Chemistry Department of Durham University, or Prof. Igor Perepichka’s group from the Chemistry Department of Bangor University. The host and transporting materials that are used in devices were purchased from Sigma Aldrich and Lumtec, and purified by sublimation before use.

3.2 Sample Preparation

3.2.1 Solution

Solutions were prepared by dissolving the compounds in organic solvents such as methylcyclohexane, toluene, dichlorobenzene, dichloromethane and ethanol. Solutions were stirred for up to several hours to ensure that compounds were fully dissolved at room temperature. For molecules showing poor solubility, stirring was carried out at higher temperatures between 50°C and 90°C, depending on the boiling point of the solvents used. For spectroscopy measurements, dilute solutions with concentrations between 10^{-5} M and 10^{-3} M were used to exclude any effect of intermolecular interactions.

3.2.2 Solid-State Film

Two methods were used for the preparation of solid-state films: spin-coating and drop-cast. For spin-coating, uniform thin films can be obtained with thicknesses of tens-to-hundreds nanometres, depending on the solution concentration, viscosity and spin speed. A small volume (~ 80 μL) of the solution (composed of known quantities of emitter and host) is deposited onto a spinning sapphire or quartz substrate using a pipette. The evaporation of the solvent then leaves a thin film deposited on the

substrate surface, which is coated evenly due to the centrifugal forces associated with the substrate spinning. For molecules dispersed in zeonex matrix (a viscous polymer), the spin speed is set to 2000 rpm; for dispersion in organic hosts (small molecules), the spin speed is lower (~ 1200 rpm) as the solution is less viscous. For the preparation of drop-cast films, a small volume ($\sim 150 \mu\text{L}$) of solution is deposited onto the substrate surface. The substrate is then either left for a few hours under vacuum at room temperature or on a hot-plate at 50°C for about half an hour to dry. Drop-casting produces thicker films meaning strong luminescence intensity signals can be obtained (depending on the luminescence efficiency of the emitter), although the thickness and uniformity of films is harder to control using this method.

3.3 Steady-State Measurements

3.3.1 Optical Absorption

A fundamental technique of optical spectroscopy is the measurement of light absorption. When light is shining on a sample, if the energy of the individual photons is greater than the energy of the lowest singlet excited state, photons can be absorbed, promoting electrons from the ground state to the singlet excited states (S_1 or higher S_n). Experimentally, the efficiency of light absorption at each wavelength λ is quantified by the absorbance (A), which follows the Beer-Lambert law given in equation (2.9). [122]

In our laboratory, UV-Vis absorption spectra are collected using a Shimadzu model UV-3600 double beam spectrophotometer, a scheme of the apparatus layout is shown in Figure 3.1. Deuterium (200–370 nm) and halogen (350–3300 nm) lamps are used to cover the entire spectral region. Quartz cuvettes are normally used to avoid absorption below 350 nm. Specific wavelengths are selected with a double-grating monochromator, and a beam-splitter is used to divide the incident light beam into two independent beams. One passes through the reference (normally a cuvette with solvent only), and the other passes through the sample. The reference beam intensity is taken as 100% transmission (or 0% absorbance), and the measurement

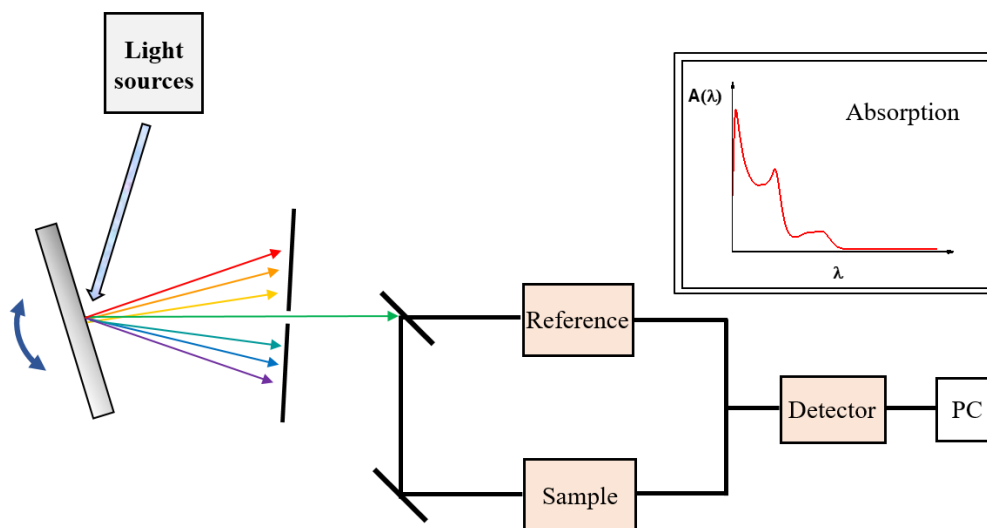


Figure 3.1: A diagram showing the setup of a double-beam UV-3600 spectrophotometer.

of $A(\lambda)$ is displayed as the ratio of the intensities of the two beams after passing through their respective independent beam paths and detected by the photodetector. The monochromator wavelength is then scanned to build up a spectrum of $A(\lambda)$ at different wavelengths.

3.3.2 Steady-State Photoluminescence

Photoexcitation promotes molecules to their excited state. This state is not stable and molecules can return spontaneously to their more stable ground state configuration by releasing the excess energy in the form of photons and/or heat. A steady-state emission spectrum is a graph representing the intensity *vs.* wavelength distribution of the light emitted by a molecule under continuous excitation. Emission obtained under photoexcitation is known as photoluminescence, in contrast to the emission that occurs following the electrical excitation which is known as electroluminescence. Besides the standard emission spectra, where the excitation wavelength is kept constant and the emission is scanned over a specific wavelength range, other spectra can also be collected. A popular form is the excitation spectrum, which is a graph of the intensity of the light that is emitted at a specific wavelength and plotted as a function of the excitation wavelength. In most cases, the excitation spectrum is a replica of the absorption spectrum, but has the advantage of a

greater sensitivity of luminescence when compared with the absorption technique, which allows the observation of the excitation spectrum at concentrations that are too low to be directly measured by absorption spectroscopy. Also if the excitation spectrum is not the same as the absorption spectrum, this gives indication for the presence of dark states which can explain the observation of any dependence of the photoluminescence quantum yield (PLQY) on excitation wavelength.

Both excitation and emission spectra are recorded using fluorometers. In our laboratory, two very similar apparatus from Horiba Jobin Yvon are used: A Fluorolog, equipped with a 450 W Xenon lamp, double monochromator and PMT detector R928P; and Fluoromax, equipped with a 150 W ozone-free Xenon arc-lamp, double monochromator and PMT detector R928P. In both cases, spectra can be collected between 250 and 750 nm. The excitation is achieved using the Xe lamp, which passes through an excitation monochromator for wavelength selection. The beam is then directed to the sample, where light is absorbed. The emitted light is collected at right angle geometry, passing through a second emission monochromator which selects a band of wavelengths and passes them to a photomultiplier tube detector. The slits of both monochromators can be tuned to increase the spectral resolution at a cost of signal intensity. Measurements can also be performed as a function of temperature using cryostats (Janis VNF100), or compared between aerated and vacuum conditions (see section 3.3.3).

3.3.3 Oxygen-Degassing

Oxygen is an important quencher of the excited triplet states in organic molecules, as the electronic ground state of molecular oxygen is a triplet state and its lowest singlet excited state has a very low energy (~ 1 eV). [23,38] Therefore, the evaluation of spectroscopic signals involving triplet states requires the investigation of degassed samples. For solutions, a special quartz cuvette with a Teflon vacuum seal is used to remove the oxygen dissolved in the solution by 4 freeze-pump-thaw cycles. After transferring the solution to the shatter resistant spherical bulb connected to the cuvette by tilting, it is immersed in a liquid nitrogen bath. Once fully solidified, the seal is opened and the cuvette is pumped down to remove the vapour. Once a high

vacuum is achieved, the cuvette is resealed and the bulb is taken out from the bath to let the solution thaw out at ambient conditions. Then the dissolved gases are evolved into the evacuated space in the cuvette assembly. These steps are repeated 4 times (or more) sequentially to ensure the solution is oxygen-free, while freezing the solution during the vacuum steps prevents the solvent evaporating away. The samples can then undergo the same photophysical measurements as normal aerated solutions. For solid-state samples, the sample is degassed by placing it in a cryostat under vacuum for at least 30 min prior to measurement.

3.3.4 Photoluminescence Quantum Yield

The photoluminescence quantum yield (PLQY) represents the ratio between the rate of emitted photons (#emitted photons/s) and the rate of absorbed photons (#absorbed photons/s):

$$\Phi_{\text{PL}} = \frac{\text{emitted photons/s}}{\text{absorbed photons/s}}. \quad (3.1)$$

The PLQY can be measured using a relative method, where Φ_{PL} of a sample is compared with a reference material of known PLQY, or using an integrating sphere to obtain an absolute PLQY measurement.

1. PLQY determination using the relative method The relative comparative method is the most common way of determining the PLQYs of solutions, as it uses cheaper and more commonly available equipment—specifically absorption and emission spectrometers. It is based on the comparison to well-characterized reference solutions with known PLQY values (measured using absolute method) and similar optical properties when compared with the samples under study. [123] If the reference and sample solutions show identical absorbance at the same excitation wavelength under the same experimental conditions, it is assumed that the solutions can absorb the same numbers of photons. Hence, the ratio of the integrated fluorescence intensity of the two solutions will then be proportional to the ratio of the PLQY values. The expression of Φ_{PL} of the sample solution is given by

$$\Phi_{\text{S}} = \Phi_{\text{R}} \left(\frac{I_{\text{S}}}{I_{\text{R}}} \right) \left(\frac{A_{\text{R}}}{A_{\text{S}}} \right) \left(\frac{n_{\text{S}}}{n_{\text{R}}} \right)^2, \quad (3.2)$$

where the subscripts S and R represent the sample and reference, respectively, Φ represents the PLQY value, A denotes the absorbance of the solution, I denotes the integrated fluorescence intensity of the emission and n is the refractive index of the solvent. Noteworthy, in order to minimize the re-absorption effects, solutions with low concentrations are required and the absorbances are limited to no more than 0.1 at and above the excitation wavelength when using 10 nm cuvettes. [124]

Rather than measuring I and A at a single value, the ratio of I over A can be determined with high precision using the gradient of the integrated fluorescence intensity (I) *vs.* absorbance (A) in a linear relation as shown in Figure 3.2.

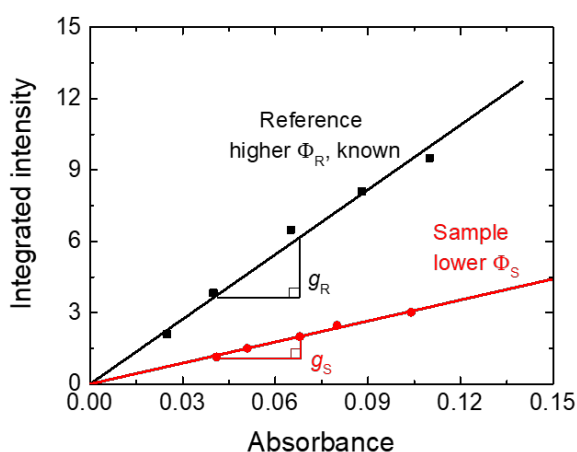


Figure 3.2: Linear plots of integrated fluorescence intensity *vs.* absorbance of reference and sample solutions used to determine relative PLQYs.

The solvent used for both solutions is normally the same, so the ratio of the two refractive indices is equal to 1. The PLQY of the sample is obtained from the product of the known PLQY of the reference and the ratios of the two gradients and two refractive indices given in equation (3.3): [123]

$$\Phi_S = \Phi_R \left(\frac{g_S}{g_R} \right) \left(\frac{n_S}{n_R} \right)^2. \quad (3.3)$$

However, the relative method cannot be used for solid-state samples as it is unlikely to get the sample alignment exactly the same every time.

2. Absolute PLQY determination using an integrating sphere The absolute PLQYs of solid-state films are determined using an integrating sphere,

coated inside with Spectralon, a white and highly reflective material. [125] By using the integrating sphere, the optical anisotropy of emission is eliminated by multiple reflections on the inner surface and all the emitted photons are sampled equally. The sphere must also be calibrated for losses that occur during the reflection. The absolute PLQY set-up consists of an excitation lamp, an integrating sphere (model 4P-GPS-040-SF Labsphere), a QE *Pro* Spectrophotometer (Ocean Optics) and the Oceanview software. LED lamps (or lasers) are used as the excitation light sources and chosen based on the absorption of the materials. The lamp beam passes through a neutral density filter and a convex lens before focusing through a window into the integrating sphere and hitting the sample. Then the excitation beam and scattered luminescence are collected through an optical fibre mounted on an adjacent part of the sphere inner surface and the combined reflected excitation and emission spectra are recorded by the QE *Pro* spectrophotometer.

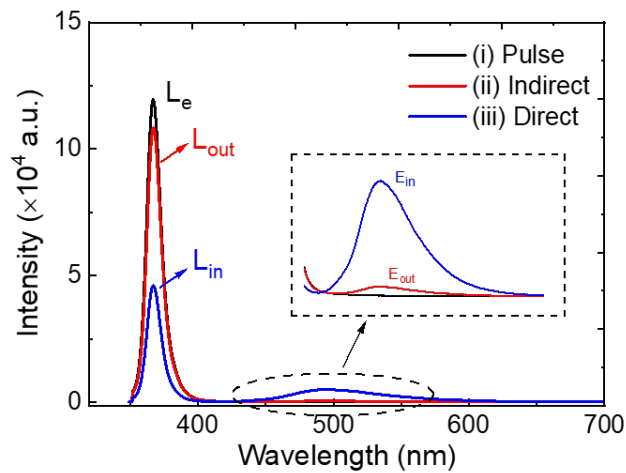


Figure 3.3: An example of the absolute PLQY measurement using integrating sphere.

To take a PLQY measurement, three spectra need to be collected using a constant excitation light as shown in Figure 3.3. (i) Collecting pulse spectrum (black line): recording the excitation profile (L_e) using two empty substrates; (ii) collecting indirect spectrum (red line): recording the excitation profile and photoluminescence spectrum with the beam hitting on the empty substrate while sample out of the lamp beam (L_{out} and E_{out} , the integrated photoluminescence contributed from the reflected secondary excitation); (iii) collecting the direct spectrum (blue line): with

the lamp beam directly exciting the sample while the empty substrate out of beam (L_{in} and E_{in}). [126] Following all the measurements, PLQY is determined as

$$\Phi_{\text{PL}} = \frac{E_{\text{in}} - (1 - \alpha)E_{\text{out}}}{L_e \alpha}, \quad (3.4)$$

where α is the film absorbance

$$\alpha = \frac{L_{\text{out}} - L_{\text{in}}}{L_{\text{out}}}. \quad (3.5)$$

Also, PLQY in nitrogen atmosphere can be measured by comparing emission under normal and saturated nitrogen atmosphere.

3.4 Time-Resolved Spectroscopy

3.4.1 Time-Correlated Single-Photon Counting

Time-correlated single-photon counting (TCSPC) is a widely used technique for the determination of fluorescence lifetimes. It works analogously to a fast stopwatch with two inputs, which is started by the START signal pulse and stopped by the STOP signal pulse. The START is generated by the detection of single photons emitted from the sample and the STOP input is generated by a fast photodiode sampling the excitation light source. [1] TCSPC relies on the fact that the probability of detecting a single photon at time t after excitation is proportional to the fluorescence intensity at that time. The time between the excitation pulse and the detection of a photon is repeatedly measured and individual time measurements are collected into a histogram of counts *vs.* time representing the emission decay curve. The width of the time channel is the ratio of the full time range and the number of channels that counts are binned into. [127] The obtained curve represents the reconstructed fluorescence intensity *vs.* the time of the single photons detected after a large number of excitation pulses. The decay of the excited state population is often expressed using a mono-exponential decay law as shown [128]

$$I(t) = I_0 \cdot e^{-t/\tau}, \quad (3.6)$$

where $I(t)$ and I_0 represent the fluorescence intensity at time t and 0, respectively, τ is the fluorescence lifetime. For single exponential decays, the fluorescence lifetime

is determined from the gradient of the linear fitting in a logarithmic scale or directly by fitting the exponential decay. Generally, more complex decays can be observed. This requires analyses with a sum of discrete exponential terms, each one associated with a different kinetic species or even more complex decay laws.

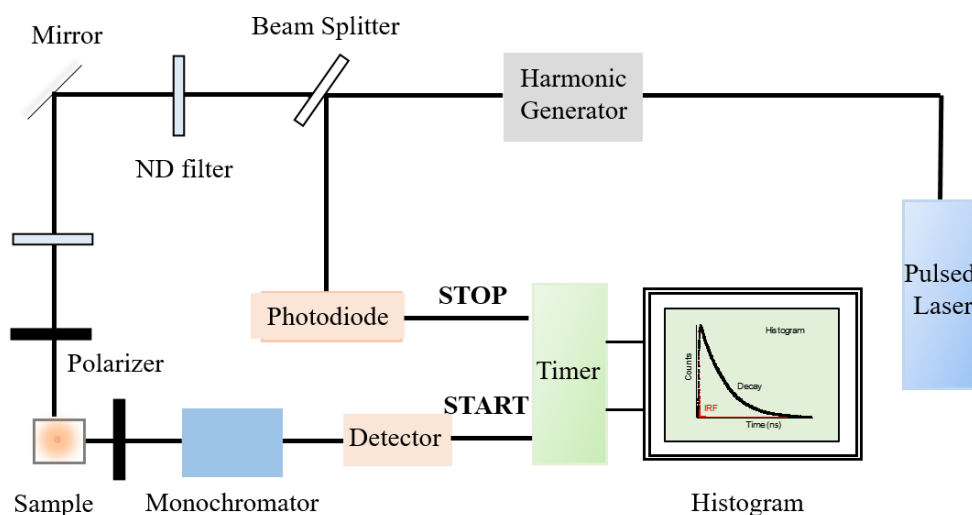


Figure 3.4: A diagram illustrating the setup of the TCSPC system.

A diagram of the TCSPC setup is shown in Figure 3.4, with part of the non-essential optics omitted. In our TCSPC system, lifetime measurements are carried out by using a tunable Ti:Sapphire Coherent Verdi VIII pulsed laser (Coherent Mira 900D), with a high repetition rate of 76 MHz ensuring the rapid acquisition of high signal-to-noise data. This also limits the longest time collection to less than 13 ns as pulses pile up. The second or third harmonic of the laser excitation beam (commonly 432 nm or 288 nm) is generated by a commercial harmonic generator (HarmoniXX, Photonic Solutions) and used as appropriate for the absorption of each sample. The laser pulse is divided into two excitation beams by a beam splitter. One beam goes directly into a fast photodiode (Becker & Hickl GmbH) as the reference pulse; the other strikes the sample after passing through several optical components. The fluorescence emission is then collected at a right angle to the excitation source, with the emission wavelength selected by a double subtractive monochromator (Acton Research Corporation 2400s) and detected by a cooled microchannel plate photomultiplier tube (Hamamatsu 3900). The monochromator grating and slits can be

automatically controlled by the Labview software.

This system has an instrument response function (IRF) of ~ 21 ps, which is the response of the instrument to a zero lifetime sample and gives the time resolution of the instrument. When fitting complex decays, the IRF used in the deconvolution process is required by measuring the TCSPC lifetime of a purely scattering sample, with the emission monochromator set at the excitation wavelength. A diluted colloidal silica solution is used to collect the IRF and no emission filter is used. TCSPC is an extremely sensitive technique as it requires low level signals so that each START pulse gets only one STOP pulse.

3.4.2 Time Gated Acquisition - iCCD

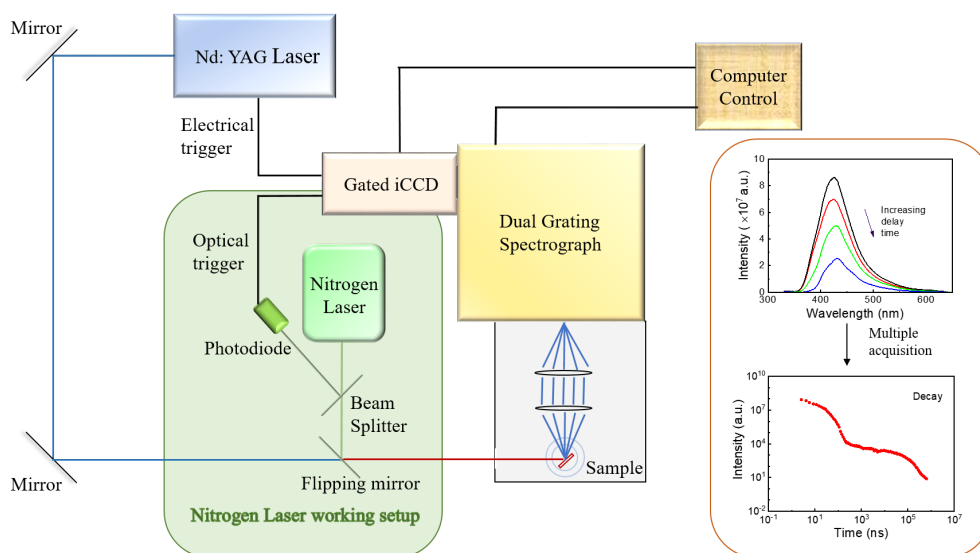


Figure 3.5: A schematic diagram of time-gated iCCD system.

Time-resolved spectroscopy is an invaluable technique to explore the excited state dynamics of molecular systems. Unlike TCSPC, time-gated iCCD acquisition gives simultaneous information about the time evolution of the intensity at a specific wavelength and the time evolution of the spectral shape. Figure 3.5 shows a schematic diagram of the time-gated iCCD layout. Measurements are carried out using a pulsed Nd:YAG laser (EKSPLA) with the excitation wavelength at 355 nm/266 nm (3rd/4th harmonic, 150 ps pulse width, 10 or 1 Hz) or a pulsed nitrogen

laser (MNL 100) with the excitation wavelength at 337 nm (2.5 ns pulse width) and adjustable repetition rate from 1 to 30 Hz. The excitation energy of each pulse can be tuned from 100 nJ to a few mJ (by using ND filters). Samples are excited at a 45° angle to the substrate plane, and hit with a beam diameter of 1.0 cm. Then emission is focused onto a spectrograph (JY-190) equipped with a 300 lines/mm dual grating at 90° to the excitation beam and detected by a sensitive gated intensified charge-coupled device (iCCD) camera (Stanford Computer Optics 4 Picos) with a time resolution of 200 ps. The iCCD camera can record up to 11-12 orders of magnitude of the intensity and 10 orders of magnitude of the delay time using different acquisition settings. Depending on the laser used, the camera and laser are synchronized in two different ways: for a Nd:YAG laser, an electrical pulse (TTL) from the laser control block is directly sent to the camera; for a nitrogen laser, the trigger provided by a fast photodiode sampling the nitrogen laser *via* a beam splitter is sent to the camera. The tunable delay time (the time following the trigger and before the collection of the emitted photons) and integration time (the time interval that the shutter is open and photons are collected) can be controlled using 4 Picos software with 0.1 ns accuracy. [129]

The emission is detected across a wavelength range between roughly 300 to 900 nm using different spectrograph settings as appropriate. Calibration lamps are used to correct the apparatus spectral response at different wavelengths, giving a corrected spectrum.

Time-resolved measurements of emission decay are performed by exponentially increasing the delay and integration times. The delay and integration times are chosen in a way that the integration times do not overlap between acquisitions. Therefore, no temporal overlap exists between the adjacent spectra corresponding to the successive delay times. As fewer photons are emitted at longer times, delay and integration times are set to increase logarithmically in order to get a good signal. The multiple individual spectra obtained directly from this process do not represent the real luminescence decay. However, this can be easily obtained by integrating the spectra and dividing each by the integration time used. Then the time-resolved decay curve is obtained against the delay time, taking the early maximum intensity

spectrum as time zero. Each point records a snap-shot of the real number of photons emitted per nanosecond. Temperature dependent measurements can be obtained using a cryostat and liquid nitrogen.

The nitrogen laser setup is also capable of recording decays but is most commonly used to measure the intensity dependence of emission on excitation dose, as it has far better shot-to-shot power stability compared to the Nd:YAG laser. The laser fluency measurement is an important method to determine whether the emission mechanism is TADF or phosphorescence (*i.e.* monomolecular) or TTA (bimolecular) process. The delay and integration times are chosen in the DF region according to the corresponding decay curves. For each sample, the spectra are collected at a set of delay and integration times with varied laser pulse energies recorded by the power meter. The intensity of integrated DF spectrum is then plotted with the laser power, giving a gradient of 1 or 2 on a double log scale, corresponding to uni- or bimolecular emission pathways, respectively.

3.5 Cyclic Voltammetry

To determine the redox potentials and the HOMO and LUMO energy levels of the studied organic molecules, a series of cyclic voltammetry (CV) measurements is carried out. It is a widely used electrochemical technique which involves cycling the potential of a working electrode and measuring the resulting current.

Figure 3.6a shows a schematic diagram of cyclic voltammetry apparatus used in this work. The electrochemical measurement is conducted in an electrochemical cell with three electrodes: a platinum disc with 1 mm diameter of working area as a working electrode, an Ag electrode as a reference electrode and a platinum wire as an auxiliary electrode. It is recorded using a BioLogic potentiostat SP-300 with a potential scan rate of 50 mV/s and calibrated against a ferrocene/ferrocenium (Fc/Fc⁺) redox couple at room temperature. Dichloromethane (DCM, 99.9%, Extra Dry, stabilized, AcroSeal[®], Acros Organics) or tetrahydrofuran (THF) solution with 0.1 M Bu₄NBF₄ (99%, Sigma Aldrich, dried) is employed as the electrolyte. Solutions are prepared with 1.0 mM concentrations in the electrolyte solution to ensure

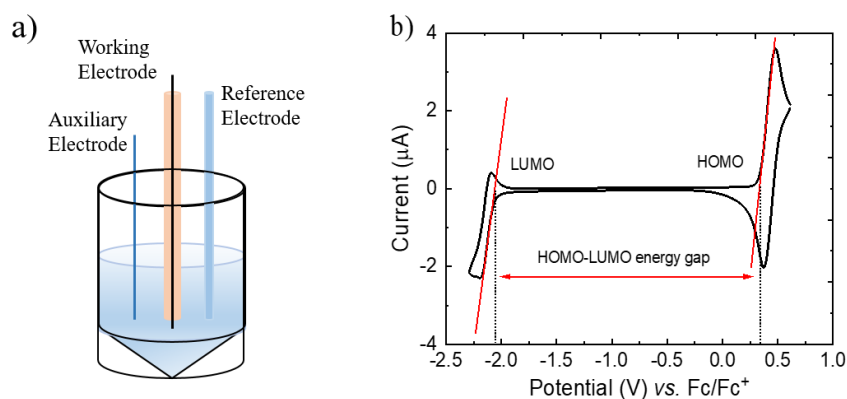


Figure 3.6: a) A schematic diagram of cyclic voltammetry apparatus and b) cyclic voltammogram of a studied molecule as an example.

sufficient conductivity. Prior to the measurement nitrogen gas is purged into the solution, as the electrochemical potential is very sensitive to the presence of oxygen and moisture, which may lead to new oxidation and reduction peaks. Moreover, the solvents must be carefully selected when taking the potential range into consideration as different solvents have different potential limits (*i.e.* the HOMO/LUMO of a material in solvents that have higher HOMO or lower LUMO cannot be measured) since the solvent will start oxidation or reduction before the dissolved material.

The CV measurement is composed of 5 steps: i) The current of a background solution (pure electrolyte) is recorded to check if any contamination exists. When additional peaks appear, the cleaning procedure should be repeated. ii) Adding a small amount of ferrocene to the electrolyte gives the standard oxidation/reduction potentials. This is independent of solvent as the iron centre of ferrocene can be relatively well shielded from the environmental effects by two surrounding cyclopentadienyl ligands. iii) Cleaning the electrochemical cell and electrode to avoid ferrocene contamination, and then measuring the oxidation potential of the solution several times to check if there are other processes occurring. iv) Ferrocene is then added to the compound solution to double check the standard potential. v) Reduction potential is recorded by applying negative voltages after purging nitrogen gas to remove the oxygen effects.

Finally, the collected current between the working and auxiliary electrodes is

plotted against the calibrated voltages between working and reference electrodes as shown in Figure 3.6b. As the HOMO energy is equal to the voltage required to oxidize the material while the LUMO energy is equal to the voltage required to reduce, HOMO and LUMO energies can be estimated using the following equations: [130, 131]

$$\text{HOMO (eV)} = |e|(E_{\text{oxi}} + 5.1), \quad (3.7)$$

$$\text{LUMO (eV)} = -|e|(E_{\text{red}} + 5.1). \quad (3.8)$$

They are calculated from the onsets of the oxidation and reduction potentials, respectively, voltages at which the current rises rapidly as the molecule oxidizes or reduces and begins to contribute to the current.

For some compounds, when the reduction potential is out of range of any solvent, LUMO energies can be calculated according to the optical band gaps (E_g), which are determined from the onsets of the UV-Vis absorption bands, since $\text{LUMO} = \text{HOMO} + E_g$.

3.6 Organic Light-Emitting Diodes

3.6.1 Fabrication of Organic Light-Emitting Diodes

Vacuum thermal evaporation is employed to produce organic light-emitting diodes (OLEDs) in this thesis, which is a common method of thin-film deposition. Figure 3.7a shows a schematic diagram of the Kurt-Lesker Spectros II deposition system, which has 6 organic and 3 inorganic evaporation sources.

Before deposition, all the organic materials used for device fabrication are sublimed to ensure purity, for better film uniformity and device performance. Glass substrates pre-patterned with indium tin oxide (ITO) as the anode electrode having a sheet resistance of $20 \Omega/\text{cm}^2$ and thickness of 100 nm are purchased from Ossila or other suppliers. The substrates are sequentially cleaned by ultra-sonication (Ultrawave U50) in acetone and isopropanol for 15 min each. Then ozone plasma cleaning (Femto, Diener Electronic) is applied for 6 min, providing a UV Ozone atmosphere to break down the surface contaminations and increase the work function

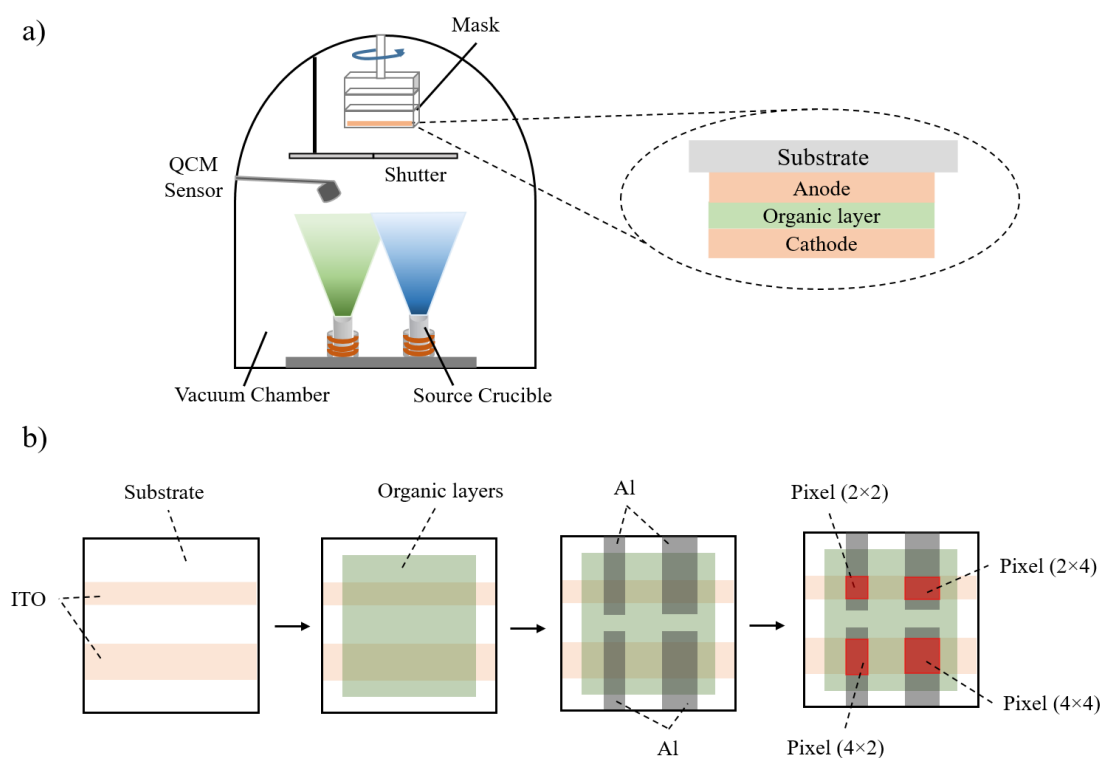


Figure 3.7: a) A simplified diagram of Kurt-Lesker Spectros II deposition system used for OLEDs production. b) A schematic illustration of top view of device fabrication.

of the ITO anode. After loading all the materials and substrates, the chamber is pumped down to keep a high vacuum ($\sim 10^{-6}$ mbar) and avoid scattering of the evaporated molecules as they are deposited to the substrates. A primary roughing vacuum pump (SCROLLVAC, Leybold Ltd.) is used to pump down to 10^{-2} mbar, followed by a turbo molecular vacuum pump (TMU521P, Pfeiffer Ltd.) to 10^{-6} mbar. Evaporation consists of two basic processes: the crucible source is heated by the surrounded ohmic heater until the material starts evaporating and then the evaporated molecular vapour particles deposit as a thin film on the cold substrate surface. During deposition, the substrates are rotated at 10 rpm to ensure film uniformity. The OLED devices have pixel sizes of $4 \times 4 \text{ mm}^2$, $4 \times 2 \text{ mm}^2$ and $2 \times 2 \text{ mm}^2$, where there are overlaps between the ITO and final Al layer as shown in Figure 3.7b. All organic materials and aluminium cathode are deposited at a rate of 1 \AA/s , while LiF (lithium fluoride) is deposited at $0.1 - 0.2 \text{ \AA/s}$.

Calibrated quartz crystal microbalances (QCM) are employed to measure the

thickness of the evaporated films with an accuracy of less than 1 nm, as the oscillation frequency of the quartz crystal resonator changes with the mass of the deposited film. However, as the crystal sensors and substrates are located at different positions in the chamber, the deposition thickness of the vapour particles detected by the QCM is different from the “real” film deposited on the substrates. To allow for accurate thickness as to be deposited, the Ellipsometer (J Woollam, JAW5964) is used to determine the tooling factor (n_{TF}), which is a calibration ratio of these two thicknesses (QCM and actual). [132, 133] Ellipsometry records the changes of polarization of an incident beam as it is reflected or transmitted after interacting with a surface. Silicon dioxide substrates with known optical properties are used for the deposition of the material based on an estimated TF (n_{TF}^i). Each organic material is initially calibrated using at least 3 different silicon dioxide thicknesses to check consistency of the ellipsometer. By Cauchy function modelling, the real film thickness (T_r) is obtained and compared to the thickness as measured by the QCM (T_i), the correct tooling factor (n_{TF}^r) values can be calculated as

$$n_{\text{TF}}^r = n_{\text{TF}}^i \cdot \frac{T_r}{T_i}. \quad (3.9)$$

Following evaporation of the material using the updated tooling factor will give QCM measured thicknesses that correspond to those deposited onto the substrate.

After evaporation, a thin glass cover plate is glued on top of the device using UV-curing adhesive while still inside the nitrogen glove box. This encapsulation process is to protect the devices from exposure to the air before testing, on account of their sensitivity to oxygen and moisture. In many cases, the electrical characterization process can be done within 10 min, so exposure to air is not always detrimental. However, encapsulation is necessary for the device lifetime measurement, which can last for several hours or days (in air).

3.6.2 Device Characterization

To evaluate the performance of OLEDs, a set of key characterizations is measured, including current density (J , mA/cm²), brightness or luminance (L , cd/m²), luminous flux (P , lm), current efficiency (η_{CE} , cd/A), power efficiency (η_{PE} , lm/W),

external quantum efficiency (EQE, %), electroluminescence (EL) spectra and Commission Internationale de l'Éclairage (CIE) chromaticity coordinates (x, y) .

In order to spatially average the emission, a calibrated integrating sphere (Lab-sphere) coated with a highly reflected material (Spectralon) is used to sample light emitted from the device placed inside it anisotropically. The sphere contains an electrical mount connected to a source meter, which drives the device and gives the current-voltage curve of each pixel. Coupled with the source meter, a calibrated spectrometer gives information on the luminous intensity and electroluminescent spectrum, respectively. Taking the pixel emitting area into account, all the parameters necessary for the characterization of the devices are calculated using computer software, including the CIE coordinates from the EL spectra.

The flow of electrical charge carriers through OLED devices per unit area is expressed as current density (J). The luminous flux (in lumens, lm) is a measure of the total amount of light emitted by a light source in all directions, scaled by the varying sensitivity of human eyes to different wavelengths of light. The luminous intensity (in candela, cd) is a parameter to measure the wavelength-weighted power in a particular direction per unit solid angle. Generally, the luminance (L) or brightness is required in the characterization, which is expressed as the luminous intensity per unit area (cd/m^2). In applications for mobile displays, the required brightness levels are *ca.* 100 – 400 cd/m^2 , while higher values of around 5000 cd/m^2 are required in lighting applications.

Typically, three efficiencies should be taken into account in OLEDs characterization: the current efficiency (η_{CE}), the power efficiency (η_{PE}) and the external quantum efficiency (EQE). The current efficiency (η_{CE}) is calculated from the luminance L when the current flows through the device within the emissive area, and expressed in cd/A as [4, 134]

$$\eta_{\text{CE}} = \frac{L \cdot A}{I} = \frac{L}{J}. \quad (3.10)$$

The power efficiency (η_{PE}) is defined as the ratio of luminous power (L_{P}) emitted in the forward direction to the total electrical power required to drive the OLED at a particular voltage. When the η_{PE} is independent of wavelength, it can also be interpreted as the ratio of the total optical power emitted to the electrical power

injected. [135] Considering the current efficiency at the operating voltage, it is expressed in lm/W as

$$\eta_{\text{PE}} = \frac{L_{\text{P}}}{I \cdot V} = \eta_{\text{CE}} \frac{f_{\text{D}}\pi}{V}, \quad (3.11)$$

with

$$f_{\text{D}} = \frac{1}{\pi I_0} \int_0^{\frac{\pi}{2}} \int_{-\pi}^{+\pi} I(\theta, \varphi) \sin \theta d\varphi d\theta, \quad (3.12)$$

where f_{D} is the angular distribution of the emitted light intensity in the forward hemisphere determined by two angles (azimuth θ and polar φ). I_0 is the light intensity measured in the forward direction. [4]

The external quantum efficiency (EQE) is the most important parameter for research devices and given by the number of photons emitted per injected electron and expressed as [136, 137]

$$\text{EQE} = \gamma \cdot \eta_{\text{ST}} \cdot \Phi_{\text{f}} \cdot \eta_{\text{out}}, \quad (3.13)$$

where γ represents the charge balance factor, depending on the probability of an exciton being formed (and can be optimized to near unity). η_{ST} is the fraction of singlets formed in recombination. Under electrical excitation, singlet and triplet are formed in a ratio of 1:3 due to spin statistics. Thus, η_{ST} is limited to 25% in conventional fluorescent emitters. TADF and phosphorescent emitters can utilize both singlet and triplet excitons which increase η_{ST} to 100% in well-optimized TADF

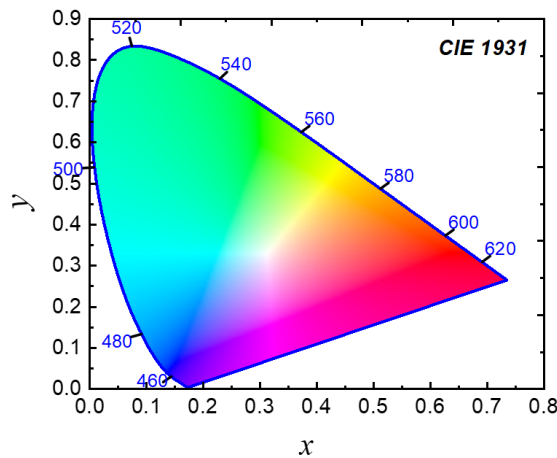


Figure 3.8: CIE 1931 (x, y).

or phosphorescent OLED devices. Φ_f is the fluorescence quantum yield, which is an intrinsic molecular property and can be as high as 100% in efficient emitters. η_{out} is the outcoupling efficiency and limited to 20–30% due to many geometrical challenges in extracting photons generated in the EML to the outside world (reabsorption, total internal reflection primarily). [45]

Finally, the colour of the light emitted by the device is subjective and depends on the response of human eyes in the red, green and blue (RGB) regions. To quantify this subjective colour, it is represented on a chromaticity diagram using the Commission Internationale de l'Eclairage 1931 chromaticity coordinates (CIE 1931 (x, y)) [138] as depicted in Figure 3.8. The outer curved boundary is the spectral locus with wavelengths shown in nanometers.

Chapter 4

The Contributions of Molecular Vibrations and Higher Triplet Levels to the Intersystem Crossing Mechanism in Metal-Free Organic Emitters

Dual luminescence – intense, simultaneous room temperature phosphorescence (RTP) and thermally activated delayed fluorescence (TADF) – is observed in a series of donor-acceptor-donor molecules. Here it is shown that this dual luminescence is stronger in the “angular” than in their “linear” regioisomers, which is consistent with an enhanced intersystem crossing (ISC) process in the former. Theoretical and experimental studies demonstrate that the small energy gap between upper triplet states (T_1 – T_n) and the lowest singlet state (S_1) in the “angular” regioisomers enhances the coupling between S_1 and T_1 states and accelerates both ISC and reverse ISC (RISC), consistent with the spin-vibronic mechanism. In the absence of this “triplet ladder” and in the presence of a larger energy difference between T_1 and T_n in the “linear” regioisomers, the ISC and RISC mechanisms are less efficient. Remarkably, the enhancement of the ISC rate in the “angular” regioisomers is also accompanied by an increase of the internal conversion rate. These results highlight

the contributions of higher triplet excited states and molecular vibronic coupling to the harvest of triplet states in organic compounds, and cast the RTP and TADF mechanisms into a common conceptual framework.

This work was published in *Journal of Materials Chemistry C* (R. Huang, J. Avó, T. Northey, E. Channing-Pearce, P. L. dos Santos, J. S. Ward, P. Data, M. K. Etherington, M. A. Fox, T. J. Penfold, M. N. Berberan-Santos, J. C. Lima, M. R. Bryce and F. B. Dias, *J. Mater. Chem. C.*, 2017, 5, 6269–6280). R. Huang performed the majority of the optical measurements with P. L. dos Santos under the supervision of F. B. Dias. J. Avó and J. C. Lima determined the fluorescence yields in zeonex and the triplet formation yields. M. A. Fox, T. Northey and T. J. Penfold performed the calculations. J. S. Ward synthesized molecules 1–4 under the guidance of M. R. Bryce. M. K. Etherington and E. Channing-Pearce performed photoinduced absorption studies and luminescence spectroscopy in zeonex. P. Data performed cyclic voltammetry experiments. M. N. Berberan-Santos investigated the temperature dependence of the luminescence of compound 2 in zeonex.

4.1 Introduction

Understanding the fundamental mechanisms of TADF and RTP are topics of strong research interest, because these processes offer excellent opportunities to investigate the excited state dynamics of triplet states and spin conversion in organic materials. [139] Such studies can provide valuable information about the role of molecular conformation, connectivity, and coupling between electronic states to promote triplet harvesting. These aspects are still not completely understood, and are extremely relevant when the properties of the triplet excited state is of importance, such as in photon up-conversion due to triplet-triplet annihilation, [140] triplet harvesting in OLEDs, [41, 141, 142] and organic spintronics. [143]

The observation of dual luminescence (TADF and RTP) at room temperature in pure organic materials is a rare phenomenon. [94] In order to observe strong photoluminescence originated from the triplet state, the triplet formation yield needs to be enhanced and the non-radiative deactivation processes need to be suppressed. A small singlet-triplet energy gap (ΔE_{ST}) is then required for the observation of strong TADF, since the RISC rate becomes exponentially slower with the increasing magnitude of ΔE_{ST} . Small ΔE_{ST} is detrimental to RTP though, since it competes with the direct radiative decay from the triplet state. TADF and RTP are therefore often understood as mutually exclusive, although here we show this is not always the case.

Instead, both TADF and RTP share the same fundamental requirements at a molecular level. By understanding both processes in a common framework, they can be tuned and selected by correctly choosing the host properties. The correct choice of host can reduce the dominance of the energy gap between the emitting singlet and triplet states, and crucially introduces complementarity between the two mechanisms that otherwise would not exist. This complementarity means that it is feasible to observe both TADF and RTP mechanisms in the same molecule, with the balance of this dual luminescence controlled by the ability to fine-tune the kinetic parameters, through the molecular structure of the emitter and the host.

Interestingly, in dual emitters showing simultaneously both long-lived forms of luminescence, the ratiometric nature of the dual-emission is preserved during the en-

time luminescence lifetime, which makes these materials desirable in gated-acquisition luminescence methods for sensing and imaging. The ratio between the RTP and TADF intensities is preserved even in the microsecond time range, allowing it to be used as internal calibration. This is in clear contrast with conventional RTP and TADF emitters, where the prompt fluorescence decays in just a few nanoseconds, and the phosphorescence or delayed fluorescence lives for microseconds or milliseconds with the spectra changing significantly as each component dominates their decays.

The factors influencing the rate of ISC and RISC in a series of pure organic emitters are discussed in this chapter. It is demonstrated that simple manipulations of the way donor (D) and acceptor (A) units are linked in D–A–D compounds have a profound influence on the efficiency of both RTP and TADF. Moreover, when the emitters are dispersed in suitable hosts (depending on the polarity of the local surroundings) simultaneous RTP and TADF are observed. This illustrates the similarity of the two mechanisms and properties required to facilitate high intersystem crossing and reverse intersystem crossing rates in organic molecules, and brings RTP and TADF into a common conceptual framework. Crucially, these synergies can be used to create and guide the design of novel emitters particularly white emitters for blue TADF and orange RTP.

4.2 Results and Discussion

4.2.1 Chemical Characterization

Figure 4.1a shows the energy diagram of photophysical mechanisms that give rise to RTP and TADF. The molecular structures of all the compounds studied in this chapter are shown in Figure 4.1b. Previously, strong TADF emission for compounds 2 and 4 in ethanol solution at room temperature and intense dual fluorescence-phosphorescence in compounds 2, 4 and 6 in ethanol solution at 100 K were reported. [144] The dual fluorescence-phosphorescence in these compounds is so intense that it can be observed in a normal fluorimeter without using gated luminescence methods. In contrast, their regioisomers 1, 3 and 5 exhibit no phosphorescence even

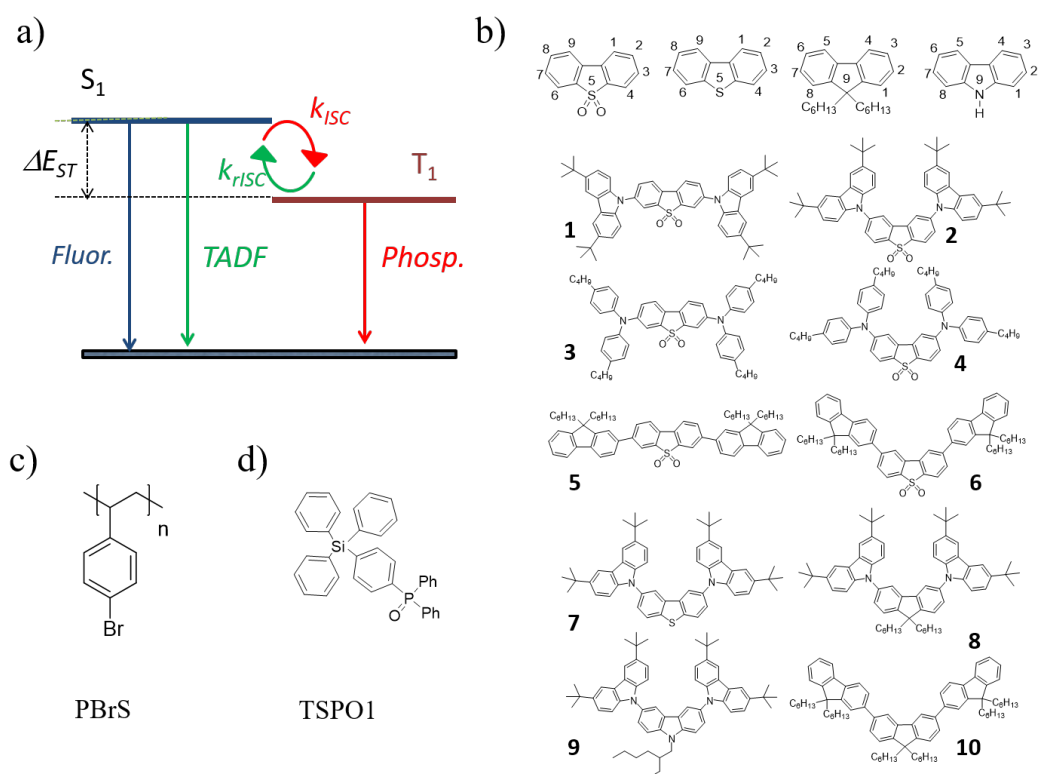


Figure 4.1: a) Energy level diagram describing the photophysical mechanisms that give rise to RTP and TADF emissions. b) Molecular structures of studied compounds in this chapter and the numbering code for molecular isomers. Molecular structures of hosts c) poly(4-bromostyrene) (PBrS) and d) diphenylphosphine oxide-4-(triphenylsilyl)phenyl (TSPO1).

at low temperatures, and their delayed fluorescence in ethanol solution at room temperature is mainly due to triplet-triplet annihilation. This markedly different behaviour of the isomers was not understood at the time, and an intermediate triplet level between the singlet and lower triplet states was proposed to justify the enhanced TADF in 2 and 4. However, this reveals little information about the mechanism sustaining RISC. In this chapter, fundamental concepts regarding how triplet states are harvested in purely organic compounds provide a new general understanding of the mechanisms of both RTP and TADF in general.

The difference in the molecular structure of these regioisomers is the linking positions of the carbazole, diphenylamine, or fluorene electron-donor units and the dibenzothiophene-*S,S*-dioxide electron-acceptor unit. In compounds 1, 3 and 5, the

A is substituted at C-3,7 positions, whereas in 2, 4 and 6, the substituents occur at C-2, 8 positions of the A unit. For easy identification, these different isomers are hereafter referred to “linear” and “angular”, respectively. Despite this seemingly small change, the effect on the dynamics of the excited states is significant in the context of RTP and TADF luminescence.

Additionally, compounds 7, 8 and 9, also with “angular” substitution, show intense dual fluorescence-phosphorescence at 100 K in solid ethanol solution, but in compound 10 no phosphorescence is observed. [144] This illustrates that the presence of heteroatoms is crucial for the observation of dual fluorescence-phosphorescence, as previously identified by others. [106] However, this is not the only required structural feature for the observation of phosphorescence, as confirmed by the absence of strong phosphorescence in compounds 1, 3 and 5. Intrinsic structure-property relations must therefore be understood to guide the future design of intense RTP and TADF emitters. [95]

4.2.2 Photophysical Properties in Solution

The absorption and emission spectra of compounds 1 and 2, 3 and 4, 5 and 6, and 7, 8, 9 and 10 in hexane solution are shown in Figure 4.2. The absorption of the “linear” compounds 1, 3 and 5 is clearly redshifted compared to their “angular” counterparts 2, 4 and 6, respectively. This is expected from the weaker conjugation of the “angular” emitters, which pushes the singlet and triplet states to higher energies. Compounds 7, 8 and 9 with “angular” geometry show blue-shifted absorption compared to the former discussed molecules, which are based on carbazole donor units, but differ in their acceptor units. Similarly, compound 10 also exhibits blue-shifted absorption with three fluorene units in the “angular” geometry. It also has less excited state charge transfer (CT) character, as evidenced by their blue-shifted and structural emission (Figure 4.2f). This is due to a lower electron affinity of fluorene, dibenzothiophene and carbazole units compared to the dibenzothiophene-*S,S*-dioxide unit.

Table 4.1 shows the photophysical data for compounds 1–9 in solution. Compounds 7–9 have high triplet energies (all above 2.8 eV) especially compound 7

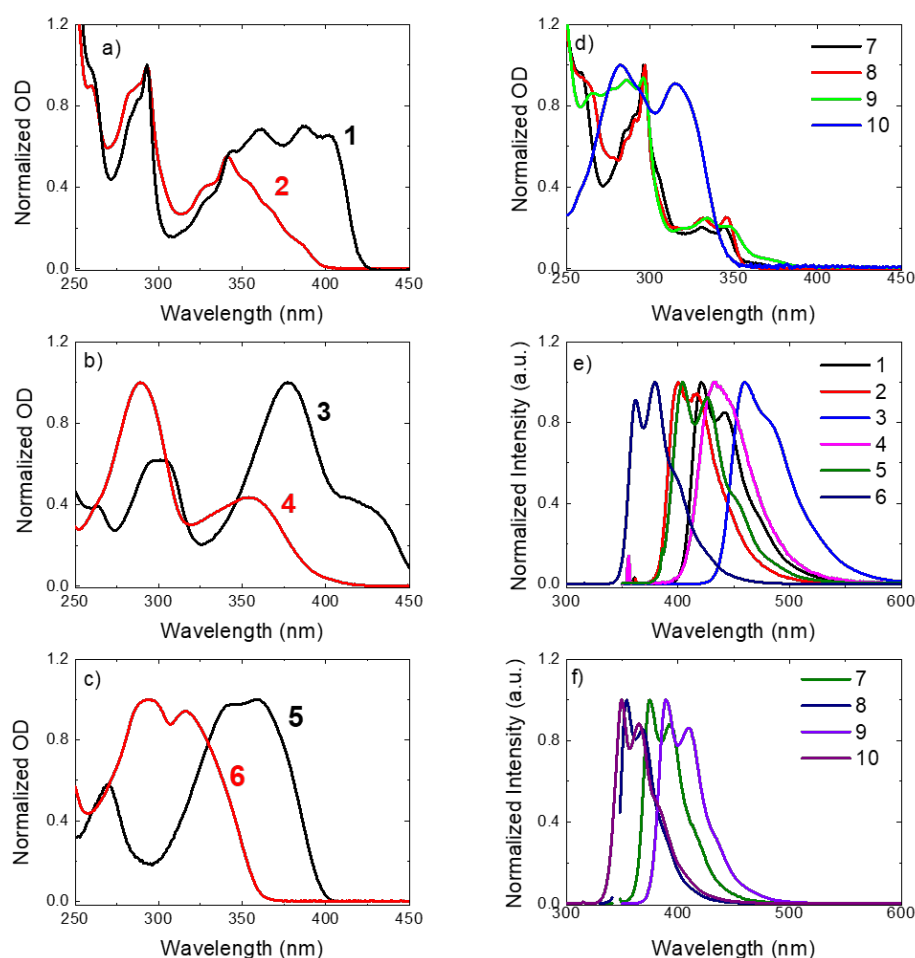


Figure 4.2: Absorption spectra of a) 1 and 2, b) 3 and 4, c) 5 and 6, and d) 7, 8, 9 and 10. Emission spectra of compounds e) 1–6 and f) 7–10. All spectra were collected in dilute hexane solution at room temperature.

(3.02 eV). For compounds 1–6, the first triplet excited states appear at lower energies, ranging from 2.20 eV in 3 to 2.70 eV in 2. As a general trend, the “angular” substitution shifts both the singlet and triplet states to higher energies relative to their “linear” counterparts owing to the broken conjugation length in the former. However, as the change in the position of substitution affects the singlet and triplet energies almost equally, the singlet-triplet energy gaps of the corresponding isomers are very similar in non-polar hexane. Because the singlet and triplet states are affected in a similar manner, this indicates that both emitting states have a similar electronic character. In the studied series, compounds 7 and 9 have the highest triplet energies and the smallest $\Delta E_{S_1-T_1}$ (0.4 eV), making them promising emitters

and hosts for other lower energy small molecules.

Table 4.1: Singlet and triplet energies (S_1 and T_1), fluorescence quantum yields (Φ_f), fluorescence lifetime (τ_f) and triplet yields (Φ_T). All determined in hexane at room temperature, with exception of T_1 energies, which were determined at 80 K in ethanol solution.

	S_1	T_1	ΔE_{ST}	Φ_f	τ_f	Φ_T	k_f	k_{ISC}	k_{IC}
	± 0.02 (eV)	± 0.02 (eV)	± 0.03 (eV)	± 0.05	± 0.05 (ns)	± 0.10	$\times 10^8$ (s^{-1})	$\times 10^8$ (s^{-1})	$\times 10^8$ (s^{-1})
1 ^l	3.07	2.54	0.53	0.94	3.08 ^b	-	3.1	-	0.2
2 ^a	3.24	2.70	0.54	0.10	1.60 ^b	0.32	0.6	1.9	3.6
3 ^l	2.84	2.20	0.64	0.72	3.66 ^b	-	1.9	-	0.8
4 ^a	3.05	2.48	0.57	0.10	1.13 ^b	0.19	0.9	1.7	6.3
5 ^l	3.21	2.36	0.85	0.80	1.05 ^b	-	7.6	-	1.9
6 ^a	3.54	2.48	1.06	0.39	1.02 ^b	0.41	3.8	4.0	1.9
7	3.42	3.02	0.40	0.05	0.88	0.42	0.6	4.8	6.0
8	3.62	2.82	0.80	0.22	3.81	0.26	0.6	0.7	1.4
9	3.33	2.97	0.36	0.14	3.99	0.33	0.4	0.8	1.3

^l and ^a represent “linear” and “angular” formations, respectively. ^bObtained from reference [144].

The fluorescence yields follow a clear pattern which can be explained by the timescales of the different contributing components. The “angular” compounds that show intense phosphorescence at low temperatures also show weak fluorescence and shorter lifetimes as shown in Table 4.1 (compounds 1 to 6). While isomers 1, 3 and 5 show no significant triplet population at room temperature in hexane, their “angular” analogues show large triplet yields, despite their similar singlet-triplet energy gaps. Marked differences are also observed in the rate constants, *i.e.*, radiative rate (k_f), intersystem crossing rate (k_{ISC}) and internal conversion rate (k_{IC}). Remarkably, the radiative decay rate decreases significantly when going from “linear” to “angular” form. This drop in the radiative rate (k_f) is accompanied by an increase of k_{ISC} and k_{IC} . This explains the observation of strong phosphorescence in the “angular” isomers, as the IC process can be greatly suppressed at low temperatures while larger k_{ISC} leads to a larger pool of triplets to undergo phosphorescence.

The simultaneous increase in IC and ISC is a general rule that points to a common intermediary state for both processes, *i.e.*, a low-lying CT state. However, a closer inspection shows another important aspect to take into account when de-

signing novel TADF/RTP emitters. The comparison of compounds 2, 4 and 6, in which the acceptor unit is conserved, shows that there is a significant increase in the rate of ISC of 6 compared to 2 and 4. This is accompanied by a decrease in the IC rate to the ground state. While in 6 the D and A moieties are linked through a C(sp²)-C(sp²) bond, a N(sp³)-C(sp²) bond in 2 and 4 performs the same function. This difference impacts both the vibrational deactivation of the singlet state and the D-A coupling, which are needed to obtain the CT state. While the main degree of freedom in 6 is the rotational motion around the C-C bond coupling the D and A groups, additional vibrational modes related to inversion around N(sp³-sp² transition) exist in 2 and 4. The contribution of these additional vibrational modes can be further observed when comparing 2 and 4. In compound 2, carbazole as a donor unit is more rigid than the diphenylamine unit in 4. Increasing the flexibility of the D unit (on the D-A linking motif) yields higher k_{IC} and lower k_{ISC} .

As previously stated, the change in the substitution from “linear” to “angular” has the strongest influence on the yield of triplet formation, giving stronger triplet yields in compounds 2, 4 and 6 and thus activating intense phosphorescence. Strong dual fluorescence-phosphorescence is also observed in ethanol solution at low temperatures in compounds 7, 8 and 9, showing that the “angular” substitution is equally effective in providing dual luminescence, even if the sulfone functionality is not present. However, it is noted that when the carbazole donors in 8 are replaced by fluorene units (*i.e.*, compound 10 with no heteroatoms), the phosphorescence is switched off. Therefore, the presence of heteroatoms in the “angular” molecular structures is of fundamental importance for the observation of strong phosphorescence in these materials, but not a sole requirement.

In polar environments, the CT states of compounds 2 and 4 shift to a lower energy, leading to small energy gaps $\Delta E_{S_1-T_1}$ of 0.10 eV and 0.21 eV, respectively. As the reverse intersystem crossing k_{RISC} and intersystem crossing k_{ISC} rates are proportional to each other, the “angular” isomers also have stronger k_{RISC} . Therefore, strong TADF can be observed. This is explained by this isomer effect and the smaller $\Delta E_{S_1-T_1}$. [144] Compound 2 was used in OLEDs giving external quantum efficiency of 14%. [145]

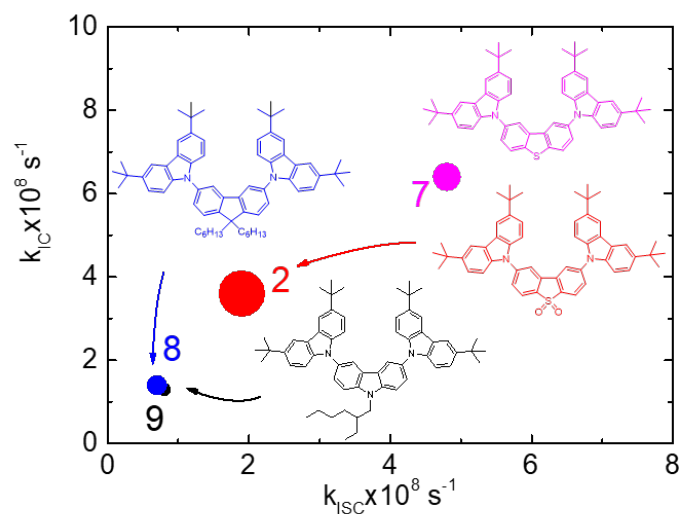


Figure 4.3: Dependence of the IC rate on the ISC rate in compounds 2, 7, 8 and 9, all with the same donor (carbazole) but different acceptors. The size of the dot represents the strength of CT character of the singlet state as evaluated by solvatochromism in the fluorescence spectra.

The correlation between the ISC and IC rates is also very important when comparing compounds 2, 7, 8 and 9. These compounds have the same carbazole donor, but different acceptor unit, where the presence of SO₂, S, N and C promotes the increasing ISC process. The rates of ISC and IC in these compounds exhibit a clear positive correlation as shown in Figure 4.3. This points to a similar mechanism and suggests that the vibrational modes responsible for IC also work to enhance ISC, by spin-vibronic coupling and mixing low-lying triplet states and S₁. The CT character of the singlet excited state, as evaluated by fluorescence solvatochromism, is represented by the size of each dot. It is shown that compound 2, with the strongest CT character in the series, shows intermediate values for both ISC and IC rates. Therefore, the variation in the ISC and IC rates is not exclusively due to the increasing CT character of the excited state. This is consistent with recent findings that not only the lowest singlet and triplet states, but higher manifold triplet states T_n are essential to understand the exciton decay dynamics in TADF emitters. [41,139] The parameters in solutions give significant information regarding the way the change in molecular connectivity influences the ISC and IC rates.

4.2.3 Photophysical Properties in zeonex Films

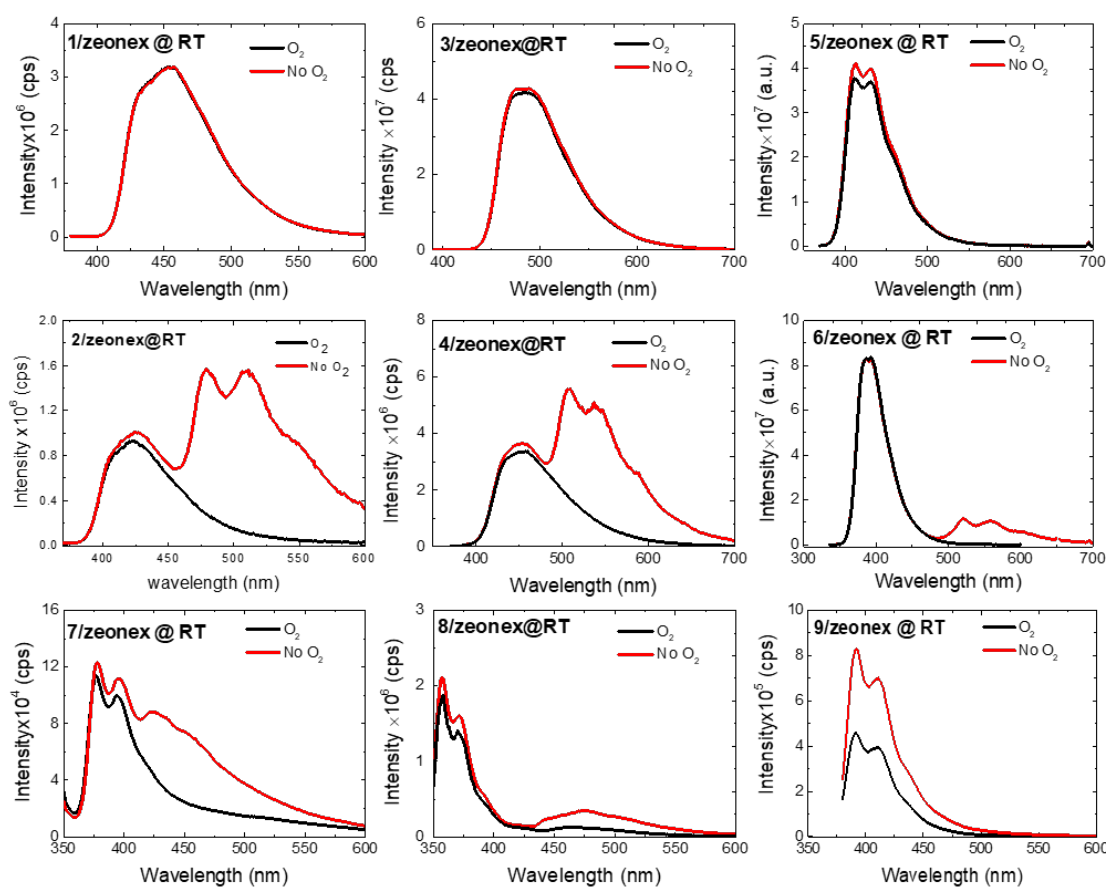


Figure 4.4: Steady-state emission in zeonex films at room temperature in vacuum and in the presence of oxygen of compounds 1 to 9.

The reasons why these “angular” compounds show high ISC rates can be explained in solid state films. Figure 4.4 shows the steady-state emission in the presence and absence of oxygen in zeonex films collected at room temperature. In oxygen-free condition, the emission spectra of the compounds with “angular” geometry show great differences, whereas the oxygen has no influence on the spectra of the “linear” compounds 1, 3 and 5. Compounds 2, 4, 6, 7 and 8 exhibit dual emission, *i.e.*, strong fluorescence and phosphorescence at room temperature. The strong quenching effect of oxygen on the redshifted emission band confirms that the extra emission band is due to phosphorescence at room temperature. The RTP is so strong that it can be easily measured in a normal fluorimeter without the need of using time-gated acquisition methods. Intense RTP is observed only for “angu-

lar” compounds and is much stronger in compounds 2, 4 and 7 than in 6 and 8. In the latter compound, the low RTP emission is explained by a slower ISC rate, which could be potentially due to the lack of heteroatoms in the fluorene acceptor. However, this is not the case in compound 6. This material instead shows a very strong ISC rate and weaker non-radiative IC rate than 2 and 4, which are beneficial for a strong RTP emission. When compared with other “angular” compounds, 6 is also different due to a higher radiative rate k_f in the S_1 and a significantly large $\Delta E_{S_1-T_1}$. Moreover, compound 6 shows a very long phosphorescence lifetime in ethanol at 100 K. [144] This indicates that the radiative rate of triplet state k_{ph} is significantly slower than those of compounds 2 and 4, which leads to a decrease in phosphorescence yield.

For compound 9 the fluorescence is strongly quenched by oxygen. This indicates that there is a significant contribution of delayed fluorescence to the overall fluorescence, which involves triplet states. Compound 9 has the smallest energy gap $\Delta E_{S_1-T_1}$ in this series, thus the triplet harvesting through RISC may be active. Note that as compound 9 is composed of three donor units, no CT character is expected for this material.

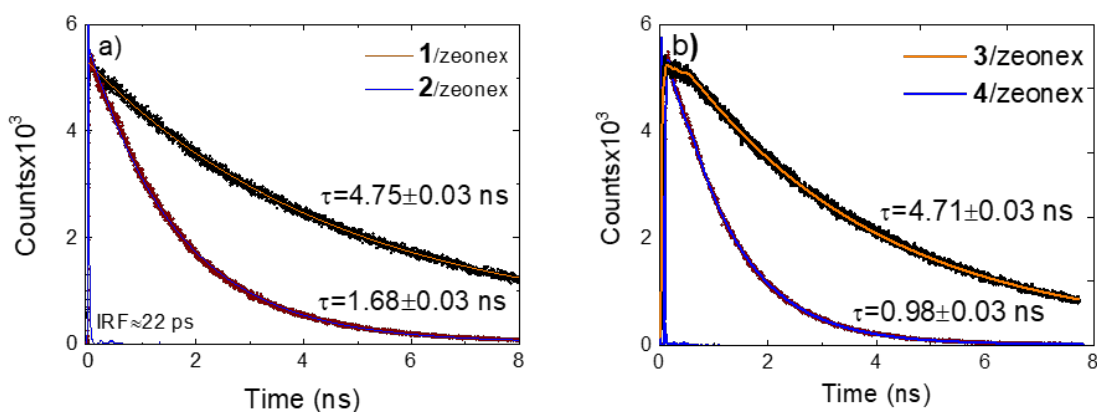


Figure 4.5: Fluorescence decays of compounds 1–4 in zeonex solid films at room temperature, collected at the fluorescence band.

Figure 4.5 shows the fluorescence decays of compounds 1 to 4 in zeonex films at RT, with the “angular” compounds 2 and 4 show significantly shorter fluorescence decays than their “linear” analogues. This is entirely consistent with their stronger

triplet formation yields as shown in Table 4.1.

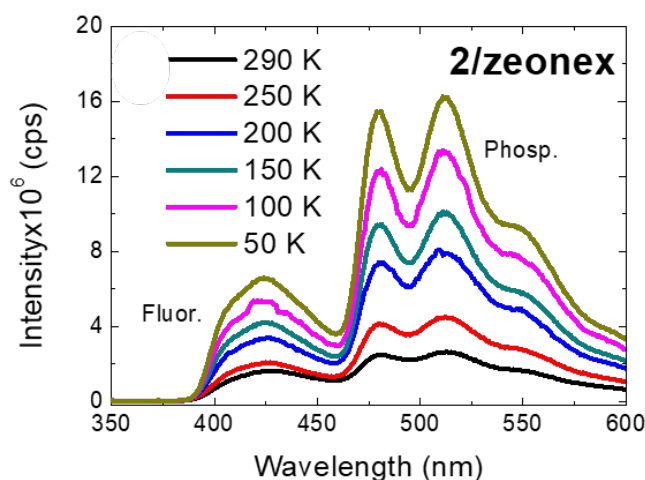


Figure 4.6: Temperature dependence of steady-state emission spectra of compound 2 in zeonex film.

To understand the reasons why compounds 1–4 show remarkable differences in regard to their RTP emission, further studies were performed on these compounds as they show the strongest regioisomerization effect. It is observed that the intensities of both fluorescence and phosphorescence bands increase with the decreasing temperature as shown in Figure 4.6. This clearly indicates that the quenching effect due to vibrations is being suppressed as the temperature drops. Moreover, while the phosphorescence in the presence of oxygen is completely quenched as expected, there is practically no difference between the intensities of the fluorescence band of the spectra collected in the presence and absence of oxygen (Figure 4.4). This shows that the triplet harvesting due to TADF is not operative in these compounds when dispersed in zeonex matrix. This is also evidenced in Figure 4.6, as TADF is a thermally activated process with a positive temperature dependence behaviour.

A summary of the photophysical data of RTP in zeonex films is given in Table 4.2, and is consistent with the data present in Table 4.1. Compounds 1 and 3 show very high photoluminescence quantum yield (PLQY), with 93% and 56%, respectively. However, the intersystem crossing and internal conversion rates are faster in 2 and 4 compared with their “linear” counterparts 1 and 3.

Table 4.2: Quantum yields of fluorescence (Φ_f) and phosphorescence (Φ_{ph}); fluorescence (τ_f) and phosphorescence lifetimes (τ_{ph}); radiative decay rates of the S_1 (k_f) and T_1 states (k_{ph}); internal conversion rate (k_{IC}), intersystem crossing rate from S_1 (k_{ISC}) and intersystem crossing rate from T_1 to S_0 ($k_{ISC}^{T_1}$) for studied compounds. All determined in zeonex films at room temperature.

	Φ_f	Φ_{ph}	Φ_{ph}/Φ_f	τ_f	τ_{ph}	k_f	k_{ISC}	k_{IC}	k_{ph}	$k_{ISC}^{T_1}$
	± 0.05	± 0.05	± 0.07	± 0.03 (ns)	± 0.50 (ms)	$\times 10^8$ (s^{-1})	$\times 10^8$ (s^{-1}) ^b	$\times 10^8$ (s^{-1}) ^b	(s^{-1}) ^b	(s^{-1}) ^b
1	0.93	-	-	4.75	-	1.9	-	0.1	-	-
2	0.09	0.26	2.9	1.68	34.3 ^a	0.5	1.9	3.5	23.7	5.5
3	0.56	-	-	4.71	-	1.2	-	0.9	-	-
4	0.06	0.14	2.3	0.98	29.8	0.6	1.9	7.6	24.7	8.9

^aThe phosphorescence decay in 2 is bi-exponential, the value given is the average lifetime.

^bDetermined using the triplet yield in solution.

4.2.4 Photophysical Properties in Polar Hosts

The photophysical measurements in solution and zeonex films show that “linear” compounds substituted at the C-3 and C-7 positions of the dibenzothiophene-*S,S*-dioxide unit exhibit no RTP at all. This is also evidenced in Figure 4.7. Even when dispersed in poly(4-bromostyrene) (PBrS) (Figure 4.1c), a well-known host that can enhance triplet formation due to the external heavy-atom effect [17], only the “angular” compounds 2 and 4 show clear RTP and TADF. “Linear” compounds 1 and 3 show only prompt fluorescence. Therefore, the “angular” substitution and the presence of the low atomic weight heteroatoms, sulphur or nitrogen, are clearly fundamental for strong RTP observation in pure organic materials.

In addition to PBrS, three other hosts with large band gaps, compounds 7, 9 and diphenylphosphine oxide-4-(triphenylsilyl)phenyl (TSPO1) are used as hosts in blends with compounds 2 and 4. TSPO1 has been used as a suitable host for blue OLEDs [146], with the molecular structure shown in Figure 4.1d. All of these host materials have higher triplet energies than those of compounds 2 and 4, and are able to act as donors to promote energy transfer to compounds 2 and 4 in photoluminescence experiments.

Considering compound 4, the steady-state emission spectra in hosts are compared

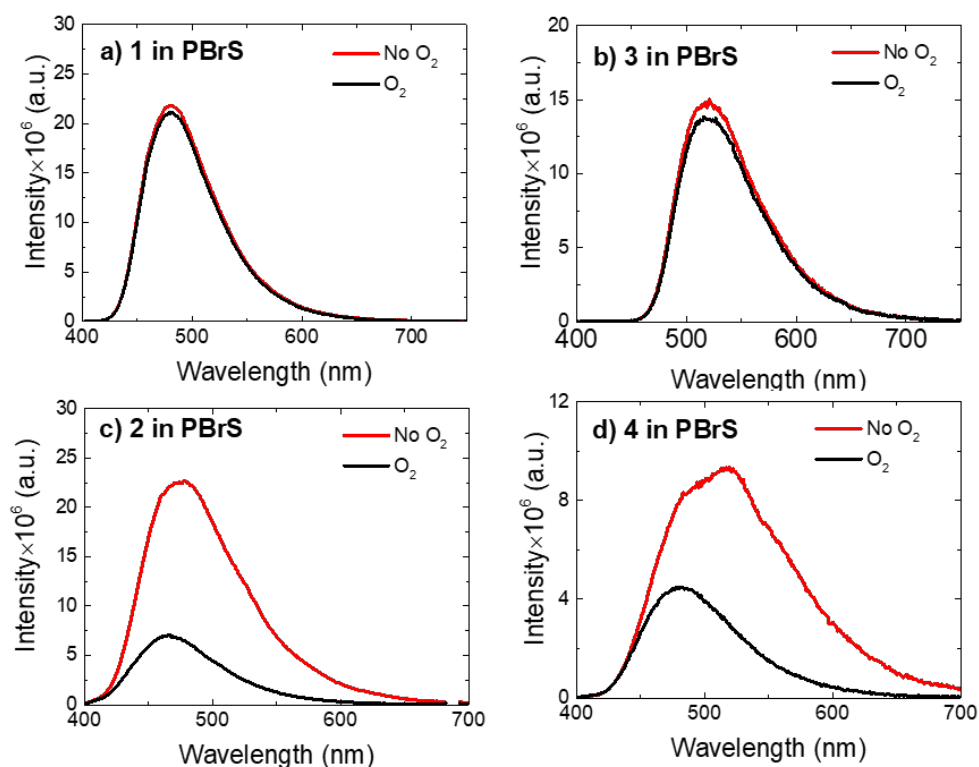


Figure 4.7: Steady-state emission spectra of compounds 1–4 dispersed in PBrS, in vacuum (red) and in air (black) equilibrated conditions at room temperature.

in vacuum and air in Figure 4.8. The emission was measured in a normal fluorimeter at room temperature and the presence of dual luminescence is clearly observed. The phosphorescence band peaks at around 515 nm in all hosts, 7 nm below the maximum of phosphorescence bands observed in zeonex film. The fluorescence band peaks at 466 nm for blends of compound 4 in hosts 7 and 9 and at 480 nm in TSPO1 and PBrS. This represents a redshift of 16 nm and 30 nm in comparison to the fluorescence maximum in zeonex (450 nm). This is due to the different polarities of all the hosts, with zeonex < compounds 7 and 9 < TSPO1 and PBrS. In a more polar environment, the ^1CT state is lowered leading to the more redshifted fluorescence spectra.

Interestingly, when compared with the emission of compound 4 doped zeonex film (where no variation in the intensity of fluorescence band is observed when oxygen is removed), in blends of 4 with 7, 9, TSPO1 and PBrS, a marked increase in the fluorescence intensity occurs upon removing oxygen. This is observed together with

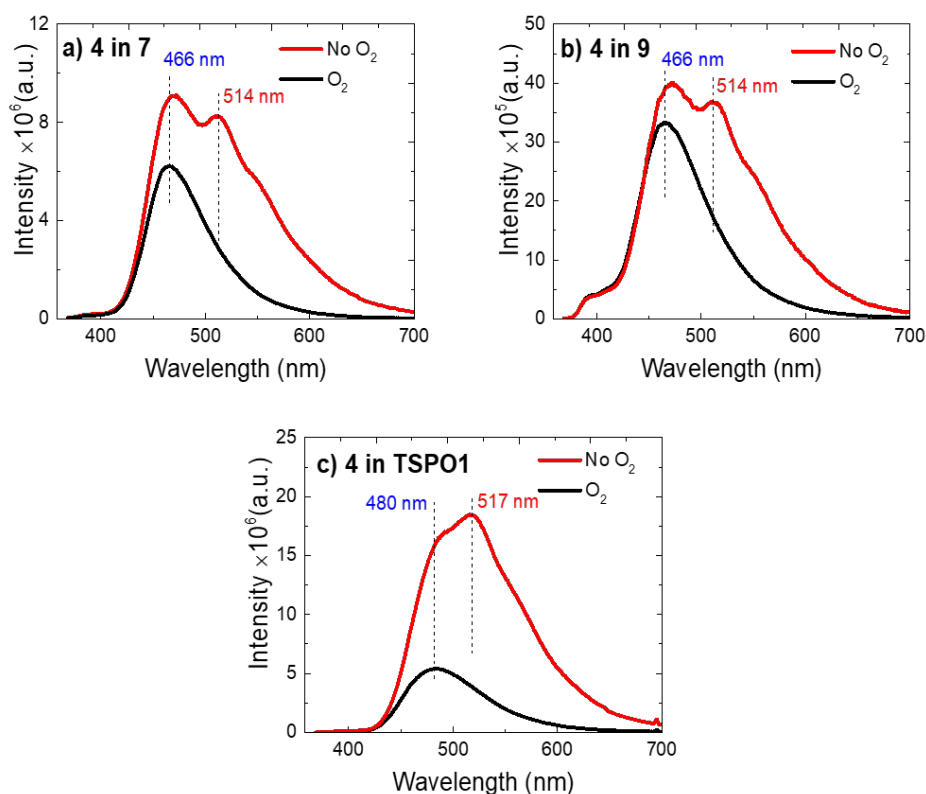


Figure 4.8: Steady-state emission spectra of compound 4 dispersed in different hosts a) 7, b) 9 and c) TSPO1, in vacuum (red) and under air (black) equilibrated conditions at room temperature.

a reduced relative contribution phosphorescence emission and is a result of the triplet states being harvested in two different ways, TADF or RTP. It is observed that the overall luminescence of compound 4 in TSPO1 decreases by more than four-fold in the presence of oxygen.

The singlet and triplet energies of compound 4 in zeonex, determined from the onsets of the fluorescence and phosphorescence bands, are 3.05 eV and 2.63 eV, respectively. For blends of compound 4 in 7 and 9, the S_1 shifts to 2.92 eV while T_1 state remains the same. In blends of compound 4 in more polar hosts TSPO1 and PBrS, S_1 and T_1 energies shift to 2.82 eV and 2.53 eV, respectively. Therefore, compared with the situation in zeonex film, the S_1 state shifts to a lower energy by 0.13 eV in 7 and 9, and by 0.23 eV in TSPO1 and PBrS. However, the triplet state exhibits no shift for blends of 4 in 7 and 9, while shifts by only 0.10 eV in TSPO1 and PBrS. Therefore, the energy gap of $\Delta E_{S_1-T_1}$ decreases from 0.42 eV in

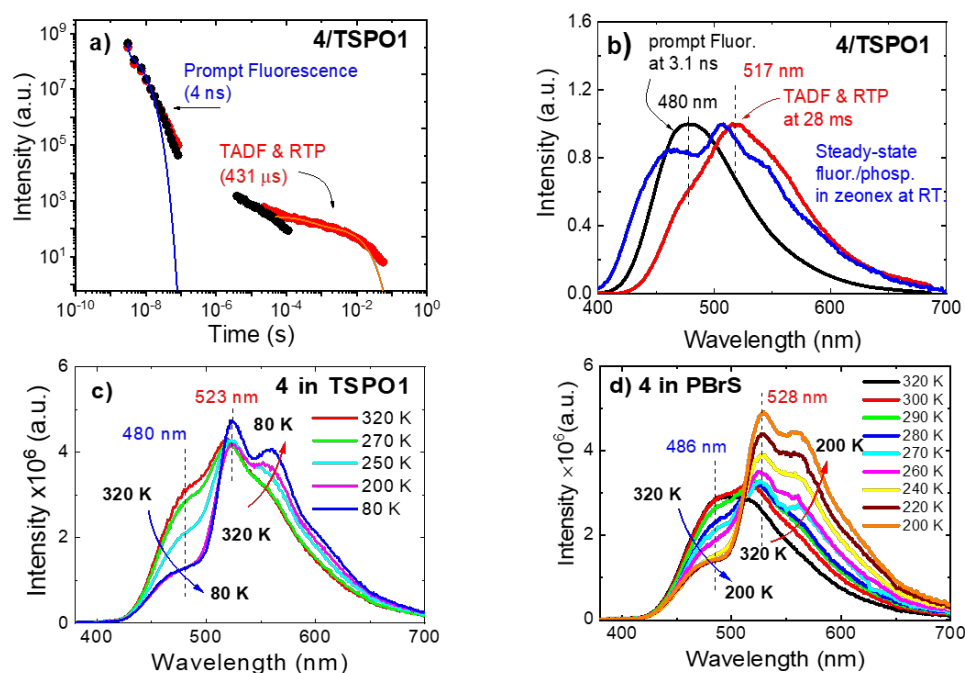


Figure 4.9: a) Time-resolved luminescence decays of compound 4 in TSP01, in vacuum (red) and in the presence of oxygen (black). b) Time-resolved spectra of 4 in TSP01, showing the spectra of the prompt fluorescence (black) and long-lived TADF and RTP (red). Both spectra are compared with the steady-state emission of 4 in zeonex (blue). c) Steady-state emission spectra of 4 in TSP01 and d) 4 in PBrS as a function of temperature.

zeonex to *ca.* 0.29 eV in all other hosts. This explains the turn-on of DF and the observation of dual luminescence, as shown in Figure 4.9. However, it is noted that given the manifold of triplet states below S_1 in the case of compound 4 (discussed in theoretical calculation), we cannot determine at present from which triplet the S_1 is thermally activated, only that the significant quenching of the fluorescence on addition of oxygen reveals an emission mechanism which passes through the triplet states.

The time-resolved luminescence of compound 4 in TSP01 is shown in Figure 4.9a. The luminescence decays – obtained in vacuum and in the presence of oxygen – show a fast decay component due to prompt fluorescence with no variation in the presence of oxygen as it is a direct radiative decay from S_1 state. A long-lived component due to TADF and RTP is only observed in vacuum, confirming that it

originates from triplet states. In Figure 4.9b, the time-resolved emission spectra obtained in PF and TADF/RTP regions are compared with the steady-state emission obtained in zeonex matrix. The spectrum is dominated by the fluorescence band at early delay times, whereas the delayed component is dominated by TADF and RTP at late delay times, appearing with an emission spectrum similar to the superposition of PF and phosphorescence. The same behaviour is also observed in blends of compound 4 in hosts 7 and 9 as shown in Figure 4.10.

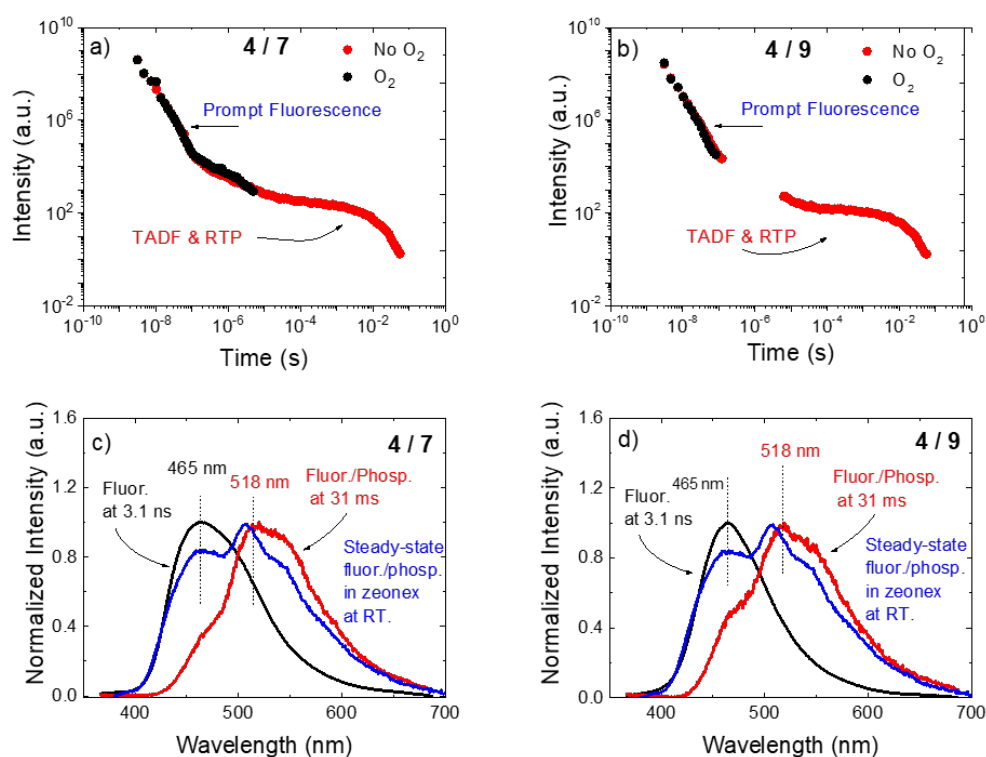


Figure 4.10: Time-resolved luminescence decay of compound 4 in hosts a) 7 and b) 9, in vacuum (red) and in the presence of oxygen (black). c) 7 and d) 9 showing the spectra of the prompt fluorescence (black), and long-lived TADF and RTP (red). Both spectra are compared with the steady-state emission of 4 in zeonex (blue).

Figures 4.9c and d show the steady-state emission spectra of compound 4 dispersed in TSP01 and PBrS, respectively. In both cases, dual emission is observed. A fluorescence band appears peaking at 480 nm, which is ascribed to a TADF mechanism, as confirmed by its positive temperature dependence (decreasing in intensity with decreasing temperature). In contrast, a well-resolved phosphorescence

band, peaking at 523 nm in TSP01 and 528 nm in PBrS increases in intensity with the decreasing temperature as nonradiative triplet decay that competes with phosphorescence is frozen out. This convincingly confirms the dual nature of the luminescence of compound 4 in these hosts. Similar trends are also observed in blends of compound 2 in these four hosts. [147]

4.2.5 Theoretical Calculations

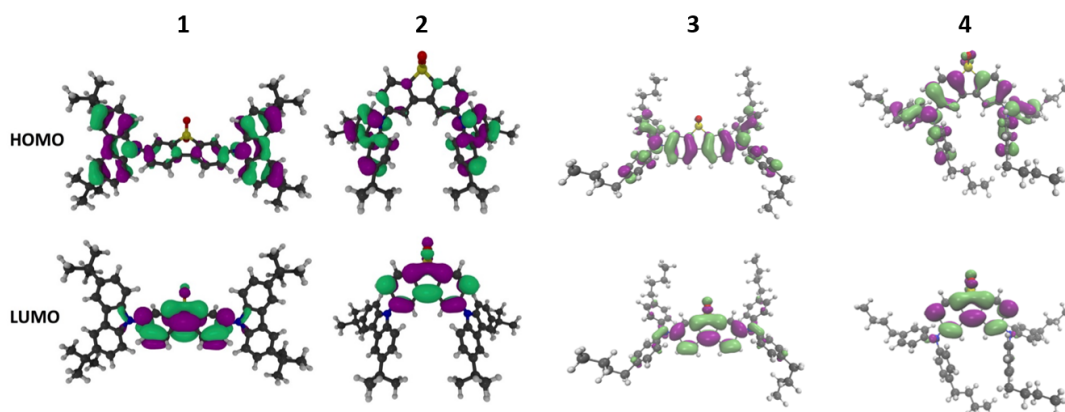


Figure 4.11: HOMO and LUMO frontier molecular orbitals of compounds 1 to 4, optimized using (U)DFT(PBE0) and a 6-31G* basis set as implemented within the Gaussian09 quantum chemistry package.

The HOMO and LUMO distributions for compounds 1 to 4 are shown in Figure 4.11, using (U)DFT(PBE0) [148, 149] and a 6-31G* basis set as implemented within the Gaussian09 quantum chemistry package. [150] These orbitals dominate the lowest transition responsible for the S_1 state. All four compounds show CT character, which can be quantified using the absolute orbital overlap $O = \langle \Psi_{\text{LUMO}} | \Psi_{\text{HOMO}} \rangle$, for which smaller overlaps implies a stronger CT character. [151] Therefore, the CT character at the ground state geometry is larger for compound 2 ($O=0.41$) than 1 ($O=0.49$), and for compound 4 ($O=0.58$) than 3 ($O=0.67$). To determine the excited state and emission properties, the molecules were optimized in the lowest singlet state using unrestricted *Kohn-Sham* (UKS) density functional theory (DFT). Importantly, the oscillator strength for the S_1 state is over an order of magnitude larger for compound 1 ($E_{S_1}=2.64$ eV, $f=0.9053$) than 2 ($E_{S_1}=2.75$ eV, $f=0.0276$).

This corresponds to a radiative lifetime for 1 of ~ 3 ns, in good agreement with the experimentally determined fluorescence lifetime, shown in Table 4.1. In contrast, the smaller oscillator strength of 2 corresponds to an excited state lifetime of ~ 50 ns. As the fluorescence lifetime calculated from the experimental results for compound 2 is less than 2 ns, this illustrates that the S_1 state in 2 is susceptible to other processes, namely ISC, consistent with the observation of phosphorescence in 2. In addition, the energies agree well with the maxima of the emission spectra shown in Figure 4.4. The same trend is observed for compounds 3 ($E_{S_1}=2.61$ eV, $f=0.9845$) and 4 ($E_{S_1}=2.82$ eV, $f=0.0200$). Therefore, the oscillator strength of the S_1 state is much smaller in 4 than that in 3, allowing ISC to outcompete the radiative decay.

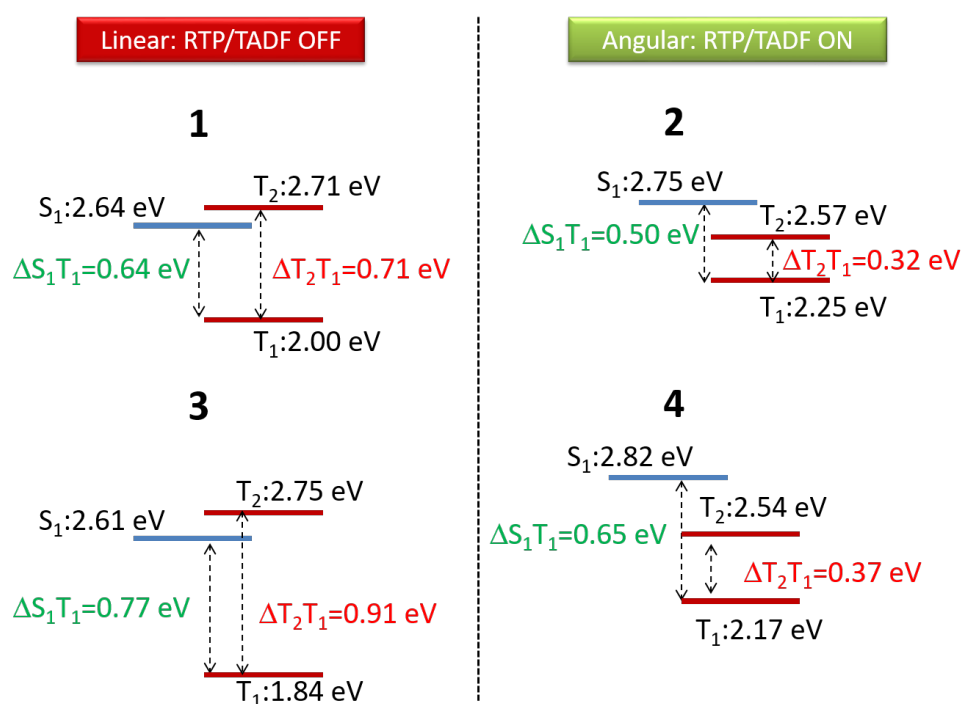


Figure 4.12: Energy level diagram of the singlet and triplet states in compounds 1 to 4, obtained from calculations.

To further interrogate the mechanism that causes the enhanced ISC in compounds 2 and 4, the energy level diagram based on theoretical calculations is present in Figure 4.12. Within each pair, the “angular” substituted compounds 2 and 4 have calculated energy gaps $\Delta E_{S_1-T_1}$ consistently smaller than their “linear” counterparts. However, this does not necessarily explain the observation of strong RTP or TADF

emission. When compared across the four structures, compound 4, which is a good RTP emitter in zeonex film (and a good TADF emitter in ethanol solution at room temperature) has a $\Delta E_{S_1-T_1}$ of 0.65 eV, whereas compound 1, which shows neither RTP or TADF in any medium, has a similar $\Delta E_{S_1-T_1}$ of 0.64 eV. Therefore, the gap $\Delta E_{S_1-T_1}$ is not the only relevant property to consider. From the calculations, a more pertinent energy gap of T_1-T_n between the manifold of triplet states closest to the S_1 state emerges as a critical feature, from where a different pattern emerges between the “linear” and “angular” compounds.

For both compounds 1 and 3, which do not exhibit RTP or TADF, the gap between T_1 and T_2 states is large (> 0.7 eV), whereas for 2 and 4, both good RTP/TADF emitters, the gap between T_1 and T_2 is small (~ 0.3 eV). This provides the potential for efficient internal conversion between the triplet states and a decay route of the initially populated triplet to decay to the lowest triplet state T_1 from where it emits, according to Kasha’s rule. [30] In this case, it was reported that the spin-vibronic mechanism, involving both spin-orbit coupling and non-adiabatic coupling, [53, 60] significantly increases the rate of ISC. The close proximity of all the triplet states in combination with the slower radiative rates of the S_1 state makes this mechanism more likely to occur in compounds 2 and 4.

These data sets therefore provide an understanding of the properties that give rise to RTP. This mechanism also explains why compounds 2 and 4 are good TADF emitters in ethanol. In this case, the strong solvent polarity shifts the S_1 state to a lower energy without affecting significantly the energy of the T_1 state, which does not have CT character. This makes the $\Delta E_{S_1-T_1}$ gap smaller and facilitates RISC. Furthermore, the results obtained in Section 4.2.4 confirm this hypothesis, when compounds 1 to 4 were dispersed in hosts with higher polarity than zeonex. With the correct tuning of the energy levels, dual luminescence (RTP and TADF) is observed. This casts the TADF and RTP mechanisms into a common conceptual framework.

4.3 Conclusions

In summary, the photophysical properties of 10 compounds were studied in this chapter. It is shown that the ISC and RISC mechanisms are enhanced in pure organic molecules by using a simple strategy based on changing the molecular connectivity of carbazole, diphenylamine and fluorene donors to a dibenzothiophene-*S,S*-dioxide acceptor, from “linear” to “angular” geometry. The latter substitution of the A unit effectively breaks the molecular conjugation, and shifts the singlet and triplet states to higher energies. More importantly, the “angular” substitution gives rise to a small energy gap between triplet levels below the S_1 state and a slower radiative rate, making the S_1 state susceptible to other decay processes such as ISC and IC. In contrast, the radiative decay rate of the S_1 state is an order of magnitude faster and the energy separation between the consecutive triplet states is much larger in the “linear” compounds. The small energy difference between triplet states below the S_1 state present in the “angular” isomers has profound implications for the ISC and RISC mechanisms. Non-adiabatic vibronic coupling between T_1 and the upper triplet states lying below S_1 state creates a fast T_1 - T_n equilibrium and strong mixing between these states. This also enhances coupling between S_1 and T_1 . The larger energy difference between T_1 and T_2 in compounds 1 and 3 causes the absence of the mixing between the triplet states lying below S_1 , which further leads to an inefficient ISC process. In addition, the radiative decay rates from singlet states in both compounds 1 and 3 are faster, reducing the triplet yield. Consequently, neither RTP nor TADF is observed even when dispersed in PBrS, a host in which the external heavy-atom effect is used to promote ISC.

Furthermore, using the host to fine-tune the energy difference between S_1 and T_1 , dual long-lived luminescence (TADF and RTP) in compounds 2 and 4 is activated simultaneously in different hosts. Therefore, this study provides a guide that can be used to design novel molecules showing alternative routes to harvest triplet states, and enhance their potentials for applications in photonic and optoelectronic devices.

Chapter 5

The Influence of Molecular Conformation on the Photophysics of Organic Room Temperature Phosphorescent Luminophores

This chapter investigates the influence of molecular conformation on RTP emitters in a series of novel D–A–D compounds featuring dibenzothiophene (DBT) as A and phenothiazine (PTZ) as D unit. Different degrees of steric hindrance are achieved by systematic changes of inward pointing D substituents (methyl, *iso*-propyl and *tert*-butyl). This leads to the tuning of the photophysical properties induced by conformational control. Unsubstituted DPTZ–DBT exists in both equatorial and axial forms in the ground state, due to the ability of PTZ to form H-extra and H-intra folded conformers. However, the H-intra equatorial conformer prevails in the excited state, leading to strong green RTP with high phosphorescence quantum yield ($60\pm 8\%$). Under the influence of the bulky substituents, the alkyl DPTZ–DBT derivatives change their molecular conformation, preventing the formation of the excited charge transfer state. Hence, blue but weaker, phosphorescence is observed. Remarkably, the less bulky methyl substituent on the donor unit results in dual RTP (blue and green), apparently violating Kasha's rule. These effects are imposed by the modulation of the barriers between excited states, with conclusions supported

by DFT calculations in the ground and excited state. It is demonstrated that the control of conformation with substituents is an effective strategy to tune the excited state properties of D–A–D molecules for RTP emission.

This work was published in *Journal of Materials Chemistry C* (R. Huang, J. S. Ward, N. A. Kukhta, J. Avó, J. Gibson, T. J. Penfold, J. C. Lima, A. S. Batsanov, M. N. Berberan-Santos, M. R. Bryce, F. B. Dias, *J. Mater. Chem. C* 2018, 6, 9238–9247). R. Huang performed the photophysical measurements under the supervision of F. B. Dias. J. S. Ward and N. A. Kukhta synthesized molecules and carried out NMR studies under the guidance of M. R. Bryce. J. Avó, J. C. Lima and M. N. Berberan-Santos carried out Flash-Photolysis studies and determined triplet formation and luminescence quantum yields. J. Gibson and T. J. Penfold theoretically tested within a quantum chemistry framework. A. S. Batsanov performed the X-ray characterization.

5.1 Introduction

Conformational isomerization is a fundamental feature of organic chemistry, with profound effects upon physical properties. However, the understanding of its role in determining excited state properties is less developed. Phenothiazine (PTZ) derivatives exhibited great potential in pharmacology, [152] and are now being revisited due to their potential to promote efficient triplet harvesting in TADF and RTP emitters for applications in electroluminescent devices. Quantum-mechanical calculations show that PTZ has great electron-donor properties and the ability to participate in complexes with charge transfer (CT) character. [153, 154]

However, less well-known are the differences in properties between its two heterogeneous conformers. [155, 156] Daub *et al.* first reported the conformation dependent properties on the emission of PTZ in phenothiazine-pyrene dyads. [157] Dual fluorescence from both localized excited (LE) and CT states was observed as a result of the energy level arrangement caused by the conformational heterogeneity. Emission from the LE state originates from a minority conformation (with CT is negligible) whereas CT emission results from the majority conformation that undergoes electron transfer.

It is the intrinsic ability of PTZ to form H-intra and H-extra folded conformers that allows formation of parallel quasi-axial (ax) and perpendicular quasi-equatorial (eq) conformers in D-A or D-A-D molecules. The existence of the conformers is rationalized by either localization of the nitrogen lone pairs along the N-S axis, or in plane of the phenyl rings as proposed by Stockmann *et al.* in 2002. [158] In addition, the dual emission arising from two CT states in a TADF molecule was also observed recently by Adachi *et al.* in molecule PTZ-TRZ, resulting from the distortion of PTZ and leading to different energy gaps ΔE_{ST} . [159] Recently, PTZ as the donor unit has been investigated in many luminescent molecules, with great success in terms of PLQY and EQE. [41, 159–163]

Molecular design strategies to enhance the ISC and RTP in metal-free molecules are still limited and relatively inefficient compared to heavy-metal containing emitters. This reflects the lack of detailed understanding of how alterations of molecular conformations, nuclear vibrations and substituents may affect the radiative rate,

non-radiative IC and ISC rates in RTP emitters. As PTZ can emit phosphorescence at room temperature in solid zeonex films, it presents an ideal test system to understand RTP better. Accordingly, four D–A–D metal-free and halogen-free organic molecules are based on PTZ as donor and dibenzothiophene (DBT) as acceptor are studied in this chapter. Three analogues, DPTZ–Me–DBT, DPTZ–*i*Pr–DBT and DPTZ–*t*Bu–DBT were designed with methyl, *iso*-propyl and *tert*-butyl groups substituting at the C(1)-position of each PTZ unit, respectively. These molecules show profoundly different excited state properties due to the different conformations (axial *vs.* equatorial) imposed by the effect of steric hindrance around D–A bonds. These equatorial and axial conformers have been identified recently in related compounds which show different RTP and TADF responses. [101,164]

5.2 Results and Discussion

5.2.1 Chemical Characterization

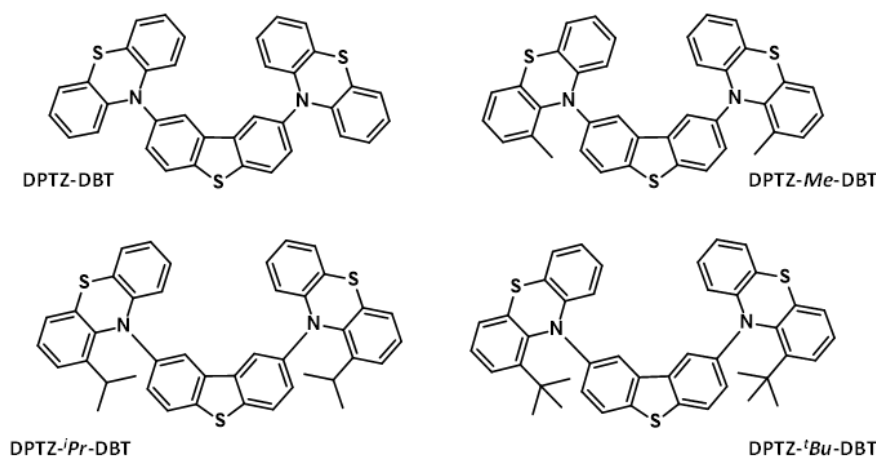


Figure 5.1: Molecular structures of the four compounds studied in this chapter.

The molecular structures of four D–A–D compounds studied in this chapter are shown in Figure 5.1. These molecules were rationally designed based on the following considerations:

i) PTZ is a strong electron donor unit, and shows a high triplet formation yield and a fast ISC rate.

ii) DBT is also a standard luminophore, usually serving as an electron-donating unit in combination with different acceptors, *e.g.* fluorene, [165,166] anthracene, [167] or benzoyl, [168] due to its electron-rich thiophene functionality. Therefore, its use as an acceptor in the present series of compounds is unusual, although there is precedent with the bis(3,6-di-*t*-butyl)*N*-carbazolyl derivatives reported previously. [144, 147] However, whether a section of a π -system acts as a donor or acceptor moiety strongly depends on the functionality to which this system is bonded. Compared with DBT, PTZ is a relatively more electron-rich unit. In addition, DBT has been previously identified as promoting a fast RISC rate in Chapter 4. [147]

iii) These four molecules are direct analogues of the dibenzothiophene-*S,S*-dioxide acceptor series, which possess an unusual combination of TADF and RTP. [102] The key distinction with the present series is the different oxidation state of thiophene sulfur. The SO₂ unit imparts strong acceptor properties with a much lower LUMO energy and increased charge-transfer properties compared to the DBT unit studied in this chapter. The 2,8-disubstitution of DBT (PTZ para to the sulphur atom) was chosen to maximize the interaction of the D and A units, compared to the isomeric 3,7-derivatives (PTZ units meta to sulphur). [144, 147, 169]

iv) Both PTZ and DBT units on their own have potential to show strong triplet formation properties, due to the presence of the sulphur and nitrogen atoms.

v) The increasing steric hindrance imparted by the alkyl substituents on PTZ units serves as a probe of steric effects on the conformation of the D–A–D system and its effect on the ISC/rISC rates as discussed in more detail below.

As shown in Figure 5.2, the X-ray molecular structures of DPTZ–DBT, DPTZ–Me–DBT and DPTZ–^{*i*}Pr–DBT revealed interesting conformational differences between properties of the molecules in the solid state. The DBT moiety is practically planar, showing only a small angle (ω) between its two arene rings. The PTZ moiety is always folded along the N...S vector, the folding angle (θ) between its arene “wings” varying substantially (*vide infra*). As reported, [158] the PTZ and DBT moieties in crystals take one of two possible orientations. These are the equatorial conformation—whereby the PTZ moiety lies astride the DBT plane and is roughly perpendicular to it and the axial conformation—where PTZ is tilted to one side of the

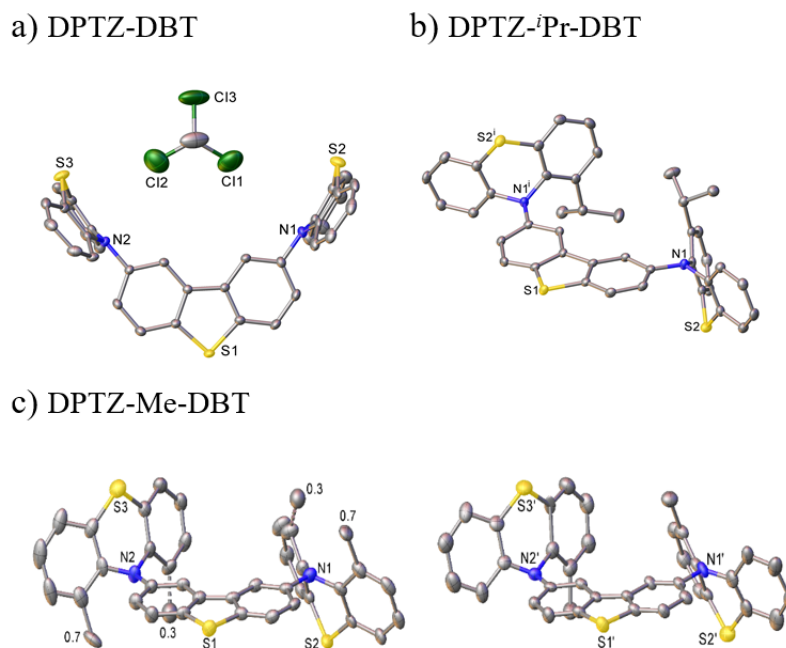


Figure 5.2: X-ray molecular structures of a) DPTZ-DBT·CDCl₃ and b) DPTZ-*i*Pr-DBT showing equatorial and axial PTZ groups, respectively. Thermal ellipsoids are drawn at the 50% probability level, H atoms are omitted for clarity, and primed atoms are generated by the twofold axis. c) DPTZ-Me-DBT molecule in the crystal of its CHCl₃ solvate. Thermal ellipsoids are drawn at the 30% probability level. Occupancies of the disordered groups/atoms are cited.

DBT plane. In the axial conformation the torsional angle (τ) around the C(DBT)-N(PTZ) bond (measured between the $p_{\pi}(\text{C})$ orbital and the N lone pair) is close to zero; in the equatorial conformation, $\tau \approx 90^{\circ}$. With two PTZ substituents present, their axial conformations can be either *cis* or *trans* with respect to the DBT plane, and there is an additional degree of flexibility (within both axial and equatorial options) as each PTZ moiety can fold in two opposite directions. The axial conformation allows the lone pair of the N atom to be conjugated with the π -system of DBT, while the equatorial conformation precludes this, thereby favouring the competing conjugation with the arene rings of PTZ itself, as indicated by the longer N-C bond lengths than the C-C bond lengths of PTZ unit in DPTZ-DBT.

As depicted in Figures 5.2a and b, the torsional angles of DPTZ-DBT and DPTZ-*i*Pr-DBT are 84.7° and 11.9° , respectively, showing that the PTZ units are

exclusively in equatorial (PTZ) and axial (PTZ-ⁱPr) conformations. DPTZ-ⁱPr-DBT has crystallographic C₂ symmetry and thus a *trans*-axial-conformation, showing no disorder. However, in the polymorphic structures of DPTZ-Me-DBT, there is a conformational disorder of the PTZ units as shown in Figure 5.2c. The asymmetric unit of DPTZ-Me-DBT·CDCl₃ comprises two host molecules, both adopting a *trans*-axial-conformation. In one molecule, the methyl substituents at both PTZ moieties are disordered, *i.e.* different conformers share the site, while the other molecule shows no disorder. This is consistent with the dual phosphorescence observed in DPTZ-Me-DBT which is ascribed to the low energy barrier to subtle molecular vibrations, as discussed in Section 5.2.3. In contrast, DPTZ-^tBu-DBT is difficult to crystallize most probably due to its very large *tert*-butyl substituents, which greatly increase the steric hindrance and vibrations frustrating crystal packing.

5.2.2 Theoretical Calculations

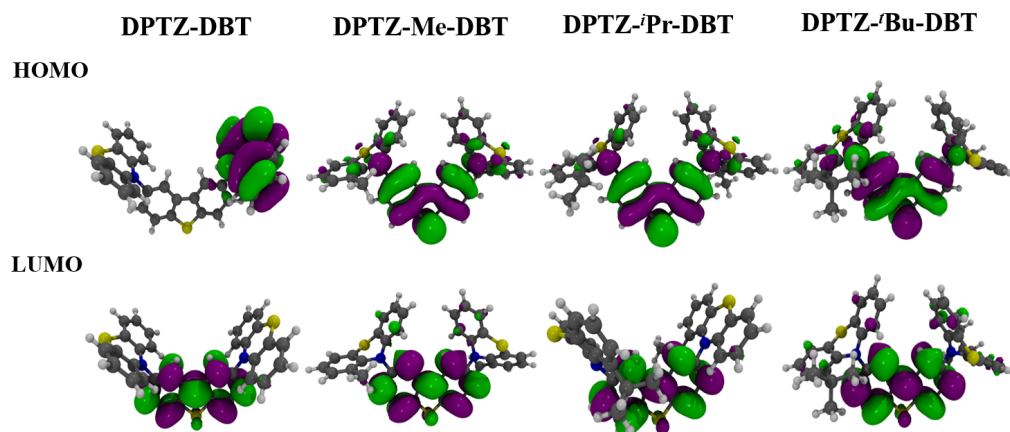


Figure 5.3: Molecular orbitals, HOMO and LUMO distributions of DPTZ-DBT (equatorial), DPTZ-Me-DBT (axial), DPTZ-ⁱPr-DBT (axial) and DPTZ-^tBu-DBT (axial) forms at DFT (M062X)/Def2SVP level of theory.

The HOMO and LUMO frontier orbitals of DPTZ-DBT, DPTZ-Me-DBT, DPTZ-ⁱPr-DBT and DPTZ-^tBu-DBT are shown in Figure 5.3. The relative energies of each conformer of all four molecules in toluene, anisole and ethanol are shown in

Table 5.1: Calculated energies of studied molecules in different conformations. S_0^{abs} is the energy (eV) of the ground state calculated relative to the lower energy. The energy (eV) of the S_1 state at the Franck-Condon (Absorption, S_1^{abs}) and excited state optimised (Emission, S_1^{em}) geometries are also reported. The oscillator strengths are in brackets. Each structure was optimized in the absence of a solvent model to aid convergence. The final excited state emission energies were calculated using a SS-PCM approach using the solvent parameters of toluene.

		DPTZ-DBT		DPTZ-Me-DBT		DPTZ- ⁱ Pr-DBT		DPTZ- ^t Bu-DBT	
		Ax.	Eq.	Ax.	Eq.	Ax.	Eq.	Ax.	Eq.
toluene	S_0^{abs}	0.06	0.00	0.00	1.09	0.00	1.22	0.00	1.06
	S_1^{abs}	4.01	3.88	4.03	-	4.04	-	4.04	-
	S_1^{em}	3.67 (0.043)	2.78 (0.002)	3.74 (0.041)	2.81 (0.005)	3.74 (0.046)	2.47 (0.003)	3.74 (0.046)	2.51 (0.003)
anisole	S_0^{abs}	0.06	0.00	0.00	1.08	0.00	1.22	0.00	1.05
	S_1^{abs}	4.01	3.91	4.03	-	4.04	-	4.04	-
	S_1^{em}	3.66 (0.044)	2.53 (0.001)	3.73 (0.042)	2.60 (0.004)	3.73 (0.048)	2.27 (0.003)	3.73 (0.048)	2.50 (0.003)
ethanol	S_0^{abs}	0.05	0.00	0.00	1.08	0.00	1.21	0.00	1.05
	S_1^{abs}	4.01	3.94	4.03	-	4.05	-	4.04	-
	S_1^{em}	3.66 (0.044)	2.19 (0.001)	3.71 (0.043)	2.31 (0.004)	3.71 (0.049)	1.98 (0.002)	3.70 (0.049)	2.48 (0.003)

Table 5.1. Both axial and equatorial conformers exist in all molecules, although in all cases one conformer is dominant. For DPTZ-DBT, both donor groups are equatorial to the acceptor, as the axial conformers are around 60 meV higher in energy. In the other three substituted molecules, both donor groups are axial to the acceptor in agreement with the X-ray structures discussed in Section 5.2.1.

Moreover, these four molecules show different HOMO and LUMO distributions. For DPTZ-DBT, HOMO and LUMO are localized on the PTZ and DBT units, respectively, whereas both orbitals are mainly distributed through the DBT unit for the substituted molecules DPTZ-Me-DBT, DPTZ-ⁱPr-DBT and DPTZ-^tBu-DBT. The axial form shows no shift with the polarity of the solvent, with a stable energy at 3.66 eV. However, the equatorial form consistently shifts to lower energies with the

increasing solvent polarity demonstrating stronger CT character. In DPTZ–DBT, the lowest singlet excited state S_1 is equatorial and the calculated emission peaks are 446, 490 and 566 nm in toluene, anisole and ethanol, respectively. In contrast, the axial conformer has significant LE character on the DBT unit at 334 nm. Therefore, it is unaffected by solvent polarity. In the ground state, only the axial form exists in the substituted molecules DPTZ–Me–DBT, DPTZ–^{*i*}Pr–DBT and DPTZ–^{*t*}Bu–DBT, which is identified by the absorption band at 380 nm. However, they show both axial and equatorial forms in the excited state, although the former is more stable due to the steric hindrance caused by the alkyl groups (Table 5.1).

5.2.3 Photophysical Properties

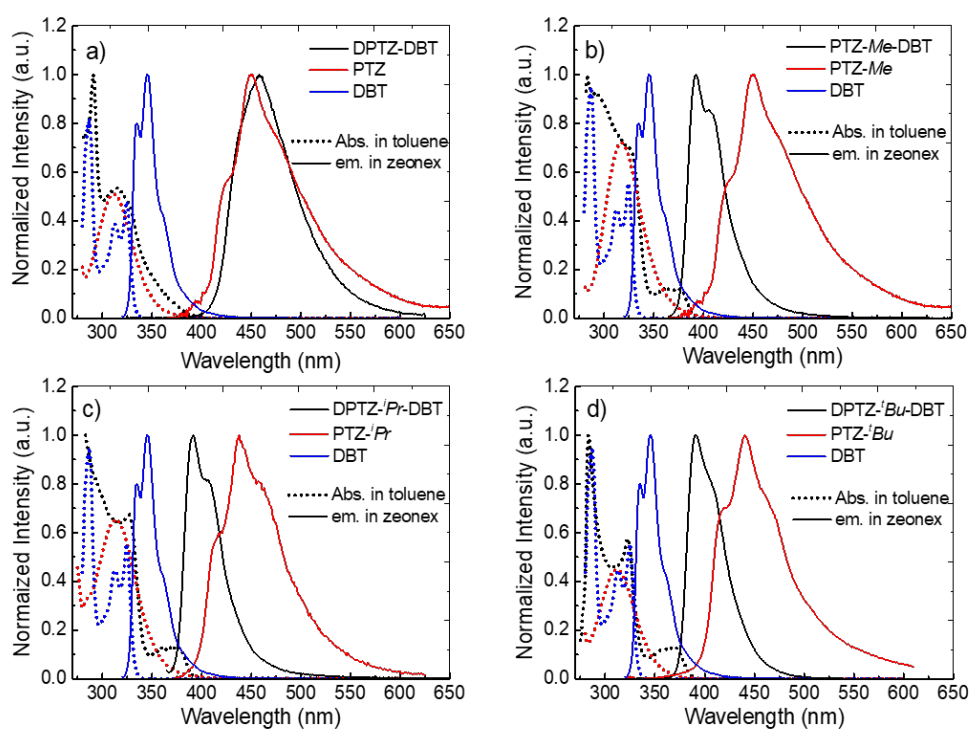


Figure 5.4: The UV–Vis absorption (toluene) and fluorescence (zeonex) spectra of a) DPTZ–DBT, and three substituted derivatives b) DPTZ–Me–DBT, c) DPTZ–^{*i*}Pr–DBT and d) DPTZ–^{*t*}Bu–DBT, in comparison to the spectra of their individual units at room temperature.

The absorption and emission spectra of all four molecules are shown in Figure 5.4

and compared with the spectra of their individual units. The onset of the absorption spectrum of DPTZ–DBT is around 400 nm, with the absorption intensity growing smoothly up to the peak of the lower energy band at 320 nm. A second absorption band is also observed below 300 nm, which is not entirely measured in toluene due to the solvent cut-off. The two transition bands are identified as the signatures of the individual PTZ and DBT units. In addition to a higher energy (below 300 nm) and a lower energy band (around 320 nm) observed in DPTZ–Me–DBT, a well-defined band peaking at 380 nm is observed, which is absent in the unsubstituted DPTZ–DBT. Similar bands are also observed in the absorption spectra of DPTZ–*i*Pr–DBT and DPTZ–*t*Bu–DBT, but not in either PTZ or DBT. This band is not a CT transition, as the CT state is not formed in the substituted compounds, as shown by the HOMO and LUMO distributions in Figure 5.3 and solvation effects in Figure 5.5. This transition instead corresponds mostly to a transition centred on the DBT unit, but with the axial conformation DBT mixing with PTZ. It is this mixing that explains why the band is absent for the absorption spectra of the two fragments and the orthogonal DPTZ–DBT.

Well-defined differences are observed in the emission spectra of these four molecules. The emission spectrum of DPTZ–DBT (peaking at 450 nm in zeonex film) is at a similar energy to the fluorescence of the donor PTZ unit (Figure 5.4a). In contrast, all the substituted molecules DPTZ–Me–DBT, DPTZ–*i*Pr–DBT and DPTZ–*t*Bu–DBT exhibit well-resolved and blue-shifted spectra, this is due to different conformers enforced by alkyl substituents.

As shown in Figure 5.5a, DPTZ–DBT exhibits a broad spectrum in toluene, peaking at 480 nm, which further red-shifts with the increasing solvent polarity. In contrast the structured and blue-shifted emissions observed in the substituted compounds DPTZ–Me–DBT, DPTZ–*i*Pr–DBT and DPTZ–*t*Bu–DBT are entirely independent of the solvent polarity. These observations are consistent with the CT character of the lowest singlet excited state in DPTZ–DBT, as expected from the HOMO and LUMO distributions in Figure 5.3. In the substituted compounds, the excited state instead has a LE character, as evidenced by the absence of solvatochromism in the emission and overlapping HOMO/LUMO from calculations.

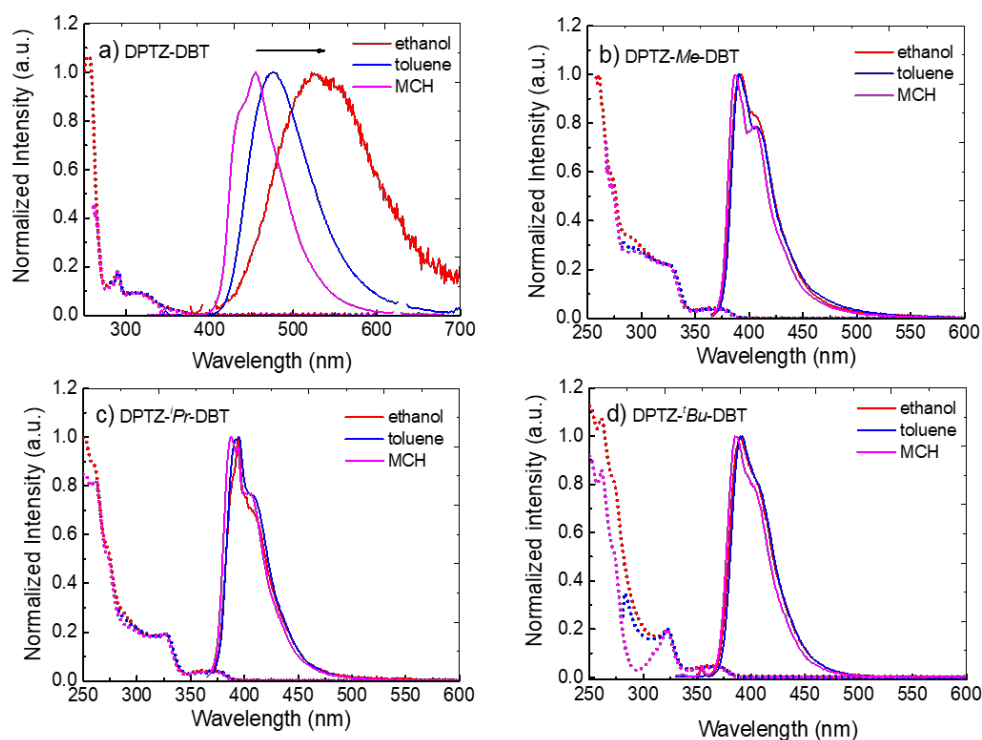


Figure 5.5: Absorption and emission spectra of a) DPTZ–DBT, b) DPTZ–Me–DBT, c) DPTZ–*i*Pr–DBT and d) DPTZ–*t*Bu–DBT in solvents of different polarity at room temperature.

Dual emission of DPTZ–DBT is observed in vacuum, composed of fluorescence and phosphorescence bands peaking at 450 nm and 540 nm in Figure 5.6a. The phosphorescence band matches with the phosphorescence of PTZ, showing that the lowest energy triplet state is localized on the PTZ unit. In the presence of oxygen, the phosphorescence is quenched and only the fluorescence band at 450 nm is observed. Figures 5.6b and c similarly show dual emission in zeonex films of DPTZ–*i*Pr–DBT and DPTZ–*t*Bu–DBT. Interestingly, fluorescence peaking around 390 nm is observed, accompanied by a phosphorescence band at 450 nm. This contrasts with DPTZ–DBT as the phosphorescence in DPTZ–*i*Pr–DBT and DPTZ–*t*Bu–DBT matches perfectly with the phosphorescence of the DBT unit, and not of PTZ. The phosphorescence behaviour in DPTZ–Me–DBT is more complex and is discussed separately in detail below.

The fluorescence and phosphorescence spectra of DPTZ–DBT, DPTZ–*i*Pr–DBT and DPTZ–*t*Bu–DBT in zeonex are observed independently at early and late delay

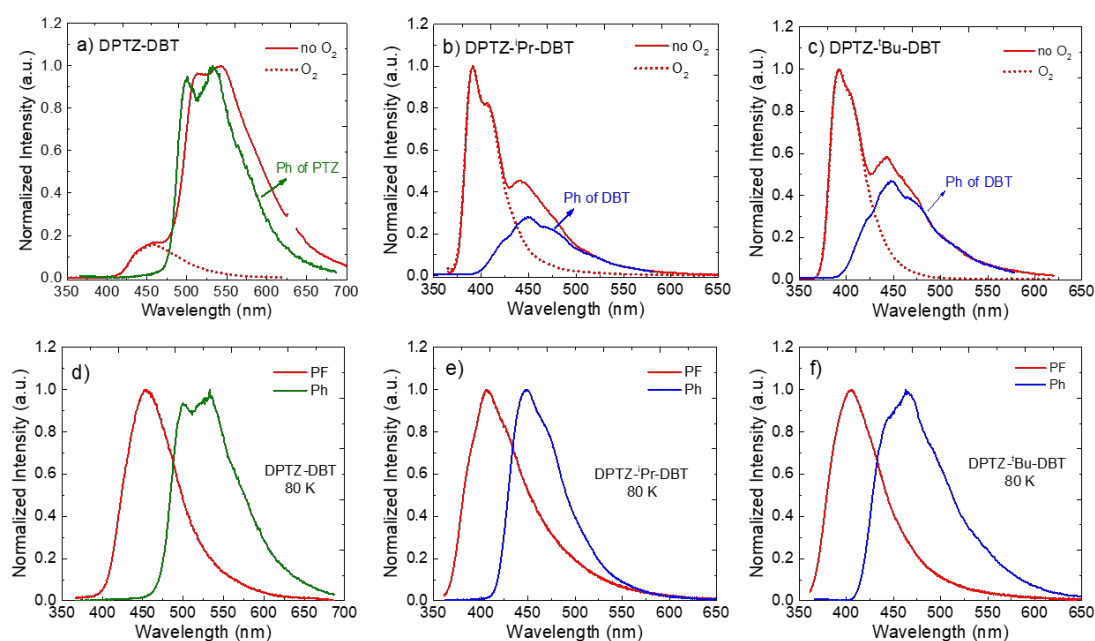


Figure 5.6: Steady-state emission spectra (zeonex at RT, in air and under vacuum) of a) DPTZ-DBT, b) DPTZ-*i*Pr-DBT and c) DPTZ-*t*Bu-DBT, in comparison to the phosphorescence of PTZ and DBT units. Time-resolved prompt fluorescence and phosphorescence spectra of d) DPTZ-DBT, e) DPTZ-*i*Pr-DBT and f) DPTZ-*t*Bu-DBT, PF and phosphorescence were collected at 80 K with delay times of 1.1 ns and 50 ms, respectively.

times in time-resolved measurements. This is due to their different lifetimes with spectra shown in Figures 5.6d-f. Remarkably, both fluorescence and phosphorescence in DPTZ-*i*Pr-DBT are blueshifted compared with the corresponding spectra of DPTZ-DBT. However, while the fluorescence does not match entirely the fluorescence of either DBT or PTZ, the phosphorescence originates from the high triplet state matching that localized on the DBT unit. DPTZ-*t*Bu-DBT with bulkier substituents show similar emission properties when compared to DPTZ-*i*Pr-DBT, and has a high triplet energy level, with phosphorescence again matching that of the DBT unit.

The observation of the blueshifted fluorescence and phosphorescence spectra is not a simple effect of substitution on the PTZ unit. The absorption, fluorescence and phosphorescence spectra of PTZ and PTZ-Me, PTZ-*i*Pr and PTZ-*t*Bu, are compared in Figure 5.7. Only minimal variations in the absorption and emission spectra are observed upon 1-alkyl substitution. Therefore, the substitution of the

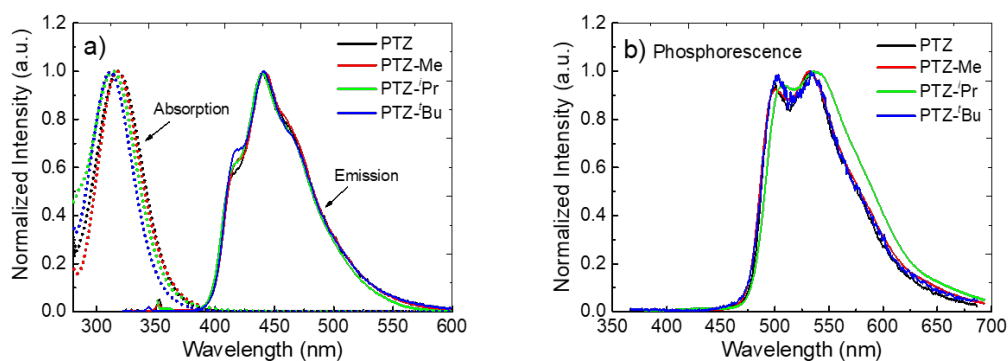


Figure 5.7: a) Comparison of the absorption (dot lines) and emission (full lines) spectra of PTZ and substituted PTZ units, PTZ-Me, PTZ-ⁱPr and PTZ-^tBu. Absorption were measured in toluene and fluorescence in zeonex at room temperature. b) Phosphorescence of PTZ derivatives in zeonex film collected at 80 K. Excitation at 355 nm.

PTZ molecule alone cannot explain the different phosphorescence spectra of the D-A-D molecules.

DPTZ-Me-DBT exhibits unique dual phosphorescence emission properties as shown in Figure 5.8a. It is proposed that the steric hindrance effect of methyl groups is less pronounced compared to *iso*-propyl and *tert*-butyl groups, leading to dual phosphorescence at room temperature in zeonex film. The steady-state emission spectrum of DPTZ-Me-DBT shows the fluorescence band peaking at 390 nm, as in the case of other two substituted molecules DPTZ-ⁱPr-DBT and DPTZ-^tBu-DBT. However, in DPTZ-Me-DBT, the fluorescence is accompanied by phosphorescence from the DBT unit (peaking at 450 nm) as well as phosphorescence from the PTZ-Me unit (540 nm). The observation of dual phosphorescence is an apparent violation of Kasha's rule. [30] The fluorescence spectrum of DPTZ-Me-DBT peaking at 390 nm was collected at an early delay time of 1.1 ns at room temperature (Figure 5.8b), as in the case of DPTZ-ⁱPr-DBT and DPTZ-^tBu-DBT. However, a broad and well-structured phosphorescence was collected at delay time of 50 ms at room temperature. As shown in Figure 5.8c, this phosphorescence spectrum composed of a low and a high energy band and is a superposition of the PTZ-Me and DBT phosphorescence. Interestingly, the phosphorescence spectrum collected at 80 K shows only the high energy feature. Figure 5.8d depicts the phosphorescence

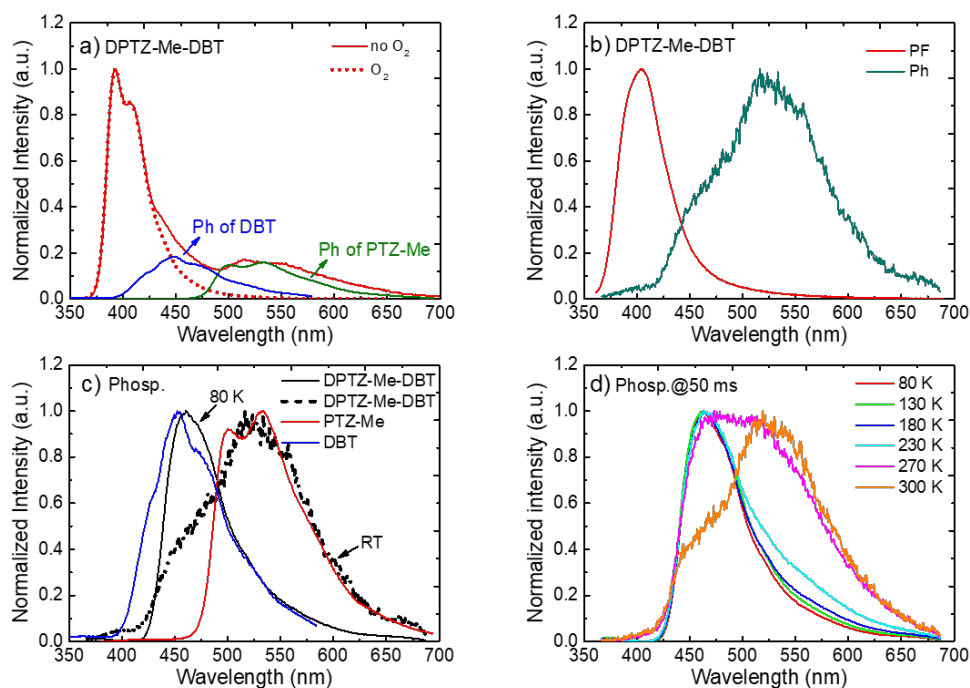


Figure 5.8: DPTZ–Me–DBT emission spectra in zeonex film: a) Steady-state emission spectra in air and in vacuum at RT. The phosphorescence of the DBT and the PTZ units are also shown, matching the two phosphorescence bands in DPTZ–Me–DBT. b) Time-resolved PF and phosphorescence spectra at RT, collected at delay time of 1.1 ns and 50 ms, respectively. c) Phosphorescence spectra at RT and 80 K, compared with the phosphorescence of DBT and PTZ–Me fragments. d) Phosphorescence as a function of temperature collected at delay times of 50 ms.

spectra as a function of temperature, with the contribution of PTZ–Me phosphorescence progressively disappearing and only the high-energy DBT phosphorescence remaining at 80 K.

Evidence of dual phosphorescence is shown in the temperature dependent steady-state emission as depicted in Figure 5.9. The phosphorescence behaviour observed in DPTZ–Me–DBT strongly indicates the presence of two conformers in all four DPTZ–DBT derivatives, which are separated by a considerable energy barrier (Figure 5.9b). The height of this barrier is very sensitive to the length of the bond between the donor and acceptor units. [58] Therefore, while the barrier is large in the ground state, it may decrease in the excited state. Figures 5.9c and d show that only phosphorescence from high energies is observed from 300 K to 80 K in DPTZ–ⁱPr–

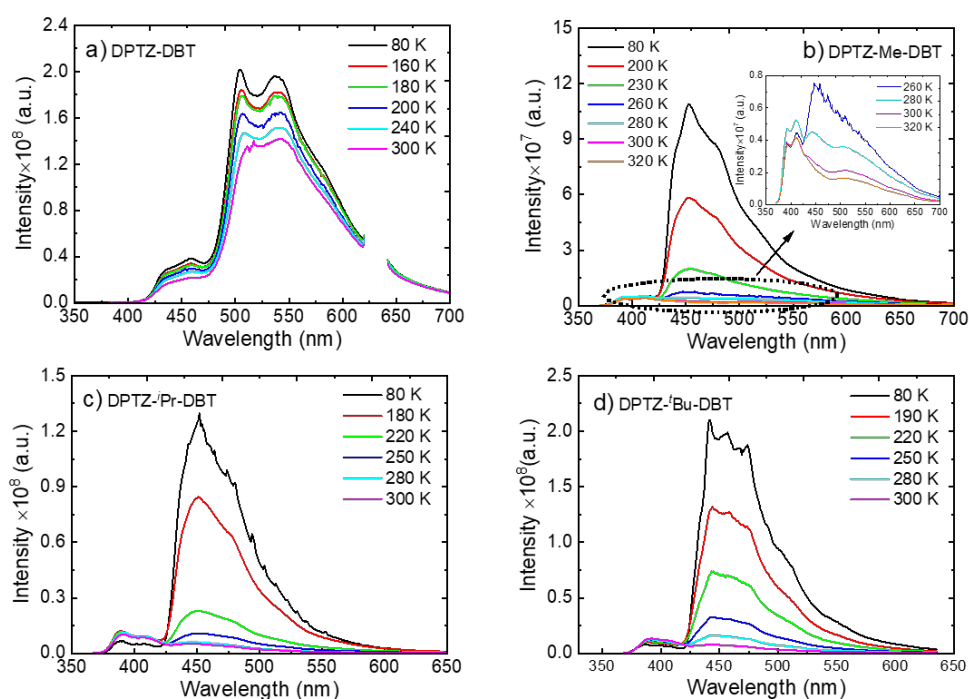


Figure 5.9: Temperature dependence of steady-state emission spectra in zeonex of a) DPTZ-DBT, b) DPTZ-Me-DBT, c) DPTZ-ⁱPr-DBT and d) DPTZ-^tBu-DBT.

DBT and DPTZ-^tBu-DBT with bulkier substituents.

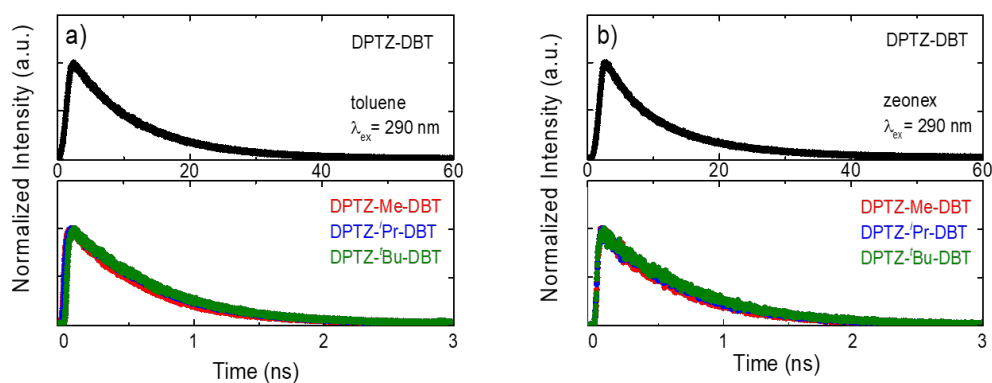


Figure 5.10: Emission decays of DPTZ-DBT, DPTZ-Me-DBT, DPTZ-ⁱPr-DBT and DPTZ-^tBu-DBT collected at the fluorescence bands in air at RT in a) toluene solution and b) zeonex film.

Figure 5.10 shows the fluorescence decays of DPTZ-DBT, DPTZ-Me-DBT, DPTZ-ⁱPr-DBT and DPTZ-^tBu-DBT in toluene and zeonex films at room temperature. The fluorescence lifetime of DPTZ-DBT emission in toluene is *ca.* 10.3 ns,

and the fluorescence can be observed up to 60 ns. This is in clear contrast with the fluorescence decays of all substituted molecules DPTZ–Me–DBT, DPTZ–*i*Pr–DBT and DPTZ–*t*Bu–DBT, which show fluorescence lifetimes of approximately 600 ps, and where the fluorescence is observed only up to 2.5 ns. Therefore, the fluorescence decay in the substituted molecules is 17 times faster than that of DPTZ–DBT. The same trend is also observed in these four molecules when dispersed in zeonex matrix shown in Figure 5.10b, DPTZ–DBT with a fluorescence lifetime of 12.6 ns while the substituted molecules DPTZ–Me–DBT, DPTZ–*i*Pr–DBT and DPTZ–*t*Bu–DBT with lifetimes of around 600 ps. All exponential fitting parameters are listed in Tables 5.2 and 5.3.

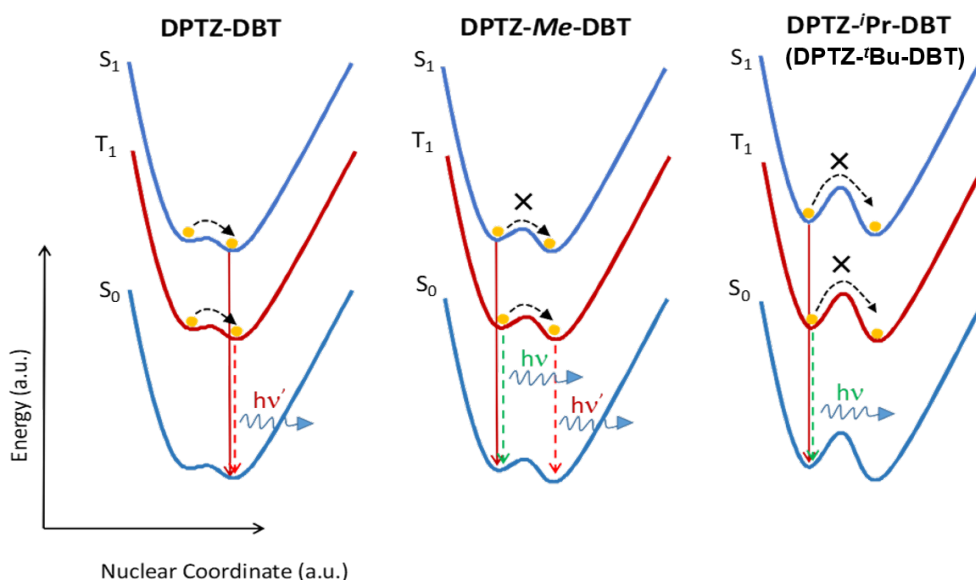


Figure 5.11: Schematic representation of the excited state relaxation in the studied molecules.

The excited state dynamics of the DPTZ–DBT derivatives studied in this chapter are summarized in a simplified scheme in Figure 5.11. As discussed in Section 5.2.2, the axial and equatorial forms are identified in both ground and excited states of DPTZ–DBT (see Table 5.1). However, both fluorescence and phosphorescence of DPTZ–DBT occur from the most stable state, which is isoenergetic with the singlet and triplet states of the PTZ unit. No emission is observed from the high energy state, even at low temperature as shown in Figure 5.9a. Therefore, the excited

state in DPTZ–DBT is able to relax to the most stable state, showing no activation barrier.

In contrast, only the axial form is identified in the ground state of DPTZ–Me–DBT, whereas both axial and equatorial forms exist in the excited state (Table 5.1). Interestingly, fluorescence occurs entirely from the higher energy state compared with that of DPTZ–DBT. This is based on the short lifetime (*ca.* 600 ps) of the singlet excited state, which promotes the decay directly to the ground state. Relaxation to the lower energy singlet state cannot compete, and so only a single fluorescence band is observed. In contrast, as the triplet state is long-lived, the relaxation to the low energy triplet is almost always possible. Therefore at high temperatures excitons in the triplet state are able to cross the barrier and give dual phosphorescence in DPTZ–Me–DBT; DBT-like phosphorescence is observed peaking at 450 nm, and PTZ–Me-like phosphorescence is observed around 540 nm. At low temperatures, this relaxation is not possible and consequently only DBT-like phosphorescence is observed. This scheme therefore reveals that the relaxation between the two triplet states involves an energy barrier separating the two states, which is thought to increase with the increasing bulkiness of the substituents. The observation of fluorescence and phosphorescence from *iso*-propyl and *tert*-butyl substituted molecules, DPTZ–*i*Pr–DBT and DPTZ–*t*Bu–DBT, confirms this scenario. In these two compounds, only the high energy fluorescence and DBT-like phosphorescence are observed (even at room temperature) as there is insufficient energy available to surmount this energy barrier.

Further evidence supporting the switching between the two excited states (probably associated with the axial and equatorial forms) of DPTZ–DBT derivatives is obtained from the time-resolved phosphorescence decays shown in Figure 5.12. In DPTZ–DBT, the switching involves a vanishingly small energy barrier and the phosphorescence decays mono-exponentially with a 47 ms time constant, from the triplet state isoenergetic with the PTZ phosphorescence (as shown in Figure 5.12a). However, for the substituted analogues, the addition of the alkyl side groups makes the switching between the high and low energy excited states sequentially more difficult as steric hindrance increases. Therefore, the phosphorescence decay of DPTZ–Me–

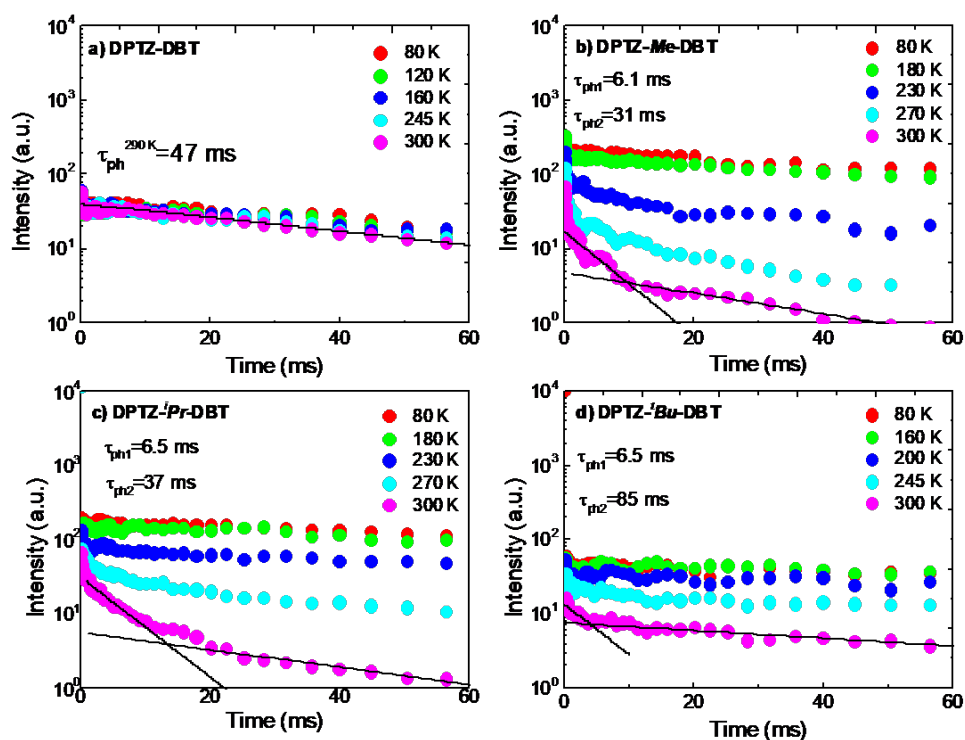


Figure 5.12: Time-resolved phosphorescence decays in zeonex obtained as a function of temperature of a) DPTZ–DBT, b) DPTZ–Me–DBT, c) DPTZ–*i*Pr–DBT and d) DPTZ–*t*Bu–DBT.

DBT in Figure 5.12b shows a double exponential profile with a fast component of 6.1 ms and a long decay component of 37 ms at 300 K. The fast component progressively disappears with decreasing temperature, becoming single exponential. The phosphorescence decays of DPTZ–*i*Pr–DBT and DPTZ–*t*Bu–DBT show similar behaviours (Figures 5.12c and d), although the fast component becomes less important in the most restricted molecule DPTZ–*t*Bu–DBT.

For the methyl and *iso*-propyl substituted compounds, the dual component of the phosphorescence decays is a 30% contribution of the fast component with a time constant around 6 ms, and a 70% contribution for the long decay component of around 35 ms. The amplitude of the fast component is larger in compound DPTZ–*i*Pr–DBT (carrying bulkier *iso*-propyl substituents), relative to the methyl substituted DPTZ–Me–DBT. In the more sterically hindered compound DPTZ–*t*Bu–DBT, the longer decay component contributes more than 91% of the phosphorescence decay,

and this is practically single exponential decaying with a time constant around 85 ms.

5.2.4 Rates and Luminescence Yields

Table 5.2: Photophysical parameters of DPTZ–DBT, DPTZ–Me–DBT, DPTZ–ⁱPr–DBT and DPTZ–^tBu–DBT in zeonex at RT.

	Φ_f	Φ_{ph}	Φ_{Lum}	τ_f	k_f	k_{ISC}^a	k_{IC}
	± 0.02	± 0.08	(Fl+Ph)	± 0.01 (ns)	$\pm 0.002 \times 10^9$ (s ⁻¹)	$\pm 0.01 \times 10^9$ (s ⁻¹)	$\pm 0.01 \times 10^9$ (s ⁻¹)
DPTZ–DBT	0.06	0.60	0.66	12.60	0.005	0.07	0.004
DPTZ–Me–DBT	0.03	0.01	0.04	0.60	0.050	1.26	0.37
DPTZ– ⁱ Pr–DBT	0.04	0.02	0.06	0.65	0.061	1.11	0.37
DPTZ– ^t Bu–DBT	0.03	0.02	0.05	0.67	0.045	0.69	0.74

^aCalculated using Φ_T determined in solution.

The photophysical parameters collected and calculated for DPTZ–DBT, DPTZ–Me–DBT, DPTZ–ⁱPr–DBT and DPTZ–^tBu–DBT in zeonex solid film are presented in Table 5.2. In zeonex, the fluorescence lifetime decreases from 12.6 ns in DPTZ–DBT to approximately 600 ps in DPTZ–Me–DBT, DPTZ–ⁱPr–DBT and DPTZ–^tBu–DBT. The marked decrease on the fluorescence lifetimes is due to the pronounced increases on the ISC and IC rates along this series. This is consistent with the increasing oscillator strength of the S₁ state obtained from the calculations in zeonex, which is 0.0017 for DPTZ–DBT, and 0.0390, 0.0442 and 0.0451 for DPTZ–Me–DBT, DPTZ–ⁱPr–DBT and DPTZ–^tBu–DBT, respectively. It is also indicative of an increase in the LE character of the emitting state. The IC rate (k_{IC}) increases consistently in the series, from 0.4×10^7 s⁻¹ in DPTZ–DBT, to 3.7×10^8 s⁻¹ in DPTZ–Me–DBT and DPTZ–ⁱPr–DBT, and 7.4×10^8 s⁻¹ in DPTZ–^tBu–DBT. The radiative rate k_f also increases, but shows no significant variation for the different substituted derivatives.

The same behaviour is observed in solution as shown in Table 5.3. The fluorescence lifetime also shows a great decrease, from 10.3 ns in DPTZ–DBT to *ca.* 600 ps in DPTZ–Me–DBT, DPTZ–ⁱPr–DBT and DPTZ–^tBu–DBT. The triplet lifetime in solution also decreases sequentially from 63.3 μ s in DPTZ–DBT to 27.6 μ s in DPTZ–Me–DBT, 6.2 μ s in DPTZ–ⁱPr–DBT and 3.5 μ s in DPTZ–^tBu–DBT

Table 5.3: Photophysical parameters of DPTZ–DBT, DPTZ–Me–DBT, DPTZ–*i*Pr–DBT and DPTZ–*t*Bu–DBT in toluene at RT.

	Φ_f	Φ_T^a	τ_f	τ_T	k_f	k_{ISC}	k_{IC}
	± 0.02	± 0.1	± 0.01 (ns)	± 0.1 (μ s)	$\pm 0.002 \times 10^9$ (s^{-1})	$\pm 0.01 \times 10^9$ (s^{-1})	$\pm 0.01 \times 10^9$ (s^{-1})
DPTZ–DBT	0.04	0.85	10.29	63.3	0.004	0.08	0.01
DPTZ–Me–DBT	0.03	0.75	0.61	27.6	0.049	1.24	0.36
DPTZ– <i>i</i> Pr–DBT	0.02	0.72	0.64	6.2	0.031	1.13	0.41
DPTZ– <i>t</i> Bu–DBT	0.02	0.47	0.66	3.5	0.030	0.72	0.77

^aMeasured in benzene.

(Table 5.3). This trend is consistent with the enhancement of the IC rate and the decrease of the phosphorescence efficiency, giving an indication of the presence of the additional vibrational modes in the substituted molecules which promote more efficient quenching of the triplet excited state population. As a result, the phosphorescence in these compounds is relatively short-lived compared to the unsubstituted DPTZ–DBT, and shows more pronounced variation with temperature (Figure 5.12). The triplet formation yield of DPTZ–DBT is also very high (85%).

The total luminescence yield determined in zeonex at room temperature is much higher in DPTZ–DBT (*ca.* $\Phi_{PF} + \Phi_{PH}=66\%$) compared to the substituted compounds, for which it is less than 6%. This is a result of the fast ISC rate and slower IC rate in DPTZ–DBT. However, the absolute fluorescence yield is low, even in DPTZ–DBT ($\Phi_{PF}=6\%$), due to the significantly faster k_{ISC} compared to the radiative rate k_f . In the substituted compounds, k_{ISC} increases significantly and becomes approximately two orders of magnitude faster than k_f , and is surprisingly fast in the methyl substituted molecule DPTZ–Me–DBT. For example, in solution, the k_{ISC} is 8.0×10^7 s^{-1} in DPTZ–DBT, 1.24×10^9 s^{-1} in DPTZ–Me–DBT, 1.13×10^9 s^{-1} in DPTZ–*i*Pr–DBT and 7.2×10^8 s^{-1} in DPTZ–*t*Bu–DBT. And in zeonex the behaviour is similar, for DPTZ–DBT $k_{ISC}=7.0 \times 10^7$ s^{-1} and in DPTZ–Me–DBT $k_{ISC}=1.3 \times 10^9$ s^{-1} . The rate constant decreases slightly with the increasing bulkiness of the substituent, along with the increasing IC rate in the substituted compounds.

To understand the influence of the alkyl substituents on the ISC rates, Fermi golden rule approximation (combined with a Marcus formalism to estimate the den-

sity of states) was used to simulate the rate of ISC:

$$k_{\text{ISC}} = \frac{2\pi}{\hbar} \left| \langle \Psi_{\text{T}} | \hat{H}_{\text{SO}} | \Psi_{\text{S}} \rangle \right|^2 \sqrt{\frac{\pi}{\lambda k_{\text{B}} T}} \exp \left(-\frac{(\lambda + \Delta E_{\text{ST}})^2}{4\lambda k_{\text{B}} T} \right). \quad (5.1)$$

Here λ corresponds to the reorganization energy, *i.e.* the energy variation in the initial singlet excited state when switching from the singlet equilibrium geometry to the triplet equilibrium geometry, while the driving force ΔE_{ST} is identified as the adiabatic singlet-triplet gap. [170] The singlet state is closest in energy to the triplet state and therefore the ISC process can occur between these states. The rates to lower triplet states were calculated, but in each case $\Delta E_{\text{ST}} > 0.15$ eV yielding very small k_{ISC} .

Table 5.4: The calculated variables required for equation 5.1 and the corresponding k_{ISC} . Due to energy considerations k_{ISC} for DPTZ–DBT was calculated in the equatorial and axial forms, while the remaining substituted compounds were calculated in their axial form.

	Conformer	SOCME (cm ⁻¹)	λ (eV)	ΔE_{ST}	$k_{\text{ISC}} \times 10^9$ (s ⁻¹)
DPTZ–DBT	Eq.	0.10	0.01	0.06	0.014
	Ax.	0.80	0.08	0.06	0.015
DPTZ–Me–DBT	Ax.	0.80	0.02	0.04	0.209
DPTZ– ⁱ Pr–DBT	Ax.	1.00	0.01	0.03	0.516
DPTZ– ^t Bu–DBT	Ax.	0.80	0.06	0.02	0.244

Calculated data obtained by evaluating equation (5.1) are shown in Table 5.4. The ISC rate is determined to be 0.014×10^9 s⁻¹ for DPTZ–DBT, and increases to 0.209×10^9 s⁻¹ for DPTZ–Me–DBT, 0.516×10^9 s⁻¹ in DPTZ–ⁱPr–DBT and 0.244×10^9 s⁻¹ in DPTZ–^tBu–DBT. This reveals calculated rates broadly consistent with the experimental observations in that k_{ISC} is larger for the substituted molecules. This is due to the smaller energy gap between the singlet and triplet states. While the trends of k_{ISC} for the substituted molecules do not exactly follow experimental observations, these differences are within the uncertainty of the calculations, which are large because the exponential dependence of λ and ΔE_{ST} in equation 5.1 magnifying any error in these values.

Finally, by comparing DPTZ–DBT with previously reported carbazole substituted analogue, 3,7-di(*N*-carbazolyl)-dibenzothiophene (DCz–DBT), [147] the influence of the sulphur atom in the PTZ units is revealed. The presence of PTZ induces a pronounced enhancement of the triplet formation yield, while showing no effect on the fluorescence yield. In the case of the PTZ H-intra conformation (equatorial form), the nitrogen lone pair is delocalized over the phenyl rings of PTZ which may explain the excellent RTP properties observed in DPTZ–DBT. Marked differences are however observed in the rate constants for radiative decay, ISC and non-radiative IC rates, all showing a pronounced decrease in DPTZ–DBT. For example, the fluorescence decay accelerates from 10 ns lifetime in DPTZ–DBT to around 0.88 ns in DCz–DBT. DPTZ–DBT can also be compared with other PTZ derivatives using the strong acceptor dibenzothiophene-*S,S*-dioxide (DBTO2) unit, where the equatorial form leads to negligible energy gap ΔE_{ST} and emergence of TADF. However, when the axial form is adopted due to the steric effect of the alkyl groups (that block the relaxation of the PTZ units in the excited-state) dual RTP instead of TADF is observed containing contributions from two triplet states matching the phosphorescence of PTZ and DBTO2. [102]

5.3 Conclusions

In summary, calculations and photophysical properties of a series of DPTZ–DBT luminophores are discussed in this chapter, providing new sights into the design of all organic RTP emitters. These results demonstrate how systematic changes in the substituents can tune the photophysical properties by conformational control. In the ground state, both equatorial and axial forms exist in DPTZ–DBT and the substituted analogues. It is demonstrated that different conformations have remarkably different photophysical properties, with the axial conformer showing enhanced ISC rate. This is accompanied by similar acceleration of the radiative and non-radiative IC rates. Switching between the electronic excited states occurs with a vanishingly small energy barrier in DPTZ–DBT. However, an increasing barrier is imposed by the presence of the bulkier side groups, and this mainly prevents the

relaxation of the singlet and triplet excited states to lower energies in these substituted molecules. The unsubstituted molecule DPTZ–DBT shows dual emission, fluorescence and strong green phosphorescence in zeonex solid film at room temperature, with a high total luminescence yield of 66%. The triplet formation yield of DPTZ–DBT is the highest in the series around 85%, and the fluorescence and phosphorescence lifetimes are relatively long-lived, 12.6 ns and 47 ms, respectively, resulting in relatively slow excited state decay rates, but dominant ISC rate.

This behaviour is markedly altered by tuning of the conformation from equatorial to axial form due to the presence of bulky side groups in the C(1)-position of each PTZ unit. All substituted molecules DPTZ–Me–DBT, DPTZ–*i*Pr–DBT and DPTZ–*t*Bu–DBT show higher singlet and triplet states, and dramatically decreased luminescence yields of *ca.* 5%. In addition, short fluorescence and phosphorescence lifetimes are observed, due to the increased radiative, ISC and IC rates. Interestingly, molecule DPTZ–Me–DBT with less bulky methyl substituents show dual phosphorescence at room temperature. This originates from a lower T_1 in the green region (2.60 eV), coinciding with the emissive triplet energy of DPTZ–DBT, and a higher T_2 in the blue region (2.88 eV), approximately the same energy of the emissive triplet in DPTZ–*i*Pr–DBT and DPTZ–*t*Bu–DBT. Interestingly, the contribution from the lower triplet state decreases with decreasing temperature, and only high energy phosphorescence is observed at 80 K as there is no sufficient energy to drive the relaxation of the excited state. The studies in this chapter show that the strategy of selective functionalization of the D unit is a viable approach to tuning the excited state properties of D–A or D–A–D molecules for RTP emission, including blue emitters.

Chapter 6

Intramolecular Charge Transfer Controls Switching Between Room Temperature Phosphorescence and Thermally Activated Delayed Fluorescence

In this chapter, a series of phenothiazine-benzophenone derivatives are studied, showing that through a simple chemical modification, the emission behaviour of triplet states can be tuned by selecting the geometry of the intramolecular charge transfer (ICT) state. A fundamental principle of planar ICT (PICT) and twisted ICT (TICT) geometries is exploited to obtain selectively for either room temperature phosphorescence (RTP) or thermally activated delayed fluorescence (TADF). Time-resolved spectroscopy and time-dependent density functional theory investigations of polymorphic single crystals demonstrate the roles of PICT and TICT states in the underlying photophysics. This is best demonstrated in RTP molecule OPM, where the triplet states contribute to 89% of the luminescence. In an isomeric TADF molecule OMP the triplet states contribute to 95% of the total emission. Electroluminescent spectra of OLED devices based on OPM and OMP also demonstrate these two mechanisms.

The work presented in this chapter is adapted from a published paper in *Angew. Chem. Int. Ed.* (C. Chen,[†] R. Huang,[†] A. S. Batsanov, P. Pander, Y.-T. Hsu, Z. Chi, F. B. Dias, M. R. Bryce, *Angew. Chem. Int. Ed.* 2018, 130, 1–6) C. Chen and R. Huang contributed equally to this work. C. Chen designed the molecules, performed the syntheses and characterizations with Y.-T. Hsu under the guidance of Z. Chi and M. R. Bryce, and also performed the theoretical calculations. R. Huang performed all the photophysical measurements under the supervision of F. B. Dias. P. Pander performed CV measurements and fabricated the devices. A. S. Batsanov performed the X-ray characterization.

6.1 Introduction

Organic luminescent materials based on donor-acceptor (D–A–D or D–A) intramolecular charge transfer (CT) emitters can efficiently harvest triplet excited states. For non-planar donors, quantum chemistry calculations suggest that specific D–A geometries facilitate different CT processes. [100, 161, 171–175] For example, different conformers of the D unit can show markedly different triplet harvesting efficiencies. [100] The quasi-axial (ax) and quasi-equatorial (eq) conformers of phenothiazine (PTZ) derivatives were computationally predicted in 2001, [157] and attracted great interest by many groups as discussed in Chapter 5. [100, 145, 164] Therefore, understanding the correlation between conformational and electronic properties becomes one of the most important issues in the chemistry of molecular luminescent materials. However, how to design molecules that promote the formation of the most efficient conformers for TADF or RTP is still a challenge.

Recently, three regimes for TADF were identified by changing the polarity of the host environment for D–A–D emitters carrying phenothiazine D units. [60] This effect arises because CT states often differ markedly in their electronic structure and molecular geometry, and are thus very sensitive to the environment surrounding the molecules. For the particular case of D–A–D and D–A derivatives carrying PTZ moieties, the CT formation involves barrierless geometrical relaxation through the rotation around the D–A single bond and planarization of the PTZ moiety in moderate and very polar solvents. In this case a twisted intramolecular CT (TICT) conformer is easily formed showing equatorial geometry, and the emission from this relaxed state exhibits a large solvatochromic shift, typical of CT states. [158]

Moreover, it has been proposed that the hybridization of the nitrogen atom in PTZ will change upon electronic excitation. In the case of complete electron withdrawal, the nitrogen can adopt a planar geometry. [158, 170] Accordingly, the development strategies that can stabilize the molecular geometry with the desirable (nearly-perpendicular) D–A arrangement in the TICT state is important. As minor changes in the structure of the substituent can induce a shift from one conformer to another, rigidity in D–A molecules can be enforced by chemical functionalization and exploited towards applications. It has been reported recently that the introduction

of bulky substituents can successfully tune the molecular steric hindrance and in turn control the conformations relevant to TADF and RTP. [176]

In this chapter, the study of a series of D–A phenothiazine-benzophenone derivatives is presented, wherein carbonyl units can provide orbitals to promote ISC from S_1 to T_n states. [95, 97] It is demonstrated that crystals with different conformers can be obtained exhibiting different triplet harvesting properties, TADF or RTP, through different crystallization methods. Moreover, the mechanism can also be tuned by the effect of methyl substituents, which impacts the steric hindrance, giving origin to different photophysical properties.

6.2 Results and Discussion

6.2.1 Chemical Characterization

Molecular Structures

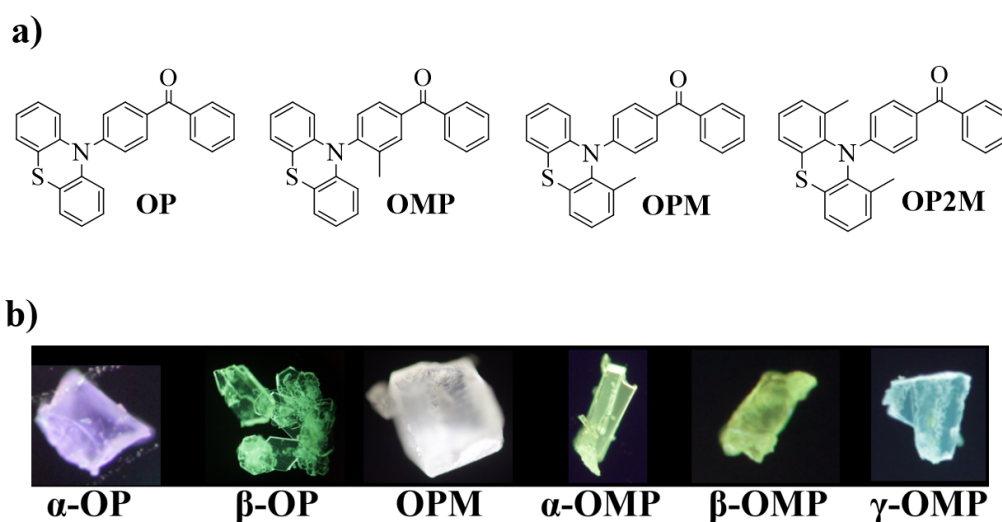


Figure 6.1: Molecular structures of a) studied molecules OP, OMP, OPM and OP2M. b) Images of α -OP, β -OP, OPM, α -OMP, β -OMP and γ -OMP crystals irradiated at 365 nm.

Figure 6.1a shows the molecular structures of the D–A derivatives studied in this chapter. 4-(*N,N*-Dimethylamino)benzophenone and its derivatives have been widely

studied to elucidate the roles of TICT and PICT states. [177] Inspired by this design principle, molecules OPM and OMP were synthesized based on a parent molecule OP, in which PTZ acts as the donor and benzophenone (BP) as the acceptor unit. OPM and OMP have a methyl substituent at a specific position on the PTZ and BP units, respectively, to provide the steric constraints and stabilize different conformations. [79, 102, 178]

Although the axial and equatorial conformers of PTZ derivatives have been widely studied, these two conformers have not previously been separated. [157, 158, 164, 178, 179] For molecule OP two very different conditions were employed to grow single crystals; a dilute solution with slow evaporation, and a saturated solution without evaporation. The axial and equatorial PTZ conformers are exclusively obtained using these two crystallization methods giving α -OP and β -OP, respectively. Emissions under irradiation of different polymorphs are shown in Figure 6.1b. In addition, two similar axial conformers were observed in the single crystals of OPM. Double methyl groups attached on the PTZ unit in OP2M strictly restrain the PTZ unit in an axial conformer. In OMP, three different polymorphs (α , β and γ) were obtained, all showing similar equatorial conformations.

X-Ray Studies

X-ray molecular structures of all single crystals are depicted in Figure 6.2. In the axial α -OP, the three C-N bonds are almost coplanar with the benzene ring of the benzophenone. The twist around the C(5)-N bond is very small (7.2°) and this bond is considerably shorter than the C-N bond within PTZ systems, average $1.396(13)$ vs. $1.429(1)$ Å. OPM shows a small torsion angle of 6.1° and a shorter C(5)-N bond ($1.400(2)$ Å). Its geometry is essentially similar with the mean PTZ folding of *ca.* 137.3° , although it is less reliable due to disorder of PTZ unit. The geometry of OP2M show similar behaviours, with negligible twisted angle (0.9°) and shorter C(5)-N bond ($1.4004(12)$ Å). However, the corresponding geometry is nearly perpendicular in the equatorial β -OP as shown in Figure 6.2b. The near-perpendicular twist around C(5)-N bond (67.1°) effectively preclude π -conjugation between the donor and acceptor fragments. This bond ($1.436(4)$ Å) is longer than C-

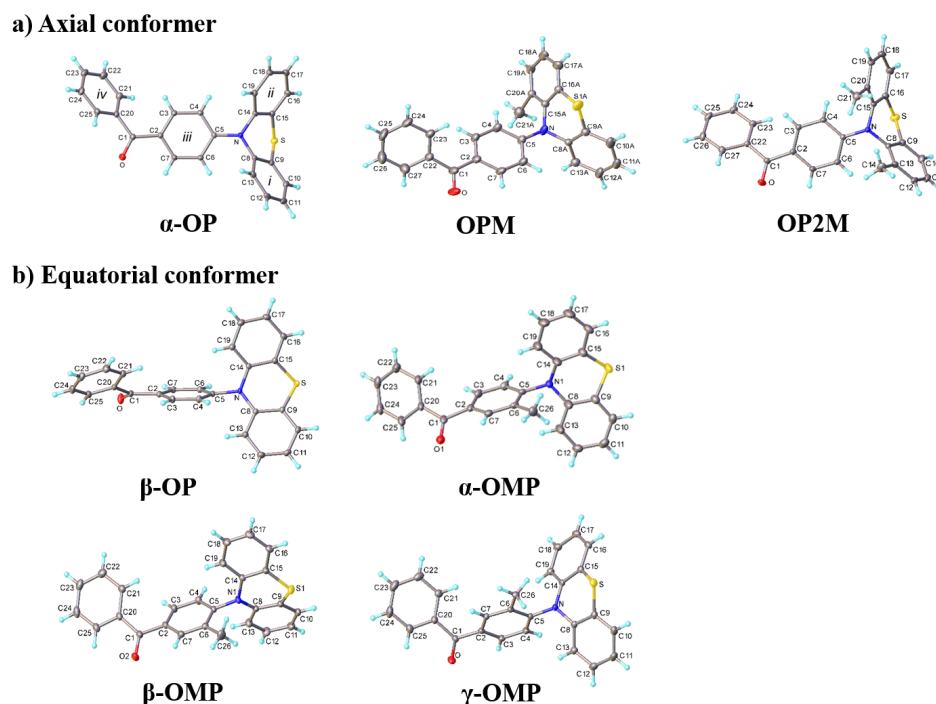


Figure 6.2: Single crystal X-ray molecular structures of α -OP, OPM and OP2M with axial conformers, and b) β -OP, α -OMP, β -OMP and γ -OMP with equatorial conformers. Thermal ellipsoids are drawn at the 50% probability level.

N bonds within phenothiazine systems (1.417(2) Å), indicating that the lone pairs of N interact predominantly with the phenothiazine rings. α -OMP and β -OMP have similar geometries to β -OP, with quasi-equatorial conformers. γ -OMP retains nearly perpendicular geometry, despite showing a different conformer.

Cyclic Voltammetry

The HOMO-LUMO energy levels of OMP and OPM were recorded by cyclic voltammetry (Figure 6.3). Ionization potential and electron affinity are calculated from oxidation and reduction potentials, respectively. The HOMO and LUMO energies of OMP are determined to be -5.34 eV and -2.98 eV, respectively. Consistent with the perpendicular geometry of OMP shown in the X-ray molecular structure, the CV data confirm that the HOMO and LUMO are mainly distributed on the D and A units, respectively. [41, 180] Thus it is demonstrated that OMP is a promising molecule for TADF. With near orthogonal D and A, a small exchange energy and

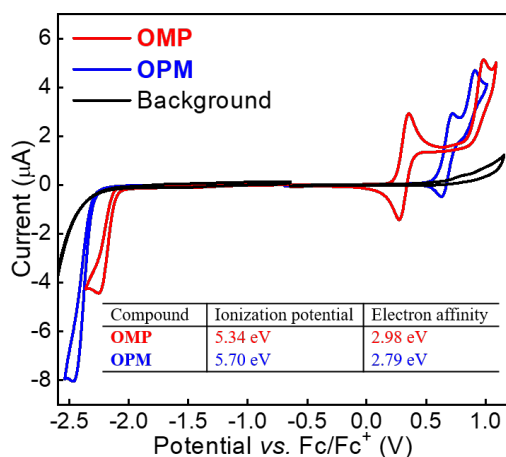


Figure 6.3: Cyclic voltammetry analysis by the estimation of the electron affinity and the ionization potentials for OMP (red) and OPM (blue) at room temperature.

singlet-triplet energy gap is obtained promoting efficient RISC. For OPM with an axial conformer, the HOMO energy level is lowered to -5.70 eV and the LUMO is elevated to -2.79 eV, which is due to the shorter C(5)-N bond and delocalized nitrogen lone pairs to the benzophenone unit that expand the HOMO distribution. The frontier orbital distributions in calculations also support these conclusions as discussed in the following section.

6.2.2 Theoretical Calculations

The frontier molecular orbitals and electronic transitions of α -OP and OPM are shown in Figure 6.4, calculated using B3LYP/6-31G*. Similar orbital distributions were obtained using M062X/6-31G*, which is another commonly used functional in TD-DFT for planar conformations, while B3LYP/6-31G* is more commonly used for TICT. The S_1 , S_2 , T_1 and T_2 of α -OP and OPM are mixed electronic states with $n\text{-}\pi^*$ (H-2 \rightarrow L) and $\pi\text{-}\pi^*$ (H \rightarrow L) transitions, involving the oxygen lone pairs (carbonyl group) and the conjugated structure, respectively. [107] The S_1 and T_2 are dominated by an $n\text{-}\pi^*$ transition, while S_2 and T_1 possess more $\pi\text{-}\pi^*$ transition character. Therefore, spin-orbit coupling occurs from $^1(n\text{-}\pi^*)$ to $^3(\pi\text{-}\pi^*)$ and from $^1(\pi\text{-}\pi^*)$ to $^3(n\text{-}\pi^*)$ because of the effective orbital overlaps according to El-Sayed's rule. [31] In addition, S_1 , S_2 , T_1 and T_2 are hybridized local and charge-transfer (HLCT) states, since H-2 \rightarrow L is assigned as an LE transition and H \rightarrow L is assigned

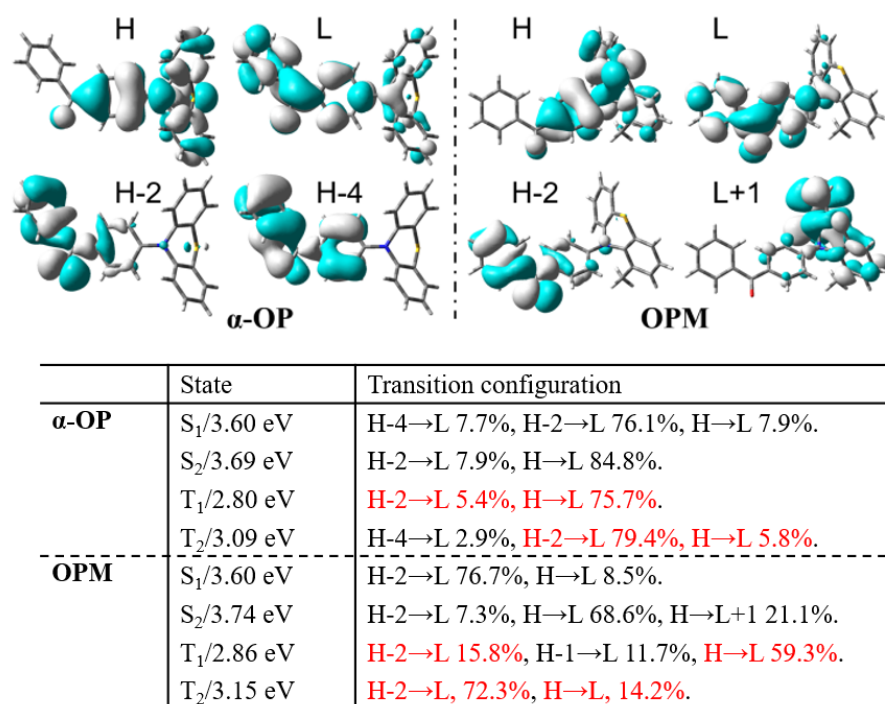


Figure 6.4: Frontier molecular orbitals of α -OP and OPM, and electronic transitions at B3LYP/6-31G* (H = HOMO; L = LUMO). The same components of S₁ are in red text.

as a CT transition. As reported for other HLCT molecules, [181] reverse intersystem crossing from upper triplet to singlet levels probably occurs in α -OP and OPM as $\Delta E_{(S_1, T_1)}$ is large (0.80 eV for α -OP and 0.74 eV for OPM). Similarly, with a higher steric hindrance, OP2M also exhibits HLCT states with mixed LE and CT electronic character and a large energy gap $\Delta E_{(S_1, T_1)}$.

The frontier molecular orbitals and electronic transitions of all equatorial conformers (β -OP, α -OMP, β -OMP and γ -OMP) are shown in Figure 6.5. It can be obviously seen that the HOMO and LUMO orbitals are effectively decoupled in all cases, while orbital expansion instead leads to more noticeable overlaps in α -OP and OPM with axial conformers. Interestingly, the ³LE emission (see Figure 6.10c) of OPM is ascribed to the contributions from the PTZ unit, according to the calculated triplet state (which shows an H→L+1 transition). Furthermore, both S₁ and T₁ show CT transitions (H→L), thus it is demonstrated that the efficient RISC model of ³CT-³LE-¹CT can be achieved in α -OMP with a small energy gap $\Delta E_{(S_1, T_1)}$ of 0.03 eV. In β -OP, β -OMP and γ -OMP, small energy gaps $\Delta E_{(S_1, T_1)}$ are obtained

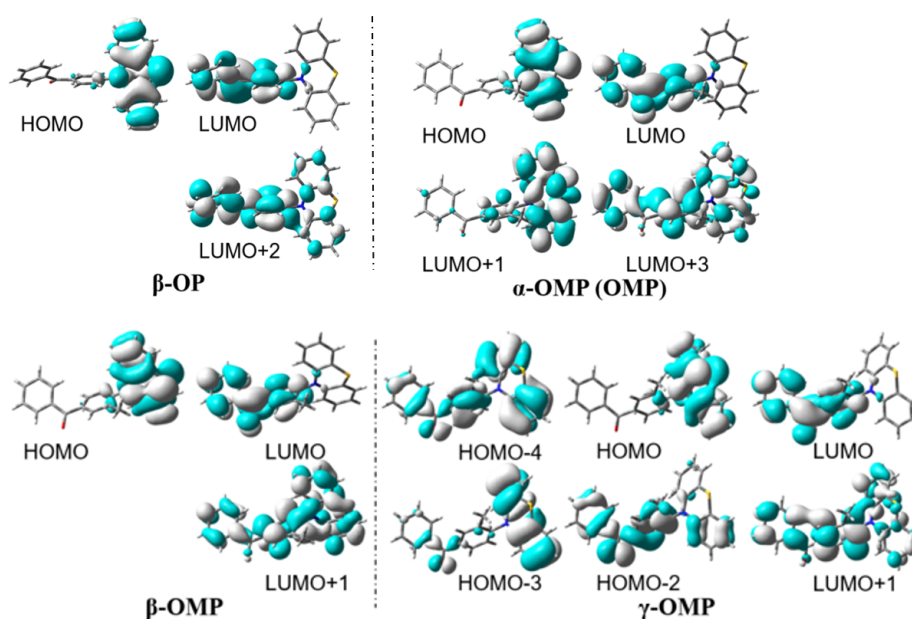


Figure 6.5: Plots of visualized orbitals based on the single crystal geometry of β -OP, α -OMP and β -OMP and γ -OMP; positive electron density in grey and negative in blue (B3LYP/6-31G*).

with 0.05 eV, 0.04 eV and 0.07 eV, respectively, which can efficiently facilitate the RISC rate. The $\Delta E_{(S_1,S_2)}$ of α -OP was calculated to be 0.09 eV, which is a negligible gap that favours the vibronic coupling between S_1 and S_2 states. Therefore, a mutually perpendicular D–A geometry is required for the typical TICT model, whereas in the PICT model, a relatively small energy gap $\Delta E_{(S_1,S_2)}$ plays a more critical role in the ICT process, rather than the co-planarity of the D–A moieties.

6.2.3 Photophysical Properties

Steady-State Photoluminescence

Photophysical properties of the derivatives were analyzed in solutions using ultraviolet-visible (UV–Vis) and photoluminescence (PL) spectroscopies. Figure 6.6 shows the absorption spectra of OP, OPM, OP2M and OMP in diluted toluene solutions, along with their individual fragments. In OP, the absorption band peaking at 330 nm is ascribed to a π - π^* transition. A slightly red-shifted tail around 400 nm (observed in neither the BP nor PTZ unit) can be assigned as a CT absorption band. The

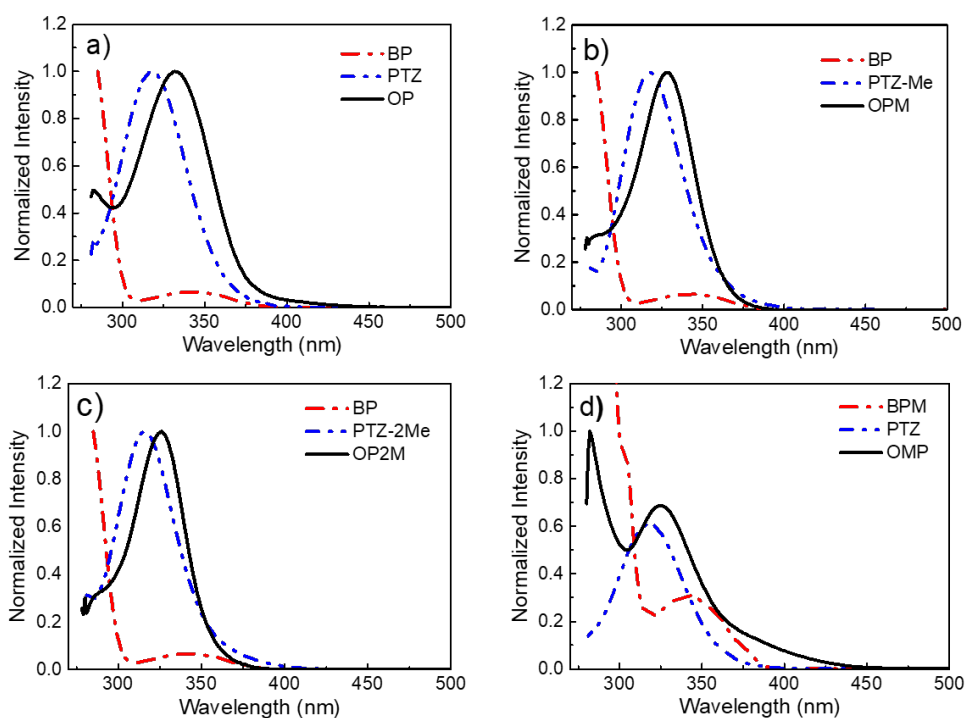


Figure 6.6: UV-Vis absorption spectra of a) OP, b) OPM, c) OP2M and d) OMP in diluted toluene solutions (1.0×10^{-5} M) at room temperature. The spectra of their individual units are shown for comparison.

X-ray and calculation sections indicate that OP crystals have two conformers - axial and equatorial. In solutions, as there are more freedom for molecules to rotate and vibrate to the most stable and lowest energy state, the H-intra conformation (equatorial) of PTZ is stabilized and more of the bridging nitrogen lone pair couples into the donor increasing the $n-\pi^*$ character. This leads to a decreased oscillator strength of the lowest energy transition and a more pronounced redshift.

However, the CT character is reduced with the introduction of the methyl groups on the donor units in OPM and OP2M. When the methyl group is substituted on the PTZ unit, the relaxation of the PTZ unit is restrained, resulting in a greater degree of H-extra folding of the PTZ. With further increased steric hindrance, doubly methylated OP2M is strictly restricted to an axial conformer, and the CT character is completely suppressed.

Substituting the acceptor BP unit with a methyl group, OMP shows a more obvious red-shifted absorption band (in the range of 380 nm to 450 nm shown in

Figure 6.6d), indicating a stronger CT character compared with that of OP. This behaviour can be linked to the H-intra folding of PTZ localizing the lone pair of nitrogen, giving stronger decoupling of the donor and acceptor units.

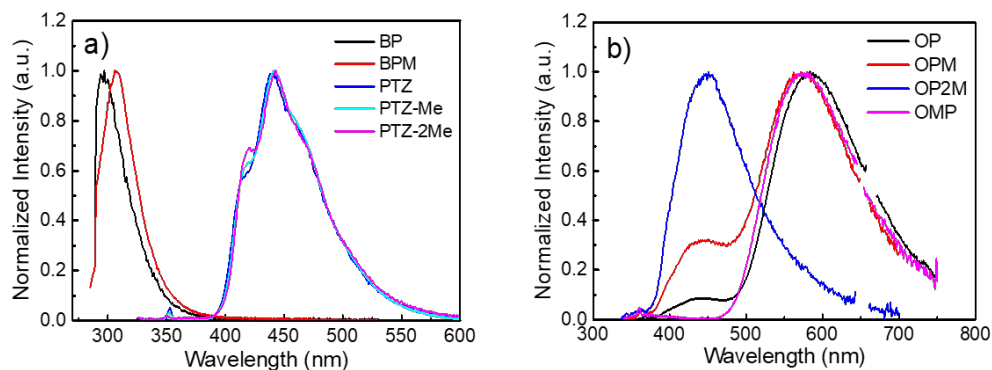


Figure 6.7: Photoluminescence spectra of a) the individual units: BP, BPM, PTZ, PTZ-Me and PTZ-2Me and b) OP, OPM, OP2M and OMP in diluted toluene (1.0×10^{-5} M) at room temperature. The second-harmonic peak at *ca.* 660 nm from the excitation beam has been removed in Figure b.

Figure 6.7 shows the emission spectra of the individual moieties and compounds in diluted toluene solutions at room temperature. Dual fluorescence emission bands are observed in OP and OPM. The emission band peaking around 450 nm matches well with that of the PTZ unit, which is assigned to the $^1\text{LE}_D$ state. The redshifted emission band peaking around 583 nm occurs from the ^1CT state, evidenced by the Gaussian band shape and a strong redshift compared to the individual D and A spectra. Dual fluorescence reveals that the radiative recombination from $^1\text{LE}_D$ can compete with electron transfer that populates the ^1CT state, indicating a weak electronic coupling between the donor $^1\text{LE}_D$ state and the molecular CT state. By substituting a methyl group on the PTZ unit in OPM, the contribution from $^1\text{LE}_D$ increases. Only emission from $^1\text{LE}_D$ is observed in OP2M, in which the CT character is completely restrained. In contrast, OMP exclusively shows a CT emission, indicating electron transfer from the $^1\text{LE}_D$ to ^1CT state fully out-competing $^1\text{LE}_D$ emission.

The contribution of triplet excited states to the overall emission was determined by comparing the emission intensity of all compounds in zeonex films in air and vacuum as shown in Figure 6.8, with atmospheric oxygen as an effective triplet

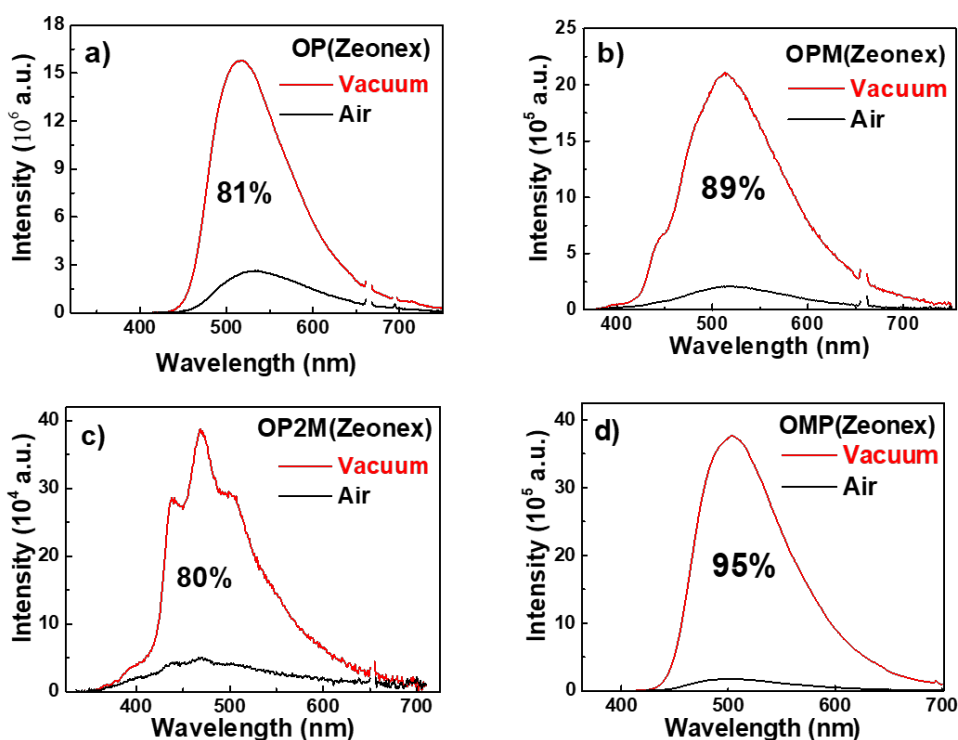


Figure 6.8: Steady-state emission in vacuum and air of a) OP, b) OPM, c) OP2M and d) OMP in zeonex films at room temperature. The % figures are the decrease in emission intensity in air.

quencher. [23] It is observed that triplet states contribute 81% and 95% of the OP and OMP luminescence, respectively. The larger contribution of DF in OMP indicates an efficient repopulation of the ^1CT state from the triplet state *via* a RISC process. In contrast, no CT is formed in both OPM and OP2M films, as zeonex is a rigid and non-polar polymer matrix. Well-resolved structured emission spectra are instead obtained for OPM and OP2M films, with the triplet contributions of 89% and 80%, respectively, attributed to RTP.

Time-Resolved Spectroscopy of Crystals

In solution and solid-state films, molecules tend to stabilize towards the lowest energy conformation. Although α -OP and β -OP crystals show almost equal energies (0.04 eV difference), they show completely different conformations. With the introduction of a methyl group at specific positions, OPM and OMP crystals are obtained with rigidified conformers and stabilized PICT and TICT states, respectively. The

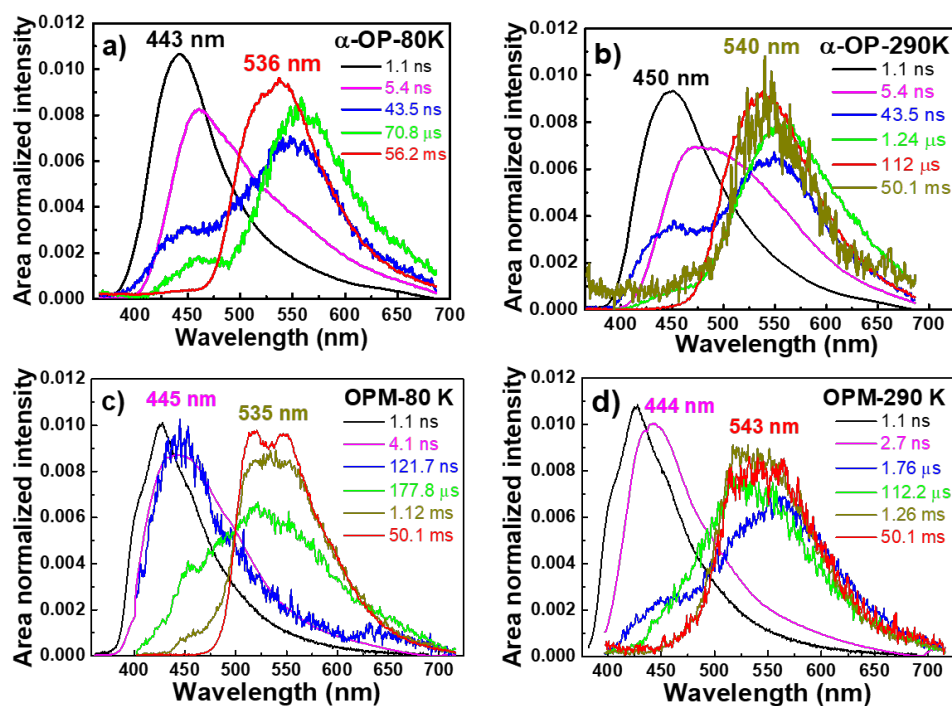


Figure 6.9: Time-resolved area normalized spectra of α -OP crystals at a) 80 K, b) 290 K; and of OPM crystals at c) 80 K, d) 290 K. Excitation wavelength at 355 nm.

attempt to explain the different photophysical properties obtained based on one selected conformation in solution or matrix is unsatisfactory as they all show mixed conformers. [158]

To investigate the PICT and TICT states, time-resolved spectroscopy was employed to measure the luminescence of crystals from 80 K to 290 K. Figures 6.9a and b show the area normalized spectra of α -OP at 80K and 290 K, respectively. At early delay time, a spectrum in the blue region is observed, matching the emission from the $^1\text{LE}_D$ state. With increasing delay times, a CT band emerges (up to 70.8 μs at 80 K and 1.24 μs at 290 K), giving a clear indication of the RISC process from triplet to singlet states. This dual emission of α -OP originating from the LE and CT states is in accordance with the PICT model. [177, 182] Since dual emission is very common in the PICT model, α -OP emits blue at around 450 nm and yellow at 540 nm, hinting at applications for white light emission from a single organic molecule. The α -OP geometry favours the $n\text{-}\pi^*$ transition of the carbonyl group and hence facilitates the ISC process. Meanwhile, the hybridized $n\text{-}\pi^*$ and $\pi\text{-}\pi^*$ orbital configurations in α -OP activates the radiative transition from T_1 to S_0 ,

leading to the efficient phosphorescence when rigidified in the crystalline state, even at room temperature.

Figure 6.9c shows that a blue emission (445 nm) in OPM exhibits an LE character from the PTZ unit. At later delay times, a well-resolved emission (540 nm) is clearly observed at both 80 K and 290 K, indicating the contribution of phosphorescence from the ^3LE state. Generally, it can only be observed in frozen conditions (*e.g.* 80 K) or in a restricted environment. The obvious RTP in crystalline OPM implies that the substituted methyl group in the PTZ unit locks the conformation into a PICT geometry, which also minimizes the non-radiative deactivation processes of triplet excitons. Similar behaviours are observed in further rigidified OP2M, which is also evidenced by the LE emission even in toluene solution and zeonex film (Figure 6.8).

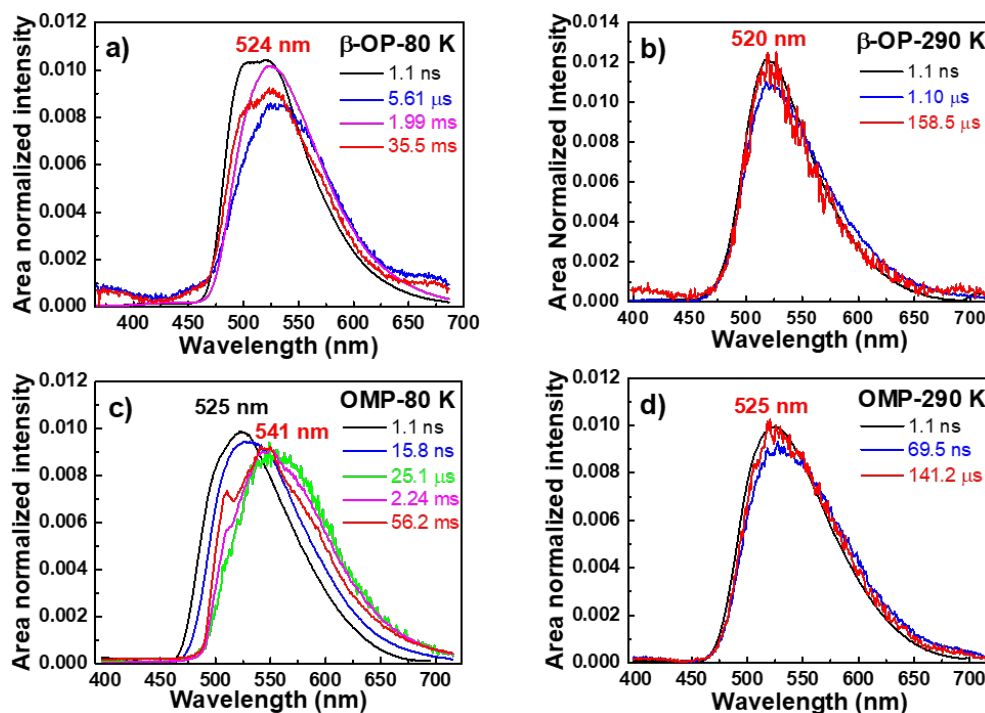


Figure 6.10: Time-resolved area normalized spectra of β -OP crystals at a) 80 K, b) 290 K; and of OMP (α -OMP) crystals at c) 80 K, d) 290 K at room temperature. Excitation wavelength at 355 nm.

In contrast to α -OP and OPM, both β -OP and OMP show fully typical TADF emission as shown in Figure 6.10. Figure 6.10a exhibits the emission spectra of β -OP peaking at 524 nm in nanoseconds and early microseconds at 80 K, which is associated with the ^1CT state. The well-resolved triplet emission comes from the

$^3\text{LE}_\text{D}$ state, matching well with the phosphorescence of the PTZ unit taken from the same experimental conditions. At 290 K (Figure 6.10b), the DF spectra of β -OP are perfectly overlapped with the prompt emission (shape and position) in the entire region of analyses, indicating the emission in both regions (PF and DF) comes from the same transition, $^1\text{CT}\rightarrow\text{S}_0$. The DF contribution is stronger at high temperatures, due to the increased thermally activated energy for efficient RISC process.

As depicted in Figures 6.10c and d, OMP shows similar behaviours as β -OP. At 80 K the slightly red-shifted emission compared to the PF is ascribed to energy relaxation of the ^1CT state. With increasing delay times the contribution from the $^3\text{LE}_\text{D}$ state dominates. Overlapped PF and DF spectra are observed in the whole range at 290 K, indicating TADF not RTP.

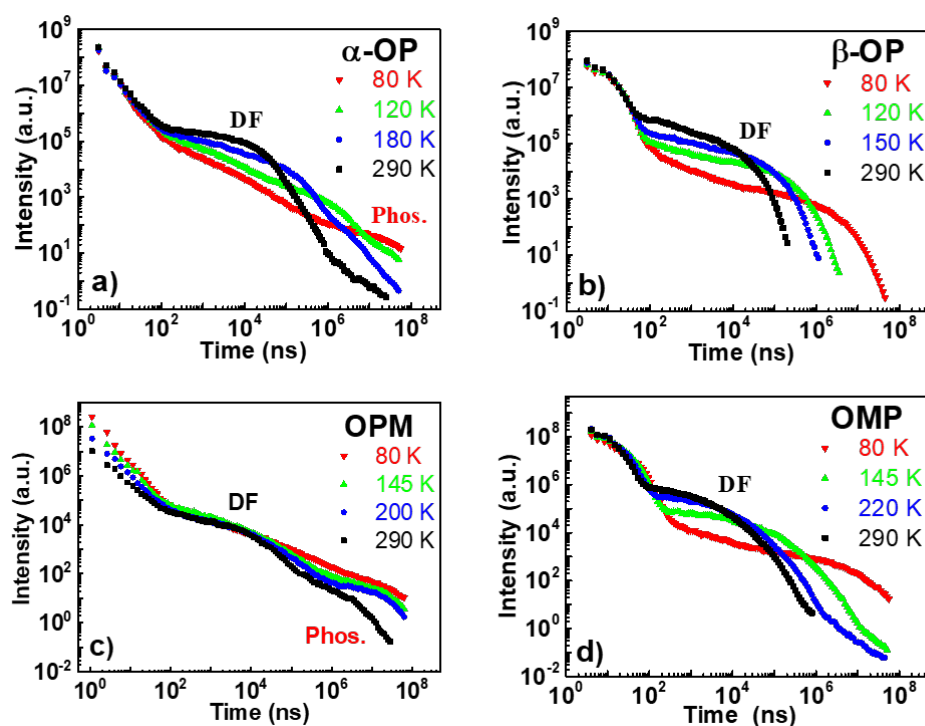


Figure 6.11: Time-resolved temperature dependent decays of a) α -OP, b) β -OP, c) OPM and d) OMP (α -OMP) crystals from 290 K to 80 K. Excitation at 355 nm.

The time-resolved temperature dependent decays of α -OP, β -OP, OPM and α -OMP were plotted from 80 K to 290 K in Figure 6.11. As shown in Figure 6.11a, three components (PF, DF and phosphorescence) are observed in α -OP.

The nanosecond fast PF component is independent of temperature, as it is a radiative direct decay from the singlet excited state. In contrast, DF and phosphorescence components show clear and opposite temperature dependence. The intensity of DF increases with the increasing temperature, indicating a TADF mechanism, while the phosphorescence shows opposite variation, *i.e.* increasing in intensity at low temperatures.

Since the methyl substituent in OPM suppresses non-radiative pathways by rigidifying the structure, triplet excitons are stabilized. Consequently, a gradual decay of phosphorescence is observed (Figure 6.11c), revealing the RTP mechanism. Accordingly, it is proposed that the hybridized $n-\pi^*$ and $\pi-\pi^*$ transitions in the triplet states of α -OP and OPM are the key to activating phosphorescence. Since α -OP and OPM are PICT systems with two singlet states (S_1 and S_2) that are very close in energy, the PICT model is demonstrated to be a new design strategy for RTP after rigidifying the geometry. Figure 6.11b shows the gradual DF decay component of β -OP with a very sensitive temperature response. This TICT molecule therefore presents efficient TADF with a small energy gap $\Delta E_{(S_1,T_1)}$ of 0.05 eV. Analogously, OMP (α -OMP) with similar TICT geometry to β -OP also exhibits efficient TADF as shown in Figure 6.11d.

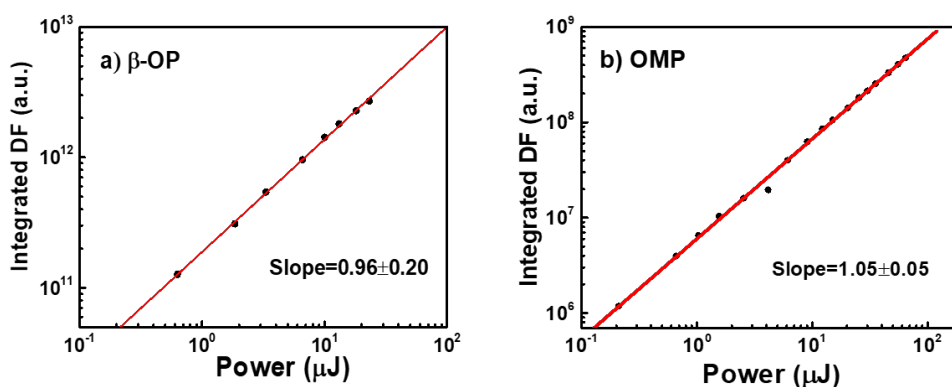


Figure 6.12: The DF intensity dependence on laser power of a) β -OP with delay and integration times of 200 ns and 200 μ s, respectively; b) OMP with delay and integration times of 200 ns and 800 μ s, respectively. Excited at 337 nm at room temperature.

To get a better understanding of the DF emissive processes involved, the intensity dependence of the DF emission of β -OP and OMP was analysed as a function of the

laser power as shown in Figure 6.12. The order of DF mechanism (1 for TADF and PH, 2 for TTA) can be determined. A strictly linear proportionality is observed in both β -OP and OMP, with gradients of 0.96 and 1.05, respectively. This indicates a single photon process, where one exciton is upconverted from triplet to singlet excited state to yield one delayed output photon. In TTA, the DF dependence will instead be quadratic with the laser power, as two triplet excitons are required for each DF photon created. Thus, the TADF mechanism is confirmed in both crystalline β -OP and OMP.

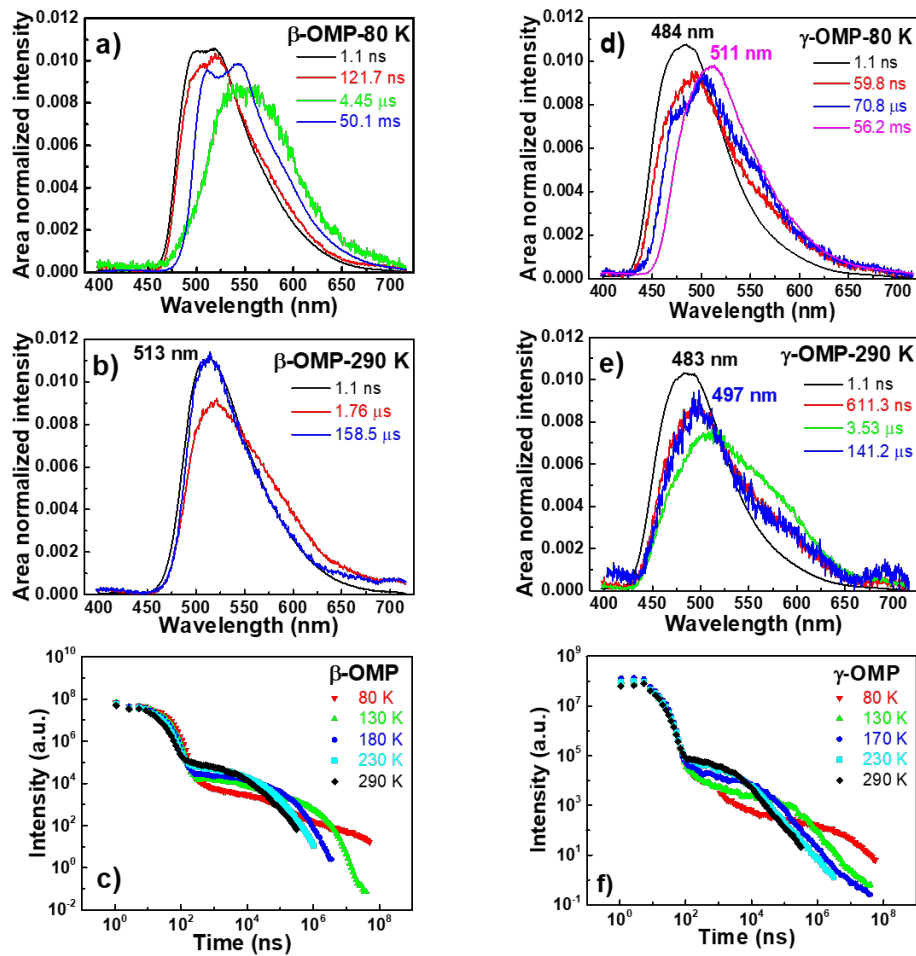


Figure 6.13: Time-resolved area normalized emission spectra of crystals: β -OMP a) at 80 K, b) 290 K and c) temperature dependence of emission decay over a temperature range from 290 K to 80 K; γ -OMP d) at 80 K, e) at 290 K and f) temperature dependence of emission decay over a temperature range from 290 K to 80 K.

The two other polymorphs of OMP (β -OMP and γ -OMP) were also studied using time-resolved spectroscopy as shown in Figure 6.13. With a similar geometry

to α -OMP, β -OMP shows a clear TADF mechanism. Interestingly, γ -OMP retains a nearly perpendicular geometry (Figure 6.2), despite showing a different conformer. Therefore γ -OMP also exhibits a very sensitive temperature response in the DF decay component. Consequently, it is demonstrated that the TICT model is strictly controlled with the substituting methyl group on the acceptor unit, and hence the TADF properties are effectively retained.

6.2.4 Device Performance

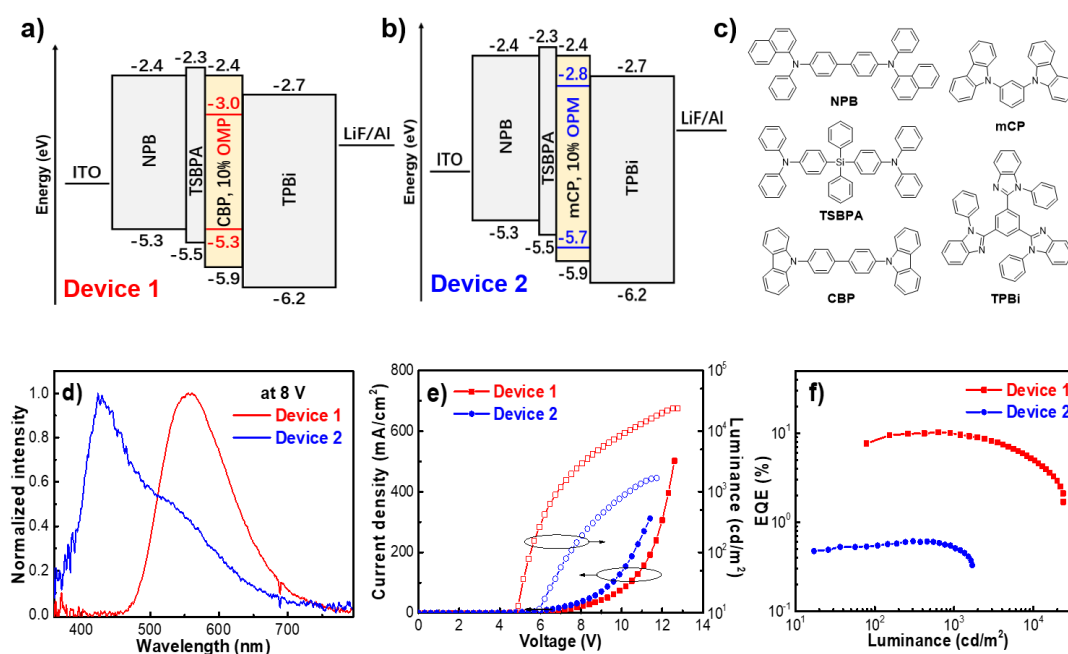


Figure 6.14: Energy level diagrams showing the HOMO/LUMO levels and structures of a) Device 1 based on OMP as an emitter and b) Device 2 based on OPM. c) Molecular structures of materials used in OLEDs. d) EL spectra of devices operating at 8 V. e) Current density-voltage-luminance characteristics. f) EQE *vs.* luminance characteristics.

To further demonstrate the triplet harvesting mechanism in the TICT and PICT models, two OLED devices were fabricated using OMP and OPM as the emitters. The energy levels and device structures are shown in Figures 6.14a and b. The device architecture is ITO/ α -NPd (40 nm)/TSBPA (10 nm)/host:10% emitter (20 nm)/TPBi (50 nm)/LiF/Al. *N,N'*-Di(1-naphthyl)-*N,N'*-diphenyl-(1,1'-

biphenyl)-4,4'-diamine (α -NPD), 4,4'- (diphenylsilanediyl)bis(*N,N*-diphenylaniline) (TSBPA) and 2,2',2''-(1,3,5-benzinetriyl)-tris(1-phenyl-1-*H*-benzimidazole) (TPBi) were employed as hole-injecting, hole-transporting and electron-transporting layers, respectively. In devices 1 and 2, 4,4'-bis(carbazol-9-yl)biphenyl (CBP) and (1,3-bis(carbazol-9-yl)benzene) (mCP) are used as hosts for OMP and OPM, respectively.

Table 6.1: Summary of OLED device characteristics.

	V_{on}^a (V)	λ_{max}^b (nm)	L_{max}^c (cd/m ²)	EQE (%)			η_{CE}^d (cd/A)		
				Max.	10 mA/cm ²	100 mA/cm ²	Max.	10 mA/cm ²	100 mA/cm ²
1	3.5	558	23800	10.2	8.6	4.5	29.6	24.6	12.8
2	4.8	427	1700	0.6	0.5	0.6	1.0	0.8	0.9

^aTurn-on voltage at brightness of 10 cd/m². ^bThe peak of EL spectra. ^cThe maximum value of brightness. ^dCurrent efficiency.

Figures 6.14d, e and f present the electroluminescence (EL) spectra, current density-voltage-luminance characteristics and EQE-luminance plots of the fabricated devices. All EL characteristics are summarized in Table 6.1. Device 1 based on TADF OMP produces a greenish-yellow emission peaking at 558 nm with a low turn-on voltage of 3.5 V at luminance of 10 mA/cm². In addition, a maximum current efficiency of 29.6 cd/A, a high EQE of 10.2% and a maximum luminance up to 23800 cd/cm² without any light out-coupling enhancement are achieved, indicating a triplet harvesting mechanism by TADF. With increasing luminance, the EQE decreases, which is attributed to the excess triplet excitons in the emitting layer causing exciton quenching by TTA or other annihilation processes.

Interestingly, dual emission is observed in Device 2 with RTP OPM as an emitter, peaking at 427 nm with a shoulder band around 540 nm. According to the photophysical results, it is proposed that the EL spectrum of Device 2 involves RTP, which is from the contribution of the ³LE_D state in OPM. Device 2 shows a relatively high turn-on voltage of 4.8 V, a low current efficiency of 1.0 cd/A and a low EQE of 0.6% at maximum. The low efficiency is associated with the RTP mechanism. However, it provides a great potential to design single layer white OLEDs.

6.3 Conclusions

In summary, this chapter presents the molecular design, theoretical calculations, photophysical properties and device performance of a series of phenothiazine-benzophenone derivatives. It is demonstrated that the axial conformer α -OP and equatorial conformer β -OP are ideal PICT and TICT model systems, respectively. Based on TD-DFT calculations and photophysical spectra, the PICT model is proposed as a new design strategy for obtaining RTP. Molecular modification is exploited to enforce rigidity in D-A molecules. By selectively attaching a methyl group onto specific positions on the OP molecules, the molecular geometry is stabilized either with the PICT conformation in OPM, or the TICT geometry in the isomer OMP. OPM with PICT geometry shows a large singlet-triplet energy gap and a strong LE character, while the perpendicular TICT geometry in OMP shows effective separation of the HOMO and LUMO distributions, giving rise to a very small optical energy gap and efficient RISC process. This rational conformational control leads to an efficient utilization of the triplet states by RTP in OPM and by TADF in OMP.

The different triplet harvesting mechanisms of PICT and TICT are also confirmed in OLED devices. White light emission from OPM is a result of dual emissive processes according to the PICT mechanism involving RTP, with a low EQE of only 0.6%. The device using OMP as an emitter achieves a low turn-on voltage of 3.5 V and a maximum EQE of 10.2%, which is ascribed to the efficient RISC process associated with the TADF mechanism.

Chapter 7

Achieving Highly Efficient Deep-Blue TADF Emitters by Subtly Tuning Donor Strength with Unconventional Electron-Rich Acceptor

Manipulation of the emission properties of deep-blue emitters exhibiting thermally activated delayed fluorescence (TADF) through molecular design is desirable yet challenging due to the complexity of the TADF mechanism. This chapter presents a simple but effective strategy to probe deeper into the role of localized (LE) and charge transfer (CT) states in the reverse intersystem crossing (RISC) mechanism. The electron-rich dibenzothiophene functionality with high triplet energy is used as an unconventional acceptor. Derivatives of 9,10-dihydro-9,9-dimethylacridine are used as electron-donors in a series of donor-acceptor-donor (D-A-D) blue emitters. The introduction of *tert*-butyl and methoxy substituents in the appropriate *para*-positions of the donor unit greatly enhances the donor strength, which allows us to explore different energy alignments among CT and LE triplet states. In the *tert*-butyl substituted compound the low energy triplet is localized on the acceptor unit, with the RISC mechanism ($k_{\text{RISC}}=0.17\times 10^5 \text{ s}^{-1}$) probably involving the mixture

of ^3CT and ^3LE states that are separated by less than 0.09 eV. However, when methoxy substituents are used, the low-energy triplet state moves away from the emissive ^1CT singlet, increasing the energy gap to 0.24 eV. Despite of the large gap, a faster RISC rate ($k_{\text{RISC}}=2.28\times 10^5 \text{ s}^{-1}$) is obtained due to the upper-state RISC occurring from the high-energy triplet state localized on the D (or A) units. This work shows the importance of fine-tuning the electronic interactions of the D and A units to control the TADF mechanism and achieve desirable deep-blue TADF emitters.

This work is submitted to *Journal of Materials Chemistry C*. R. Huang carried out the photophysical and electrochemical characterization of all compounds under the supervision of F. B. Dias. N. A. Kukhta and J. S. Ward synthesized the studied compounds under the supervision of M. R. Bryce. N. A. Kukhta performed the DFT calculations. A. Danos performed and interpreted PLQY measurements with R. Huang. A. S. Batsanov carried out the X-ray analysis.

7.1 Introduction

A multitude of various colour TADF emitters have been reported to date. [68, 69, 74, 78, 146, 183, 184] The majority are composed of well-decoupled donor (D) and acceptor (A) units, which create excited states with strong charge transfer (CT) character. This molecular design works remarkably well for the preparation of red, green and even sky-blue TADF emitters. [68, 70–73] However, developing design rules to effectively match D and A units in order to maximize TADF emission and simultaneously achieve fast radiative decay rates remain challenging, especially in the deep-blue region most desirable for applications. [75, 78, 185] A small singlet-triplet energy gap (ΔE_{ST}) requires careful consideration and matching of electron D and A strengths, but emission with strong CT character is almost inevitably shifted to longer wavelengths and shows slow radiative decay rate. In contrast, with weaker D or A units the CT excited states are created with more blue emission and faster radiative rates, but a larger ΔE_{ST} is created due to a large HOMO–LUMO overlap and a slower RISC rate is obtained. This results in longer-lived triplet excited states that are more susceptible to suffer from luminescence quenching, leading to pronounced efficiency roll-off and potential device instability.

Despite the current reasonable understanding of the RISC mechanism, many aspects are still unclear. In particular, the role of localized triplet and charge transfer states is not comprehensively understood. In this chapter, a new strategy to design an efficient deep-blue TADF emitter is presented. The new emitter (DAc–DBT) has the unconventional dibenzothiophene (DBT) unit as a weak electron acceptor and 9,10-dihydro-9,9-dimethylacridine (Ac) derivatives as the donor units in a D–A–D configuration. The strategy was to align both the localized triplet states of the donor and acceptor (3LE_D and 3LE_A , respectively) and the singlet 1CT emissive states of the DAc–DBT molecule, to generate deep-blue TADF with high efficiency. DBT is renowned for its rigid planar structure, narrow emission spectrum and strong intersystem crossing (ISC) properties due to the existence of the sulphur atom. [100] DBT is thus expected to enhance ISC/RISC rates. Moreover, the DBT fragment was utilized previously as an electron acceptor in a series of carbazole-based host materials, [186] but we are not aware of its previous use as an acceptor in TADF

emitter materials. As both DBT and Ac units possess similar triplet levels, both ${}^3\text{LE}_\text{D}$ and ${}^3\text{LE}_\text{A}$ are expected to participate in the RISC mechanism for highly efficient triplet-harvesting. The fine-tuning of the donor strength by substitution on the Ac units allows the modulation of the CT energy to probe varying energy alignments between LE and CT states. Investigations into how the different states contribute to RISC are presented. Clear evidence for upper-state crossing from a local-triplet state to the singlet charge transfer manifold is observed in a methoxy substituted analogue, giving origin to a fast RISC rate although with the lowest ${}^3\text{LE}$ state acting as a trap.

7.2 Results and Discussion

7.2.1 Chemical Characterization

Molecular Structures

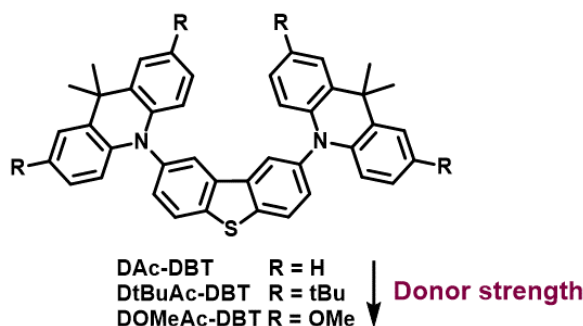
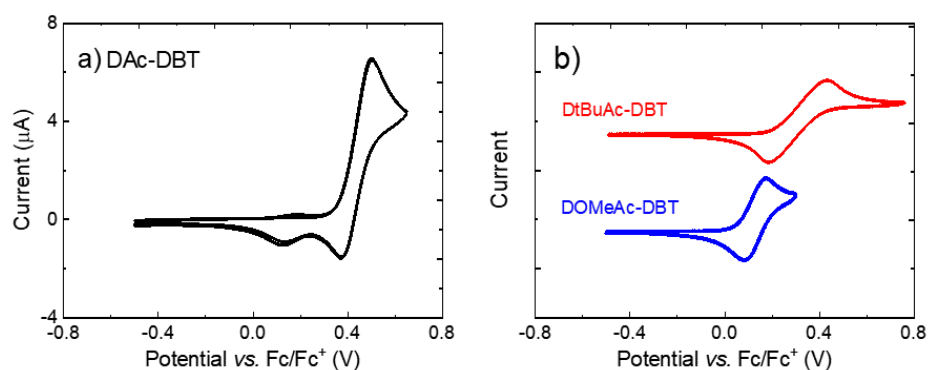


Figure 7.1: Molecular structures of the studied compounds.

The molecular structures of the DAC-DBT derivatives are presented in Figure 7.1. The design of DAC-DBT derivatives is inspired by the molecules studied in Chapter 5, which used DBT as the A unit and phenothiazine (PTZ) as the D to promote efficient room-temperature phosphorescence. [100] The fast ISC rate [147] and high triplet level [100] of DBT aligned with the singlet ${}^1\text{CT}$ state of DPTZ-DBT, efficiently populates a lower triplet state localized on the PTZ unit resulting in an inefficient RISC rate. This previous rationale of aligning the singlet and triplet

energies of the D and A constituents is extended to the DAc-DBT derivatives. This strategy has facilitated RISC, promoted high TADF efficiency and shifted the emission into the deep-blue region. Firstly, the low triplet level of PTZ was replaced by a high triplet Ac unit to achieve a small ΔE_{ST} . Secondly, the donor strength of the Ac unit was tuned by donor substitution with *tert*-butyl and methoxy groups, which simultaneously protect the 2,8-positions of Ac to enhance the chemical and electrochemical stability. The 1CT state of DAc-DBT is aligned with its triplet excited states localized on the Ac and DBT units, thereby promoting fast ISC/RISC rates.

Cyclic Voltammetry



Compound	HOMO (eV)	LUMO (eV)	E_g (eV)
DAc-DBT	-5.45	-2.18	3.27
DtBuAc-DBT	-5.31	-2.15	3.12
DOMeAc-DBT	-5.15	-2.05	3.10

Figure 7.2: Cyclic voltammograms of a) DAc-DBT, b) DtBuAc-DBT and DOMeAc-DBT at concentrations of 1 mM.

The HOMO and LUMO energy levels of the three compounds were recorded by cyclic voltammetry (CV) as shown in Figure 7.2. For DAc-DBT, a new peak is observed on the reverse scan at a lower potential, which probably results from molecular degradation or reaction leading to the formation of a conducting layer on the working electrode. This peak was not observed in the substituted molecules

(DtBuAc-DBT and DOMEAc-DBT), suggesting that its origin may be the reactivity at the 2,8-positions of acridine. Similar behaviour was also observed in other unsubstituted acridine derivatives, pointing to the lack of the electrochemical stability. [187] Moreover, the HOMO energies are elevated with the increasing donor strength with DAc-DBT (-5.45 eV) < DtBuAc-DBT (-5.31 eV) < DOMEAc-DBT (-5.15 eV) while the LUMO shows a slight change.

7.2.2 Theoretical Calculations

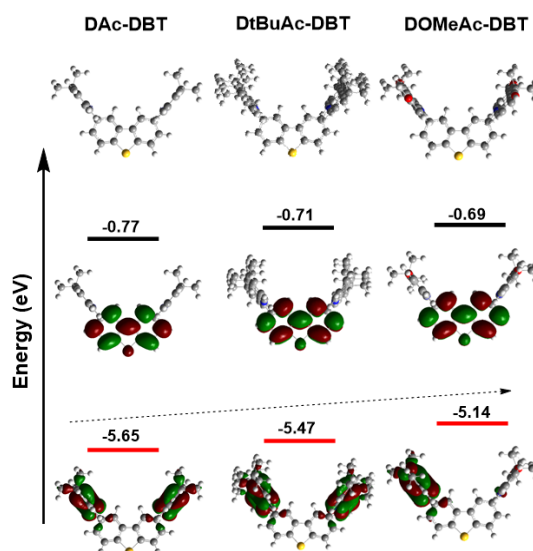


Figure 7.3: Optimized molecular geometries with HOMO (red) and LUMO (black) levels and energies of DAc-DBT, DtBuAc-DBT and DOMEAc-DBT (rBMK/6-31G(d) level of theory).

DFT calculations were carried out at the rBMK level of theory. [188] The BMK functional was preferred for the geometry optimization and prediction of the optical properties for the description of the low energy absorption band of D-A CT compounds. [188–190] As shown in Figure 7.3, the overall geometry of the DAc-DBT derivatives is determined by the rigid skeleton of the DBT acceptor, to which planar Ac donors are attached almost orthogonally. The HOMO and LUMO are effectively decoupled in all cases, but with the HOMO expanding slightly onto the DBT unit with the addition of the electron donating substituents. The HOMO lev-

els of all three compounds increase, while the LUMOs are localized solely on the DBT unit and remains almost unchanged. This is consistent with the CV measurements, which leads to a lower energy of the CT state in DOMEAc-DBT compared to DtBuAc-DBT.

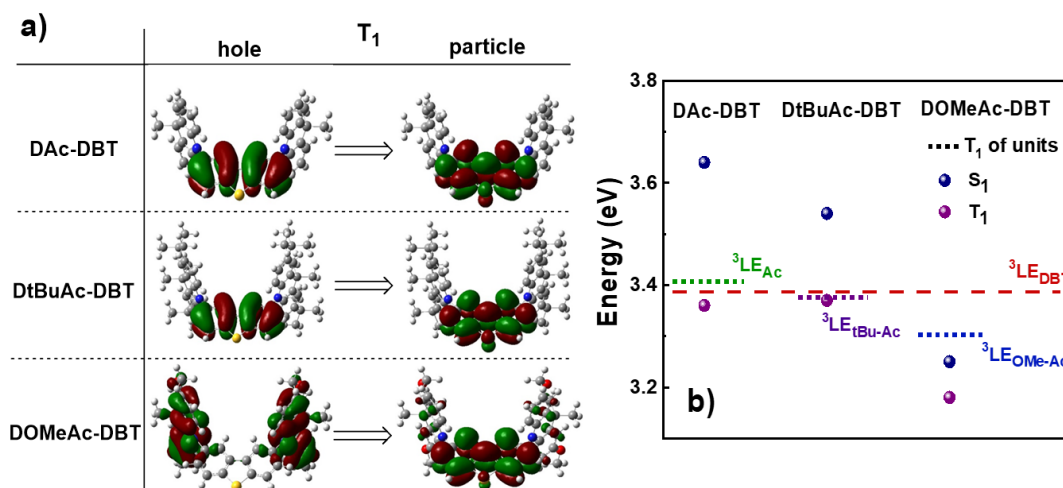


Figure 7.4: a) Natural transition orbitals (NTO) corresponding to the first triplet transitions. b) Singlet and triplet energy diagram of DAC-DBT, DtBuAc-DBT and DOMEAc-DBT along with the energy levels of the individual units (TD-DFT rBMK/6-31G(d)). [3] Hole refers to the Highest Occupied Natural Transition Orbital (HONTO), while particle refers to Lowest Unoccupied Natural Transition Orbital (LUNTO).

In DFT calculations, the geometries and distributions of the excited states are interpreted using natural transition orbitals (NTOs), which is a qualitative description of electric excitations. However, the excited states cannot be described as simple particle-hole pairs due to many contributions, such as HOMO-1 \rightarrow LUMO and HOMO \rightarrow LUMO+1. NTOs depict the superposition of all possible transitions, with the highest occupied natural transition orbital (HONTO) and lowest unoccupied natural transition orbital (LUNTO) referring to the superposition of the HOMO and LUMO levels, respectively. The calculated triplet energy of the three target compounds varies significantly as shown in Figure 7.4. The introduction of *tert*-butyl groups does not significantly affect the T_1 value (3.37 eV and 3.36 eV for DAC-DBT and DtBuAc-DBT, respectively), while the methoxy groups on

the Ac lower the triplet energy of DOMEAc-DBT significantly to 3.18 eV. Triplet NTOs indicate that DAc-DBT and DtBuAc-DBT have the T_1 localized on the DBT acceptor, demonstrating the LE character of the triplet state. However, the triplet hole and particle of DOMEAc-DBT involve both DBT and OMe-Ac units, thus indicating a CT character for the lowest triplet state. It can be clearly seen that the triplet level of DtBuAc-DBT almost coincides with the local triplets of the DBT acceptor and the tBu-Ac donor (Figure 7.4b), suggesting that both units might participate in triplet harvesting. Thus, the difference in triplet energies is expected to be a significant contributor to the differences in the observed TADF efficiency.

7.2.3 Steady-State Properties

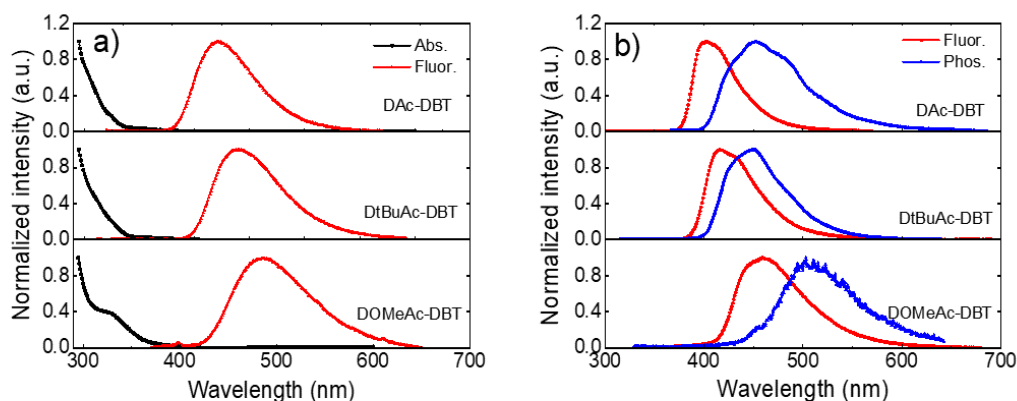


Figure 7.5: a) UV-Vis absorption and fluorescence spectra of DAc-DBT, DtBuAc-DBT and DOMEAc-DBT in toluene solutions (1.0×10^{-5} M) measured at room temperature. b) Steady-state fluorescence collected at room temperature and time-resolved phosphorescence spectra collected with delay time of 56 ms at 80 K in zeonex films (1 wt%).

The low-lying energy levels and photophysical properties of DAc-DBT, DtBuAc-DBT and DOMEAc-DBT were investigated in solutions and in zeonex. UV-Vis absorption and photoluminescence (PL) spectra of all the molecules in toluene are shown in Figure 7.5a. Slightly red-shifted absorption tails are observed in DAc-DBT, DtBuAc-DBT and DOMEAc-DBT, which can be attributed to the direct

CT transition. All compounds show structureless and Gaussian shaped emission spectra ranging from deep-blue to sky-blue. With increasing solvent polarity, a solvatochromic shift is observed (Figure 7.6), further confirming the CT nature of the excited states. The emission peaks of DtBuAc-DBT and DOMEAc-DBT are red-shifted by 25 and 49 nm, respectively, compared with that of DAC-DBT in toluene. This is consistent with the theoretical calculations, showing that by increasing the electron-donating ability of the substituted donor moieties, the HOMO energy levels are shifted upwards while the LUMO levels remain essentially unchanged. Therefore, narrowed band gaps and red-shifted spectra are obtained.

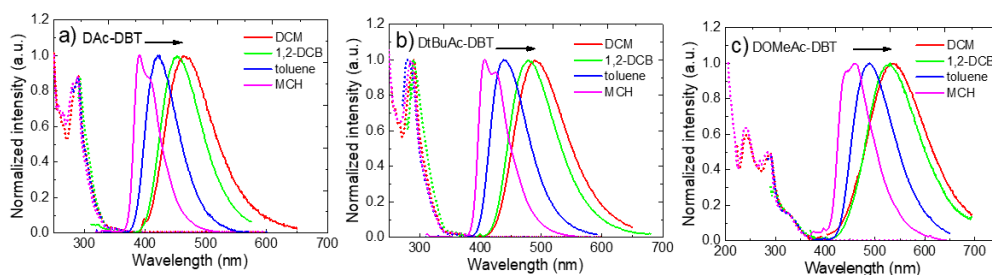


Figure 7.6: The normalized absorption and photoluminescence in various solvents of a) DAC-DBT, b) DtBuAc-DBT and c) DOMEAc-DBT.

With the increasing donor strength, DAC-DBT, DtBuAc-DBT and DOMEAc-DBT films show red-shifted emission, with the peak wavelength remaining in the blue region as shown in Figure 7.5b. The ^1CT energies calculated from the high-energy onsets of the emission spectra are 3.28 eV, 3.17 eV and 3.00 eV, for DAC-DBT, DtBuAc-DBT and DOMEAc-DBT, respectively. The phosphorescence spectra of the three molecules in zeonex films at 80 K are also shown in Figure 7.5b. DAC-DBT and DtBuAc-DBT show well-resolved phosphorescence spectra with clear vibronic structures, indicating the localized character of their triplet excited states (^3LE). The triplet energies of DAC-DBT and DtBuAc-DBT in zeonex were determined from the onsets of their phosphorescence spectra to be 3.08 eV, both isoenergetic with the DBT unit. The phosphorescence spectrum of DtBuAc-DBT shows contribution from both the donor tBu-Ac and acceptor DBT units as depicted in Figure 7.7b. Thus, the *tert*-butyl substituted molecule DtBuAc-DBT represents an ideal case

with ${}^3\text{LE}_D$ and ${}^3\text{LE}_A$ at essentially identical energies.

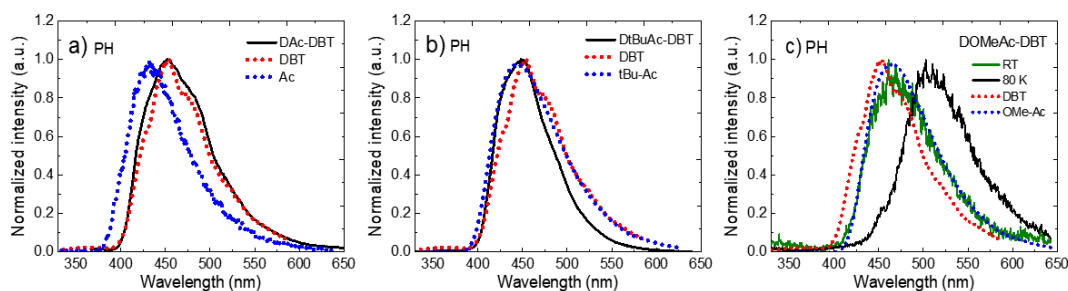


Figure 7.7: Phosphorescence spectra of a) DAC–DBT and b) DtBuAc–DBT collected at 80 K, c) DOMEAc–DBT measured at room temperature (dark green line) and 80 K (black line). All in zeonex films in comparison to their individual D and A units.

In contrast, the introduction of the methoxy substituents significantly enhances the donor strength and efficiently increases the HOMO energy in DOMEAc–DBT. A rather broad and unstructured phosphorescence spectrum is observed, indicating that the lowest energy T_1 state can be identified as a ${}^3\text{CT}$ state. This is also in agreement with the analysis of the triplet NTOs, which show donor-localized hole and acceptor-localized particle for the $S_0 \rightarrow T_1$ excitation. Consequently, the low energy singlet and triplet states in DOMEAc–DBT are both of CT character. The phosphorescence of DOMEAc–DBT appears at a lower energy (2.76 eV) compared to DAC–DBT and DtBuAc–DBT and is no longer isoenergetic with either D or A unit (Figure 7.7c). Therefore, it is very interesting to evaluate the effect of the triplet character on the efficiency of the RISC mechanism. A schematic energy diagram of DAC–DBT, DtBuAc–DBT and DOMEAc–DBT based on all the reported data is presented in Figure 7.8.

As oxygen is a well-known triplet quencher, delayed fluorescence (DF) appearing as a result of triplet harvesting is not able to contribute to the overall emission when oxygen is present. [23] The effect of oxygen-quenching on the PL spectra of DAC–DBT, DtBuAc–DBT and DOMEAc–DBT was thus analysed in toluene solution and zeonex films to quantitatively determine the contribution of DF to the total emission (Figure 7.9). A larger DF contribution is observed in DtBuAc–DBT and

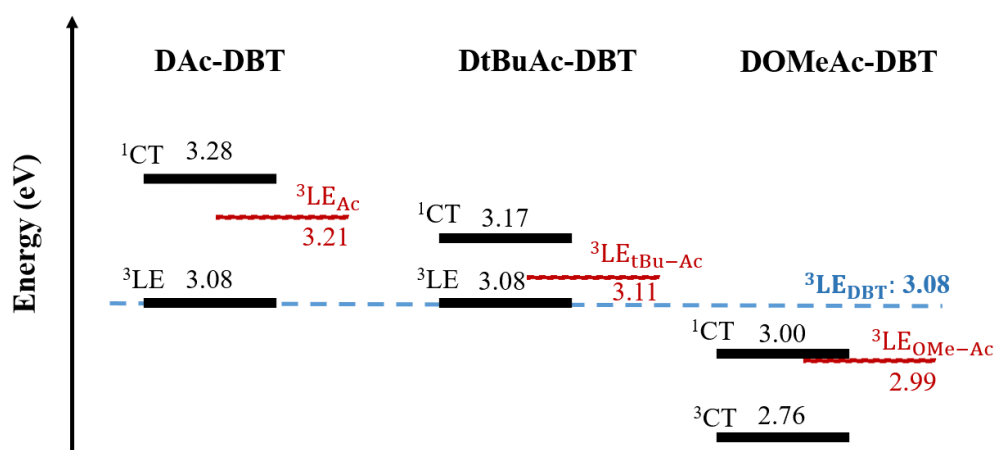


Figure 7.8: A schematic energy diagram of DAC-DBT, DtBuAc-DBT and DOMeAc-DBT. All energies are given in eV and were calculated from the onsets of the corresponding spectra in zeonex films, compared with their individual D and A moieties.

can be easily explained. The introduction of *tert*-butyl groups increases the donor strength and shifts the ^1CT state to a lower energy, narrowing the ΔE_{ST} to 0.09 eV in DtBuAc-DBT in comparison to DAC-DBT (0.20 eV). Therefore, the alignment of the singlet and triplet excited states in DtBuAc-DBT gives rise to an efficient RISC for a higher DF contribution. The high triplet contribution and deep-blue emission in DtBuAc-DBT makes it a very promising deep-blue TADF emitter.

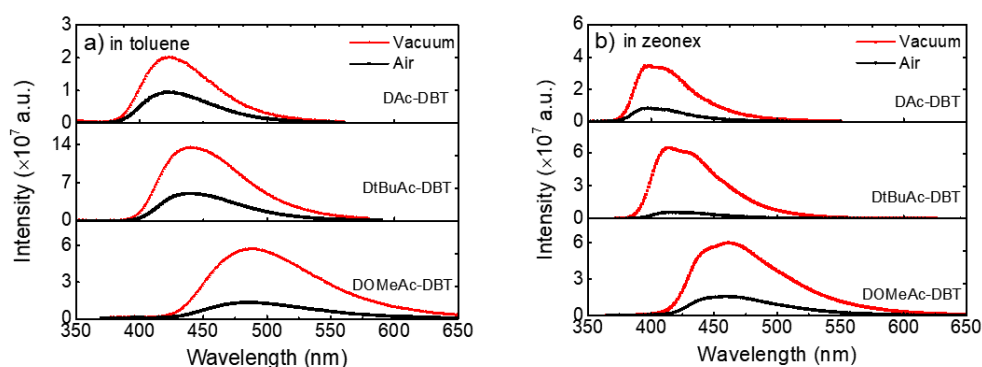


Figure 7.9: The steady-state emission spectra of DAC-DBT, DtBuAc-DBT and DOMeAc-DBT in a) diluted toluene solution (1×10^{-5} M) and b) zeonex films (1 wt%) in the absence (red) and presence (black) of oxygen at room temperature.

The methoxy groups on DOMeAc-DBT were then introduced to tune the ^1CT

state closer to the two localized triplet states. However, the donating ability of the two methoxy groups is too strong and the ^3CT drops even lower in energy, which decreases the DF contribution. This leads to a relatively small increase of the PLQYs in DOMEAc–DBT zeonex film from 35% in air to 48% in nitrogen, compared to DtBuAc–DBT with well-aligned energy states (20% in air and 54% in nitrogen). Calculations also show that a further increase of the donor strength induced by the presence of the methoxy groups leads to an expanded HOMO distribution, resulting in a relatively large overlap between the frontier orbitals. This is consistent with the experimental results, which show a large ΔE_{ST} of 0.24 eV. This in turn explains the observation of a higher PLQY in air (35% in DOMEAc–DBT *vs.* 20% in DtBuAc–DBT), the reduced formation of triplet states, and less DF contribution to the overall emission. However, the PLQYs of DAc–DBT are very low (1% in air and 6% in nitrogen condition), which will be discussed in the following section.

7.2.4 Time-Resolved Spectroscopy

To further investigate the photophysical properties, time-resolved decays were collected. DAc–DBT was also measured but found to undergo irreversible laser induced breakdown over the timescale of the measurements, which is confirmed by the red-shifted prompt emission appearing at delay time of 11 ns as shown in Figure 7.10a. It is also evidenced by the extra CV feature of a new oxidation peak (Figure 7.2a). As the emission decays very rapidly (in the nanosecond region), we tentatively suggest that this may be due to the dimerization by intermolecular π - π stacking, which occurs even in zeonex at low concentrations but is too weak to be detected in steady-state emission (Figure 7.10b). Therefore, the DF spectra and decay lifetimes of DAc–DBT are unreliable and are not included. Such shifts were not observed for the substituted compounds of the series, suggesting that blocking the 2,8-positions of acridine can help to prevent possible aggregation, which will be discussed below.

The time-resolved decays of DtBuAc–DBT and DOMEAc–DBT zeonex films are shown in Figures 7.11a and b. The nanosecond timescale prompt fluorescence (PF) decay component shows no significant change with temperature, while the microsec-

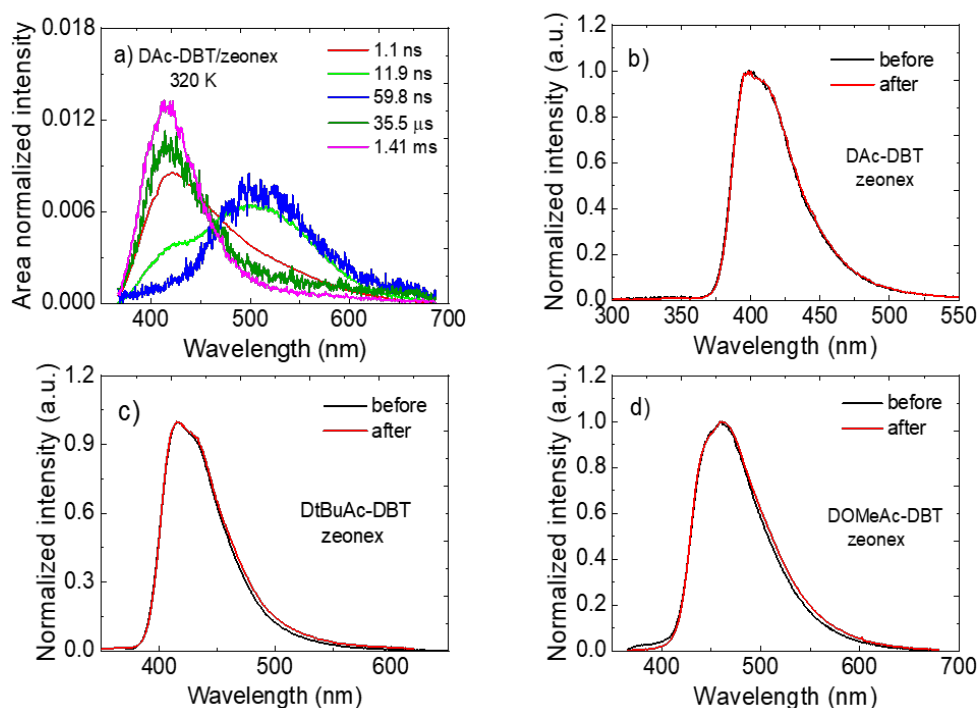


Figure 7.10: a) Time-resolved area normalized emission of DAC–DBT zeonex film at 320 K. Steady-state emission before and after laser radiation of b) DAC–DBT, c) DtBuAc–DBT and d) DOMeAc–DBT in zeonex films collected at room temperature.

and DF and millisecond phosphorescence (PH) components show clear temperature dependence. The DF intensity increases with increasing temperature, indicating a TADF mechanism in both DtBuAc–DBT and DOMeAc–DBT. The strictly linear power dependence on the excitation dose also confirms this scenario (Figures 7.11c and d). The PH component shows the opposite dependence on temperature, as expected since non-radiative processes dominate at higher temperatures in this time region.

Time-resolved area normalized spectra of DtBuAc–DBT in zeonex matrix at 290 K and 80 K are shown in Figure 7.12. In both cases, the DF spectra perfectly match the PF emission (delay time at 1.2 ns), indicating an efficient triplet up-conversion to the lowest singlet state. At 80 K, no DF is observed, with only PH occurring from the ^3LE state.

The photophysical parameters are presented in Table 7.1. For DOMeAc–DBT, the fluorescence rate constant (k_f) of $3.6 \times 10^7 \text{ s}^{-1}$ is obtained, which is similar to

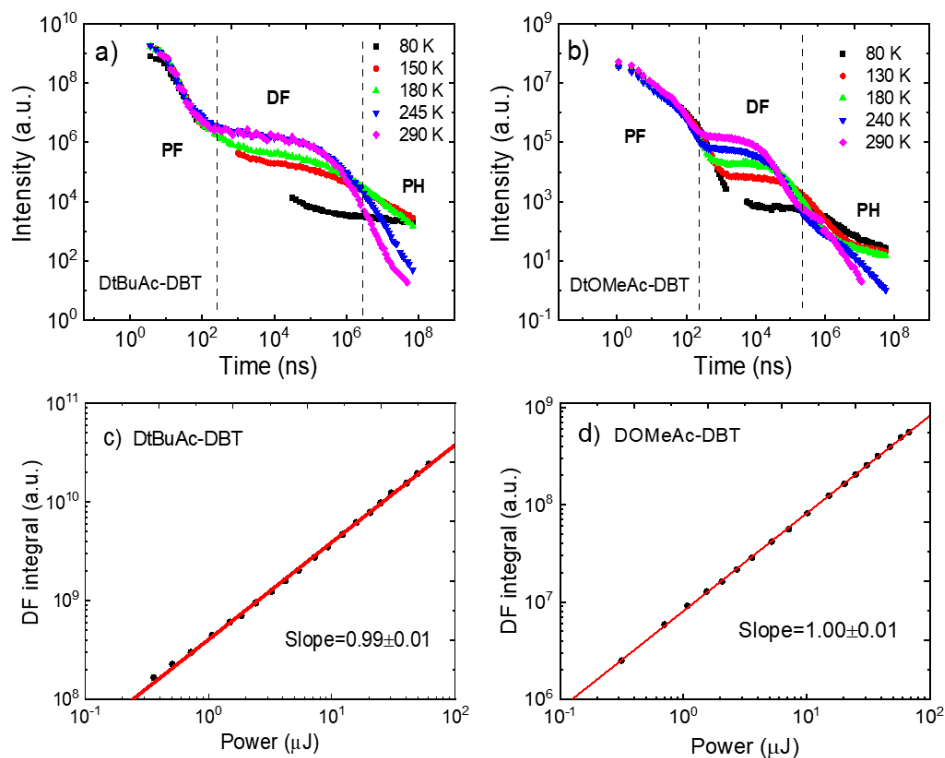


Figure 7.11: Temperature dependent time-resolved decays of a) DtBuAc-DBT and b) DOMEAc-DBT in zeonex films (1 wt%) collected at various temperatures. Power dependent measurements with delay/integration times of $1 \mu\text{s}/1 \text{ms}$, $1 \mu\text{s}/200 \mu\text{s}$ for c) DtBuAc-DBT and d) DOMEAc-DBT films, respectively, excitation at 337 nm at room temperature.

the rate determined for DtBuAc-DBT ($3.4 \times 10^7 \text{ s}^{-1}$). However, the non-radiative rate (k_{nr}) for DOMEAc-DBT is slower at $6.8 \times 10^7 \text{ s}^{-1}$. The shorter PF lifetime of DtBuAc-DBT (5.9 ns) is thus consistent with the faster ISC or IC pathways in this compound. The ISC rate (k_{ISC}) in DtBuAc-DBT can be estimated using the DF/PF ratio obtained from the comparison between PLQY measurements in nitrogen atmosphere and under air. [41] Then the ISC rate in DtBuAc-DBT is determined as $k_{\text{ISC}} = (1.0 \pm 0.7) \times 10^8 \text{ s}^{-1}$, which is faster than the total rate of non-radiative decay for DOMEAc-DBT, further explaining the shorter fluorescence lifetime of DtBuAc-DBT and consistent with the smaller ΔE_{ST} (0.09 eV). Moreover, a faster RISC rate in DtBuAc-DBT is also expected compared to DOMEAc-DBT, as the ΔE_{ST} is much larger in DOMEAc-DBT (0.24 eV).

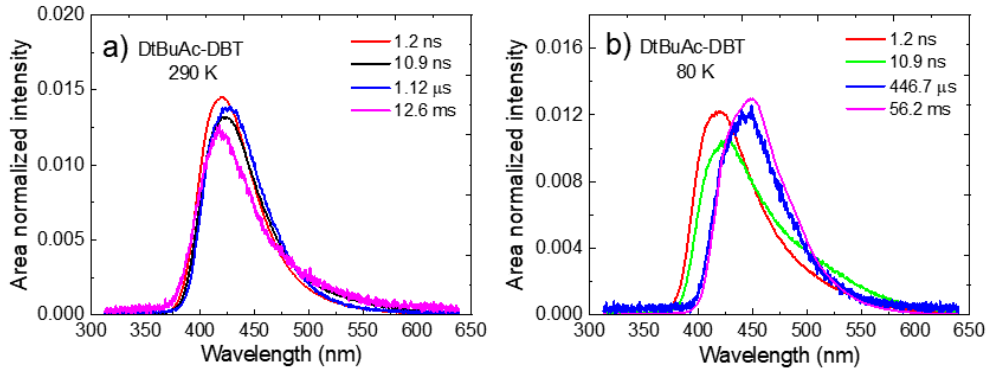


Figure 7.12: Time-resolved area normalized emission spectra of DtBuAc-DBT in zeonex matrix at a) 290 K and b) 80 K.

Table 7.1: Photophysical parameters of DAc-DBT, DtBuAc-DBT and DOMEAc-DBT in zeonex films.

	λ_{em}^a (nm)	S_1/T_1^b (eV)	ΔE_{ST}^c (eV)	$\Phi_f/\Phi_{\text{PL}}^d$ ($\pm 5\%$)	τ_f^e (ns)	τ_{DF}^e (μs)	k_f^f ($\times 10^7 \text{ s}^{-1}$)	k_{nr}^f ($\times 10^7 \text{ s}^{-1}$)	k_{RISC}^f $\times 10^7 \text{ s}^{-1}$
DAc-DBT	398	3.28/3.08	0.20	1/6	-	-	-	-	-
DtBuAc-DBT	414	3.17/3.08	0.09	20/54	5.9	136.4	3.4	14	0.002
DOMEAc-DBT	460	3.00/2.76	0.24	35/48	9.6	10.5	3.6	6.8	0.023

^aAbsorption and emission maximum in toluene at room temperature; ^b S_1 and T_1 energies estimated from the onsets of the fluorescence and phosphorescence spectra collected at RT and 80 K (delay time of 56 ms), respectively; ^cEnergy gaps between S_1 and T_1 . ^dAbsolute PLQY using integrating sphere in air (Φ_f) and nitrogen (Φ_{PL}) at RT; ^eLifetimes of PF (τ_f) and DF (τ_{DF}) fitted from time-resolved decays at 290 K; ^fRate constants of fluorescence (k_f), non-radiative (k_{nr}) and RISC (k_{RISC}).

Surprisingly, DOMEAc-DBT shows a shorter DF lifetime than DtBuAc-DBT, suggesting a faster RISC rate in the former, but the TADF contribution to the overall emission is much smaller. This apparent discrepancy is puzzling and therefore warranted further study of the TADF mechanism of DOMEAc-DBT. The ^1CT and the $^3\text{LE}_D$ states in DOMEAc-DBT are very well aligned, showing an energy gap of less than 0.01 eV (*ca.* 0.08 eV between ^1CT and $^3\text{LE}_A$ shown in Figure 7.8), while the ^3CT state is at a much lower energy ($\Delta E_{^1\text{CT}-^3\text{CT}}=0.24$ eV). RISC originating

directly from the low-lying ^3CT state is thus inefficient. However, any triplets occupying the $^3\text{LE}_A$ (or $^3\text{LE}_D$) states would be able to undergo down-hill RISC to ^1CT proceeding very rapidly as the $\Delta E_{^1\text{CT}-^3\text{LE}} < 0.01$ eV. This ordering of excited states therefore explains why the DF lifetime is shorter in DOMEAc-DBT, but the overall TADF contribution is smaller. We proposed that the rapid upper-state crossing RISC between ^3LE and ^1CT in DOMEAc-DBT competes with the ^3LE triplets relaxing to the low energy ^3CT triplet. This IC relaxation to a non-emissive triplet state quenches DF contribution, resulting in a smaller contribution to the total emission despite a faster RISC rate.

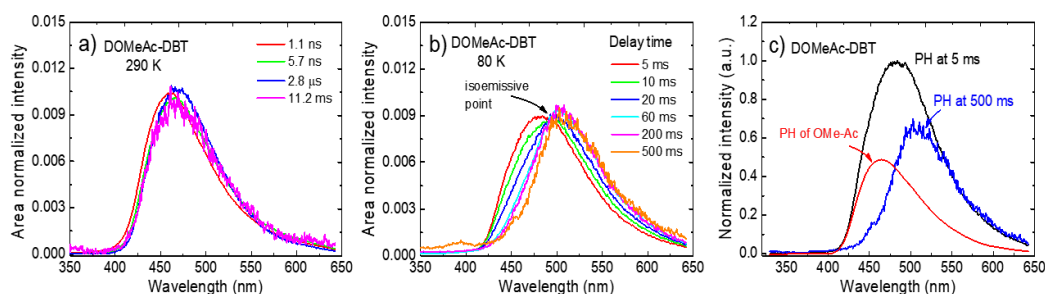


Figure 7.13: DOMEAc-DBT in zeonex film: time-resolved area normalized emission spectra at a) 290 K and b) 80 K. c) Phosphorescence spectra recorded at delay times of 5 ms and 500 ms, compared with that of the donor OMe-Ac unit measured at 80 K.

This interpretation is also supported by the time-resolved spectra of DOMEAc-DBT as shown in Figure 7.13. At 290 K, the emission spectrum shows practically no shift over the entire time range from 1.1 ns to 11.2 ms, showing that TADF mostly dominates the long-lived emission at RT. However, at a low temperature an emission intensity increase is observed in the millisecond time region (Figure 7.11b), showing that phosphorescence instead of TADF is dominant. The emission of DOMEAc-DBT is therefore composed of PF at early times (< 100 ns), TADF in the microsecond range, and PH at later times (ms). The fluorescence and phosphorescence spectra are very similar to each other, which is only possible if the PH originates from the triplet state localized on the donor unit ($^3\text{LE}_D$) that is isoenergetic with the ^1CT state. Consistently, the emission spectrum of DOMEAc-DBT at very-long delay times,

obtained at room temperature, matches the PH of the OMe–Ac single fragment (Figure 7.7c). The PH from the ^3CT state is not observed at RT as this state has a much slower radiative rate thus longer lifetime, and can be easily quenched. However, PH from both ^3LE and ^3CT states are observed at low temperatures. At delay time of 5 ms, the PH of DOMeAc–DBT shows features from both the $^3\text{LE}_\text{D}$ state localized on the OMe–Ac donor unit and the ^3CT state (Figure 7.13c). The ^3LE phosphorescence appears at a higher energy and relaxes over time, whereas the ^3CT phosphorescence appears at a lower energy and shows longer lifetime. The time-resolved spectra therefore give full support to the role of the ^3LE state in mediating RISC, and assist in revealing the upper-state RISC mechanism in DOMeAc–DBT.

7.3 Conclusions

In summary, the photophysical characterization of a series of blue TADF emitters with a D–A–D architecture utilizing the unconventional electron-rich DBT unit as the acceptor and Ac derivatives as donor units are investigated. The substitution of *tert*-butyl or methoxy groups on the D unit enhances the donor strength of the Ac and helps to tune the singlet and triplet energy levels. Excellent energy alignment between the $^3\text{LE}_\text{D}$ and $^3\text{LE}_\text{A}$ triplet states and the ^1CT singlet state is obtained in DtBuAc–DBT. This leads to a decrease in the energy gap ($\Delta E_{^1\text{CT}-^3\text{LE}}$) from 0.20 eV in DAc–DBT to 0.09 eV in DtBuAc–DBT, which greatly facilitates the RISC process occurring from the low energy ^3LE triplet to the ^1CT state. Interestingly, when the donor strength is further enhanced by using methoxy groups in DOMeAc–DBT, a small energy gap of <0.01 eV between ^1CT and the high-energy triplet $^3\text{LE}_\text{D}$ is obtained. However, a lower energy triplet state with CT character is also observed, showing an energy gap of 0.24 eV to the ^1CT state. DOMeAc–DBT shows a smaller TADF contribution in comparison to DtBuAc–DBT, but surprisingly with a much faster rate. It is ascribed to an upper-state crossing from $^3\text{LE}_\text{D}$ to ^1CT promoted by the small $\Delta E_{^1\text{CT}-^3\text{LE}}$ (0.01 eV). The small TADF contribution in DOMeAc–DBT is attributed to the competition between the fast RISC rate (from $^3\text{LE}_\text{D}$ to ^1CT) and triplet $^3\text{LE}_\text{D}$ relaxation to the low ^3CT state by rapid IC. This work expands the

range of acceptor units that can be used in TADF emitters and shows the importance of precisely tuning the local and triplet states by carefully selecting complementary donor and acceptor units to achieve efficient TADF.

Chapter 8

The Effect of Substitution

Patterns on Tuning Emission and Luminescence Efficiency in TADF Emitters

The effect of different acceptor substitution patterns on the photophysical properties of a series of TADF molecules is presented in this chapter. By introducing substituents (methoxy, methylthio, fluorine and cyano) into the *meta*-position of the acceptor unit the electron-withdrawing strength is greatly altered, resulting in a colour-tuning effect towards the red region. Small singlet-triplet energy gaps (less than 0.10 eV) are obtained in all substituted molecules when dispersed in a polar host, accompanied by high photoluminescence quantum yields. TADF OLEDs fabricated with the cyano substituted molecule as the emitter exhibit high performance with external quantum efficiency up to 13.8% and orange-red (590 nm) electroluminescence.

The work presented in this chapter is under preparation for publication. R. Huang performed all the photophysical measurements under the supervision of F. B. Dias. R. Huang fabricated OLED devices with the support from D. Pereira. I. Perepichka synthesized and purified all molecules.

8.1 Introduction

To promote TADF efficiency, a small singlet-triplet energy gap (ΔE_{ST}) is sought after by decreasing the exchange interactions. However, the small ΔE_{ST} that this small exchange brings also diminishes the electronic coupling between the excited state and the ground state, resulting in a slow radiative rate and thus low PLQYs. This is especially true in TADF molecules where donor (D) and acceptor (A) are oriented nearly orthogonally. Therefore, a top priority is to find a balance between PLQY and triplet harvesting efficiency most suitable for application in OLEDs. [61, 191] This can be in principle achieved by studying the effects of selectively tuning structured and electronic factors that affect TADF efficiency.

The work presented in this chapter is inspired by recently published TADF molecules based on dibenzothiophene-*S,S*-dioxide (DBTO2) as the strong A unit, in combination with a range of donor units, such as carbazole, diphenylamine and phenothiazine to design TADF emitters. [41, 144, 147, 164] The basic and most popular concepts that were introduced in previous work rely mostly on the modifications of the donor units, to efficiently engineer the twist angles between D and A fragments to minimize ΔE_{ST} . However, in compounds where this strategy was used with phenothiazine (PTZ) donors, conformational changes had severe detrimental effect on the TADF efficiency. [102] Steric groups have also been introduced in the A unit of TADF compounds based on PTZ donors. The TADF performance in the acceptor substituted compounds was in general superior showing excellent TADF contributions to the overall emission. [101, 192]

Recently, based on DBTO2 as the A unit and acridine (Ac) as the D, two TADF regioisomers 3ASOA and 4ASOA were reported. [193] In 3ASOA the two Ac units are linked at positions C-3,7 of DBTO2, whereas in 4ASOA they are substituted at the C-2,8 positions. The two compounds exhibit clear TADF contributions with PLQYs of 72% and 88%, and the ΔE_{ST} of 0.26 eV and 0.09 eV, respectively. However, the lifetimes of DF are relatively long, 1.4 and 4.8 ms, respectively. To the best of our knowledge, substitution at the position C-1(9) of DBTO2 has not been so far explored as a strategy to tune the CT strength of the excited state. Here a series of molecules based on DBTO2-DAc (*i.e.* 3ASOA) were investigated to ex-

plore the effect of substituents with different electron-withdrawing capabilities at the C-1(9) position of the DBTO2 unit, aiming to alter the acceptor strength. The incorporation of these substituents efficiently lowers the LUMO in comparison to the HOMO energy levels, leading to a clear colour-tuning effect towards the red region – increasing in order from methoxy, methylthio, fluorine to cyano. When doped into a polar host with a very high triplet state, small ΔE_{ST} are obtained while retaining high PLQYs. OLEDs employing cyano substituted compound CNDBTO2–DAc as the emitter demonstrated a high EQE of 14% with orange-red emission peaking at 590 nm.

8.2 Results and Discussion

8.2.1 Fundamental Photophysical Characterization

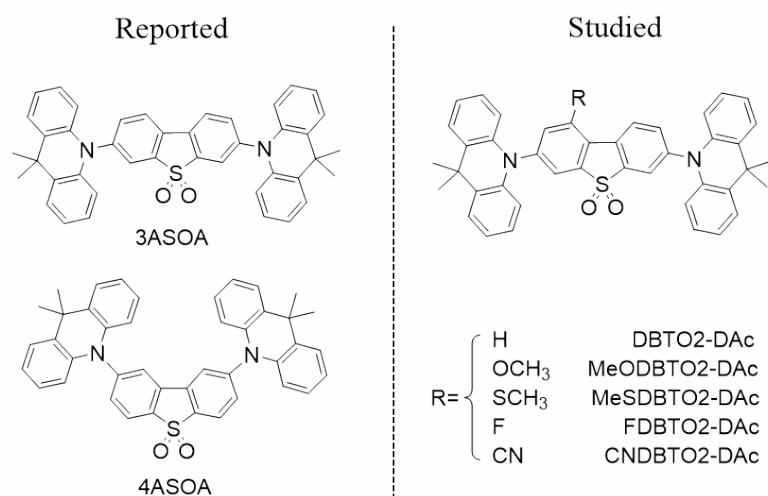


Figure 8.1: Molecular structures of the reported and studied compounds.

Molecular structures of the five compounds studied in this chapter are presented in Figure 8.1. The absorption and emission spectra of the five compounds in dilute toluene solutions are shown in Figure 8.2. All compounds show an intense absorption band below 325 nm that is associated with the individual D and A fragments, and two other bands (between 325 nm and 375 nm, and between 375 nm and 500 nm) in a region where no absorption band is observed in either D or A unit. The former

is more obvious in MeSDBTO2-DAC, but vestiges of its presence are detected in all the other compounds. The lowest energy band is observed in all compounds, and shifts to longer wavelength with increasing electron-withdrawing strength of the substituents. Therefore, it is assigned to the direct excitation of the ^1CT state.

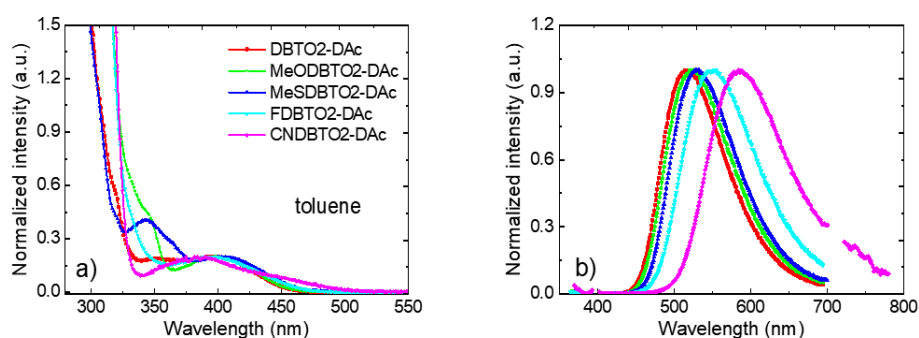


Figure 8.2: a) UV-Vis absorption and b) emission spectra of the studied D-A-D molecules in dilute toluene solutions (1.0×10^{-5} M) at room temperature.

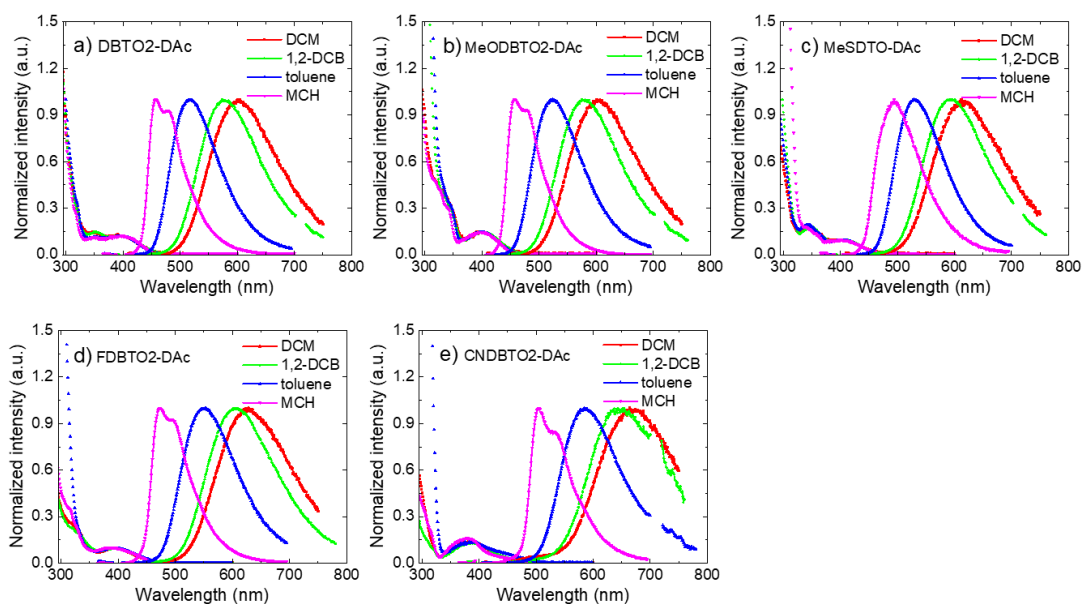


Figure 8.3: Comparison of the absorption and emission spectra of a) DBTO2-DAC, b) MeODBTO2-DAC, c) MeSDBTO2-DAC, d) FDBTO2-DAC and e) CNDBTO2-DAC in solvents of different polarities at room temperature.

The introduction of the substituents strongly affects the emission properties. All

molecules show structureless and Gaussian shaped spectra in toluene, which shifts to a longer wavelength with the increasing substituting acceptor strength. The emission of CNDBTO2–DAc for example peaks at 590 nm in toluene, and shifts to 680 nm in dichloromethane (DCM). A strong positive solvatochromic effect is also observed in the other compounds with increasing solvent polarity, indicative of the CT character of the excited state in all five compounds (Figure 8.3).

Table 8.1: Photophysical, electrochemical parameters of the investigated molecules in solution and zeonex films.

	$\lambda_{\text{abs.}}^a$ (nm)	$\lambda_{\text{em.}}^a$ (nm)	Φ_{f}^b ($\pm 5\%$)	Φ_{PL}^b ($\pm 5\%$)	τ_{f}^c (ns)	HOMO/LUMO ^d (eV)	E_{g}^e (eV)	S_1/T_1^f (eV)	ΔE_{ST}^g (eV)
DBTO2–DAc	398	515	19	61	8.0	-5.62/-3.15	2.47	2.84/2.55	0.29
MeODBTO2–DAc	403	524	20	45	7.9	-5.75/-3.29	2.46	2.83/2.55	0.28
MeSDBTO2–DAc	398	529	12	45	4.9	-5.68/-3.31	2.37	2.79/2.54	0.25
FDBTO2–DAc	398	552	20	63	7.2	-5.70/-3.40	2.30	2.81/2.56	0.25
CNDBTO2–DAc	395	588	19	56	8.2	-5.67/-3.55	2.12	2.66/2.42	0.24

^aThe maxima of absorption and emission spectra in toluene at RT; ^bAbsolute PLQY in zeonex films using integrating sphere in air (Φ_{f}) and nitrogen (Φ_{PL}) atmosphere at RT; ^cFluorescence lifetimes fitted from time-resolved decays of zeonex films at RT; ^dHOMO and LUMO energies estimated from the redox potentials in cyclic voltammetry; ^eEnergy band gaps; ^f S_1 and T_1 energies calculated from the onsets of the fluorescence and phosphorescence spectra collected at RT and 80 K (56.2 ms), respectively; ^gEnergy splitting between S_1 and T_1 of zeonex films.

To further clarify the reasons for the red-shifted emission spectra with increasing electron-withdrawing properties of the substituents (–MeO, –MeS, –F and –CN), cyclic voltammograms of all molecules were recorded. The HOMO and LUMO energy levels calculated from the voltammograms are presented in Table 8.1. Compared with DBTO2–DAc, the HOMO is just slightly shifted to a lower energy while the LUMO is significantly affected, shifting gradually to lower energies with the increasing electron-withdrawing strength of the substituents. Therefore, the band gaps (E_{g}) are narrowed, resulting in lower singlet excited states and thus red-shifted emission.

The fluorescence and phosphorescence spectra of all five compounds in zeonex films are shown in Figure 8.4a. As expected, the fluorescence exhibits a slight red-

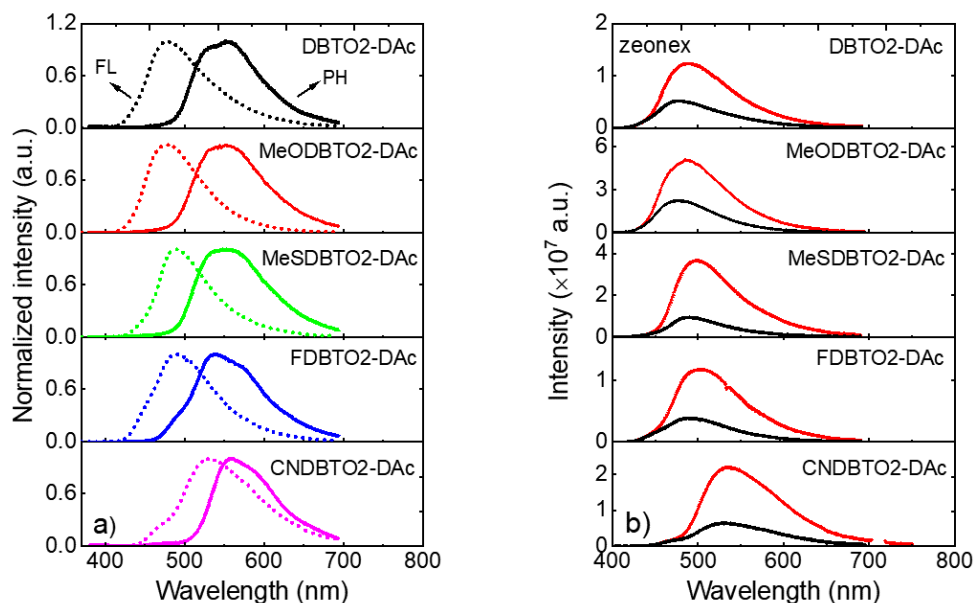


Figure 8.4: a) Fluorescence (dotted line) and phosphorescence (solid line) spectra of DBTO2–DAc, MeODBT02–DAc, MeSDBT02–DAc, FDBT02–DAc and CNDBT02–DAc in zeonex solid films, collected at room temperature and 80 K, respectively. b) Steady-state emission spectra of all five molecules in zeonex matrix in the presence (black) and absence (red) of oxygen at room temperature.

shift with the increasing electron-withdrawing abilities of the substituents. The profiles of the phosphorescence of molecules MeODBT02–DAc, MeSDBT02–DAc and FDBT02–DAc are similar to their parent molecule DBTO2–DAc, showing almost isoenergetic triplet energies-determined from the onsets of the spectra to be around 2.55 eV. As an outlier, both fluorescence and phosphorescence of CNDBT02–DAc shows a more pronounced red-shift, resulting in lower S_1 and T_1 energies of 2.66 and 2.42 eV, respectively. This is ascribed to the stronger electron-withdrawing ability of the cyano group. However, the energy difference between singlet and triplet states (ΔE_{ST}) is almost invariant across the five compounds, ranging from 0.29 eV to 0.24 eV, as shown in Table 8.1.

Although the values of ΔE_{ST} are relatively large, strong DF emission is observed with high PLQYs in all five compounds. The contributions of the triplet excited state to the overall emission were determined from the difference between

emission intensities in the presence and absence of oxygen at room temperature (Figure 8.4b). [23] The PLQYs of all molecules demonstrate strong dependence on the presence of oxygen (Table 8.1). Molecules DBTO2–DAc, MeODBTO2–DAc, FDBTO2–DAc and CNDBTO2–DAc in zeonex films show PLQYs around 20% in air, which increase *ca.* 3 times in nitrogen atmosphere. While MeSDBTO2–DAc exhibits a smaller PLQY of 12% in air, this increases almost fourfold to 45% when oxygen is removed. The strongest DF contribution to the total emission (74%) observed in MeSDBTO2–DAc results from the fast ISC process promoted by the sulphur atom, with RISC in turn also enhanced.

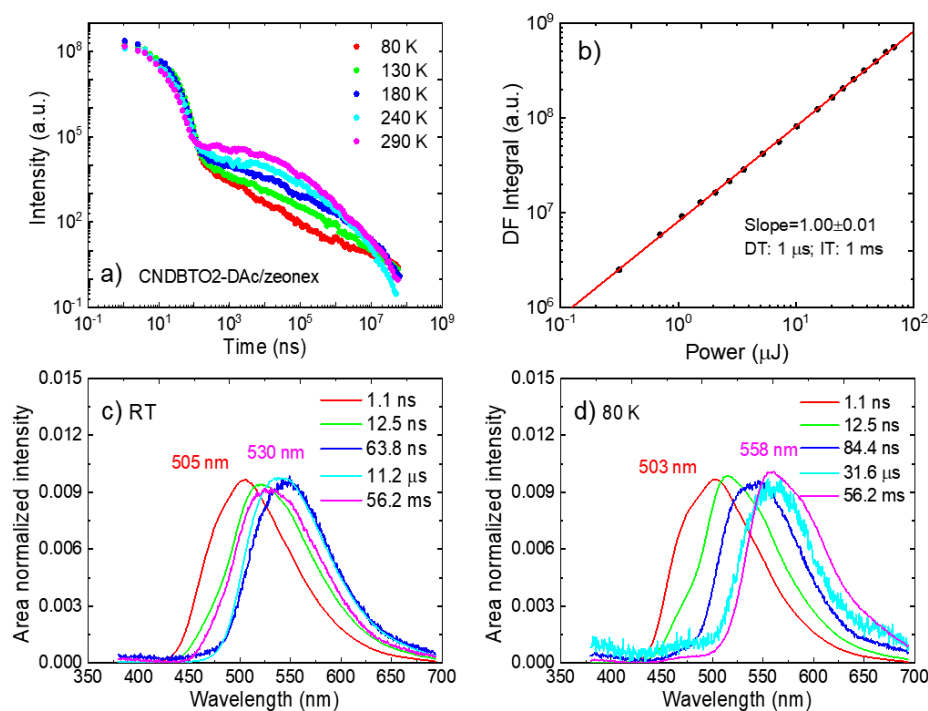


Figure 8.5: CNDBTO2–DAc zeonex film: a) Temperature dependent time-resolved decays. b) The dependence of DF intensity on laser power with delay and integration times of 1 μ s and 1 ms, respectively. Excitation at 337 nm at room temperature. Time-resolved area normalized spectra c) at room temperature and d) 80 K.

To further explore the photophysical properties, time-resolved decays of the CNDBTO2–DAc zeonex film were measured as shown in Figure 8.5a. The decays show a fast temperature independent PF component, followed by a slower DF

decay showing positive temperature dependence, in accordance with the expected TADF mechanism. The strictly linear dependence of the DF integral on excitation dose with a unity slope in a logarithmic plot further confirms its monomolecular TADF mechanism excluding TTA from consideration (Figure 8.5b). At longer delay times, the emission intensity slightly increases and shows a longer lifetime at low temperature as a result of phosphorescence.

Figure 8.5c shows the area normalized spectra of CNDBTO2–DAc at room temperature. Strong spectral shifts are observed over time, potentially due to the presence of different conformers. The spectrum at 1.1 ns time delay is assigned to the fluorescence emission of the unrelaxed ^1CT state, and may also contain a component of ^1LE emission. However, the emission shifts to longer wavelength over time (up to 60 ns), reflecting the changes in molecular conformations to relax towards the excited-state charge distribution. Later the spectrum is blue-shifted, again giving indication that different conformers are present and contribute differently to the TADF emission. Basically, “blue emitting” conformers have slightly larger ΔE_{ST} than the “red emitting” conformers, and thus show longer TADF lifetimes and dominate the emission at later delay times. [25,58] As a result, the emission initially shifts to longer wavelength, due to the growing contribution and the energetic relaxation of the ^1CT excited state, but then blue-shifts from 545 to 530 nm due to dispersion of population of conformers. [41] In contrast, a continuous dynamic red-shift is observed when the temperature is decreased to 80 K, as shown in Figure 8.5d. The initial spectral shift observed at early times (up to 84 ns) is again assigned to the structural relaxation occurring as a response to changes in electron density between the ground and excited state. Interestingly, the blue-shift at room-temperature is no longer observed at later times, since TADF is strongly suppressed at low temperatures. At 80 K, strong phosphorescence instead dominates.

As shown in Figure 8.6, similar phenomena are also observed in DBTO2–DAc, MeODBTO2–DAc, MeSDBTO2–DAc and FDBTO2–DAc zeonex films. All decays show two components (PF and DF) and linear power dependence confirming their TADF mechanism. Fluorescence lifetimes are *ca.* 8 ns, with exception of MeSDBTO2–DAc at 4.9 ns, consistent with its faster ISC rate. In DBTO2–DAc,

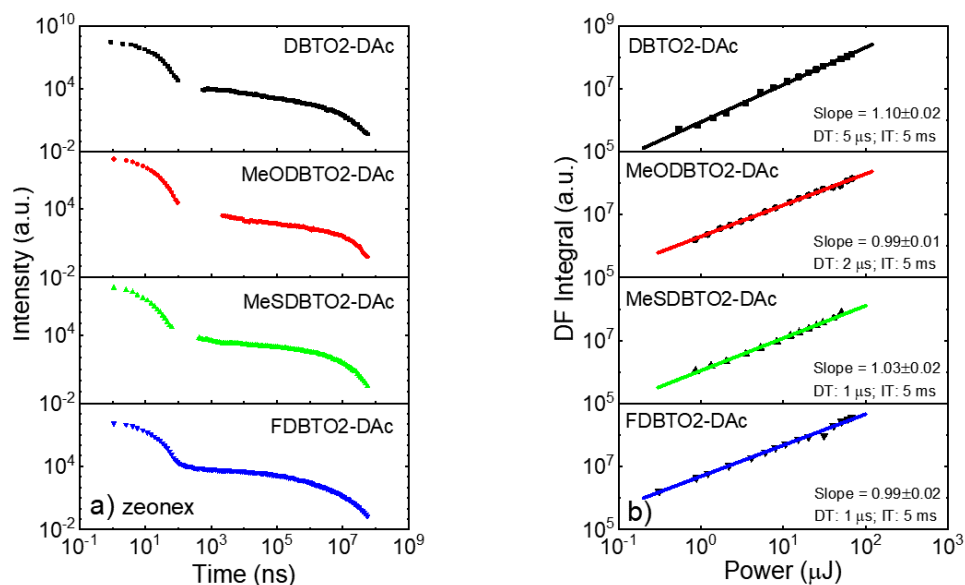


Figure 8.6: Time-resolved decays of DBTO2–DAc, MeODDBTO2–DAc, MeSDBTO2–DAc and FDBTO2–DAc films at room temperature, excitation at 355 nm. b) Power dependence of DF with excitation dose. Excitation at 337 nm at room temperature.

MeODDBTO2–DAc and MeSDBTO2–DAc, there is a time-interval between the PF and DF decays where the emission dips below the noise baseline of the instrument. This is due to the slower RISC rate in these compounds, and thus too few photons being collected within the integration times used in this delay-time region. For FDBTO2–DAc and CNDBTO2–DAc such emission-gap is not present as the RISC rate is faster, allowing the detection of more intense TADF with relatively shorter integration times.

8.2.2 Photophysical Properties in DPEPO

Following characterization in an inert zeonex host, we proceeded to characterize all compounds in a polar host DPEPO (bis[2-(di-(phenyl)phosphino)-phenyl]ether oxide), commonly used in the fabrication of devices. This is important as the polarity of the host has a strong influence on the emission energy of the ^1CT state, ΔE_{ST} , and thus triplet harvesting and device performance. Fluorescence and phosphorescence spectra of the five compounds in DPEPO films are shown in Figure 8.7a. As

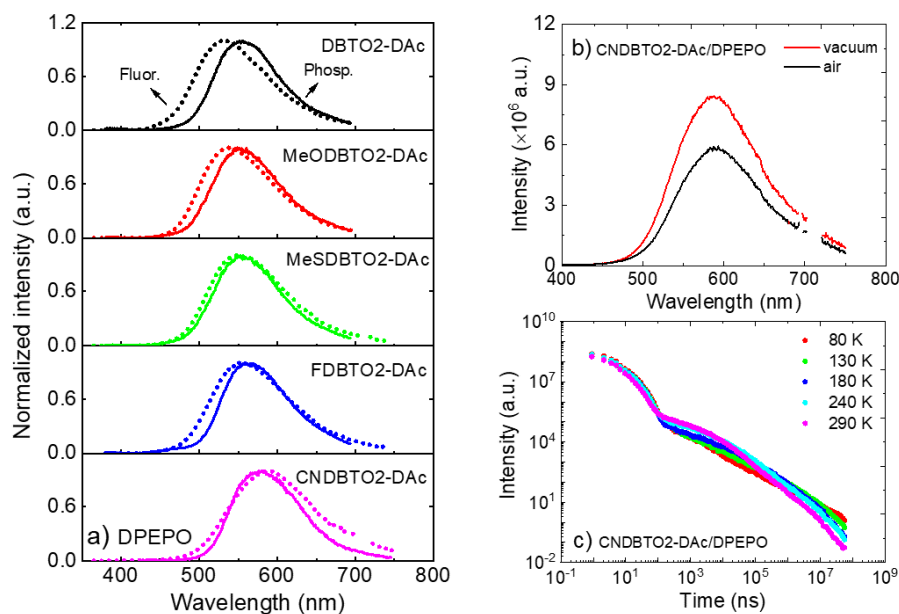


Figure 8.7: a) Comparison of fluorescence (dotted line) and phosphorescence (solid line) spectra of the doped DPEPO films, collected at room temperature and 80 K (delay time of 56.2 ms), respectively. b) Steady-state emission of CNDBT02–DAc in DPEPO (10% w/w) in the presence and absence of oxygen at room temperature. c) Temperature dependent time-resolved decays of CNDBT02–DAc doped DPEPO film. Excitation at 355 nm.

expected, in comparison to the zeonex films, the ^1CT emission in DPEPO films shifts to a lower energy. However, the low energy triplet state is of local character and is less affected by host polarity. Therefore, ΔE_{ST} decreases from 0.25 eV to less than 0.10 eV in all substituted molecules (Table 8.2).

Steady-state emission of CNDBT02–DAc in DPEPO film in aerated and degassed conditions are shown in Figure 8.7b. After removing oxygen, emission intensity increases with a DF contribution of 31% to the overall emission. The relatively small TADF contribution observed in DPEPO in comparison to the zeonex film is probably due to some more efficient non-radiative processes quenching the triplet population in this host, and thus competing with the RISC rate. Figure 8.7c shows the time-resolved temperature dependent decays of CNDBT02–DAc in DPEPO film, confirming its TADF mechanism. The decays show more complex excited state dynamics than in zeonex, which can be ascribed to a broader conformational

Table 8.2: Photophysical parameters of the investigated molecules in DPEPO films.

	Φ_f^a ($\pm 5\%$)	Φ_{PL}^a ($\pm 5\%$)	τ_f^b (ns)	τ_{DF}^b (μs)	S_1^c (eV)	T_1^c (eV)	ΔE_{ST}^d (eV)
DBTO2–DAc	41	71	8.7	13.6	2.69	2.54	0.15
MeODBT02–DAc	33	63	10.6	38.7	2.63	2.57	0.06
MeSDBT02–DAc	33	53	4.5	32.6	2.59	2.56	0.03
FDBT02–DAc	34	44	12.6	12.7	2.59	2.49	0.10
CNDBT02–DAc	30	37	8.1	10.2	2.49	2.43	0.06

^aAbsolute PLQY using integrating sphere in air (Φ_f) and nitrogen (Φ_{PL}) at RT; ^bLifetimes of PF (τ_f) and DF (τ_{DF}) fitted from time-resolved decays at 290 K; ^c S_1 and T_1 energies estimated from the onsets of the fluorescence and phosphorescence spectra collected at RT and 80 K (delay time of 56 ms), respectively; ^dCalculated energy splitting between S_1 and T_1 states.

distribution in a more polar environment. Owing to a small ΔE_{ST} (0.06 eV), efficient RISC between ^1CT and ^3LE states is achieved yielding a relatively short-lived DF emission. Inverse temperature dependence of the emission intensity is observed at long delay times, indicating the increasing contribution of ^3LE phosphorescence.

DBTO2–DAc, MeODBT02–DAc, MeSDBT02–DAc and FDBT02–DAc in doped DPEPO films all show similar properties as shown in Figure 8.8. The energy difference ΔE_{ST} of DBTO2–DAc decreases sharply to 0.15 eV in DPEPO, while showing very high PLQYs of 41% and 71% in aerated and nitrogen atmosphere, respectively. The smallest energy gap of 0.03 eV is obtained in MeSDBT02–DAc, which in turn promotes the fast RISC process ($k_{\text{RISC}} \sim 10^5 \text{ s}^{-1}$).

8.2.3 Device Performance

To evaluate the electroluminescence (EL) properties of these new TADF emitters, OLEDs were fabricated using DPEPO as a host. Devices 1 to 5 are based on emitters DBTO2–DAc, MeODBT02–DAc, MeSDBT02–DAc, FDBT02–DAc and CNDBT02–DAc, respectively. The device architecture is shown in Figure 8.9a: ITO/ α -NPD (40 nm)/TCTA (10 nm)/DPEPO:10% emitter (20 nm)/TPBi (40

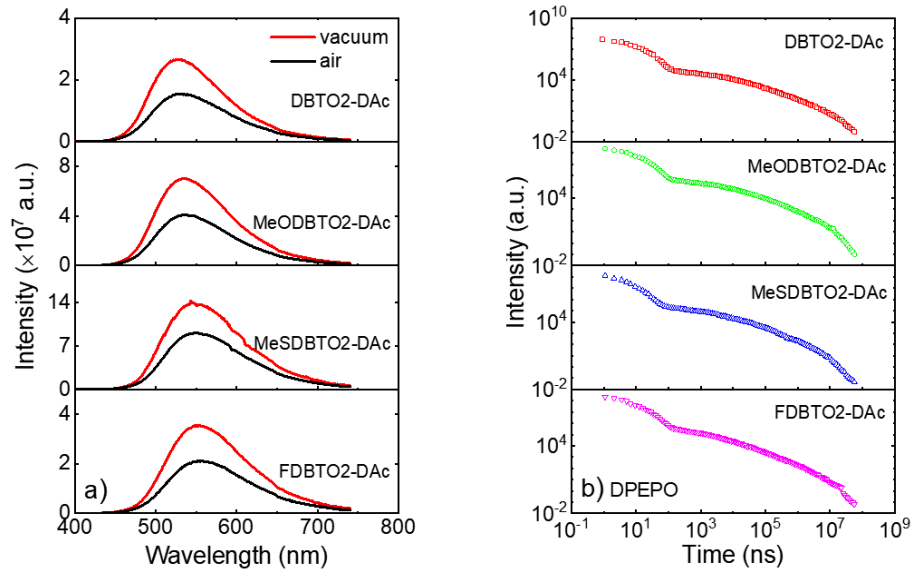


Figure 8.8: a) Steady-state emission of DBTO2-DAc, MeODBT02-DAc, MeSDBT02-DAc and FDBT02-DAc doped DPEPO films in aerated and vacuum conditions at room temperature. b) Time-resolved decays at room temperature. Excitation at 355 nm.

nm)/LiF (1 nm)/Al. Here *N,N'*-di(1-naphthyl)-*N,N'*-diphenyl-(1,1'-biphenyl)-4,4'-diamine (α -NPD), tris(4-carbazoyl-9-ylphenyl)amine (TCTA) and 2,2',2''-(1,3,5-benzenetriyl)-tris(1-phenyl-1-*H*-benzimidazole) (TPBi) were employed as the hole-injecting, hole-transporting and electron-transporting layers, respectively. All EL parameters of the OLEDs are summarized in Table 8.3.

Table 8.3: Summary of OLED device characteristics.

	λ_{\max}^a (nm)	V_{on}^b (V)	EQE (%)		η_{CE}^c (cd/A)	η_{PE}^d (lm/W)
			Max.	100 cd/m ²		
Dev. 1	538	4.0	14.8	12.6	44.7	35.1
Dev. 2	539	4.0	13.1	10.5	37.9	26.5
Dev. 3	555	3.8	11.4	10.1	37.6	26.3
Dev. 4	563	4.0	12.1	9.7	25.5	14.6
Dev. 5	590	3.8	13.8	9.4	29.8	20.8

^aThe peak of EL spectra. ^bTurn-on voltage at the brightness of 10 cd/m². ^cThe maximum value of current efficiency. ^dThe maximum value of power efficiency.

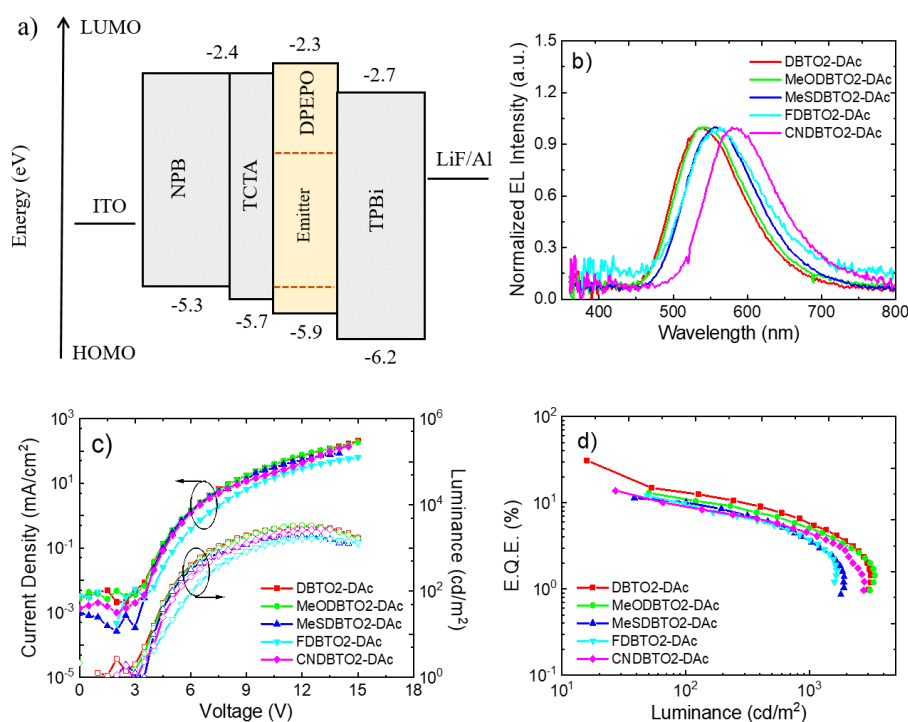


Figure 8.9: a) Architecture and energy levels of OLED devices. b) EL spectra collected at 9 V. c) Current density-voltage-luminance characteristics. d) EQE *vs.* luminance characteristics.

Figure 8.9b exhibits the EL spectra of the OLEDs collected at 9 V, which are consistent with their PL spectra in DPEPO films. The spectra are independent of the applied voltages, indicating efficient host-guest energy transfer. Dev. 1 and 2 emit green light with emission peaking at 538 and 539 nm, respectively. Further increasing the electron-withdrawing ability of the emitters, red-shifted EL from yellow to orange-red (peaking at 555, 563 and 590 nm, respectively) is observed from Dev. 3 to 5. All devices show low turn-on voltages (< 4.0 V) and high luminance (2000 cd/m^2 at 12 V Figure 8.9c). As shown in Figure 8.9d, Dev. 3 and 4 emit in the yellow region and exhibit maximum EQE of 11.4% and 12.1%, respectively. The current and power efficiencies are 37.6 cd/A , 26.3 lm/W and 25.5 cd/A , 14.6 lm/W , respectively. Orange-red emission is observed in Dev. 5 exhibiting a high EQE of 13.8% based on CNDBTO2-DAc emitter. Unfortunately, the long-lived triplet excitons are easily quenched by bimolecular processes, including triplet-triplet annihilation and

triplet-polaron annihilation [49, 82], which result in the efficiency roll-off to 9.4% at a luminance of 100 cd/m². Taking PLQY into consideration, Dev. 5 shows a high EL performance in orange-red region consistent with an outcoupling efficiency of 20~30%.

8.3 Conclusions

In summary, the colour-tuning effect of the emission from green towards orange-red is discussed in a series of DBTO2–DAc derivatives. By substituting methoxy, methylthio, fluorine and cyano groups on the C-1(9) position of the acceptor DBTO2, the electron-withdrawing strength increases sequentially due to the significantly lowered LUMO energy. Based on the photophysical investigations in non-polar zeonex host, DPEPO was chosen as a host to tune the energy of the ¹CT state. All substituted molecules exhibit reduced ΔE_{ST} of less than 0.10 eV in doped DPEPO films, while retaining relatively high PLQYs. This is favourable to achieve high TADF efficiency and extremely promising for OLED applications. Owing to the presence of the sulphur atom, MeSDBTO2–DAc shows a higher DF contribution with a PLQY of 53%. A remarkable EQE of 13.8% is achieved using CNDBTO2–DAc as the emitter in an orange-red OLED.

Chapter 9

Concluding Remarks

Photophysical characterizations of two triplet harvesting mechanisms (TADF and RTP) in a variety of metal-free organic molecules with D–A–D or D–A structures have been the focus of this thesis. The molecules in each chapter were designed to enhance the ISC and RISC processes and explore the role of the singlet and triplet excited states with charge transfer (CT) or localized character (LE). Together, these studies provide significant guidance for designing more efficient organic TADF and RTP emitters for applications.

9.1 General Conclusion

The influence of D–A molecular connectivity on the activity of TADF and RTP mechanisms was investigated in chapter 4. The “angular” substitution on the A unit effectively breaks the molecular conjugation and decreases the energy gap for fast ISC and RISC processes. By using hosts to tune the energy difference, dual long-lived luminescence (TADF and RTP) was activated. This chapter illustrates the similarity of the two mechanisms and brings them into a common conceptual framework.

Based on the “angular” structure presented in the previous chapter, molecular conformations imposed by the effect of the steric hindrance around the D–A bonds were investigated in chapters 5 and 6, exhibiting profoundly different excited state properties. The energy barrier between two triplet states can be tuned by conformational control, due to the alteration of the bulky substituents on the D unit (chapter 5). With increasing bulkiness of the substituents, the origin of the phosphorescence changes from a lower triplet to a higher triplet state, while the intermediate case shows dual phosphorescence at room temperature. Chapter 6 investigates the PICT and TICT conformers, which were selectively controlled by substituting a methyl group either on the D or A unit. This conformational control led to efficient triplet harvesting by a TADF mechanism in TICT, or RTP in PICT geometries. This work involves the study of molecular crystals and provides guidelines to control the mechanism of triplet harvesting through conformational change.

Further studies of the TADF mechanism were carried out to investigate how to fine-tune the electronic interactions of the D and A units by manipulating the donor or acceptor strength in D–A–D molecules (chapters 7 and 8). In chapter 7, energy alignment between the ^3LE and $^1\text{CT}/^3\text{CT}$ states was achieved by matching the D and A strength. Further increasing the donor strength led to a low-lying triplet state of CT character (^3CT) and a larger ΔE_{ST} , but unexpectedly a faster RISC. This alternate TADF mechanism involved the upper-state crossing from a high-lying triplet state $^3\text{LE}_{\text{D}}$ to the ^1CT , while the smaller DF contribution was ascribed to the competitive relaxation from $^3\text{LE}_{\text{D}}$ to (non-emissive) ^3CT . Chapter 8 presents the colour-tuning effect on the emission of a series of D–A–D materials (from green

to orange-red) by changing the acceptor substitution patterns. This study provides a simple strategy to design organic molecules with high PLQYs and small ΔE_{ST} necessary for high TADF efficiency.

9.2 Future Work

Several improvements in our understanding of the fundamental mechanisms of TADF and RTP were outlined previously, which will inform in molecular design and performance improvements in future. There are nonetheless several aspects not completely understood, mainly concerning the current state-of-the-art applications in OLEDs.

One limitation for OLED applications is a lack of stable blue TADF emitters, which requires a small ΔE_{ST} and a weak CT character. However, these two criteria are currently believed to be mutually exclusive. This is because matching of the D and A strength for a small ΔE_{ST} gives a strong CT character, with emission almost inevitably shifted to longer wavelengths. Emitters with weaker D or A units show more blue emission and faster radiative rates, but with a large ΔE_{ST} . This results in longer-lived triplet excited states that are more susceptible to luminescent quenching, leading to pronounced efficiency roll-off and potential device instability. This limitation also makes the current metal-free RTP emitters unsuitable for applications in OLEDs. In the other hand, the short lifetime of RTP emitters caused by the outcompeting nonradiative processes limits the developments in other applications. Therefore, more research needs to address molecular designs to reduce the lifetime of the triplet excitons and suppressing the nonradiative channels, possibly through wholly new emission mechanisms, *e.g.* designing hyper blue TADF emitters and rigidifying molecular structures for ultralong RTP.

Ideal TADF emitters with high RISC rates should also have a fast radiative rate constant to promote strong luminescence and a short excited state lifetime, which is highly beneficial to device stability. Thus, a balance between PLQY and triplet harvesting efficiency is required to bring significant advantages for application in OLEDs. This trade-off can be potentially solved either by using multiple D and A units to increase the CT channels or choosing suitable D and A units.

More future directions are promising towards this field, such as employing new D and A linking patterns, achieving organic long persistent luminescence through charge separation and charge recombination. These feasible studies will certainly have strong impact on future applications.

Bibliography

- [1] Valeur, B. & Berberan-Santos, M. N. *Molecular fluorescence: principles and applications* (John Wiley & Sons, 2012).
- [2] Northey, T., Stacey, J. & Penfold, T. The role of solid state solvation on the charge transfer state of a thermally activated delayed fluorescence emitter. *Journal of Materials Chemistry C* **5**, 11001–11009 (2017).
- [3] Martin, R. L. Natural transition orbitals. *The Journal of Chemical Physics* **118**, 4775–4777 (2003).
- [4] Reineke, S., Thomschke, M., Lüssem, B. & Leo, K. White organic light-emitting diodes: Status and perspective. *Reviews of Modern Physics* **85**, 1245 (2013).
- [5] Tang, C. W. & VanSlyke, S. A. Organic electroluminescent diodes. *Applied Physics Letters* **51**, 913–915 (1987).
- [6] Baldo, M., O’Brien, D., Thompson, M. & Forrest, S. Excitonic singlet-triplet ratio in a semiconducting organic thin film. *Physical Review B* **60**, 14422 (1999).
- [7] Baldo, M. A. *et al.* Highly efficient phosphorescent emission from organic electroluminescent devices. *Nature* **395**, 151 (1998).
- [8] Kawamura, Y. *et al.* 100% phosphorescence quantum efficiency of Ir (III) complexes in organic semiconductor films. *Applied Physics Letters* **86**, 071104 (2005).

- [9] de Moraes, I. R., Scholz, S., Lüssem, B. & Leo, K. Analysis of chemical degradation mechanism within sky blue phosphorescent organic light emitting diodes by laser-desorption/ionization time-of-flight mass spectrometry. *Organic Electronics* **12**, 341–347 (2011).
- [10] Seifert, R. *et al.* Chemical degradation mechanisms of highly efficient blue phosphorescent emitters used for organic light-emitting diodes. *Organic Electronics* **14**, 115–123 (2013).
- [11] Fukagawa, H., Shimizu, T., Iwasaki, Y. & Yamamoto, T. Operational lifetimes of organic light-emitting diodes dominated by Förster resonance energy transfer. *Scientific Reports* **7**, 1735 (2017).
- [12] Uoyama, H., Goushi, K., Shizu, K., Nomura, H. & Adachi, C. Highly efficient organic light-emitting diodes from delayed fluorescence. *Nature* **492**, 234 (2012).
- [13] Lee, C. W. & Lee, J. Y. Systematic control of photophysical properties of host materials for high quantum efficiency above 25% in green thermally activated delayed fluorescent devices. *ACS Applied Materials & Interfaces* **7**, 2899–2904 (2015).
- [14] Zhang, Q. *et al.* Design of efficient thermally activated delayed fluorescence materials for pure blue organic light-emitting diodes. *Journal of the American Chemical Society* **134**, 14706–14709 (2012).
- [15] Miwa, T. *et al.* Blue organic light-emitting diodes realizing external quantum efficiency over 25% using thermally activated delayed fluorescence emitters. *Scientific Reports* **7**, 284 (2017).
- [16] Hirata, S. *et al.* Efficient persistent room temperature phosphorescence in organic amorphous materials under ambient conditions. *Advanced Functional Materials* **23**, 3386–3397 (2013).
- [17] Reineke, S. & Baldo, M. A. Room temperature triplet state spectroscopy of organic semiconductors. *Scientific Reports* **4**, 3797 (2014).

- [18] De Broglie, L. *Particules de spin 1/2* (Gauthier-Villars, Paris, 1952).
- [19] Wardle, B. *Principles and applications of photochemistry* (John Wiley & Sons, 2009).
- [20] Köhler, A. & Bässler, H. Triplet states in organic semiconductors. *Materials Science and Engineering: R: Reports* **66**, 71–109 (2009).
- [21] Pauli, W. Exclusion principle, Lorentz group and reflection of space-time and charge.
- [22] Griffiths, D. J. & Schroeter, D. F. *Introduction to quantum mechanics* (Cambridge University Press, 2018).
- [23] Gijzeman, O. & Kaufman, F. Oxygen quenching of aromatic triplet states in solution. Part 2. *Journal of the Chemical Society, Faraday Transactions 2: Molecular and Chemical Physics* **69**, 721–726 (1973).
- [24] Turro, N. J., Ramamurthy, V., Ramamurthy, V. & Scaiano, J. C. *Principles of molecular photochemistry: an introduction* (University science books, 2009).
- [25] Dias, F. B., Penfold, T. J. & Monkman, A. P. Photophysics of thermally activated delayed fluorescence molecules. *Methods and Applications in Fluorescence* **5**, 012001 (2017).
- [26] Born, M. & Oppenheimer, R. Zur quantentheorie der molekeln. *Annalen der Physik* **389**, 457–484 (1927).
- [27] Dirac, P. A. M. The quantum theory of the emission and absorption of radiation. *Proceedings of the Royal Society of London. Series A, Containing Papers of a Mathematical and Physical Character* **114**, 243–265 (1927).
- [28] Heitler, W. *The quantum theory of radiation* (Courier Corporation, 1984).
- [29] Bowen, E. J. *The chemical aspects of light* (Clarendon Press, 1949).
- [30] Kasha, M. Characterization of electronic transitions in complex molecules. *Discussions of the Faraday society* **9**, 14–19 (1950).

- [31] El-Sayed, M. Spin-Orbit coupling and the radiationless processes in nitrogen heterocyclics. *The Journal of Chemical Physics* **38**, 2834–2838 (1963).
- [32] Marian, C. M. Spin-orbit coupling and intersystem crossing in molecules. *Wiley Interdisciplinary Reviews: Computational Molecular Science* **2**, 187–203 (2012).
- [33] Ogiwara, T., Wakikawa, Y. & Ikoma, T. Mechanism of intersystem crossing of thermally activated delayed fluorescence molecules. *The Journal of Physical Chemistry A* **119**, 3415–3418 (2015).
- [34] Niu, L. *et al.* Hyperfine interaction *vs.* spin-orbit coupling in organic semiconductors. *RSC Advances* **6**, 111421–111426 (2016).
- [35] Hercules, D. M. Fluorescence and phosphorescence analysis: principles and applications. *Fluorescence and Phosphorescence Analysis: Principles and Applications/Ed. David M. Hercules. New York, NY: Interscience Publishers, c1966.* (1966).
- [36] Agranovich, V. M. & Hochstrasser, R. M. *Spectroscopy and excitation dynamics of condensed molecular systems*, vol. 4 (North Holland, 1983).
- [37] Kouimtzi, S. D. Localized states in crystalline semiconductors. *Physica Status Solidi (b)* **153**, 675–681 (1989).
- [38] Turro, N. J. *Modern molecular photochemistry* (University science books, 1991).
- [39] Hung, W.-Y. *et al.* Highly efficient bilayer interface exciplex for yellow organic light-emitting diode. *ACS Applied Materials & Interfaces* **5**, 6826–6831 (2013).
- [40] Graves, D., Jankus, V., Dias, F. B. & Monkman, A. Photophysical investigation of the thermally activated delayed emission from films of m-MTDATA: PBD exciplex. *Advanced Functional Materials* **24**, 2343–2351 (2014).

- [41] Dias, F. B. *et al.* The role of local triplet excited states and D-A relative orientation in thermally activated delayed fluorescence: photophysics and devices. *Advanced Science* **3**, 1600080 (2016).
- [42] Grabowski, Z. R., Rotkiewicz, K. & Rettig, W. Structural changes accompanying intramolecular electron transfer: focus on twisted intramolecular charge-transfer states and structures. *Chemical Reviews* **103**, 3899–4032 (2003).
- [43] Nigam, S. & Rutan, S. Principles and applications of solvatochromism. *Applied Spectroscopy* **55**, 362A–370A (2001).
- [44] Marini, A., Munoz-Losa, A., Biancardi, A. & Mennucci, B. What is solvatochromism? *The Journal of Physical Chemistry B* **114**, 17128–17135 (2010).
- [45] Reineke, S. *et al.* White organic light-emitting diodes with fluorescent tube efficiency. *Nature* **459**, 234 (2009).
- [46] Tobita, S., Arakawa, M. & Tanaka, I. The paramagnetic metal effect on the ligand localized S_1 . *aprx.. fwdarw. T_1 intersystem crossing in the rare-earth-metal complexes with methyl salicylate. The Journal of Physical Chemistry* **89**, 5649–5654 (1985).
- [47] Parker, C. & Hatchard, C. Triplet-singlet emission in fluid solutions. Phosphorescence of eosin. *Transactions of the Faraday Society* **57**, 1894–1904 (1961).
- [48] Parker, C. & Hatchard, C. Delayed fluorescence of pyrene in ethanol. *Transactions of the Faraday Society* **59**, 284–295 (1963).
- [49] Baldo, M. A., Adachi, C. & Forrest, S. R. Transient analysis of organic electrophosphorescence. II. Transient analysis of triplet-triplet annihilation. *Physical Review B* **62**, 10967 (2000).
- [50] Kondakov, D., Pawlik, T., Hatwar, T. & Spindler, J. Triplet annihilation exceeding spin statistical limit in highly efficient fluorescent organic light-emitting diodes. *Journal of Applied Physics* **106**, 124510 (2009).

- [51] Sinha, S. & Monkman, A. Delayed electroluminescence *via* triplet–triplet annihilation in light emitting diodes based on poly [2-methoxy-5-(2'-ethylhexyloxy)-1,4-phenylene vinylene]. *Applied Physics Letters* **82**, 4651–4653 (2003).
- [52] Endo, A. *et al.* Efficient up-conversion of triplet excitons into a singlet state and its application for organic light-emitting diodes. *Applied Physics Letters* **98**, 42 (2011).
- [53] Gibson, J., Monkman, A. P. & Penfold, T. J. The importance of vibronic coupling for efficient reverse intersystem crossing in thermally activated delayed fluorescence molecules. *ChemPhysChem* **17**, 2956–2961 (2016).
- [54] Lim, B. T., Okajima, S., Chandra, A. & Lim, E. Radiationless transitions in electron donor-acceptor complexes: selection rules for $S_1 \rightarrow T$ intersystem crossing and efficiency of $S_1 \rightarrow S_0$ internal conversion. *Chemical Physics Letters* **79**, 22–27 (1981).
- [55] Hontz, E. *et al.* The role of electron-hole separation in thermally activated delayed fluorescence in donor-acceptor blends. *The Journal of Physical Chemistry C* **119**, 25591–25597 (2015).
- [56] Chen, X.-K., Zhang, S.-F., Fan, J.-X. & Ren, A.-M. Nature of highly efficient thermally activated delayed fluorescence in organic light-emitting diode emitters: nonadiabatic effect between excited states. *The Journal of Physical Chemistry C* **119**, 9728–9733 (2015).
- [57] Marian, C. M. Mechanism of the triplet-to-singlet upconversion in the assistant dopant ACRXTN. *The Journal of Physical Chemistry C* **120**, 3715–3721 (2016).
- [58] Penfold, T., Dias, F. & Monkman, A. The theory of thermally activated delayed fluorescence for organic light emitting diodes. *Chemical Communications* **54**, 3926–3935 (2018).

- [59] Gibson, J. & Penfold, T. Nonadiabatic coupling reduces the activation energy in thermally activated delayed fluorescence. *Physical Chemistry Chemical Physics* **19**, 8428–8434 (2017).
- [60] Etherington, M. K., Gibson, J., Higginbotham, H. F., Penfold, T. J. & Monkman, A. P. Revealing the spin–vibronic coupling mechanism of thermally activated delayed fluorescence. *Nature Communications* **7**, 13680 (2016).
- [61] Baleizão, C. & Berberan-Santos, M. N. Thermally activated delayed fluorescence as a cycling process between excited singlet and triplet states: Application to the fullerenes. *The Journal of Chemical Physics* **126**, 204510 (2007).
- [62] Rajamalli, P. *et al.* A new molecular design based on thermally activated delayed fluorescence for highly efficient organic light-emitting diodes. *Journal of the American Chemical Society* **138**, 628–634 (2016).
- [63] Kim, M. *et al.* Correlation of molecular structure with photophysical properties and device performances of thermally activated delayed fluorescent emitters. *The Journal of Physical Chemistry C* **120**, 2485–2493 (2016).
- [64] Zeng, W. *et al.* Achieving nearly 30% external quantum efficiency for orange-red organic light emitting diodes by employing thermally activated delayed fluorescence emitters composed of 1, 8-naphthalimide-acridine hybrids. *Advanced Materials* **30**, 1704961 (2018).
- [65] Wu, K. *et al.* Realizing highly efficient solution-processed homojunction-like sky-blue OLEDs by using thermally activated delayed fluorescent emitters featuring an aggregation-induced emission property. *The Journal of Physical Chemistry Letters* **9**, 1547–1553 (2018).
- [66] Matulaitis, T. *et al.* Impact of donor substitution pattern on the TADF properties in the carbazolyl-substituted triazine derivatives. *The Journal of Physical Chemistry C* **121**, 23618–23625 (2017).
- [67] dos Santos, P. L. *et al.* Triazatruxene: A rigid central donor unit for a D–A3 thermally activated delayed fluorescence material exhibiting sub-microsecond

- reverse intersystem crossing and unity quantum yield *via* multiple singlet–triplet state pairs. *Advanced Science* 1700989 (2018).
- [68] Choi, J., Ahn, D.-S., Oang, K. Y., Cho, D. W. & Ihee, H. Charge transfer-induced torsional dynamics in the excited state of 2, 6-bis (diphenylamino) anthraquinone. *The Journal of Physical Chemistry C* **121**, 24317–24323 (2017).
- [69] Tanaka, H., Shizu, K., Miyazaki, H. & Adachi, C. Efficient green thermally activated delayed fluorescence (TADF) from a phenoxazine–triphenyltriazine (PXZ–TRZ) derivative. *Chemical Communications* **48**, 11392–11394 (2012).
- [70] Tachibana, H., Aizawa, N., Hidaka, Y. & Yasuda, T. Tunable full-color electroluminescence from all-organic optical upconversion devices by near-infrared sensing. *Acs Photonics* **4**, 223–227 (2017).
- [71] Zhang, Q. *et al.* Nearly 100% internal quantum efficiency in undoped electroluminescent devices employing pure organic emitters. *Advanced Materials* **27**, 2096–2100 (2015).
- [72] Zhang, Q. *et al.* Efficient blue organic light-emitting diodes employing thermally activated delayed fluorescence. *Nature Photonics* **8**, 326 (2014).
- [73] dos Santos, P. L., Ward, J. S., Bryce, M. R. & Monkman, A. P. Using guest–host interactions to optimize the efficiency of TADF OLEDs. *The Journal of Physical Chemistry Letters* **7**, 3341–3346 (2016).
- [74] Bui, T.-T., Goubard, F., Ibrahim-Ouali, M., Gigmès, D. & Dumur, F. Recent advances on organic blue thermally activated delayed fluorescence (TADF) emitters for organic light-emitting diodes (OLEDs). *Beilstein Journal of Organic Chemistry* **14**, 282–308 (2018).
- [75] Tao, Y. *et al.* Thermally activated delayed fluorescence materials towards the breakthrough of organoelectronics. *Advanced Materials* **26**, 7931–7958 (2014).
- [76] Hatakeyama, T. *et al.* Ultrapure blue thermally activated delayed fluorescence molecules: efficient HOMO–LUMO separation by the multiple resonance effect. *Advanced Materials* **28**, 2777–2781 (2016).

- [77] Cai, X. & Su, S.-J. Marching toward highly efficient, pure-blue, and stable thermally activated delayed fluorescent organic light-emitting diodes. *Advanced Functional Materials* **28**, 1802558 (2018).
- [78] Im, Y. *et al.* Molecular design strategy of organic thermally activated delayed fluorescence emitters. *Chemistry of Materials* **29**, 1946–1963 (2017).
- [79] Cui, L.-S. *et al.* Controlling singlet–triplet energy splitting for deep-blue thermally activated delayed fluorescence emitters. *Angewandte Chemie International Edition* **56**, 1571–1575 (2017).
- [80] Kim, M., Jeon, S. K., Hwang, S.-H. & Lee, J. Y. Stable blue thermally activated delayed fluorescent organic light-emitting diodes with three times longer lifetime than phosphorescent organic light-emitting diodes. *Advanced Materials* **27**, 2515–2520 (2015).
- [81] Park, I. S., Lee, J. & Yasuda, T. High-performance blue organic light-emitting diodes with 20% external electroluminescence quantum efficiency based on pyrimidine-containing thermally activated delayed fluorescence emitters. *Journal of Materials Chemistry C* **4**, 7911–7916 (2016).
- [82] Masui, K., Nakanotani, H. & Adachi, C. Analysis of exciton annihilation in high-efficiency sky-blue organic light-emitting diodes with thermally activated delayed fluorescence. *Organic Electronics* **14**, 2721–2726 (2013).
- [83] Taneda, M., Shizu, K., Tanaka, H. & Adachi, C. High efficiency thermally activated delayed fluorescence based on 1, 3, 5-tris(4-(diphenylamino) phenyl)-2, 4, 6-tricyanobenzene. *Chemical Communications* **51**, 5028–5031 (2015).
- [84] Kabe, R., Notsuka, N., Yoshida, K. & Adachi, C. Afterglow organic light-emitting diode. *Advanced Materials* **28**, 655–660 (2016).
- [85] Hirata, S. & Vacha, M. White afterglow room-temperature emission from an isolated single aromatic unit under ambient condition. *Advanced Optical Materials* **5**, 1600996 (2017).

- [86] Xu, B. *et al.* White-light emission from a single heavy atom-free molecule with room temperature phosphorescence, mechanochromism and thermochromism. *Chemical Science* **8**, 1909–1914 (2017).
- [87] Yang, Z. *et al.* Intermolecular electronic coupling of organic units for efficient persistent room-temperature phosphorescence. *Angewandte Chemie* **128**, 2221–2225 (2016).
- [88] Zhang, G., Palmer, G. M., Dewhirst, M. W. & Fraser, C. L. A dual-emissive-materials design concept enables tumour hypoxia imaging. *Nature Materials* **8**, 747 (2009).
- [89] Xu, S., Chen, R., Zheng, C. & Huang, W. Excited state modulation for organic afterglow: materials and applications. *Advanced Materials* **28**, 9920–9940 (2016).
- [90] Wolfbeis, O. S. Sensor paints. *Advanced Materials* **20**, 3759–3763 (2008).
- [91] Feng, Y., Cheng, J., Zhou, L., Zhou, X. & Xiang, H. Ratiometric optical oxygen sensing: a review in respect of material design. *Analyst* **137**, 4885–4901 (2012).
- [92] Jethi, L., Krause, M. M. & Kambhampati, P. Toward ratiometric nanothermometry *via* intrinsic dual emission from semiconductor nanocrystals. *The Journal of Physical Chemistry Letters* **6**, 718–721 (2015).
- [93] Xiao, L. *et al.* Highly efficient room-temperature phosphorescence from halogen-bonding-assisted doped organic crystals. *The Journal of Physical Chemistry A* **121**, 8652–8658 (2017).
- [94] Reineke, S. *et al.* Highly efficient, dual state emission from an organic semiconductor. *Applied Physics Letters* **103**, 163.1 (2013).
- [95] Zhao, W. *et al.* Rational molecular design for achieving persistent and efficient pure organic room-temperature phosphorescence. *Chem* **1**, 592–602 (2016).

- [96] Schmidt, K. *et al.* Intersystem crossing processes in nonplanar aromatic heterocyclic molecules. *The Journal of Physical Chemistry A* **111**, 10490–10499 (2007).
- [97] Bolton, O., Lee, K., Kim, H.-J., Lin, K. Y. & Kim, J. Activating efficient phosphorescence from purely organic materials by crystal design. *Nature Chemistry* **3**, 205 (2011).
- [98] Wang, J. *et al.* A facile strategy for realizing room temperature phosphorescence and single molecule white light emission. *Nature Communications* **9**, 2963 (2018).
- [99] Chen, X. *et al.* Versatile room-temperature-phosphorescent materials prepared from n-substituted naphthalimides: Emission enhancement and chemical conjugation. *Angewandte Chemie International Edition* **55**, 9872–9876 (2016).
- [100] Huang, R. *et al.* The influence of molecular conformation on the photophysics of organic room temperature phosphorescent luminophores. *Journal of Materials Chemistry C* **6**, 9238–9247 (2018).
- [101] Chen, C. *et al.* Intramolecular charge transfer controls switching between room temperature phosphorescence and thermally activated delayed fluorescence. *Angewandte Chemie* **130**, 16645–16649 (2018).
- [102] Ward, J. S. *et al.* The interplay of thermally activated delayed fluorescence (TADF) and room temperature organic phosphorescence in sterically-constrained donor–acceptor charge-transfer molecules. *Chemical Communications* **52**, 2612–2615 (2016).
- [103] Gong, Y. *et al.* Achieving persistent room temperature phosphorescence and remarkable mechanochromism from pure organic luminogens. *Advanced Materials* **27**, 6195–6201 (2015).
- [104] Yang, L. *et al.* Aggregation-induced intersystem crossing: a novel strategy for efficient molecular phosphorescence. *Nanoscale* **8**, 17422–17426 (2016).

- [105] Xiong, Y. *et al.* Designing efficient and ultralong pure organic room-temperature phosphorescent materials by structural isomerism. *Angewandte Chemie International Edition* (2018).
- [106] Mukherjee, S. & Thilagar, P. Recent advances in purely organic phosphorescent materials. *Chemical Communications* **51**, 10988–11003 (2015).
- [107] He, Z. *et al.* White light emission from a single organic molecule with dual phosphorescence at room temperature. *Nature Communications* **8**, 416 (2017).
- [108] Xie, Y. *et al.* How the molecular packing affects the room temperature phosphorescence in pure organic compounds: Ingenious molecular design, detailed crystal analysis, and rational theoretical calculations. *Advanced Materials* **29**, 1606829 (2017).
- [109] An, Z. *et al.* Stabilizing triplet excited states for ultralong organic phosphorescence. *Nature Materials* **14**, 685 (2015).
- [110] Sun, C. *et al.* Twisted molecular structure on tuning ultralong organic phosphorescence. *The Journal of Physical Chemistry Letters* **9**, 335–339 (2018).
- [111] Yang, J. *et al.* The influence of the molecular packing on the room temperature phosphorescence of purely organic luminogens. *Nature Communications* **9**, 840 (2018).
- [112] Cai, S. *et al.* Visible-light-excited ultralong organic phosphorescence by manipulating intermolecular interactions. *Advanced Materials* **29**, 1701244 (2017).
- [113] Shimizu, M. *et al.* Siloxy group-induced highly efficient room temperature phosphorescence with long lifetime. *The Journal of Physical Chemistry C* **120**, 11631–11639 (2016).
- [114] Ma, H., Peng, Q., An, Z., Huang, W. & Shuai, Z. Efficient and long-lived room-temperature organic phosphorescence: theoretical descriptors for molecular designs. *Journal of the American Chemical Society* **141**, 1010–1015 (2018).

- [115] Kulkarni, A. P., Tonzola, C. J., Babel, A. & Jenekhe, S. A. Electron transport materials for organic light-emitting diodes. *Chemistry of Materials* **16**, 4556–4573 (2004).
- [116] Kalyani, N. T. & Dhoble, S. Organic light emitting diodes: Energy saving lighting technology—A review. *Renewable and Sustainable Energy Reviews* **16**, 2696–2723 (2012).
- [117] Lu, S.-Y., Mukhopadhyay, S., Froese, R. & Zimmerman, P. M. Virtual screening of hole transport, electron transport, and host layers for effective OLED design. *Journal of Chemical Information and Modeling* **58**, 2440–2449 (2018).
- [118] Adachi, C., Baldo, M. A., Thompson, M. E. & Forrest, S. R. Nearly 100% internal phosphorescence efficiency in an organic light-emitting device. *Journal of Applied Physics* **90**, 5048–5051 (2001).
- [119] Hung, L., Tang, C. W. & Mason, M. G. Enhanced electron injection in organic electroluminescence devices using an Al/LiF electrode. *Applied Physics Letters* **70**, 152–154 (1997).
- [120] Park, Y. H., Kim, Y., Sohn, H. & An, K.-S. Concentration quenching effect of organic light-emitting devices using DCM1-doped tetraphenylgermole. *Journal of Physical Organic Chemistry* **25**, 207–210 (2012).
- [121] Brunner, K. *et al.* Carbazole compounds as host materials for triplet emitters in organic light-emitting diodes: tuning the HOMO level without influencing the triplet energy in small molecules. *Journal of the American Chemical Society* **126**, 6035–6042 (2004).
- [122] Masters, B. R. Principles of fluorescence spectroscopy. *Journal of Biomedical Optics* **13**, 029901 (2008).
- [123] Williams, A. T. R., Winfield, S. A. & Miller, J. N. Relative fluorescence quantum yields using a computer-controlled luminescence spectrometer. *Analyst* **108**, 1067–1071 (1983).

- [124] Dhimi, S. *et al.* Phthalocyanine fluorescence at high concentration: dimers or reabsorption effect? *Photochemistry and Photobiology* **61**, 341–346 (1995).
- [125] Greenham, N. *et al.* Measurement of absolute photoluminescence quantum efficiencies in conjugated polymers. *Chemical Physics Letters* **241**, 89–96 (1995).
- [126] Pålsson, L.-O. & Monkman, A. P. Measurements of solid-state photoluminescence quantum yields of films using a fluorimeter. *Advanced Materials* **14**, 757–758 (2002).
- [127] Becker, W. *Advanced time-correlated single photon counting techniques*, vol. 81 (Springer Science & Business Media, 2005).
- [128] Hirvonen, L. M. & Suhling, K. Wide-field TCSPC: methods and applications. *Measurement Science and Technology* **28**, 012003 (2016).
- [129] Rothe, C. & Monkman, A. P. Triplet exciton migration in a conjugated polyfluorene. *Physical Review B* **68**, 075208 (2003).
- [130] Cardona, C. M., Li, W., Kaifer, A. E., Stockdale, D. & Bazan, G. C. Electrochemical considerations for determining absolute frontier orbital energy levels of conjugated polymers for solar cell applications. *Advanced Materials* **23**, 2367–2371 (2011).
- [131] Data, P., Motyka, R., Lapkowski, M., Suwinski, J. & Monkman, A. P. Spectroelectrochemical analysis of charge carriers as a way of improving poly (p-phenylene)-based electrochromic windows. *The Journal of Physical Chemistry C* **119**, 20188–20200 (2015).
- [132] McCrackin, F. L., Passaglia, E., Stromberg, R. R. & Steinberg, H. L. Measurement of the thickness and refractive index of very thin films and the optical properties of surfaces by ellipsometry. *J. Res. Nat. Bur. Sec. A* **67**, 363–377 (1963).
- [133] Fujiwara, H. *Spectroscopic ellipsometry: principles and applications* (John Wiley & Sons, 2007).

- [134] Pereira, D. d. S. & Monkman, A. P. Methods of analysis of organic light emitting diodes. *Display and Imaging* **2**, 323–337 (2017).
- [135] Forrest, S. R., Bradley, D. D. & Thompson, M. E. Measuring the efficiency of organic light-emitting devices. *Advanced Materials* **15**, 1043–1048 (2003).
- [136] Patel, N., Cina, S. & Burroughes, J. High-efficiency organic light-emitting diodes. *IEEE Journal of Selected Topics in Quantum Electronics* **8**, 346–361 (2002).
- [137] Gather, M. C. & Reineke, S. Recent advances in light outcoupling from white organic light-emitting diodes. *Journal of Photonics for Energy* **5**, 057607 (2015).
- [138] Jones, L. A. The historical background and evolution of the colorimetry report. *JOSA* **33**, 534–543 (1943).
- [139] Kobayashi, T. *et al.* Contributions of a higher triplet excited state to the emission properties of a thermally activated delayed-fluorescence emitter. *Physical Review Applied* **7**, 034002 (2017).
- [140] Simon, Y. C. & Weder, C. Low-power photon upconversion through triplet–triplet annihilation in polymers. *Journal of Materials Chemistry* **22**, 20817–20830 (2012).
- [141] Ratzke, W. *et al.* Effect of conjugation pathway in metal-free room-temperature dual singlet–triplet emitters for organic light-emitting diodes. *The Journal of Physical Chemistry Letters* **7**, 4802–4808 (2016).
- [142] Endo, A. *et al.* Thermally activated delayed fluorescence from Sn⁴⁺–porphyrin complexes and their application to organic light emitting diodes—A novel mechanism for electroluminescence. *Advanced Materials* **21**, 4802–4806 (2009).
- [143] Dediu, V. A., Hueso, L. E., Bergenti, I. & Taliani, C. Spin routes in organic semiconductors. *Nature Materials* **8**, 707 (2009).

- [144] Dias, F. B. *et al.* Triplet harvesting with 100% efficiency by way of thermally activated delayed fluorescence in charge transfer OLED emitters. *Advanced Materials* **25**, 3707–3714 (2013).
- [145] Jankus, V. *et al.* Highly efficient TADF OLEDs: How the emitter–host interaction controls both the excited state species and electrical properties of the devices to achieve near 100% triplet harvesting and high efficiency. *Advanced Functional Materials* **24**, 6178–6186 (2014).
- [146] Lee, I. & Lee, J. Y. Molecular design of deep blue fluorescent emitters with 20% external quantum efficiency and narrow emission spectrum. *Organic Electronics* **29**, 160–164 (2016).
- [147] Huang, R. *et al.* The contributions of molecular vibrations and higher triplet levels to the intersystem crossing mechanism in metal-free organic emitters. *Journal of Materials Chemistry C* **5**, 6269–6280 (2017).
- [148] Perdew, J. P., Burke, K. & Ernzerhof, M. Generalized gradient approximation made simple. *Physical Review Letters* **77**, 3865 (1996).
- [149] Adamo, C. & Barone, V. Toward reliable density functional methods without adjustable parameters: The PBE0 model. *The Journal of Chemical Physics* **110**, 6158–6170 (1999).
- [150] Frisch, M. *et al.* 09, Revision D. 01, Gaussian. *Inc., Wallingford, CT* (2009).
- [151] Penfold, T. J. On predicting the excited-state properties of thermally activated delayed fluorescence emitters. *The Journal of Physical Chemistry C* **119**, 13535–13544 (2015).
- [152] Raw, S. A. & Taylor, R. J. Recent advances in the chemistry of 1, 2, 4-triazines.
- [153] Pullman, B. & Pullman, A. The oxido-reductive properties of organic dyes of biological importance. *Biochimica et Biophysica Acta* **35**, 535–537 (1959).
- [154] Tech. Rep.

- [155] Malrieu, J.-P. & Pullman, B. Sur les propriétés électroniques de la phénothiazine et de son radical. *Theoretica Chimica Acta* **2**, 293–301 (1964).
- [156] Coubeils, J. & Pullman, B. Molecular orbital study of the conformational properties of phenothiazines. *Theoretica Chimica Acta* **24**, 35–41 (1972).
- [157] Daub, J. *et al.* Competition between conformational relaxation and Intramolecular electron transfer within phenothiazine- pyrene dyads. *The Journal of Physical Chemistry A* **105**, 5655–5665 (2001).
- [158] Stockmann, A. *et al.* Conformational control of photoinduced charge separation within phenothiazine- pyrene dyads. *The Journal of Physical Chemistry A* **106**, 7958–7970 (2002).
- [159] Tanaka, H., Shizu, K., Nakanotani, H. & Adachi, C. Dual intramolecular charge-transfer fluorescence derived from a phenothiazine-triphenyltriazine derivative. *The Journal of Physical Chemistry C* **118**, 15985–15994 (2014).
- [160] dos Santos, P. L., Ward, J. S., Batsanov, A. S., Bryce, M. R. & Monkman, A. P. Optical and polarity control of donor–acceptor conformation and their charge-transfer states in thermally activated delayed-fluorescence molecules. *The Journal of Physical Chemistry C* **121**, 16462–16469 (2017).
- [161] Wang, K. *et al.* Avoiding energy loss on TADF emitters: controlling the dual conformations of D–A structure molecules based on the pseudoplanar segments. *Advanced Materials* **29**, 1701476 (2017).
- [162] Gan, S. *et al.* Integration of aggregation-induced emission and delayed fluorescence into electronic donor–acceptor conjugates. *Journal of Materials Chemistry C* **4**, 3705–3708 (2016).
- [163] Okazaki, M. *et al.* Thermally activated delayed fluorescent phenothiazine–dibenzo [a, j] phenazine–phenothiazine triads exhibiting tricolor-changing mechanochromic luminescence. *Chemical Science* **8**, 2677–2686 (2017).

- [164] Etherington, M. K. *et al.* Regio- and conformational isomerization critical to design of efficient thermally-activated delayed fluorescence emitters. *Nature Communications* **8**, 14987 (2017).
- [165] Dias, F. B. *et al.* Dipolar stabilization of emissive singlet charge transfer excited states in polyfluorene copolymers. *The Journal of Physical Chemistry B* **112**, 6557–6566 (2008).
- [166] Wang, L. *et al.* New blue host materials based on anthracene-containing dibenzothiophene. *Organic Electronics* **12**, 595–601 (2011).
- [167] Lee, H. W., Jeong, S., Lee, S. E., Kim, Y. K. & Yoon, S. S. Blue emitting materials containing dibenzo[b, d]furan and dibenzo[b, d]thiophene for organic light-emitting diodes. *Japanese Journal of Applied Physics* **55**, 06GK07 (2016).
- [168] Guo, J. *et al.* Achieving high-performance nondoped OLEDs with extremely small efficiency roll-off by combining aggregation-induced emission and thermally activated delayed fluorescence. *Advanced Functional Materials* **27**, 1606458 (2017).
- [169] Tang, X. *et al.* Efficient deep-blue electroluminescence based on phenanthroimidazole-dibenzothiophene derivatives with different oxidation states of the sulfur atom. *Chemistry—an Asian Journal* **12**, 552–560 (2017).
- [170] Beljonne, D., Shuai, Z., Pourtois, G. & Bredas, J. Spin-orbit coupling and intersystem crossing in conjugated polymers: A configuration interaction description. *The Journal of Physical Chemistry A* **105**, 3899–3907 (2001).
- [171] Kasha, M. & RAWLS, H. R. Correlation of orbital classification of molecular electronic transitions with transition mechanism: the aromatic amines. *Photochemistry and Photobiology* **7**, 561–569 (1968).
- [172] Chen, X.-K. *et al.* A new design strategy for efficient thermally activated delayed fluorescence organic emitters: from twisted to planar structures. *Advanced Materials* **29**, 1702767 (2017).

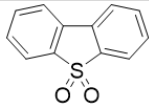
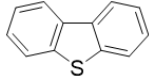
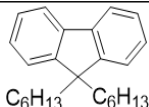
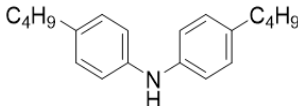
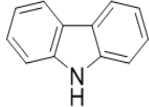
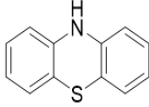
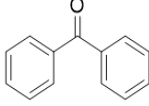
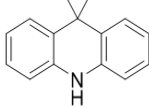
- [173] Di, D. *et al.* High-performance light-emitting diodes based on carbene-metal-amides. *Science* 4345 (2017).
- [174] Shi, Y.-Z. *et al.* Intermolecular charge-transfer transition emitter showing thermally activated delayed fluorescence for efficient non-doped OLEDs. *Angewandte Chemie International Edition* **57**, 9480–9484 (2018).
- [175] Liu, Y., Li, C., Ren, Z., Yan, S. & Bryce, M. R. All-organic thermally activated delayed fluorescence materials for organic light-emitting diodes. *Nature Reviews Materials* **3**, 18020 (2018).
- [176] Zhang, Z. *et al.* Tuning the conformation and color of conjugated polyheterocyclic skeletons by installing ortho-methyl groups. *Angewandte Chemie* (2018).
- [177] Druzhinin, S. I. *et al.* Intramolecular charge transfer with 1-*tert*-butyl-6-cyano-1, 2, 3, 4-tetrahydroquinoline (ntc6) and other aminobenzonitriles. a comparison of experimental vapor phase spectra and crystal structures with calculations. *Journal of the American Chemical Society* **132**, 7730–7744 (2010).
- [178] Aizawa, N., Tsou, C.-J., Park, I. S. & Yasuda, T. Aggregation-induced delayed fluorescence from phenothiazine-containing donor–acceptor molecules for high-efficiency non-doped organic light-emitting diodes. *Polymer Journal* **49**, 197 (2017).
- [179] Xu, B. *et al.* Achieving remarkable mechanochromism and white-light emission with thermally activated delayed fluorescence through the molecular heredity principle. *Chemical Science* **7**, 2201–2206 (2016).
- [180] Lee, S. Y., Yasuda, T., Komiyama, H., Lee, J. & Adachi, C. Thermally activated delayed fluorescence polymers for efficient solution-processed organic light-emitting diodes. *Advanced Materials* **28**, 4019–4024 (2016).
- [181] Yao, L. *et al.* Highly efficient near-infrared organic light-emitting diode based on a butterfly-shaped donor–acceptor chromophore with strong solid-state fluorescence and a large proportion of radiative excitons. *Angewandte Chemie International Edition* **53**, 2119–2123 (2014).

- [182] Mataga, N., Okada, T. & Masuhara, H. *Dynamics and mechanisms of photoinduced electron transfer and related phenomena* (Elsevier, 2012).
- [183] Kawasumi, K. *et al.* Thermally activated delayed fluorescence materials based on homoconjugation effect of donor–acceptor triptycenes. *Journal of the American Chemical Society* **137**, 11908–11911 (2015).
- [184] Santos, P. L. *et al.* Engineering the singlet-triplet energy splitting in a TADF molecule. *Journal of Materials Chemistry C* **4**, 3815–3824 (2016).
- [185] Nobuyasu, R. S. *et al.* Rational design of TADF polymers using a donor–acceptor monomer with enhanced TADF efficiency induced by the energy alignment of charge transfer and local triplet excited states. *Advanced Optical Materials* **4**, 597–607 (2016).
- [186] Kang, J. S. *et al.* High-performance bipolar host materials for blue TADF devices with excellent external quantum efficiencies. *Journal of Materials Chemistry C* **4**, 4512–4520 (2016).
- [187] Hladka, I. *et al.* Polymorphism of derivatives of *tert*-butyl substituted acridan and perfluorobiphenyl as sky-blue OLED emitters exhibiting aggregation induced thermally activated delayed fluorescence. *Journal of Materials Chemistry C* **6**, 13179–13189 (2018).
- [188] Boese, A. D. & Martin, J. M. Development of density functionals for thermochemical kinetics. *The Journal of Chemical Physics* **121**, 3405–3416 (2004).
- [189] Kukhta, N. A., da Silva Filho, D. A., Volyniuk, D., Grazulevicius, J. V. & Sini, G. Can fluorenone-based compounds emit in the blue region? Impact of the conjugation length and the ground-state aggregation. *Chemistry of Materials* **29**, 1695–1707 (2017).
- [190] Bredas, J.-L. Organic electronics: does a plot of the HOMO–LUMO wave functions provide useful information? (2017).
- [191] Adachi, C. Third-generation organic electroluminescence materials. *Japanese Journal of Applied Physics* **53**, 060101 (2014).

- [192] Ward, J. S. *et al.* Bond rotations and heteroatom effects in donor–acceptor–donor molecules: implications for thermally activated delayed fluorescence and room temperature phosphorescence. *The Journal of Organic Chemistry* **83**, 14431–14442 (2018).
- [193] Kim, J. U. *et al.* Thermally activated delayed fluorescence of bis(9, 9-dimethyl-9, 10-dihydroacridine)dibenzo[b, d]thiophene 5, 5-dioxide derivatives for organic light-emitting diodes. *Journal of Luminescence* **190**, 485–491 (2017).

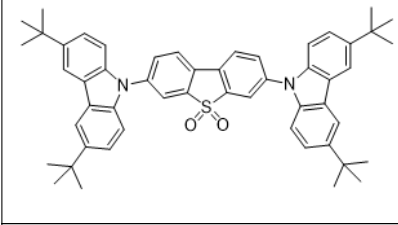
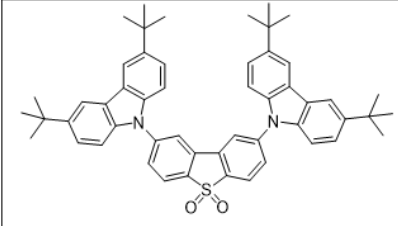
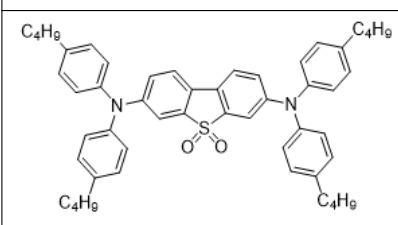
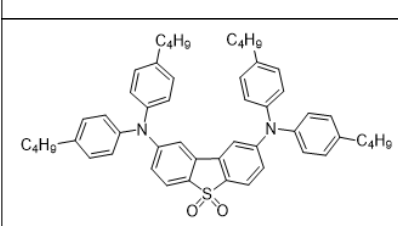
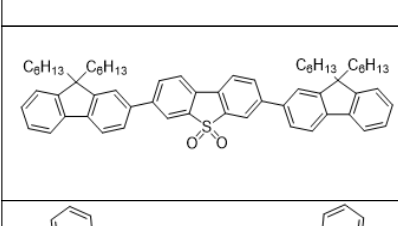
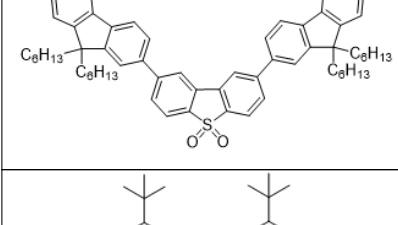
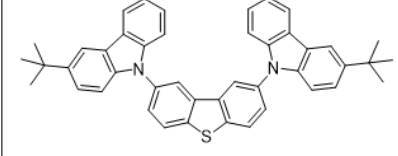
Appendix A

A.1 Chemical Structures

Chemical Structure	Name	Short Name	Chapter
Donor and Acceptor Units			
	Dibenzothiophene- <i>S,S</i> -dioxide	DBTO2	4,8
	Dibenzothiophene	DBT	4,5,7
	9,9-Dihexyl-9H-fluorene	fluorene	4
	<i>N,N</i> -Bis-4- <i>n</i> -butylphenylamine	DPA	4
	9 <i>H</i> -Carbazole	Cz	4
	Phenathazine	PTZ	5,6
	Benzophenone	BP	6
	Acridine	Ac	7,8

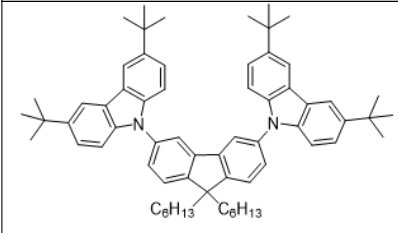
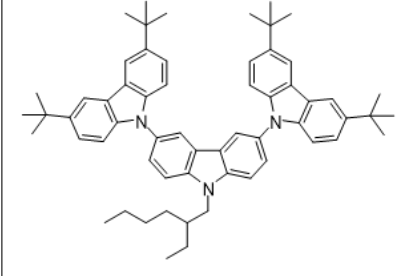
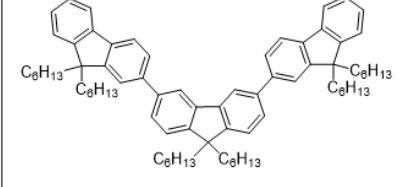
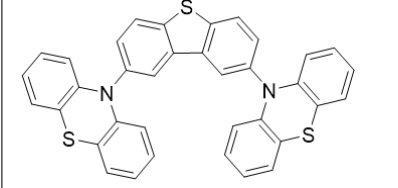
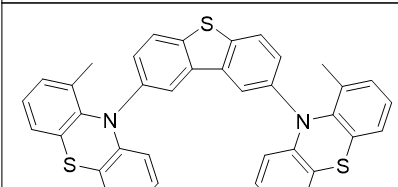
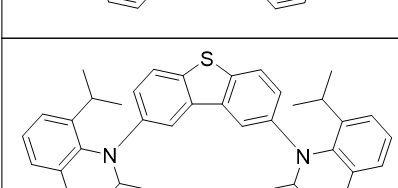
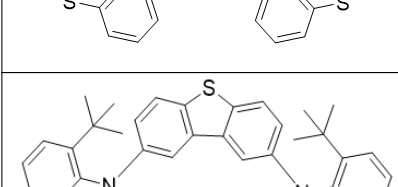
see next page

continue

Chemical Structure	Name	Short Name	Chapter
D–A–D (D–A) Molecules			
	3,7-Bis(3,6-di- <i>tert</i> -butyl-9 <i>H</i> -carbazol-9-yl)dibenzothiophene- <i>S,S</i> -dioxide	1	4
	2,8-Bis(3,6-di- <i>tert</i> -butyl-9 <i>H</i> -carbazol-9-yl)dibenzothiophene- <i>S,S</i> -dioxide	2	4
	3,7-Bis[<i>N,N</i> -di(4-butylphenyl)amino]dibenzothiophene- <i>S,S</i> -dioxide	3	4
	2,8-Bis[<i>N,N</i> -di(4-butylphenyl)amino]dibenzothiophene- <i>S,S</i> -dioxide	4	4
	3,7-Bis(9,9-dihexyl-9 <i>H</i> -fluorene)dibenzothiophene- <i>S,S</i> -dioxide	5	4
	2,8-Bis(9,9-dihexyl-9 <i>H</i> -fluorene)dibenzothiophene- <i>S,S</i> -dioxide	6	4
	2,8-Bis(3,6-di- <i>tert</i> -butyl-9 <i>H</i> -carbazol-9-yl)dibenzothiophene	7	4

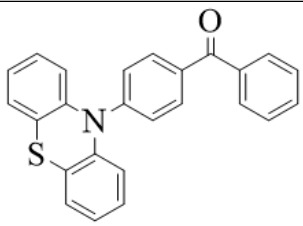
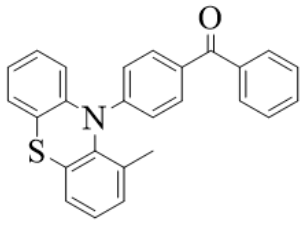
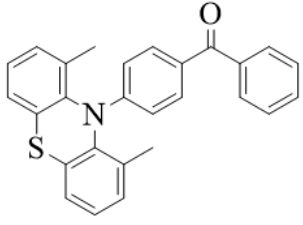
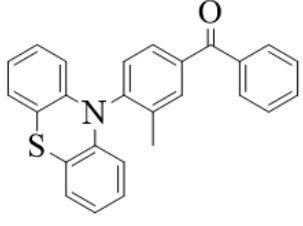
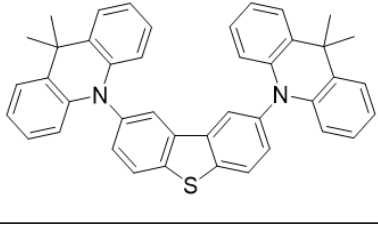
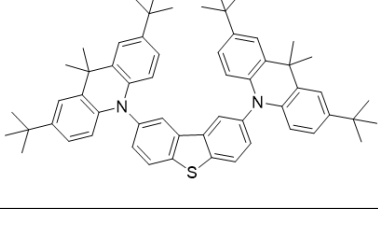
see next page

continue

Chemical Structure	Name	Short Name	Chapter
	2,8-Bis(3,6-di- <i>tert</i> -butyl-9 <i>H</i> -carbazol-9-yl)-9,9-dihexyl-9 <i>H</i> -fluorene	8	4
	2,8-Bis(3,6-di- <i>tert</i> -butyl-9 <i>H</i> -carbazol-9-yl)-9-(2-ethylhexyl)-9 <i>H</i> -carbazole	9	4
	2,8-Bis(9,9-dihexyl-9 <i>H</i> -fluorene)-9,9-dihexyl-9 <i>H</i> -fluorene	10	4
	2,8-Bis(10 <i>H</i> -phenothiazin-10-yl)dibenzo[<i>b,d</i>]thiophene	DPTZ-DBT	5
	2,8-Bis(1-methyl-10 <i>H</i> -phenothiazin-10-yl)dibenzo[<i>b,d</i>]thiophene	DPTZ-Me-DBT	5
	2,8-Bis(1- <i>isopropyl</i> -10 <i>H</i> -phenothiazin-10-yl)dibenzo[<i>b,d</i>]thiophene	DPTZ- <i>i</i> Pr-DBT	5
	2,8-Bis(1- <i>tert</i> -butyl-10 <i>H</i> -phenothiazin-10-yl)dibenzo[<i>b,d</i>]thiophene	DPTZ- <i>t</i> Bu-DBT	5

see next page

continue

Chemical Structure	Name	Short Name	Chapter
	(4-(10 <i>H</i> -Phenothiazin-10-yl)phenyl) (phenyl)methanone	OP	6
	(4-(1-Methyl-10 <i>H</i> -phenothiazin-10-yl)phenyl) (phenyl)methanone	OPM	6
	(4-(1,9-Dimethyl-10 <i>H</i> -phenothiazin-10-yl)phenyl) (phenyl)methanone	OP2M	6
	(3-Methyl-4-(10 <i>H</i> -phenothiazin-10-yl)phenyl) (phenyl)methanone	OMP	6
	2,8-Bis(9,9-dimethylacridin-10(9 <i>H</i>)-yl)dibenzo[<i>b,d</i>]thiophene	DAc-DBT	7
	2,8-Bis(2,7- <i>tert</i> -butyl-9,9-dimethylacridin-10(9 <i>H</i>)-yl)dibenzo[<i>b,d</i>]thiophene	DtBuAc-DBT	7

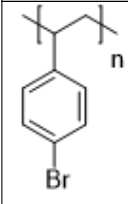
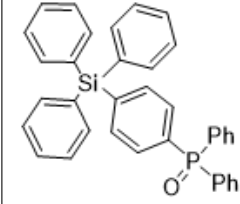
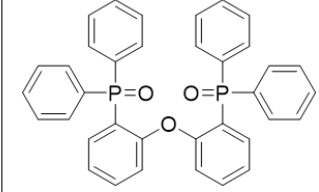
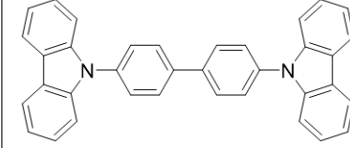
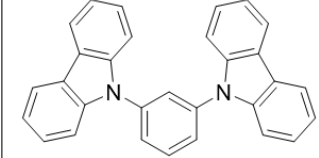
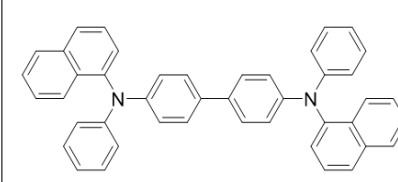
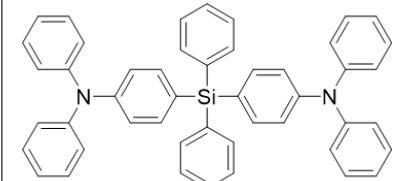
see next page

continue

Chemical Structure	Name	Short Name	Chapter
	2,8-Bis(2,7-dimethoxy-9,9-dimethylacridin-10(9H)-yl)dibenzo [b,d]thiophene	DOMeAc-DBT	7
	3,7-Bis(9,9-dimethylacridin-10(9H)-yl)dibenzothiophene-S,S-dioxide	DBTO2-DAC	8
	3,7-Bis(9,9-dimethylacridin-10(9H)-yl)-1-methoxy-dibenzo thiophene-S,S-dioxide	MeODBT02-DAC	8
	3,7-Bis(9,9-dimethylacridin-10(9H)-yl)-1-methylthio-dibenzo thiophene-S,S-dioxide	MeSDBT02-DAC	8
	3,7-Bis(9,9-dimethylacridin-10(9H)-yl)-1-fluorine-dibenzo thiophene-S,S-dioxide	FDBT02-DAC	8
	3,7-Bis(9,9-dimethylacridin-10(9H)-yl)-1-cyano-dibenzo thiophene-S,S-dioxide	CNDBT02-DAC	8
Host Compounds			
	Cyclo olefin polymer (COP)	zeonex	4,5,6,7,8

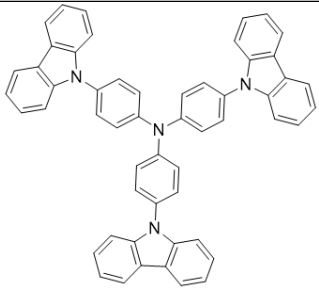
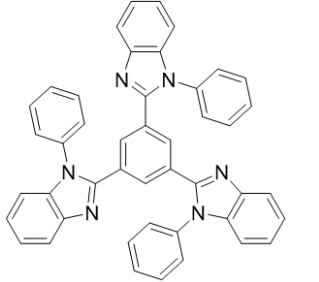
see next page

continue

Chemical Structure	Name	Short Name	Chapter
	Poly(4-bromostyrene)	PBrS	4
	Diphenylphosphine oxide-4-(triphenylsilyl)phenyl	TSPO1	4
	Bis[2-(diphenylphosphino)phenyl]ether oxide	DPEPO	4,8
	1,3-Bis(carbazol-9-yl)benzene	mCP	6
	4,4'-Bis(carbazol-9-yl)biphenyl	CBP	6
Transport Compounds			
	<i>N,N'</i> -Di(1-naphthyl)- <i>N,N'</i> -diphenyl-(1,1'-biphenyl)-4,4'-diamine	α -NPD	6,8
	4,4'-(Diphenylsilanediy)bis(<i>N,N</i> -diphenylaniline)	TSBPA	6

see next page

continue

Chemical Structure	Name	Short Name	Chapter
	Tris(4-carbazoyl-9-ylphenyl)amine	TCTA	8
	2,2',2''-(1,3,5-Benzenetriyl)-tris(1-phenyl-1- <i>H</i> -benzimidazole)	TPBi	6,8

A.2 Publications

- 1) C. Chen,[†] **R. Huang**,[†] A. S. Batsanov, P. Pander, Y.-T. Hsu, Z. Chi, F. B. Dias, M. R. Bryce, “Intramolecular Charge Transfer Controls Switching Between Room Temperature Phosphorescence and Thermally Activated Delayed Fluorescence.” *Angew. Chem.*, **2018**, 130(50), 16645-16649 (*Angew. Chem. Int. Ed.* **2018**, 57, 16407-16411).
- 2) **R. Huang**, J. S. Ward, N. A. Kukhta, J. Avó, J. Gibson, T. J. Penfold, J. C. Lima, A. S. Batsanov, M. N. Berberan-Santos, M. R. Bryce, F. B. Dias, “The influence of molecular conformation on the photophysics of organic room temperature phosphorescent luminophores.” *J. Mater. Chem. C*, **2018**, 6(34), 9238-9247.
- 3) **R. Huang**, J. Avó, T. Northey, E. Channing-Pearce, P. L. dos Santos, J. S. Ward, P. Data, M. K. Etherington, M. A. Fox, T. J. Penfold, M. N. Berberan-Santos, J. C. Lima, M. R. Bryce and F. B. Dias, “The contributions of molecular vibrations and higher triplet levels to the intersystem crossing mechanism in metal-free organic emitters.” *J. Mater. Chem. C*, **2017**, 5(25), 6269-6280.
- 4) X. Lv, **R. Huang**, S. Sun, Q. Zhang, S. Xiang, S. Ye, P. Leng, F. B. Dias, L. Wang, “Blue TADF Emitters Based on Indenocarbazole Derivatives with High Photoluminescence and Electroluminescence Efficiencies.” *ACS Appl. Mater. Interfaces*, **2019**, 11(11), 10758-10767.
- 5) P. L. dos Santos, O. J. Silveira, **R. Huang**, G. A. M. Jardim, M. J. S. Matos, E. N. da Silva Júnior, A. P. Monkman, F. B. Dias and L. A. Cury, “Dynamics of aggregated states resolved by gated fluorescence in films of room temperature phosphorescent emitters.” *Phys. Chem. Chem. Phys.*, **2019**, 21, 3814-3821.
- 6) **R. Huang**,[†] N. A. Kukhta,[†] J. S. Ward, A. Danos, A. S. Batsanov, M. R. Bryce, F. B. Dias, “Upper-State Crossing from a Local Triplet State Induced by Control of Donor Strength in Blue Thermally Activated Delayed Fluorescent Emitters.” *J. Mater. Chem. C* under review.
- 7) X. Zheng,[†] **R. Huang**,[†] C. Zhong, M. Huang, G. Xie, F. B. Dias, C. Yang, “Multi-(Donor/Acceptor) TADF Emitter with Simultaneous Through-Space and Through-Bond Charge Transfer: Non-doped, Solution-Processed Sky-Blue OLEDs with High Efficiency.” *Angew. Chem.* under review.